UNIVERSITÄT OSNABRÜCK

Department of Physics
Numerical Physics: Modeling

Analysis of Particle Precipitation and Development of the Atmospheric Ionization Module OSnabrück - Aimos

A dissertation submitted to the
University of Osnabrück
for the degree of

DOCTOR OF SCIENCES

presented by
Jan Maik Wissing,

Diplom Physicist
born February, 20th 1980

examiners:
Prof. Dr. May-Britt Kallenrode
Prof. Dr. Bernd Heber
Prof. Dr. Karl-Heinz Glaßmeier

2010

Abstract

The goal of this thesis is to improve our knowledge on energetic particle precipitation into the Earth's atmosphere from the thermosphere to the surface. The particles origin from the Sun or from temporarily trapped populations inside the magnetosphere.

The best documented influence of solar (high-) energetic particles on the atmosphere is the Ozone depletion in high latitudes, attributed to the generation of HO_x and NO_x by precipitating particles (*Crutzen et al.*, 1975; *Solomon et al.*, 1981; *Reid et al.*, 1991). In addition *Callis et al.* (1996b, 2001) and *Randall et al.* (2005, 2006) point out the importance of low-energetic precipitating particles of magnetospheric origin, creating NO_x in the lower thermosphere, which may be transported downwards where it also contributes to Ozone depletion.

The incoming particle flux is dramatically changing as a function of auroral/geomagnetical activity and in particular during solar particle events. As a result, the degree of ionization and the chemical composition of the atmosphere are substantially affected by the state of the Sun. Therefore the direct energetic or dynamical influences of ions on the upper atmosphere depend on solar variability at different time scales.

Influences on chemistry have been considered so far with simplified precipitation patterns, limited energy range and restrictions to certain particle species, see e.g. *Jackman et al.* (2000); *Sinnhuber et al.* (2003b, for solar energetic protons and no spatial differentiation), and *Callis et al.* (1996b, 2001, for magnetospheric electrons only). A comprehensive atmospheric ionization model with spatially resolved particle precipitation including a wide energy range and all main particle species as well as a dynamic magnetosphere was missing.

In the scope of this work, a 3-D precipitation model of solar and magnetospheric particles has been developed. Temporal as well as spatial ionization patterns will be discussed. Apart from that, the ionization data are used in different climate models, allowing (a) simulations of NO_x and HO_x formation and transport, (b) comparisons to incoherent scatter radar measurements and (c) inter-comparison of the chemistry part in different models and comparison of model results to MIPAS observations. In a bigger scope the ionization data may be used to better constrain the natural sources of climate change or consequences for atmospheric dynamics due to local temperature changes by precipitating particles and their implications for chemistry. Thus the influence of precipitating energetic particles on the composition and dynamics of the atmosphere is a challenging issue in climate modeling. The ionization data is available online and can be adopted automatically to any user specific model grid.

Zusammenfassung

Ziel dieser Arbeit ist es, unser Wissen über den Einfall energetischer Teilchen in die Atmosphäre zu erweitern. Die Studie erstreckt sich vom Erdboden bis zur Thermosphäre und umfasst sowohl Teilchen solaren Ursprungs als auch Teilchen aus der zeitweise gefangenen magnetosphärischen Population.

Der am besten dokumentierte Einfluss hochenergetischer solarer Teilchen auf die Atmosphäre ist der Ozonabbau in hohen Breiten. Dieser wird durch die beim Teilcheneinfall entstehenden HO_x und NO_x Moleküle erzeugt (*Crutzen et al.*, 1975; *Solomon et al.*, 1981; *Reid et al.*, 1991). Des Weiteren werden die weniger energiereichen Teilchen aus der Magnetosphäre als wichtige Quelle für die NO_x Produktion in der unteren Thermosphäre angesehen. Vertikaler Transport der Stickoxyde ermöglicht auch hier den Ozonabbau in geringeren Höhen (*Callis et al.*, 1996b, 2001; *Randall et al.*, 2005, 2006).

Der einfallende Teilchenfluss wird entscheidend durch die aurorale/geomagnetische Aktivität bestimmt und steigt insbesondere bei solaren Teilchenereignissen sprunghaft an. Damit wird die atmosphärische Ionisation und Zusammensetzung durch die solare Aktivität und deren zeitlichen Verlauf beeinflusst.

Auswirkungen auf die Chemie sind bislang nur mit vereinfachten Einfallsmustern, beschränkten Energiebereichen der einfallenden Teilchen oder Vernachlässigung einzelner Teilchenspezies durchgeführt worden, z.B. *Jackman et al.* (2000); *Sinnhuber et al.* (2003b, jeweils ohne räumliche Auflösung und nur für solare Protonen) und *Callis et al.* (1996b, 2001, ausschließlich für magnetosphärische Elektronen). Ein übergreifendes Modell für die atmosphärische Ionisation mit räumlich aufgelöstem Teilcheneinfall, einem magnetosphärische und solare Teilchen umfassenden Energiebereich, allen wichtigen Teilchensorten sowie einer dynamischen Magnetosphäre gab es bislang nicht.

Im Rahmen dieser Arbeit wurde das 3-D Ionisationsmodell AIMOS entwickelt, das sowohl solare als auch magnetosphärische Teilcheneinfälle berücksichtigt. Zeitliche wie auch räumliche Ionisationsmuster werden diskutiert. Außerdem werden die Ionisationsdaten in verschiedenen Klimamodellen verwendet, um (a) NO_x und HO_x Produktion und deren Transport zu simulieren, (b) die simulierte Elektronendichte mit IS-Radar Messungen zu vergleichen und (c) die Chemiemodule verschiedener Klimamodelle bei gleichem Teilcheneinfall miteinander zu vergleichen sowie deren Ergebnisse MIPAS-Messungen gegenüber zu stellen. Weitere Anwendungsbereiche des Ionisationsmodells sind beispielsweise die Untersuchung der natürlichen Ursachen für Klimawandel oder die Auswirkung von Teilcheneinfall und dessen Auswirkungen auf die atmosphärische Dynamik, insbesondere durch lokale Temperaturänderungen. Folglich sind die einfallenden Teilchen ein anspruchsvolles Thema im Bereich der Klimamodellierung. Die Ionisationsraten des entwickelten Modells sind online verfügbar und können dort automatisch an beliebige Modellgitter angepasst werden.

Acknowledgment

First of all, I would like to thank ***Prof. Dr. May-Britt Kallenrode***. Thank you for mentoring me during all the years, discussing so many topics and widening my scientific horizon.

In the same way, my sincere thanks are given to ***my parents*** for their support in any ways as only parents can do.

In the scientific community I would like to thank:

Jens Kieser (MPI Meteorology, Hamburg) for providing atmospheric parameters as well as cooperation on many presentations, the ARTOS-project and the AIMOS-3 paper,

Hauke Schmidt (MPI Meteorology, Hamburg) for cooperation in the ARTOS-project and valuable comments and discussions concerning the AIMOS-3 paper,

Miriam Sinnhuber (Institute of Environmental Physics, Bremen, now at Karlsruhe Institute of Technology) and her Bremen group members ***Holger Winkler***, ***Nadine Wieters*** and ***Shahin Kazeminejad*** for collaboration in different papers and presentations,

Bernd Funke (Instituto de Astrofísica de Andalucía) as well as ***the whole HEPPA-MIPAS community*** (see Table 8.1) for fruitful results of the model inter-comparison which identified a problem in the highest electron channel,

Mary McCready (SRI International, California), ***Phil Erickson*** (Haystack Observatory, Massachusetts Institute of Technology) and in particular ***Mike Rietveld*** (EISCAT, Tromsø) for explaining details of the incoherent scatter radar measurements,

David Evans and ***Susan Greer*** (National Oceanic and Atmospheric Administration, NOAA, USA) for providing the satellite data and answering a lot of questions concerning data extraction and data quality,

Xiaohua Fang (University of Colorado, Boulder) for discussions on the impact of the geomagnetic field on lateral particle transport inside the atmosphere,

Richard Mewaldt (California Institute of Technology) for pointing out flux differences on different GOES satellites, and

Jan Philipp Bornebusch (University of Osnabrück, now at Cornelsen, Berlin) as a representative of the modeling group at my university. I would like to thank you for very illuminative discussions during the early phase of my thesis.

My personal thanks go to:

Natalie Wilson, thank you for correcting mistyped spellings and

Natalia and ***Natalie***, as you gave me some sportive balance. I enjoyed dancing as well as spending some time outside the university.

Last but definitely not least:

Олеси, you know why you are listed here. Let's say 'for emotional support'. *

Contents

Chapter 1

Introduction

This chapter is giving a brief introduction on the precipitation of energetic charged particles into the atmosphere. Particle sources as well as the impact of these particles on the atmosphere will be discussed. The development of *Atmosphere Ionization Module OSnabrück* (AIMOS) has been the core of the work leading to this thesis. Therefore I will also illustrate the evolution of ionization models in this introduction. Before dealing with details of particle precipitation, some observations of its impact on the atmosphere will be discussed to provide a broader scope.

1.1 Atmospheric Effects of Particle Precipitation

In the early 1970s *Weeks et al.* (1972) gave first evidence that large **s**olar **p**roton **e**vents (SPEs) could have a depleting effect on ozone. The change in ozone was measured by solar absorption spectroscopy on two rockets, the first flying during the initial phase of the November 1969 SPE, the other one during the final phase two days later. The amount of ozone during the initial phase was up to a factor 4 lower than during quieter conditions at the final phase (at 67 km altitude). In the mid 70s *Crutzen et al.* (1975) and *Heath et al.* (1977) discussed the role of proton precipitation on oxides of nitrogen in the August 1972 event. *Crutzen et al.* (1975) calculated the production of nitric oxide based on proton measurements from *Explorer 43*, while *Heath et al.* (1977) presented ozone depletion in the polar cap as given by measurements from the *Nimbus 4* satellite. They argued that ionization in high latitudes generates NO_x and HO_x which in return influences the ozone chemistry in the stratosphere by catalytic (ozone depleting) reactions. Chemical reaction chains involved in the generation of NO_x and HO_x due to ions as well as in ozone depletion were described by *Solomon and Crutzen* (1981). HO_x has a short lifetime (days) in the atmosphere and therefore the HO_x induced ozone decrease is short-lived, too. However, since NO_x has a rather long lifetime (weeks to months) in the atmosphere, consequences of precipitating particles from subsequent events might add up (*Jackman et al.*, 1990).

In the 1990s *Callis et al.* (1996a) showed the time- and energy-dependent correlation of electron precipitation from the radiation belts into the atmosphere and NO_x concentration within a small particle event in October 1993. At first the low energetic electron (several ten keV) flux rose while later the high energetic electron (hundreds of keV to the MeV range) flux[*] increased. NO-measurements by HALOE[†] for the same period showed first a rise of the NO-column in 51–120 km and later an enhancement of the 51–81 km column.

---

[*] measured by the Proton/Electron Telescope (PET) and Low Energy Ion Composition Analyzer (LICA) instruments on the Solar Anomalous and Magnetospheric Particle Explorer (SAMPEX)

[†] HALogen Occultation Experiment on Upper Atmosphere Research Satellite (UARS)

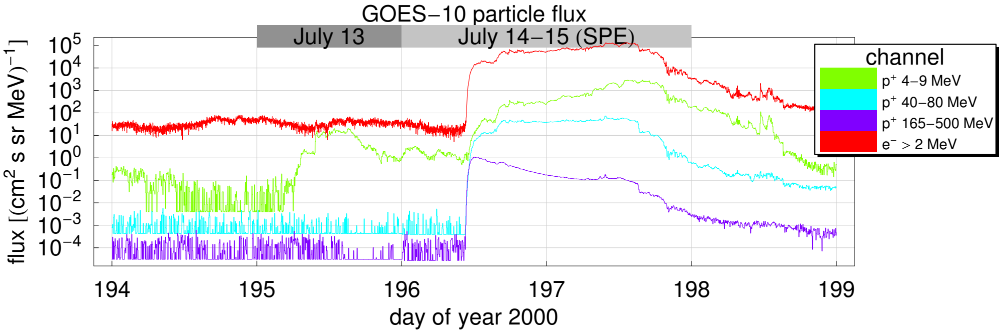

Figure 1.1: Particle count rates from GOES-10 during the July 2000 event

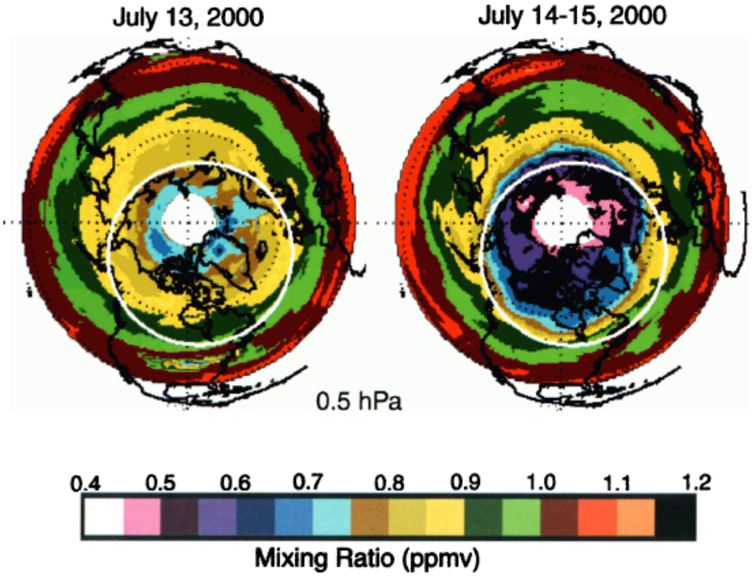

Figure 1.2: Ozone measurements on the northern hemisphere from NOAA POES-14 SBUV/2 for 0.5 hPa (approx. 55 km) show the situation before and at the time of the July 14–15 2000 SPE. The white curve outlines the polar cap (*Jackman et al.*, 2001).

An example for the influence of energetic particle precipitation (the corresponding particle flux is shown in Fig. 1.1) on ozone is illustrated in Figure 1.2. Ozone measurements for 0.5 hPa (approx. 55 km) show the mixing ratio before and at the time of the July 14–15 2000 SPE. Inside the polar cap, ozone is significantly depleted while the changes outside the cap are negligible. Comparing July 12–13 and July 14–15 the ozone depletion, as measured by HALOE, exceeded 70% between 0.3 and 0.01 hPa (*Jackman et al.*, 2001). Since the ozone layer is in the stratosphere and the ozone depletion is largest in the mesosphere and upper stratosphere, the contribution to total column ozone is relatively small. The total ozone reduction associated with this event is just <1 % in the polar Northern Hemisphere (*Jackman et al.*, 2001). However, this shows only the instantaneous effect on ozone.

Randall et al. (2005, 2006) indicate that downward transport of nitric oxides and hydroxyl radicals can affect regions beside the main precipitation area/altitude of the particles. As a consequence, delayed ozone losses are largest in the winter hemisphere where the downward transport of NO_x is most efficient (*Sinnhuber et al.*, 2003b).

The largest particle induced impact on total ozone occurs several months after the initial particle precipitation as NO_x reaches altitudes below 30 km, where ozone concentrations are largest (*Sinnhuber et al.*, 2003b). Model calculations from *Sinnhuber et al.* (2003b, scenario with present-day magnetic field) show a decrease in the total ozone of 2.5 to 5% for a period of one year after the October 1989 event, while the initial effect is a decrease about 0.5 to 2.5%.

Apart from the chemical composition particle precipitation has an impact on temperature. (a) Particle precipitation causes temperature increase due to joule heating: *Banks* (1979) calculated temperature increase of 1 to 10 K per day in the mesosphere as a result of the August 1972 SPEs. (b) On the other hand ozone is one of the primary radiation absorption gases and therefore correlated to the atmospheric temperature. *Randel and Cobb* (1994) showed coherent variations of the total ozone and lower stratospheric temperatures as measured by *Nimbus 7* and *NOAA operational satellites*. Likewise, the depletion of ozone due to SPEs leads to temperature decrease at low altitudes. *Reagan et al.* (1981) calculated a decrease of 2.2 K at 50 km again on the basis of the August 1972 events. (c) Still speculative is the impact on surface air temperatures. Due to various circulation processes a verification is delicate. However, *Seppälä et al.* (2006) compared ERA-40[*] surface air temperatures of high and low $\mathrm{A_p}$-index[†] from 1957 to 2006, showing temperature variations of $\pm$4.5 K depending on location and $\mathrm{A_p}$.

1.2 Overview on energetic Particles

We have seen the atmospheric response to energetic particles and we will now set the focus to the particle sources: the particle composition, their distribution, energy range and origin.

There are three main sources of energetic particles impairing the Earth's atmosphere: solar and magnetospheric particles which will be addressed in the next paragraph as well as the very high energetic galactic cosmic rays (GCR) which will not be topic of this work. The reason why GCRs are not considered is twofold: (a) practically, due to energy restrictions of the instruments, (b) for modeling reasons, since the exact position of the tropopause can not be calculated for sure. Therefore the energy deposition of/ionization by GCRs cannot be processed reliably in the subsequent atmospheric model. The main $\mathrm{NO_x}$ production by GCRs is slightly above or below the tropopause. Unfortunately, the life-time of $\mathrm{NO_x}$ strongly depends on its position. While $\mathrm{NO_x}$ below the tropopause will be washed out with the next rain or snow, $\mathrm{NO_x}$ has a long life-time of weeks to months in the dry strato- and mesosphere. Hence including the low-altitude ionizing GCRs is not expected to give a real benefit to the ionization model and most general chemistry models are designed for the stratosphere and do not include the troposphere. To give a rough estimate, the amount of stratospheric $\mathrm{NO_x}$ produced by a single SEP may be comparable to or even exceed the annual $\mathrm{NO_x}$ production

---

[*] re-analyzed meteorological data for 45-years as modeled by the European Centre for Medium-Range Weather Forecasts (ECMWF) and based on various measurements (radiosondes, balloons, aircraft, buoys, satellites, scatterometers)

[†] global geomagnetic index as calculated from GFZ Potsdam, based on various magnetometer stations

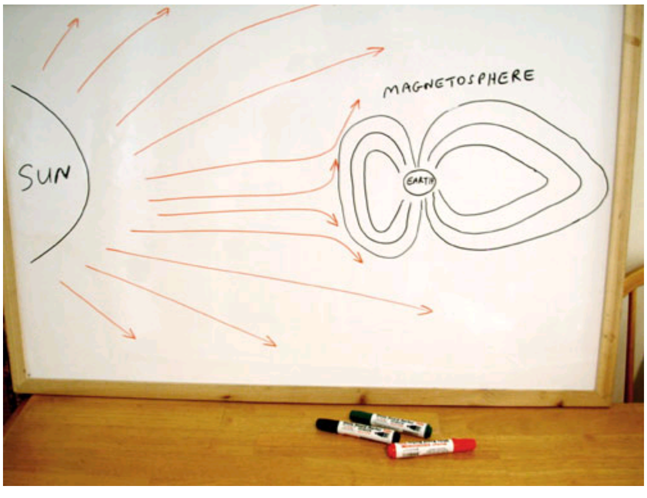

Figure 1.3: Simple first order approximation of the quite-time solar-terrestrial relationship: the solar wind shapes the magnetosphere, from `http://www.coolflying.com.au/cool_info/images/photos/magnetism/magnetosphere_web.jpg`.

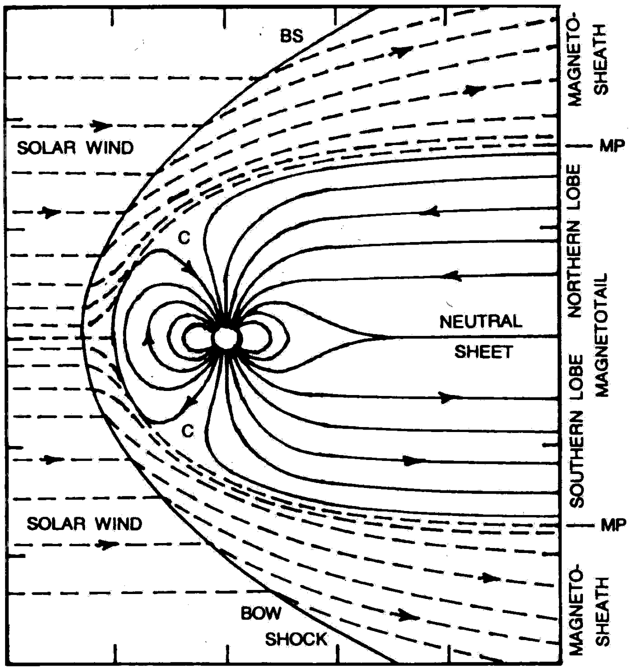

Figure 1.4: A graph of the magnetosphere as described in this section. The magnetopause (MP) is indicated by the inner dashed line in the region of the magnetotail. On the sunward side the outer solid line of the geomagnetic field continues the magnetopause (*Schulz*, 2007).

by GCRs (*Crutzen et al.*, 1975, calculated for SPEs in November 1960, September 1966 and August 1972).

Furthermore, the signal-to-noise ratio in GCRs is rather poor and GCRs are modulated by the strength of the interplanetary magnetic field, or in other words by the 11-year solar cycle[*] and besides this variation no intense fluctuations on short time-scales are expected. On the other hand, solar energetic and magnetospheric particles give a short and strong stimulus to the atmosphere chemistry (e.g., the increase in particle fluxes is by several orders of magnitude, see also Figure 1.1). Thus atmospheric consequences of energetic particle precipitation in turn give a kind of “pulse-answer”. In a linear system we would describe this as a Green’s function.

1.2.1 Solar Wind and Magnetosphere

Due to the pressure difference between the solar corona and interplanetary space, the Sun emits ionized plasma (*Chian and Kamide*, 2007). The pressure in lower parts of Sun’s atmosphere is higher than the weight of the upper atmosphere and corona, blowing a fraction off the upper atmosphere, as so-called solar wind, away.

The solar wind consists mostly of electrons and protons and is emitted continuously but not homogeneously, neither in space nor time. It reflects all the variances of the corona and solar activity, that is the non-recurrent solar flares, coronal mass ejections (CME) and shock waves as well as the recurrent plasma properties during a 27-day solar rotation or the 11-year solar cycle.

When the solar wind hits the Earth’s magnetic dipole field it is deflected, forming a cavity: the magnetosphere (see Figure 1.3). The border of this cavity is the magnetopause. In the region towards the Sun a bow shock is formed (see Figure 1.4) where the supersonic solar wind is decelerated to subsonic speed. Within this shock, kinetic energy is converted into thermal energy, filling the region between bow shock and magnetopause, the magnetosheath, with hot subsonic plasma. The geomagnetic (dipole) field and with it the magnetopause is deformed, being compressed in direction to the Sun, and extended into the opposite direction (magnetotail). The sunward boundary is characterized by the balance

---

[*] Our focus is the solar activity. However, the *magnetic* solar cycle is 22-years.

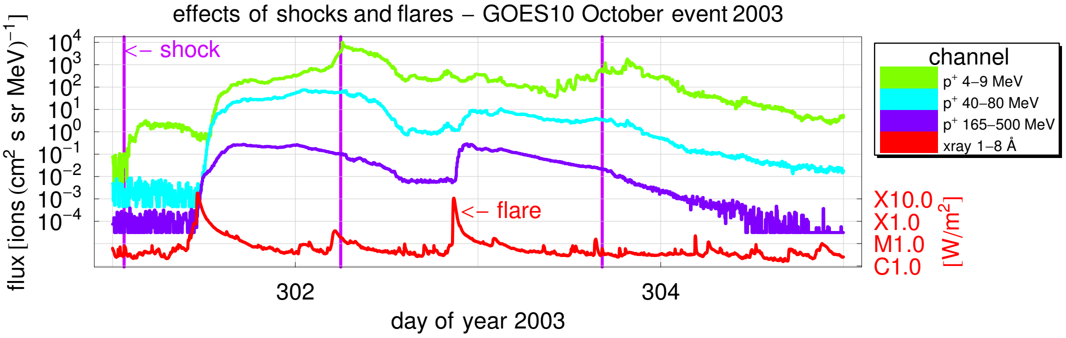

Figure 1.5: Particle count rates from GOES-10 for the October 2003 event; shocks and flares are indicated. Shock lists based on ACE's MAG & SWEPAM-I/E from Qiang Hu and Vasiliy Vorotnikov (`http://www-ssg.sr.unh.edu/mag/ace/ACElists/obs_list.html`). Flares are indicated by high values of the 1–8 Å X-ray flux.

between dynamic plasma pressure of the solar wind, pv^2, and the magnetic pressure of the magnetosphere, $\frac{B^2}{2\mu_0}$. This defines the location of the magnetopause, which is normally around 10 R_E in the solar direction. Fast solar wind streams can increase the plasma pressure, pushing the day-side magnetopause inside the geostationary orbit at 6.6 R_E (*Koskinen and Huttunen*, 2006).

During geomagnetic quiet times (resulting from low solar activity) the Earth's magnetic field is an effective shield against particles arriving from outside the magnetosphere. This applies in particular for the lower latitudes whereas the area around the geomagnetic pole can easily be accessed by solar particles as the field lines are assumed to be open (*Leske et al.*, 2001).

1.2.2 SEPs, CMEs and geomagnetic Activity

The Sun is known to produce significant fluxes of highly energetic particles (*Forbush*, 1946). Pointing out the different characteristics Figure 1.5 shows the temporal evolution of particle fluxes in three proton channels, the 4–9 MeV, 40–80 MeV and 165–500 MeV, representing the solar energetic particles. One acceleration mechanism for high energetic particles are solar flares low in the corona. Their occurrence corresponds with the X-ray bremsstrahlung emission (*Anderson and Winckler*, 1962). Another dominant acceleration mechanism are shock waves (*Cliver et al.*, 2002) driven by fast coronal mass ejections (CMEs) in the upper corona and in interplanetary space. In contrast to flares, a CME's shock wave affects the solar wind plasma, increasing mean velocity and pressure. More precise, impulsive SEP events were related to flares and gradual SEP events were related to coronal mass ejections (CME) driving coronal and interplanetary shocks (see review papers *Reames*, 1999; *Kallenrode*, 2003). In addition, CMEs are believed to be the main source of major non-recurrent geomagnetic storms (*Brueckner*, 1998; *Kamide and Maltser*, 2007).

During geomagnetic storms a restructuring of the magnetosphere enlarges the size of the auroral oval (*Leske et al.*, 2001) and allows plasma/energy transfer from the interplanetary space into the magnetosphere. Physical mechanism for the solar wind energy transfer into the magnetosphere is magnetic reconnection between the strong southward interplanetary magnetic field and the northward dipole field of the Earth (*Dungey*, 1961) on the day-side. While the interconnected field lines are convected to the night-side by the solar wind, reconnecting northern and southern field lines in the tail lead to an injection of plasma-sheet plasma deep into the night-side of the magnetosphere. As a consequence the magnetosphere falls in a strongly disturbed state, which can be observed, e.g., as an intensification of the ring current (*Daglis et al.*, 1997; *Gonzalez et al.*, 1999) and frequent injection of energetic

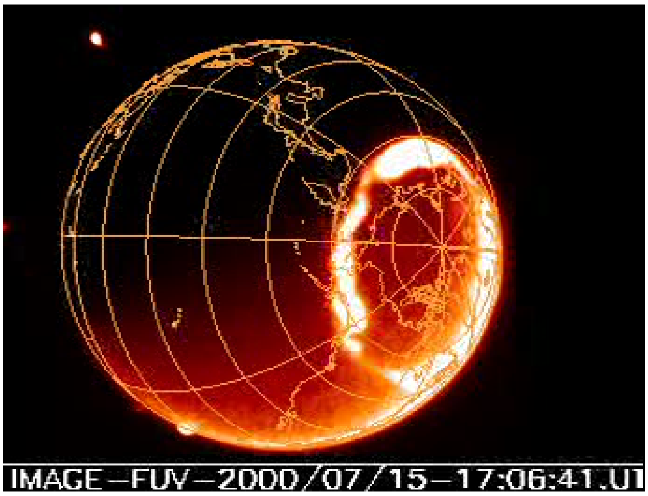

Figure 1.6: Aurora as seen from IMAGE (Imager for Magnetopause-to-Aurora Global Exploration), by S. Mende and H. Frey, Space Sciences Laboratory, University of California, Berkeley; Randy Gladstone, Southwest Research Institute (`http://pluto.space.swri.edu/image/FUV_images2.html`)

Figure 1.7: Aurora as seen from Earth. Photography was taken by *Shaviv* (2009) in Saariselkä, northern Finland, at low auroral activity. The green color commonly seen in the aurora is related to the atomic oxygen line at 557.7 nm which occurs typically at altitudes from 100 to 200 km.

electrons and ions into the inner magnetosphere (*Baker*, 1998). Therefore, the solar wind is the main source of the magnetospheric particles. The strength of these geomagnetic storms is measured by *Disturbance Storm Time* (DST, e.g., *Koskinen and Huttunen* (2006)) index or *Planetare Kennziffer* (K_p index, available at `http://swdcwww.kugi.kyoto-u.ac.jp/kp/`, *Bartels et al.* (1939); *Gonzalez et al.* (1994)).

1.2.3 Magnetospheric Particles

Within the inner magnetosphere, high energetic particles form the *Van Allen* radiation belt(s)[*]. These particles are trapped within the geomagnetic field, spinning around their guiding field line, bouncing back and forth between North and South and drifting azimuthally around the Earth. These motions can be described by the 3 adiabatic invariants (*Alfven and Faelthammar*, 1963). The mirror points of the trapped radiation belt (magnetospheric) particles are above the atmosphere, but due to scattering or compression of the magnetosphere some of these particles have mirror points within the dense atmosphere and they get lost as auroral precipitation (see Figure 1.6 and 1.7) or, in case of sufficient high particle energies, lead to ionization down to the mesosphere or even the stratosphere.

---

[*] Depending on the rigidity of the particle the position of the peak density position differs. Therefore, some scientists separate inner and outer radiation belts, describing electron and proton populations separately. But there are belts of heavier particles, too, and in addition, as rigidity depends on kinetic energy, the energy spectrum modifies the belt's position.

1.3 Evolution of Models

The aim of this thesis is the development of an ionization model. To put this model into the context of current scientific literature, let us take a look at the evolution of ionization models. Early models were mostly concerned with the precipitation of solar protons into the polar cap, the region of open field lines. This region was regarded as being homogeneously filled and invariant in size, although the enlargement of the polar cap during geomagnetic active periods was known from the observations of the aurora. Accounting for solar protons only, this approach persists with its main features unaltered even in recent publications (*Jackman et al.*, 2001, 2005a; *Rohen et al.*, 2005; *Verronen et al.*, 2002). The proton energy range was small (some MeV to some hundred MeV), defined not by the properties of the incident solar energetic particles but by the detectors of the specific satellites*. Contributions of heavy elements and electrons to the ionization of the atmosphere were considered as being negligible (*McPeters and Jackman*, 1985). Solar electrons, e.g., were assumed to contribute less than 10% to the total ionization (*Jackman and McPeters*, 1985).

Looking at the second main precipitation zone, the auroral oval, the role of electrons to atmospheric ionization was treated differently. The influence of magnetospheric electrons is well documented (*Thorne*, 1977; *Callis et al.*, 1996a, 2001). Models describing homogeneous electron precipitation in the auroral oval can be found at *Callis et al.* (1996a,b, 1998). The impact of magnetospheric protons precipitation in auroral latitudes has been modeled in *Hardy et al.* (1989); *Fang et al.* (2007). Although the protons may contribute up to 45% of the total energy flux in the evening sector (*Hardy et al.*, 1989, in the morning sector it is approximately 4%), a combined model for the total magnetospheric particle precipitation does not exist so far.

To sum it up, in most cases electrons in modeling are regarded as precipitation of magnetospheric particles in the auroral oval (*Callis et al.*, 1998) whereas protons are regarded as solar particles precipitating at the poles. But this separation into magnetospheric electrons and solar protons is not accurate. On the one hand, solar electrons are accelerated in flares and CMEs, which is supported by observations of electrons up to tens of MeV in intense solar energetic particle events (*Datlowe*, 1971, near 1 AU), and, more recent, by SOHO measurements at 0.25–0.7 MeV associated with a coronal shock (*Klassen et al.*, 2002). For a more detailed discussion see also *Reames* (1999); *Kallenrode* (2003). On the other hand, the Earth's magnetic field is a trap for charged particles of any kind as long as pitch-angle and energy/rigidity allow trapping. Consequently low-energetic protons (and even some heavier ions) from the magnetosphere precipitate inside the auroral oval (*Fang et al.*, 2007) while the polar cap sometimes shows significant population of high energetic solar electrons.

To put it in a nutshell the separation in solar and magnetospheric particles is reasonable from the point of energetic and spatial classification, but the distinction by particle species as used in these models is not. Anyhow, the atmospheric response does not pay attention to the particle's origin.

Looking on particle species and fluxes is just one side of the coin. Particle events are often accompanied by Coronal Mass Ejections (CMEs), which affect the shape of the magnetosphere and that is why the precipitation area changes as well. Most important is the enlargement of the polar cap with geomagnetic activity as described in *Leske et al.* (1995); *Kahler and Ling* (2001); *Leske et al.* (2001) using SAMPEX and *Wissing et al.* (2008) using POES (see also Chapter 3). Furthermore these authors describe the equatorward motion of the auroral oval, the precipitation area of the magnetospheric particles, during geomagnetic active periods.

First attempts to describe the variable global proton precipitation pattern were made by *Hardy et al.* (1989) using several years of ion measurements by Defense Meteorological Satellite Program (DMSP) satellites. *Hardy et al.* (1989) sorted the measurements as a

---

*depending on time often the satellites ISEE, IMP or GOES were used function of 7 K_p values. However the global picture was limited to protons in a narrow energy range (30 eV to 30 keV).

A recent ionization model by *Fang et al.* (2007) based on satellite measurements of POES-15/16 describes global auroral proton precipitation without averaged patterns sorted by K_p. Here 3 h data of POES is used only to derive an actual global pattern. Linear-fitting in meridional direction and cosine-fitting in latitudinal direction are used. In order to get enough fitting points, values from the southern hemisphere are mirrored in the north and vice versa. This may imply problems as the geomagnetic symmetry is only fractional which is most obvious in the South Atlantic Anomaly. Anyhow the restriction to auroral protons (30–240 keV) and to auroral latitudes does not allow simulation of solar particle events.

A different approach is parametrization of (in this case electron-) ionization based on hemispheric power (e.g., *Roble and Ridley*, 1987). The WACCM3 GCM model even uses this parametrization by substituting hemispheric power against the geomagnetic K_p-index (*Marsh et al.*, 2007).

An overview of some typical ionization models is given in Table 1.1. The predominant aspects are the particle species and particle energy as well as the covered location. Additional information as the fit function of the particle spectra will be discussed in Section 2.1.1.

To keep up with the development of climate models covering stratosphere and thermosphere (e.g., HAMMONIA *Schmidt et al.*, 2006) the ionization models have to be extended. Recent ionization models mostly just cover the atmosphere up to the mesosphere (*Jackman et al.*, 2001; *Schröter et al.*, 2006) or are limited to auroral particles and the thermosphere (e.g., *Roble and Ridley*, 1987; *Hardy et al.*, 1989). To our knowledge a model combining solar and magnetospheric precipitation in addition to a wide energy range of electrons and protons including geomagnetic variation does not exist – except for AIMOS developed during this thesis.

Besides geomagnetic variation the magnetic local time (MLT) is important for the 3-D precipitation pattern. *Tohmatsu* (1990) compared the shape and the intensity of the auroral oval within several time sectors and found significant differences. Further investigation by *Wissing et al.* (2008) using polar satellites with a 90° shifted orbit showed variations of a factor of 5 simultaneously observed in different local time sectors. Therefore measurements of the auroral precipitation should be taken by at least two satellites in a shifted orbit. *Fang et al.* (2007), for example, uses two POES satellites, identical in construction but with an orbit shift, to obtain "global" coverage. We will come back to a different approach with two POES satellites in Chapter 4.

Using multiple satellites is not only restricted to the orbit information. It also provides a wider energy range as far as different instruments are involved (*Mewaldt et al.*, 2005). In particular energy spectra that include low energetic magnetospheric precipitation as well as high energetic solar particles need a combination of different instruments which are seldom on the same satellite. However none of the existing models I know uses different satellites to increase the energy range[*].

---

[*] and therefore altitude range, see Figure 4.2

model	particle	particle species	precipitation pattern		based on		internal	spectra fit	temp.
	source	and energy	location	fix or variable	satellites	index	mechanism	function	res.
Berger et al. (1970)	magneto-spheric	e^- (2–20 keV)	no pattern		no measurements		Monte Carlo	mono-energetic (no spectra)	-
Roble and Ridley (1987)	magneto-spheric	e^- ($<$100 keV)				hemi-spheric power	empirical energy dissipation function	Maxwellian	
Hardy et al. (1989)	magneto-spheric	p^+ (30 eV–30 keV)	global	dynamic, depending on $\mathrm{K_p}$	DMSP[a]	mean values sorted by $\mathrm{K_p}$			
Callis (1997); *Callis et al.* (1998); *Callis and Lambeth* (1998)	magneto-spheric	e^- (4.25–1050 keV)	NH and SH auroral ovals		POES-6 and successors (8, 12)	-	*Walt et al.* (1968)	piecewise Maxwellian[b]	24 h
(*Jackman et al.*, 2001, 2005a)	solar	p^+ (1–300 MeV)	polar cap ($>60°$)	fixed	GOES-11 and prede-cessors	-	range-energy relation	3 Maxwellian	1 h
Fang et al. (2007)	magneto-spheric	p^+ (30–240 keV)[c]	global	dynamic	POES-15/16	-			
Schröter et al. (2006)	solar	e^- (0.5–5 MeV) p^+ (0.29–440 MeV)	polar cap	static	IMP/GOES	-	Monte Carlo (GEANT4)	power-laws	
AIMOS	solar & magneto-spheric	e^- (154 eV–5 MeV) p^+ (154 eV–500 MeV) α (4–500 MeV)	global	dynamic, depending on $\mathrm{K_p}$	POES-15/16 GOES-10 or 11	$\mathrm{K_p}$, F10.7	Monte Carlo (GEANT4)	up to 5 power-laws	2 h

Table 1.1: Overview of some typical ionization models.

---

[a] Defense Meteorological Satellite Program

[b] private communication, Natarajan

[c] Electrons are not mentioned in *Fang et al.* (2007), however the description of the (multi- and two-stream) energy deposition method in *Fang et al.* (2008) deals with electrons (100 eV–1 MeV). Therefore, an extension to electrons suggests itself.

1.4 Aim of this Work

This work discusses spatial and temporal patterns of the highly variable particle flux affecting the Earth's atmosphere. The solar particle events in October 2003 are used as a test case but for comparison it also deals with particle fluxes during geomagnetic quiet times. Ionization rates are e.g. needed as input for *Global Climate Models*. Thus my task is also to construct a model describing the global particle induced ionization rate.

As shown in Section 1.3 existing ionization rate models are valid only with restrictions in altitude, particle species, local position and geomagnetic activity and require the modeler's attention and familiarization. In contrast *Atmosphere Ionization Module OSnabrück* will cover the topic of particle precipitation as comprehensive as possible including:

- all major particle species (electrons, protons and alpha-particles),
- a wide energy range (6 orders of magnitude, covering auroral and solar energetic particles),
- global coverage and high spatial resolution,
- and an altitude range from 18 km up to the upper thermosphere (250–600 km, $1.7 \cdot 10^{-5}$ Pa).

Hence the ionization data can be used easily at various prospects. Apart from the ionization itself it may be used to provide a realistic particle forcing data for chemistry models and GCMs. Table 1.2 lists the different interactions that can be modeled by (1) the ionization model itself, (2) a chemistry model using ionization rates, and (3) a GCM using ionization rates. A chemistry model (*Bremen 3d CTM*) is used in Chapter 5 while a GCM (HAMMONIA) is used in Chapter 6.

interaction	model	example
primary: ionization	continuous energy loss Monte Carlo Bethe-Bloch	*Jackman et al.* (2001) AIMOS
secondary: chemistry	Sciamachy, Bremen 3d CTM	production of NO_x and HO_x, depletion of Ozone, impact on local temperatures
tertiary: circulation	HAMMONIA, SOCOL	local temperature change affects transport

Table 1.2: The interaction of particle precipitation can be subdivided into 3 steps: (1) the ionization process, (2) the impact of enhanced ionization on chemistry and (3) the coupling of induced temperature changes to the whole circulation.

During the time of my thesis various members of the modeler's community asked me for data for their specific model grid or a local destination. Therefore customized ionization rates will be freely available via web-applet at `http://aimos.physik.uos.de`. I would like to mention the HEPPA-MIPAS model inter-comparison (*Funke et al.*, 2010) in this context, as it uses AIMOS ionization rates as identical forcing for 10 different GCMs and CTMs (for details see Table 8.1) and shows the variation range of simulation results on the one hand and a comparison to MIPAS satellite measurements on the other. As the results have not been published yet, some anticipations will be shown in the outlook (Chapter 8).

1.5 Structure

This dissertation subdivides into a brief overview on the scientific background and the evolution of ionization models (Chapter 1). Chapter 2 deals with issues of direct relevance to the development of *Atmosphere Ionization Module OSnabrück* (AIMOS). There are several questions been discussed such as:

- Whether to use a magnetic field in the model?
- Can we use the homospheric approach or is it an oversimplification of the atmospheric composition?
- How to transform the mean energy loss into ion pair production?
- Which kind of particle distribution function should be used?

Chapter 3 was published in *Advances in Space Research* and honored with "The Outstanding Paper Award for Young Scientists". It deals with the dependence of particle precipitation on local magnetic time as well as the shift of the auroral position with increasing K_p during storm time and different behavior of solar and magnetospheric particles. Most of the characteristics of particle precipitation being used for the development of AIMOS will be discussed. In Chapter 4, which was published in *Journal of Geophysical Research* (*JGR*), the description of AIMOS is given, followed by Chapter 5 where AIMOS ionization rates are compared to an ordinary ionization pattern using the Bremen chemistry model. This paper was likewise published in *JGR*. The final comparison to incoherent scatter radar measurements follows in Chapter 6. Here the ionization rates are used as input for the general climate model HAMMONIA. The resulting electron densities are globally compared with incoherent scatter radar measurements. A more detailed discussion of model assumptions and limitations of AIMOS can be found in Chapter 7. Finally Chapter 8 sums up the main aspects of this thesis and will give some final remarks and future prospects. A description of the satellites and their particle instruments can be found in the appendix (Chapter 9).

Chapter 2

Model Conception

The aim of this work is to describe the ionizing effect of global particle precipitation into the atmosphere. The major difficulty is given by very limited observations on the one hand and the desired global coverage on the other. In addition, the model shall include the local differences in a static horizontal precipitation pattern as well as the displacements of these patterns corresponding to a dynamic magnetosphere. As second challenge the ionization model shall cover most of the (relevant) precipitating particle populations (species and energy range) while former models just covered a fraction of it (see Table 1.1). The relevant populations and their upper energy thresholds (representing the lowest altitude of ionization) are given by the tropopause: Secondary interactions (chemistry, see Table 1.2) produce nitric oxides and hydroxyls. Produced below the tropopause, these oxides are washed out quickly. Produced in the dry layer above the tropopause, they remain and destroy Ozone by catalytic reactions. Therefore it is our aim to describe the ionization above the tropopause as accurate as possible. However, the exact altitude of the tropopause can not be determined exactly. It is between 6 and 16 km and represents the desired lower boundary of the ionization model. The upper boundary of the ionization model is given by the 1.7×10^{-5} Pa isobar (respectively 250–600 km altitude) and allows ionization modeling in stratosphere, mesosphere and thermosphere. Due to limitations of the available particle instruments not all species cover the desired altitude range (see Table 2.1).

species	energy	pressure	approx. altitude
protons	154 eV–500 MeV	10^{-5}–10^{4} Pa	18–240/440 km
electrons	154 eV–5 MeV	10^{-5}–10^{2} Pa	48–240/440 km
αs	4–500 MeV/particle	10^{-1}–10^{3} Pa	33–92 km

Table 2.1: AIMOS particle energy ranges and the corresponding pressure and altitude levels. As the upper altitude boundary for protons and electrons is situated in the thermosphere it varies subject to solar activity. The first number indicates solar minimum conditions while the second number represents solar maximum.

The relevant particle populations are magnetospheric and solar energetic particles. Since the lower favored boundary of the model is the tropopause (6–16 km, which is corresponding to the main ionization altitude of 500 MeV protons) the galactic cosmic rays are included to a very limited extend only. Section 2.1 will enlarge on the topic of particle populations.

The basic idea of generating ionization rates can be subdivided into two separate tasks. At first it is a description of the particle population on top of the atmosphere. This includes satellite measurements of the temporal as well as the spatial distribution and will result in a particle spectra for every single grid point with a 2 h resolution. This is the empirical part of

AIMOS. Secondly the ionization for every grid point will be calculated using a *Monte Carlo* model. Input are particle spectra from the empirical model which are injected into different model atmospheres selected by latitude, season and solar activity.

Chapter 3 enlarges on the particle precipitation pattern and therefore indicates which circumstances have to be considered in the model. A detailed description on this model will be given in Chapter 4. However, the model construction needs some preconsiderations that are not directly linked with particle precipitation patterns. Therefore this chapter states these preliminary considerations, which answer e.g. the following questions:

- How can the particle distribution be described?
- Can homospheric conditions be used (like in, e.g., *Schröter et al.*, 2006)?
- Is the consideration of a magnetic field necessary?
- Which aspects have to be considered in the Monte Carlo simulation?
- How to combine both particle spectra and Monte Carlo ionization profiles?

The reader may decide if he wants to start with the model preconsiderations (see below) of if he wants to look at the precipitation patterns and model implementation first (Chapter 3 and 4).

2.1 Particle Populations

The particle populations (listed in Table 2.2) originate from three different sources, (1) magnetospheric particles, (2) solar energetic particles, and (3) galactic cosmic rays (mostly protons and αs). Figures 2.1 and 2.2 represent typical spectra for solar energetic particles, respectively galactic cosmic rays. Magnetospheric populations underly strong spatial variations thus we refrain from showing a “typical” magnetospheric spectrum.

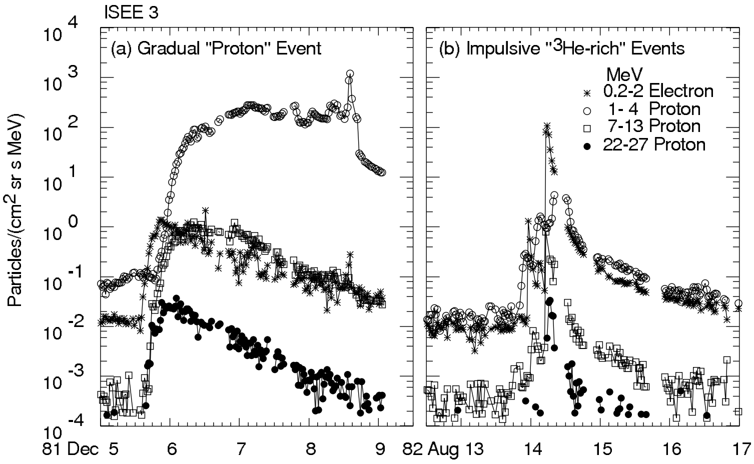

Figure 2.1: Gradual (right) and impulsive (left) spectra of a solar particle event (*Reames*, 1999).

The precipitating particle population will always be a superposition of these three sources, inheriting the strong spatial variation of magnetospheric particles, the temporal variation of the SEPs and the comparatively constant background of the galactic cosmic rays. For a complete spectrum (necessary for the model) the different satellite channels have to be combined and interpolated with a proper function; for GCRs even ground based observations would have to be included. As for the above reasons, GCRs will not (or just to a very limited extend) be considered in this study.

2.1.1 Which Function describes the precipitating Particle Distribution?

The particle distribution function has to be suitable over a wide energy range and should be able to match to very different spectra. The description of the particle distribution depends

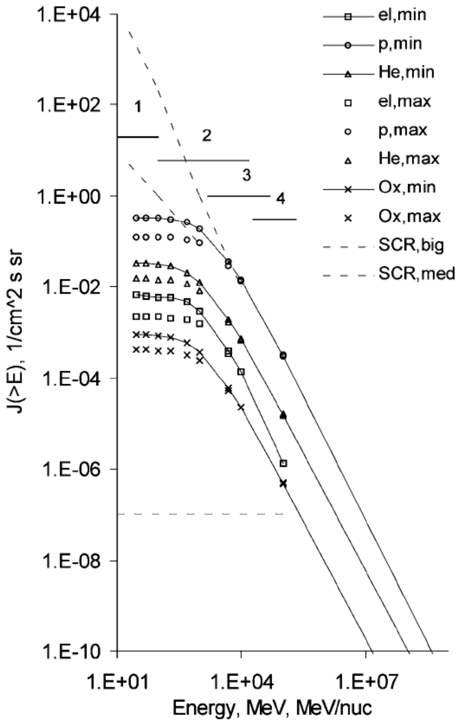

Figure 2.2: Galactic cosmic ray spectra (*Bazilevskaya*, 2000): The integral energy spectrum of comic rays at energies $\leq$109 MeV for protons and electrons and $\leq$109 MeV/nucleon for nuclei. The horizontal dashed line indicates the region where cosmic ray intensity is modulated by solar activity. The two upper dashed lines relate to solar proton events of different amplitudes. The solid horizontal bars cover the energy regions of the following observations: (1) spacecraft, (2) balloon, (3) neutron monitor, (4) muon telescope.

	magnetospheric particles	solar particles		galactic cosmic rays
		impulsive	gradual	
energy range	e^- eV to keV p^+eV to some MeV α eV to some MeV	e^- keV to some MeV p^+ keV to hundreds of MeV α keV to hundreds of MeV		hundreds of MeV to 10^{14} MeV
main ionization altitude	max. at 110 km	35–100 km		3–55 km
composition	local variations (see Section 3.4.1)	electron rich	proton rich	p^+ ≈89%, α ≈10%, e^- ≈1%
“source”	geomagn. disturbance (e.g., CME, shock, CIR)	flare	(flare+) CME	e.g., supernovae
temporal pattern	low energies always present, strong dependence to geomagn. disturbance for higher energies	hours to days	days	always present, depending on solar cycle
precipitation pattern	auroral oval	polar cap		global corresponding to magn. shielding

Table 2.2: Overview of particle populations. Information on solar particles taken from *Reames* (1999), galactic cosmic rays from *Bazilevskaya* (2000), respectively.

on the observer's specific energy range. Recent models were restricted either to low energetic solar wind particles or to the high energetic tail of the spectrum. Thus two common approaches are used to describe a "fractional" particle spectrum.

(a) Maxwell-Boltzmann: A very low energetic (thermal) population can be described by the Maxwell-Boltzmann distribution. If only the high energetic tail is considered an exponential function represents the spectra (*Roble and Ridley*, 1987)[*]. [†]

(b) power-law: The power-law has its justification by theoretical description of the shock acceleration. *Fermi* (1949) suggested that stochastic reflections across a shock caused acceleration. He deduced that the resulting energy distribution could be characterized by a power law[‡]. This is also a common approach in the description of observed spectra (e.g. *Mewaldt et al.*, 2005).

Given that the total particle spectrum should be a combination of the thermal Maxwell-Boltzmann distribution and the high energetic population (*Gosling et al.*, 1981), it can be characterized theoretically by a Kappa-distribution (*Kallenrode*, 2004, p. 117). However, as the galactic cosmic rays can not be described using the Kappa-distribution and the solar energetic population may be generated by various acceleration processes (e.g. superposition of multiple shocks that generate breaks in the spectra) even the Kappa-function is limited to an ideal-theoretic spectrum.

Considering the particle energies used by AIMOS, the particle spectrum can be described by power-laws. Even so, some models even use the Maxwell-Boltzmann distribution to describe the solar energetic particles (e.g. *Jackman et al.*, 1980). That is why the next Section will focus on the expected differences of these two distributions.

Comparison of Maxwell-Boltzmann and Power-Law Fits with respect to the Position of Intersections

Two main kind of fit functions for particle spectra are (a) the power-law fit (straight line in a log-log graph) and (b) the "exponential" Maxwell-Boltzmann fit (straight line in a linear-log graph). Without any limitation for other particle species we will use protons in this comparison. We want to keep the comparison as simple as possible, leaving out smooth crossovers (see e.g. *Mewaldt et al.*, 2005) and concentrate on fundamental fitting functions. Considering the physical background (see above), the power-law distribution is expected to be adequate for the particle energies in AIMOS. Nevertheless, some models use the tail of the Maxwell-Boltzmann particle distribution at these energies. For this reason we will discuss the differences.

As any influence besides the fitting function should be suppressed in this section, both approaches will use:

- identical particle data (GOES-11, SEM, 1–300 MeV, for more information on GOES see *Wilkinson* (2010)),
- the same number of intersections resulting in 3 different fits,
- and to show the effect on ionization the same energy deposition algorithm (GEANT4, Monte Carlo).

At the moment we do not need any details on the ionization algorithm except that it maps the particle spectrum into an atmospheric ionization rate; the details of the ionization algorithm will be discussed in Section 2.2.

The Maxwell-Boltzmann fit was adopted from *Jackman et al.* (1980, 2005b), available at the SOLARIS website `http://www.geo.fu-berlin.de/en/met/ag/strat/forschung/`

---

[*] High energetic tail of the Maxwell-Boltzmann distribution: $\Phi(E) = C_1 exp\left(-\frac{E}{E_0}\right)$, where C_1 and E_0 result from the fit.

[†] Observing the mixed population at the aurora *Fang et al.* (2008, and references therein) says that normally no Maxwell-Boltzmann distribution is observed. Especially the high-energetic end of the spectra shows differences.

[‡] Power-Law: $\Phi(E) = \Phi_0(E_0) \cdot \left(\frac{E}{E_0}\right)^{-\gamma}$, where $\Phi_0(E_0)$ and γ result from the fit, while E_0 is set to e.g. 1 MeV.

`SOLARIS/Input_data/SOLARIS_Jackman_SPEs.pdf`. In Jackman's work the fit is used pairwise on energy channels using fixed intersections, respectively fixed energy ranges of 1–10 MeV, 10–50 MeV and 50–300 MeV. Consequently the transitions between these intervals are not necessarily continuous. And as a second consequence of the pairwise fitted energy channels, the intervals at higher particle energy are assigned to a higher spectral temperature.

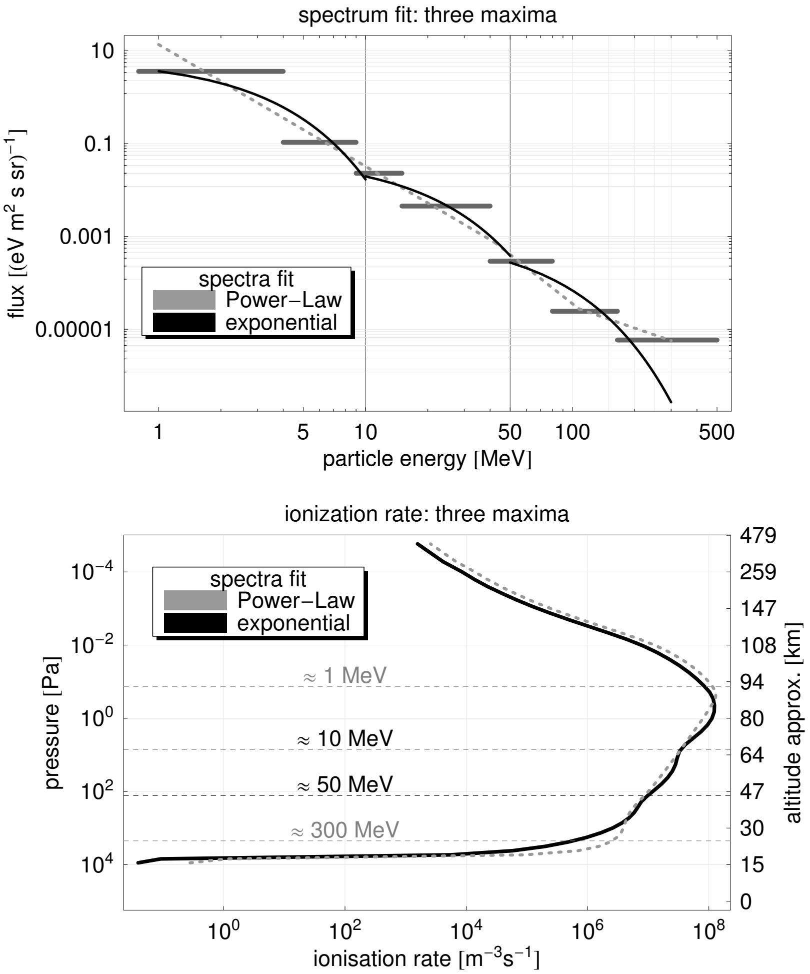

Figure 2.3: (top) Comparison of Maxwell-Boltzmann (exponential) and power-law fit. (bottom) The resulting ionization rate. The dashed lines indicate the altitude of maximum ionization for a specific particle energy. A sample from 4 Nov. 2003, 22–24 UTC is shown.

On the other hand the power-law algorithm calculates multiple fits for every spectrum, varying in position of the intersections. Each of these fits is recursively determined by adjusting the barycentric energy center of the energy channels corresponding to the recent spectral slope. Transitions between different fit intervals are continuous. The best fit (and therefore the final position of the intersections) is selected by a correlation coefficient for the fit. Since very bumpy particle spectra may need a couple of fit functions on a small energy band, the rest of the energy range will be less accurate as it might be using fixed intersections. So the fixed intersections might have advantages in regard to stability. Nevertheless, a stability problem in the variable position of intersections has not been observed.

Now both fit functions are used to fit/represent the particle flux spectra in the range of 1–300 MeV. Figure 2.3 (top) shows the energy spectrum (horizontal bars) as measured by the SEM instrument on GOES. The solid and black lines indicate the resulting spectra of the two fitting methods. A distinctive feature in the comparison of ionization rates derived for both fit mechanisms is that the energy intervals recur in the ionization profile (see Figure 2.3, bottom). The combination of fixed energy intervals and exponential fit will lead to local (artificial) minima at these positions (see 10 MeV and 50 MeV as indicated by vertical bars in the upper panel).

Power-law and exponential fit will never achieve a perfect congruence. In fact, if the intersections will be at fixed positions in both fits, the power-law fit (and its corresponding ionization rate, see Figure 2.3, bottom) will always exceed the exponential one at these intersections while it is vice versa in the mid between them. Considering that we used a power-law fit with variable intersections, this statement declines from a must to only a tendency as shown in Figure 2.4. Anyhow different fit functions can easily lead to variations in the ionization rate in the order of a factor of 2 at certain altitudes. Considering that in the exponential fit the position of an intersection is fixed in energy (and therefore altitude) it implies that some characteristic maxima and minima in the ionization profile always persist at the same altitude. In this case we expect the exponential fit to show larger ionization rates at approximately 35, 55 and 80 km while it should be vice versa at 25, 65 and 92 km.

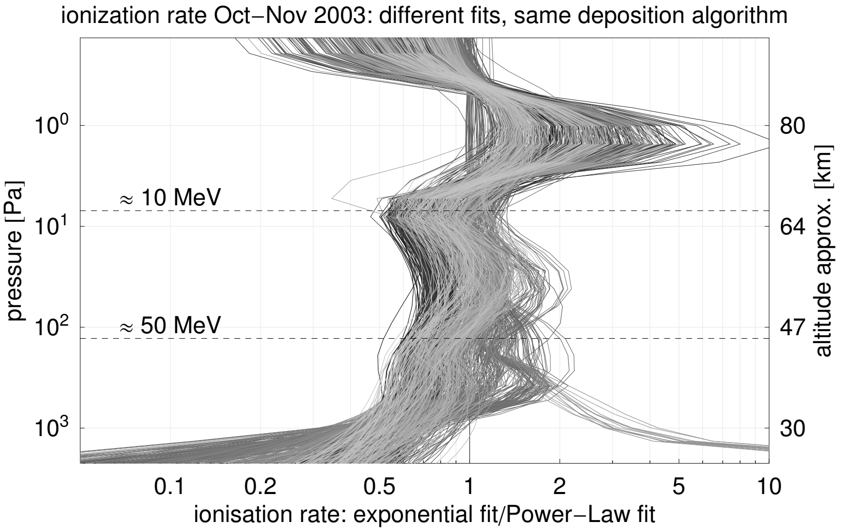

Figure 2.4: Relation of ionization rate by exponential fit and power-law fit: Excursions to the right indicate that the exponential fit leads to higher ionization rates than the power-law fit. The discrepancy on bottom right is an effect of high count rates in the upper GOES-11 energy channel: Whenever the flux of an higher energy channel exceeds the one of a lower one it will be ignored by the AIMOS power-law fitting routine- assuming that it shows erroneous counts. However, the resulting energy range is confined at 165 MeV, meaning that the exponential fit exceeds in this case. For GOES-11 1.8% of the data sets Okt–Nov 2003 are affected. In case of the AIMOS standard data set (GOES-10 for year 2003) it is 0.3%, only.

If the position of the intersections represents the shape of the particle spectrum, this will not add artificial information to the data. However, accordance of a break in the spectrum and the position of a fixed intersection is only given by chance. In addition, the fit function is not the exclusive criteria of fixed intersections: within the measuring process, the limited amount of energy channels on a satellite has a comparable impact on the spectra.

Summing up, it should not matter whether to use fixed or variable intersections in a single time step. Every version includes some unavoidable assumptions on the spectrum (given by direct selection of energy ranges as shown in Section 2.1.1 or by energy channel ranges). However, looking at long term modeling (e.g., see Figure 2.4 for a two months overview) the variable intersections will be leveled out whereas the fixed intersections persist as typical characteristics in the ionization rate profile. This should be kept in mind when interpreting ionization rates and results derived from these.

Comparison: bumpy Particle Spectra The comparison of power-law and exponential fits strongly depends on the smoothness of the particle flux within different channels. Within a geomagnetical quiet period for example the lowest GOES channel shows high count rates resulting from trapped particles (see Figure 2.5, top). These produce an outlier in the particle spectrum. The comparatively high flux in the low energetic GOES channel in combination with different intersections (10 MeV in the case of the exponential fit and the barycentric energy mean of the second energy channel with approx. 5 MeV) lead to divergent ionization profiles (see Figure 2.5, bottom).

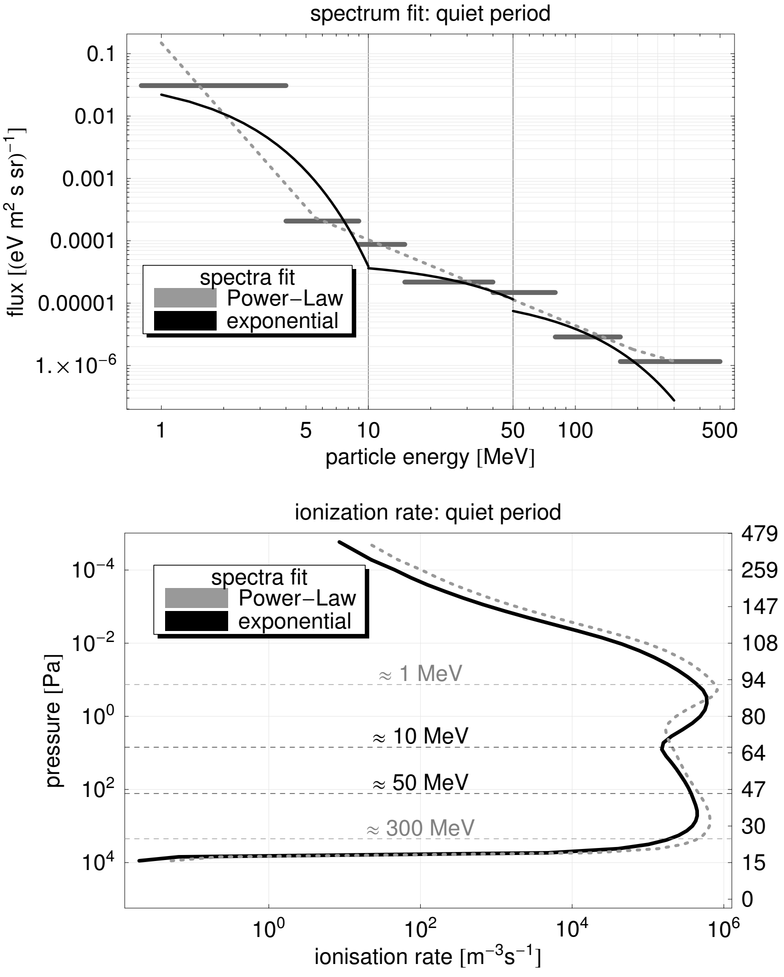

Figure 2.5: Spectrum fit (top) and ionization profile (bottom) in a geomagnetic quite period: Further explanation see Section 2.1.1. A sample from 9 Oct. 2003, 10–12 UTC is shown.

As Figure 2.4 also shows strong deviance around 80 km the high (trapped particle) count rates in GOES z_p1 channel (protons: 0.8–4 MeV) persist in a significant fraction of the examined time period. However, this should not be typical characteristic of a “quiet period” but since many ionization model use this energy channel we mention it. In the case of AIMOS, the GOES z_p1 channel will be exchanged against the POES channels to avoid using the high (trapped flux) count rates as fluxes inside the polar cap, but nevertheless this example shows the different behavior of the two fit methods at a bumpy particle spectra.

Comparison: smooth Particle Spectra Within an event (see Figure 2.6), the energy channels are mostly devoid of outliers and both fit functions are an adequate numerical representation of the particle spectrum. Therefore, the resulting ionization profiles are much closer together than it would be for a bumpy spectra.

The difference regarding the 150–300 MeV fit remains and recurs in the profile. We assume that it is due to a different post-processing of the GOES energy channels. While the power-law fit use the differential interpretation of these channels, the Maxwell-Boltzmann fit is based on integral channels of the same satellite. Consequently the difference is visible all time (see Figure 2.4, below 30 km).

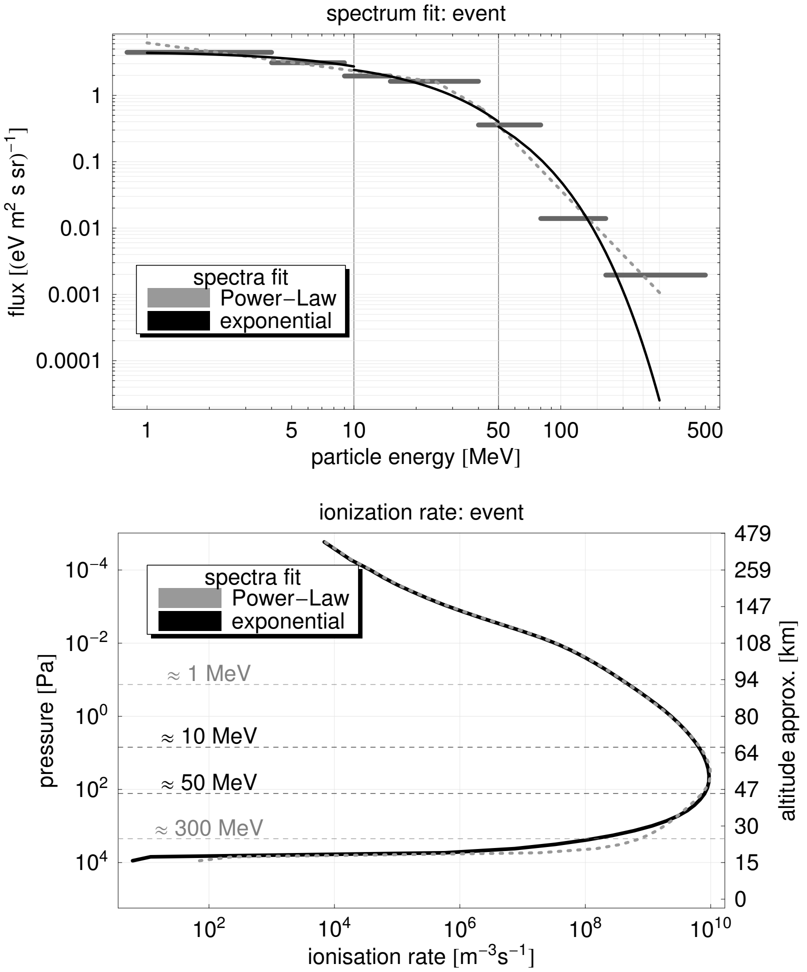

Figure 2.6: Spectrum fit (top) and ionization profile (bottom) in the event. A sample from 28 Oct. 2003, 20–22 UTC is shown.

Summary and Selection of Fit Function AIMOS should describe realistic spectra over a wide energy range and has to cope with breaks, accounting for intersections with changing steepness of the spectra. While the Maxwell-Boltzmann fit is difficult to reconcile with the underlying physics at high energies and shows artificial characteristics of minima and maxima in the ionization profile, power-law fit is based on a well grounded acceleration process for the favored particle energy (stochastic reflections within a shock). Consequently we will use the power-law fit. In order to minimize artificial extrema at characteristic altitudes variable intersections will be used.

Variation at different Energy Ranges

Using the power-law fit with variable intersections as intended for AIMOS, we can discuss the impact of different energy ranges on the ionization rate. Ionization by charged particles shows a distinct characteristic, the Bragg Peak: most particle energy is deposited at the end of the path. Hence the range of the particle energy spectra specifies the altitude range which should be accurately described. An extension of the energy range -in this case down to lower particle energy which ionizes in the upper atmosphere (thermosphere)- should have no or (only) little effect on the ion pair production in lower altitudes.

However, different energy ranges (a proton spectrum 1–500 MeV and another with the favored energy range for AIMOS: 154 eV–500 MeV) show severe differences in ionization values (see Figure 2.7, bottom). The small-range model run uses GOES-10 data (1–500 MeV, see Section 9.1.2 for details on GOES) whereas the enlarged-range model run uses a combined spectra from GOES-10 and measurements over the northern polar cap by POES 15/16 (see Section 9.1.1 for details on POES). The POES data include low energy TED (154 eV–9.457 keV subdivided in four channels) and mep0P1 to mep0P3 (30 keV–800 keV subdivided three channels) in order to extend the particle spectrum to lower energy.

Anyway, the problem is simple: An enlargement of the energy range causes variations in the fitting function. These variations might seem unimportant (see Figure 2.7) but since the function is a power-law (the same would be true for the Maxwell-Boltzmann fit) the effect on the ionization profile is severe (40% at 66 km altitude, respectively 200% at 20 km in this case).

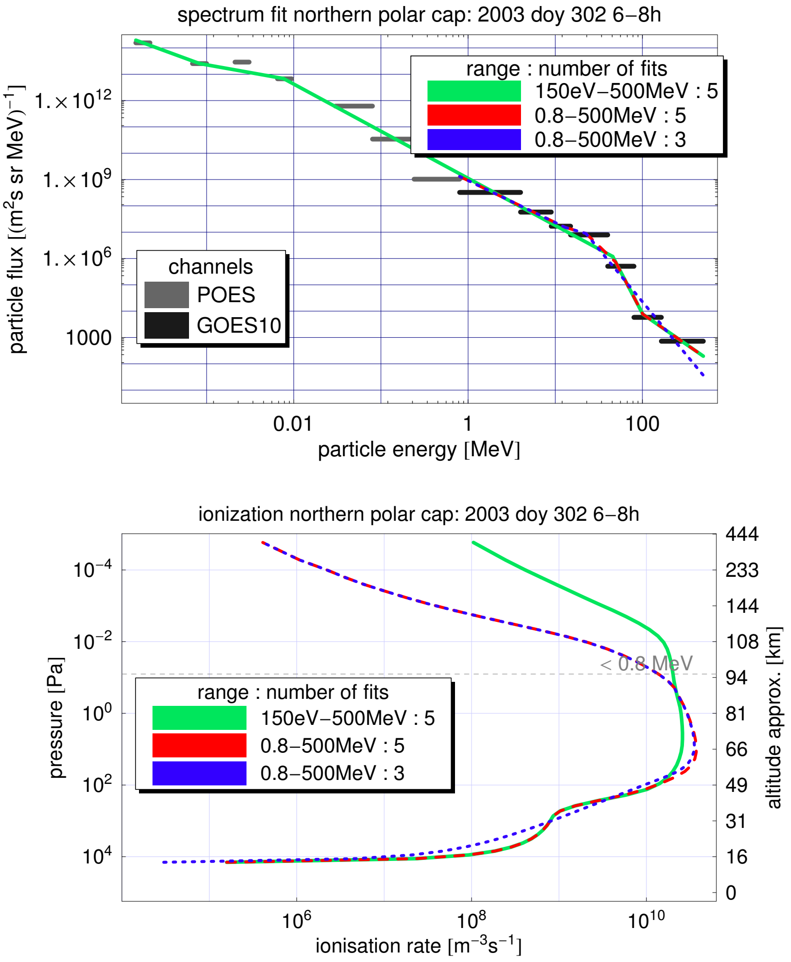

Figure 2.7: (top) The energy spectra shows only minor variations. But since the fit is logarithmic even small deviations have significant impact on the ionization profile. The extended range has been fitted by 3 and 5 fitting functions. (bottom) Ion pair production corresponding to the energy spectrum fits shown on top. The deviation of both energy ranges is visible at mid altitudes (66 km).

Every ionization model that is based on particle measurements uses energy fits. Therefore variations due to the fit function are an inherent and universal problem of all ionization data. Every direct comparison of a single time step that uses either different energy ranges, different fitting functions or number/position of intersections is problematic as the internal variation of the fitting function will be in the order of a factor of 2 (referring to ionization in some specific altitudes within our comparison of different energy ranges as shown in Figure 2.8).

A close look at the polar cap ionization rate of October and November 2003 (see Figure 2.8) gives an overview of the long-term behavior of both energy ranges in relation to each other. The ionization rate of the extended spectra is divided by the ionization rate of the narrow spectra. A factor of 1 would indicate an exact match. At mid altitudes (see the inset in Figure 2.8) deviations will seldom exceed the factors 0.5 (-50%) respectively 2 (+100%). In contrast, the strong impact of low energetic particles boost the extended spectra in the upper atmosphere (everything significantly above the <0.8 MeV line). A question at first glance might be the poor correlation around the 0.8 MeV line which is strongly affected by high and unwanted trapped particle count rates in the lowest GOES channel. This channel is influenced by trapped particles that are not visible in the low POES orbit and is omitted in the standard AIMOS routines. The extended data has an additional channel at 0.24–0.8 MeV. As channels with higher energy and higher count rates will be neglected by the fitting routine, the extended data range is much less affected by the z_p1 high count rates.

Recapitulatory, the biggest deviations can be found, as expected, in high altitudes as given by the enlarged spectra. The altitudes covered by both particle spectra show differences in the ionization rate up to a factor of 2. In addition the ionization rates at the bottom border suffer from poor congruence of the fit at the high energetic end of the spectrum.

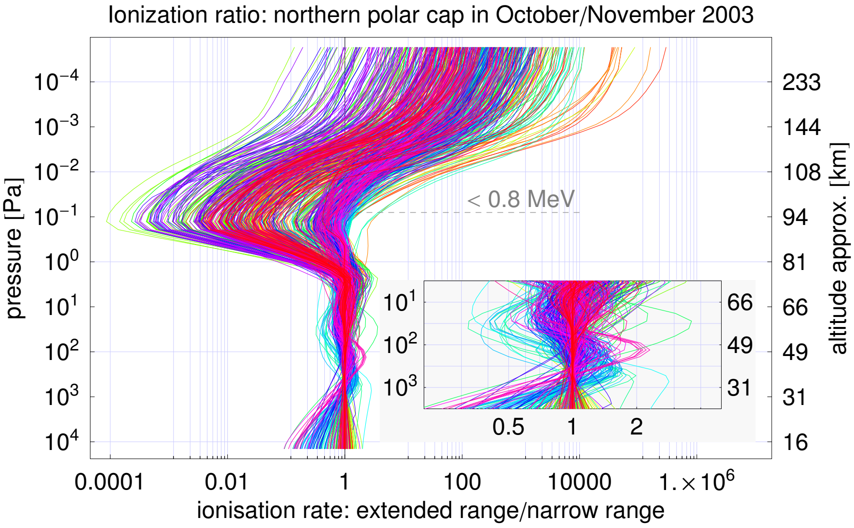

Figure 2.8: October/November 2003 2h-ionization profiles from the extended and the narrow energy range are shown in ratio. For detailed information look at Section 2.1.1.

From Figure 2.8 we can expect that the influence of these variations (in the altitude range covered by both model runs) minimize on longer time periods. Nevertheless we can deduce that comparisons of different models -and even the same model with a different energy range- at a single time step very likely lead to misinterpretations without a long-term comparison. The inherent problem of a (slightly) variable fit can not be avoided.

2.2 Definition of the atmospheric Detector

2.2.1 Atmospheric Parameters

An atmospheric model needs input parameters such as composition, temperature, pressure and altitude profiles. The atmosphere is not a static environment. Some aspects, such as seasonal and latitudinal variations, are obvious and need no discussion here. However, the large altitude range in general and in particular the high altitudes may be influenced by additional factors. This section gives an overview of the impact of sedimentation at high altitudes (heterosphere) and the impact of different solar states to composition and density profiles. The consideration of these aspects in AIMOS will be based on these results.

Homosphere or Heterosphere

Former ionization models like *Schröter et al.* (e.g. 2006); *Jackman et al.* (e.g. 2005b) use homospheric conditions for the atmosphere. However, AIMOS should cover an enlarged altitude range, starting at 1.7×10^{-5} Pa (respectively 250–600 km altitude) in the thermosphere. Since the constituents order corresponding to their scale height, light components (and in particular atomic constituents) are more common in the upper atmosphere. Consequently the atmospheric constituents are not homogeneously mixed in high altitudes. This paragraph shall discuss whether a heterosphere has to be considered in the model. We will focus on the resulting electron density of the atmospheric composition which has, at least in the Bethe-Bloch formalism, a linear impact on the energy deposition (and therewith ionization).

Please note that the electron density in this Section describes the *total number of electrons per volume* while the term is also common for the number of free electrons per volume.

Homosphere Assuming a homosphere, the total atmospheric electron density per volume can be described as a function of pressure and temperature. In detail, if we assume a charge-balanced atmosphere the total electron density per volume n_e is given by:

$$n_e = \frac{N \left\langle Z_{\mathrm{Atm}} \right\rangle}{V}. \tag{2.1}$$

Within this equation $\langle Z_{\mathrm{Atm}} \rangle$ is the mean atmospheric atomic number determined by weighted mean: $\langle Z_{\mathrm{Atm}} \rangle = \frac{\sum_{i=1}^{n} \nu_i a_i Z_i}{\sum_{i=1}^{n} \nu_i a_i}$. ν_i is the volume mix ratio and a_i represents the number of atoms per molecule. In a homosphere the mean atomic number is given by $\langle Z_{\mathrm{Atm}} \rangle = 7.37$, according to *ICRU* (NIST-Pstar/Astar 1993) definition of air and its constituents at ground level. While all atmospheric constituents except the noble gases (which add up to ≈1%) are assembled as molecules, a factor $\sum_{i=1}^{n} \nu_i a_i = 1.99$ has to be inserted into equation 2.1.

Using the ideal gas law: $pV = N k_{\mathrm{B}} T$, the altitude dependent homospheric electron density is given by:

$$n_e(h) = 1.99 \left\langle Z_{\mathrm{Atm}} \right\rangle \frac{p(h)}{k_{\mathrm{B}} T(h)}. \tag{2.2}$$

Heterosphere Assuming hererospheric conditions atmospheric constituents sedimentate at high altitude and molecules suffer from dissociation. Using atmospheric composition as given by the GCM HAMMONIA (*Schmidt et al.*, 2006) and the MSIS model* for the noble gas concentrations, the heterospheric electron density can be determined by:

$$n_e(h) = N_{\mathrm{a}} \rho_{\mathrm{Ham}}(h) \sum_{i=1}^{n_{\mathrm{matter}}} \frac{m_{\mathrm{ratio}}(i,h)}{A(i)} Z(i). \tag{2.3}$$

Within this equation A represents the atomic (molecular) mass, Z is the atomic number (or the sum of atomic numbers for molecules, respectively). m_{ratio} represents the mass ratio and ρ_{Ham} is the density according to the HAMMONIA GCM.

Figure 2.9 compares the homospheric and heterospheric electron density for an October atmosphere of 60°N (during solar maximum). The difference till layer 49 (90 km) is small as expected for the lower altitudes (< 1%). In higher altitudes the heterospheric electron density decreases faster than the homospheric one: layer 56 (ca. 110 km) to 90%, layer 62 (ca. 160 km) to 78% and in the highest layer 67 (ca. 400 km) to only 63% of the homospheric value.

Summing up, since the electron density has an impact on the energy deposition (according to Bethe-Bloch) the heterospheric calculation is essential in high altitudes above 90 km. Consequently AIMOS will use heterospheric compositions.

---

*NRLMSISE-00 Model 2001, available at `http://modelweb.gsfc.nasa.gov/atmos/nrlmsise00.html`.

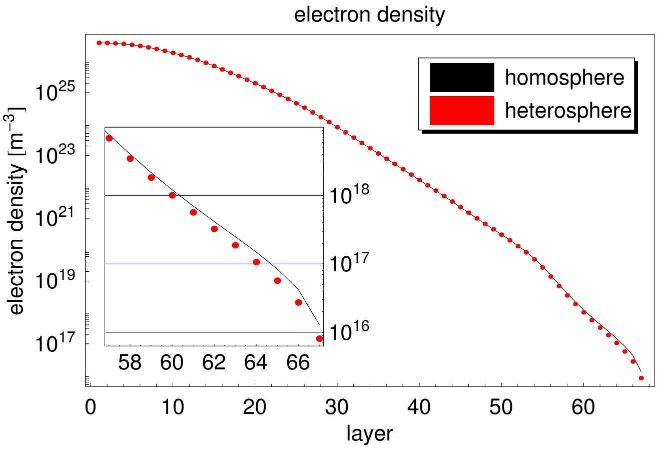

Figure 2.9: Comparison of homospheric and heterospheric electron density: difference till layer 49 (approximately 90 km) is less than 1%. For the upper atmosphere the difference increases. The electron density is shown for a mean October atmosphere at 60°N (during solar maximum).

Impact of Solar Cycle on atmospheric Input Parameters

The Sun is subject to a 22-year activity cycle affecting atmospheric parameters on Earth. The 10.7 cm radio flux (see Figure 2.10) can be used as indicator for the solar state. As the 10.7 cm radio flux (bremsstrahlung) requires strong magnetic fields (>0.03 T), it origins from active zones on the Sun and highly correlates to the Sun spot number (*Tapping and DeTracey*, 1990).

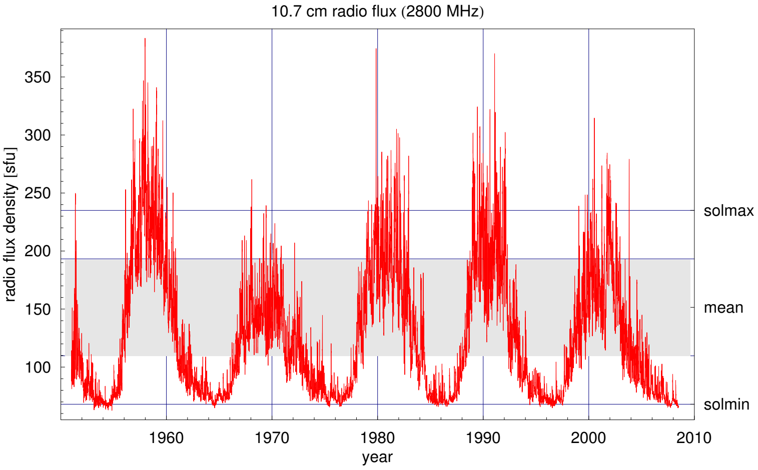

Figure 2.10: 10.7 cm radio flux including the values used for modeling (data from http://modelweb.gsfc.nasa.gov/solar/ottawa.html).

While the layers in the atmospheric model are defined by pressure levels, the corresponding altitudes and densities depend on solar activity. Atmospheric parameters for a solar minimum (68 sfu*) and solar maximum (235 sfu) state, generated within a 20-year long-term HAMMONIA simulation, are provided by the MPI of Meteorology (priv. comm. Jens Kieser and Hauke Schmidt). Since both states describe extreme conditions, a mean value characterizing moderate solar activity was calculated (in agreement with Jens Kieser, priv. comm.). Depending on daily 10.7 cm flux† the solar condition will be classified as minimum, moderate or maximum (see white and gray shadings in Figure 2.10) and the associated parameters will be used in the AIMOS model atmosphere.

Figure 2.11 shows the variation of the half level‡ altitude for solar maximum and minimum. In order to present the range of this variation the most extreme conditions of January

---

*solar flux unit, 10^{-22} W m^{-2}Hz^{-1}

†Additional information on the F10.7 cm flux is given on http://modelweb.gsfc.nasa.gov/solar/ottawa.html. The daily 10.7 radio flux was obtained from http://www.ngdc.noaa.gov/stp/SOLAR/ftpsolarradio.html, unfortunately this website is not hosted by NOAA any more.

‡The half level altitude is defined by the geometric mean of the upper and lower cell boarder. It corresponds to

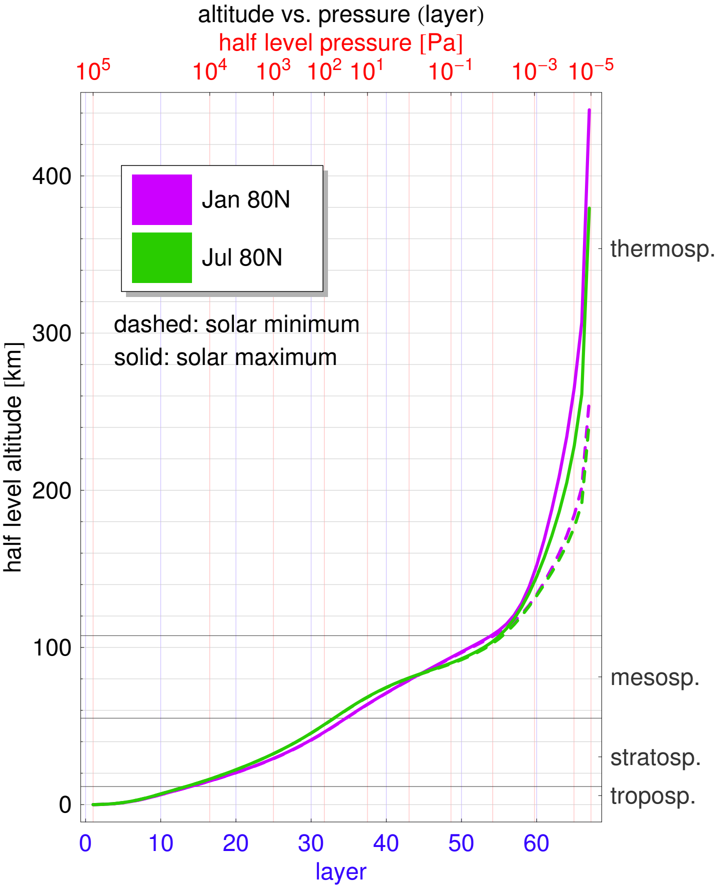

Figure 2.11: Overview on the pressure levels in AIMOS: The corresponding altitudes vary depending on season, latitude and, in the thermosphere, on solar activity. The conditions of January and July 80°N represent the variation range of the 48 different model atmospheres.

and July (at 80°N) are shown. As indicated by the upper and lower frame ticks, the half level pressure is fixed for every layer and allows a direct mapping. Some of the following figures will just use layer ticks for simplicity. As given by Figure 2.11, the altitude-pressure function below 100 km is dominated by season (and latitude) while the most obvious impact above 100 km is given by the solar state.

Please note that recent parameters may differ from the 20-year long-term HAMMONIA simulation. However, this is not a limitation to the AIMOS model itself but to the use of inaccurate data sets.

2.2.2 Is the magnetic Field (below 850 km) necessary for Simulation?

As only charged precipitating particles are considered, the geomagnetic field affects their trajectory. The satellite-borne particle maps (see Section 4.8) at 850 km already consider the main part of the magnetic influence. This Section will examine whether influence of the geomagnetic field can be neglected below 850 km.

We will focus on two aspects: (a) the magnetic field's impact on the particle flux due to pitch-angle rearrangement and mirroring in converging flux tubes and (b) the vertical and lateral displacement of the energy deposition/ionization in comparison to the model resolution. The displacement will be discussed separately for the two main precipitation zones, the polar cap and the auroral latitudes.

---

the altitude witch represents mean pressure for every layer.

Impact of the magnetic Field on Particle Flux

Pitch-angle rearrangement and mirroring in converging magnetic flux tubes affect the particle flux. Incoming particles encounter an increasing magnetic field. As long as the first adiabatic invariant is not violated this implies an increase in pitch-angle. For this reason a certain part of the particle flux will be mirrored (*magnetic bottle effect*) before entering the (dense) atmosphere. Apart from that an increasing magnetic field strength leads to a decrease in gyro radii. The *Liouville theorem* (*Vampola and Gorney*, 1983) says that the particle count rate within the loss cone is constant and independent of altitude. The loss of particles due to mirroring will be balanced by the decreasing size of the flux tube. Therefore the particle count rates at 850 km (POES orbit) or 36000 km (geostationary orbit) can be taken as particle flux entering into the atmosphere – as long as the locations are connected by the same field line. This has also been discussed in *Bornebusch et al.* (2010).

Displacement of the Energy Deposition

Charged particles are affected by the geomagnetic field. To gain a simple overview, we expect that a magnetic field focuses the particle flux close to the guiding field line. If we ignore particle scattering, the maximum distance to the guiding field line will be given by the Lamor radius. Using the maximum and minimum geomagnetic field strengths as given by the IGRF model (see Table 2.3), the resulting relativistic gyro radii were listed in Table 2.4. Assuming a tilted magnetic field, the guiding field line (and therefore the particle flux) will be displaced laterally from the initial point. The energy deposition in a tilted magnetic field is lifted due to different particle's path. In the dense atmosphere (meaning layers where collision frequency is comparable to or even exceeds gyration frequency), the magnetic field can obviously be neglected: collisions are too frequent to allow the charged particle to be guided by the magnetic field. We will discuss the lateral and vertical energy displacements for the two main particle precipitation zones (solar particles in the polar cap and magnetospheric particles in the auroral latitudes) and their main particle energies in comparison to the model grid.

Table 2.3: Absolute magnetic field strength as calculated by the IGRF model for mid 2003. The global minima lies at 30°S, 300°E, and for altitude 200 km and above at 20°S. The global maximum is located at 70°S, 200°E. Values for the polar cap region were taken at 80° geographic and poleward while the values for the auroral region were taken at 60–70° geographic North and South.

	global		polar	auroral
altitude	minimum	maximum	minimum	
0 km	$23.0\ \mu T$	$61.6\ \mu T$	$47.2\ \mu T$	$31.0\ \mu T$
50 km	$22.6\ \mu T$	$60.0\ \mu T$	$46.2\ \mu T$	$30.5\ \mu T$
100 km	$22.2\ \mu T$	$58.5\ \mu T$	$45.2\ \mu T$	$30.0\ \mu T$
200 km	$21.4\ \mu T$	$55.7\ \mu T$	$43.2\ \mu T$	$29.0\ \mu T$
300 km	$20.5\ \mu T$	$53.0\ \mu T$	$41.4\ \mu T$	$28.1\ \mu T$
400 km	$19.7\ \mu T$	$50.5\ \mu T$	$39.7\ \mu T$	$27.2\ \mu T$
500 km	$19.0\ \mu T$	$48.2\ \mu T$	$38.0\ \mu T$	$26.4\ \mu T$
600 km	$18.3\ \mu T$	$46.0\ \mu T$	$36.5\ \mu T$	$25.5\ \mu T$

Model Grid The model grid of AIMOS is adopted from GCM-modeling and agrees to the T31[*] resolution. In more detail the grid resolution is 400 km at the equator in meridional (North-South) as well as zonal (East-West) direction. Towards the poles the zonal grid distance declines due to the converging meridians. At 60° latitude the zonal grid distance is approximately 200 km. In total the grid has 96 cells along geographic longitude and 48 cells along geographic latitude. Some of the cells will be combined as e.g. inside the polar cap. As spatial variation in particle precipitation is determined by (geomagnetic) latitude, the 400 km meridional grid size is most important here. Table 2.5 lists the most important information of the AIMOS model grid.

As the model is expected to calculate every cell with an unlimited horizontal extent, no transport between neighboring cells will be considered. This Section should assess if this

---

[*] triangular truncation of wavenumber 31

		(relativistic) lamor radius				(relativistic) lamor radius	
	energy	B$_{\mathrm{min,aurora}}$	B$_{\mathrm{min,cap}}$		energy	B$_{\mathrm{min,aurora}}$	B$_{\mathrm{min,cap}}$
electrons	154 eV	1.6 m	1.1 m	protons	154 eV	70 m	49 m
	9.5 keV	13 m	9.0 m		9.5 keV	552 m	386 m
	30 keV	23 m	16 m		30 keV	981 m	686 m
	100 keV	44 m	31 m		80 keV	1.60 km	1.12 km
	300 keV	82 m	58 m		240 keV	2.78 km	1.94 km
	2.5 MeV	388 m	271 m		800 keV	5.07 km	3.54 km
	5 MeV	718 m	501 m		2.5 MeV	8.97 km	6.26 km
alphas	4 MeV	11.3 km	7.89 km		4 MeV	11.3 km	7.93 km
	10 MeV	17.9 km	12.5 km		9 MeV	17.0 km	11.9 km
	21 MeV	25.9 km	18.1 km		15 MeV	22.0 km	15.4 km
	60 MeV	43.9 km	30.7 km		40 MeV	36.2 km	25.3 km
	150 MeV	69.9 km	48.8 km		80 MeV	51.8 km	36.2 km
	250 MeV	90.8 km	63.4 km		165 MeV	75.9 km	53.0 km
	500 MeV	130 km	91.1 km		500 MeV	143 km	99.6 km

Table 2.4: Relativistic gyro radii have been calculated for minimum magnetic field in polar cap (B$_{\mathrm{min,cap}}$ $= 36.5\mu$T) and auroral oval (B$_{\mathrm{min,aurora}}$ $= 25.5\mu$T) for different particle species and energies. Therefore, the size of the gyro radii represent the upper limit within the corresponding region. The magnetic field origins from the IGRF model for mid 2003 (see Table 2.3). The relativistic Lamor radii r_{L} have been calculated based on $r_{\mathrm{L}} = \frac{\gamma m_0 v}{qB}$, with γ being the Lorentz factor $\gamma = \left(1 - \frac{v^2}{c^2}\right)^{-1/2}$. The velocity v has been derived from $E_{\mathrm{Kin,relatvistic}} = (\gamma - 1) m_0 c^2$.

region	latitude	zonal grid size
equatorial	0°	400 km
auroral	60°	200 km
polar cap	82°	60 km

Table 2.5: Zonal (East-West) grid size at different latitudes. The smallest zonal grid size is 34 km at 85°, but this lies inside the (combined) polar cap region and therefore exact differentiation of the precipitation pattern is not needed here. The meridional (North-South) grid border is 400 km at all places.

side condition can compensate the effect of a magnetic field. Therefore, our main interest is if particles enter (or should enter) a neighboring cell.

Displacement inside the Polar Cap At first approximation the main solar energetic particle precipitation area, the polar cap, has a vertical magnetic field (90°). Considering the track-length of an incoming particle and its corresponding deposition altitude there is no difference between the scenario with or without magnetic field. In both cases the track length l can be described by $l = h_p \cos\alpha$, while h_p is the penetration depth into the atmosphere and α is the incident angle (in relation to the vertical). The only difference is that a charged particle in a magnetic field will move on a helix instead of a straight line. For this reason the vertical energy deposition in a vertical magnetic field is equal to the deposition without magnetic field.

The lateral energy deposition, however, will be affected by magnetic focusing. Regarding electrons the Lamor radii (see Table 2.4) are two orders of magnitude smaller than the smallest grid resolution at the polar cap (see Table 2.5), so no relevant horizontal displacement of ionization is expected for a vertical magnetic field.

Protons and alphas are expected to have gyro radii of up to 100 km inside the polar cap. The smallest grid size (the zonal grid) here is 60 km. But as the polar cap is assumed to be homogeneously filled with particles, the zonal neighboring cells will not be affected by these particle transports. The grid size in meridional direction is about 400 km. Consequently no significant transport along the latitude is being expected.

Displacement inside the Auroral Oval Particle precipitation inside the auroral oval will be affected by a tilted magnetic field. An inclination of 60° reflects the "worst case" within the auroral oval. In auroral latitudes we are mainly interested in magnetospheric particles, so this Section will focus on low energetic particles. At first, we will discuss the vertical energy displacement which is to show a slight uplift in deposition altitude. *Fang et al.* (2005) simulated this effect for auroral protons (see Figure 2.12, lower graph). The altitudinal displacement at the central field line can only be seen at approximately 120 km altitude. Considering that the AIMOS vertical grid will be approximately 5 km here and the real angular distribution of the precipitating population is unknown[*], the magnetic field is not obligatory to give a significant benefit to the vertical energy deposition.

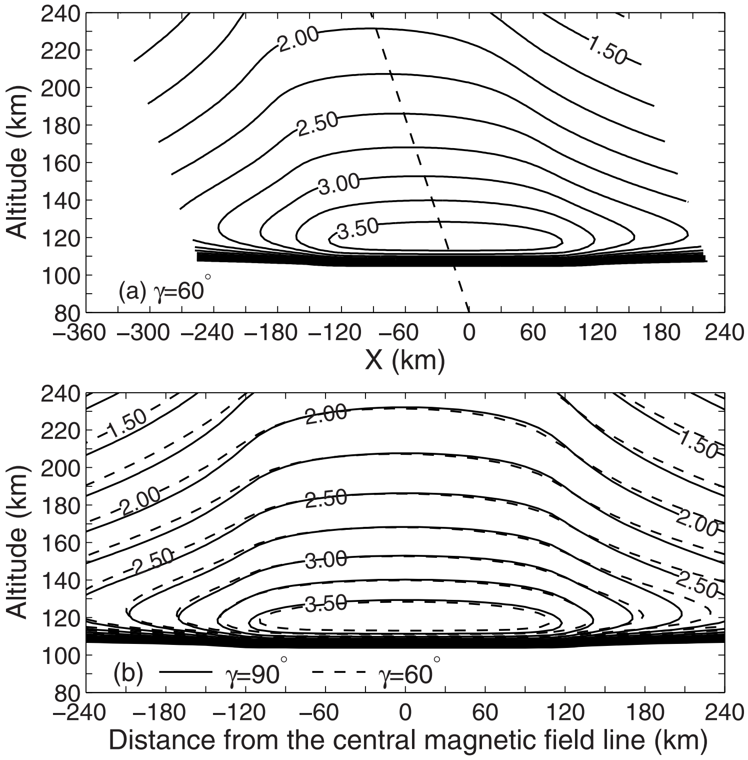

Figure 2.12: Upper figure (a): lateral ionization $(cm^{-3}s^{-1})$ displacement of a Maxwellian proton arc ($E_0 = 8$ keV, precipitation zone (arc width) $|X| \leq 120$ km) due to a tilted magnetic field (60°) and beam spreading effect. Lower figure: same as (a) but plotted against the central field line in comparison to a vertical magnetic field. Solid lines show the results for 90° (solid) and 60° tilted (dashed) magnetic field. Both figures by *Fang et al.* (2005).

In addition to the vertical displacement, we expect a lateral displacement of the ionization in a tilted magnetic field. As shown in Figure 2.12 (top), the proton energy deposition follows strictly the tilt of the magnetic field. According to Figure 2.12 (bottom), which compares the ionization in a vertical and a tilted magnetic field corresponding to the central field line, the main ionization area is almost identical. Therefore, the most important aspect will be the lateral displacement along the field line, which can be approximated by $\frac{750\text{ km}}{\tan 60^\circ} \approx 433\text{ km}$ (equivalent to the meridional resolution). In this equation, the 750 km describe the altitude difference between the satellite measurement and the main deposition altitude of magnetospheric particles at approximately 100 km altitude. According to *Fang et al.* (2005), the effect of the tilted magnetic field will be even less in the auroral zone as the dip angles are typically between 90° and 60°. Assuming an accuracy goal of one horizontal bin, no magnetic field is needed for the simulation.

Looking at low energetic protons the charge exchange has to be considered, too. Since an energetic Hydrogen atom is not attached to magnetic field lines, the so-called beam spreading effect results in strong lateral displacement of the energy deposition. In contrast to

---

[*] Since the pitch-angle distribution can not be measured by POES or GOES it is assumed to be isotropic. Strong fractions of vertical injections will cause a deeper atmospheric penetration therefore more fine tuning of the penetration depth is useless without the actual angular distribution.

electrons the energy dependence of the lateral displacement is decreasing with energy as a consequence of the penetration depth of energetic protons: collisions and therefore possible charge exchange reactions of high energetic protons in the lower (dense) atmosphere lead to a short mean free path. In contrast, low energetic protons may interact (and capture an electron) in the thin upper atmosphere, allowing strong lateral displacement by long mean free path. *Fang et al.* (2004) gives an impression of the beam radii of monoenergetic protons with different energies in Figure 2.13. As a consequence we expect repercussions at area borders affected by severe regional flux distinctions as seen in the auroral oval or the cap border. However, even if charge exchange generates a strong lateral displacement in the proton ionization, the total effect is limited. According to Xiaohua Fang (priv. comm.) beam spreading of incident protons may be neglected in a first order approximation as auroral electrons carry the majority of the kinetic particle energy to the Earth's upper atmosphere.

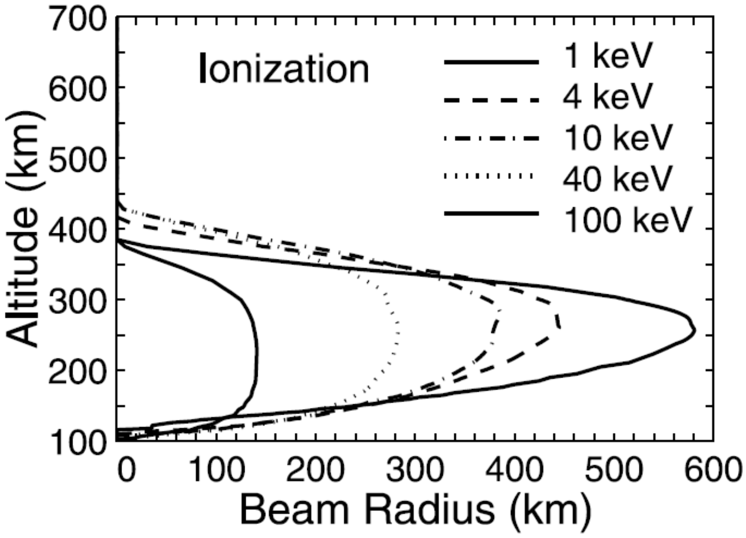

Figure 2.13: The effective beam radius including 80% of the primary ionization rate is plotted against altitude. The result for monoenergetic vertical proton injection at 1 keV is confined by the outer solid curve while the inner solid curve shows the 100 keV result. In between the injections at 4 and 10 keV are given (*Fang et al.*, 2004).

As electrons (of magnetospheric energy) have an even smaller gyro radii (see Table 2.4) and no charge exchange has to be considered, the ionization will be more attached to the field lines. Considering particle collisions *Berger et al.* (1970) show the small horizontal broadening around a central field line for magnetospheric electron energies in Figure 2.14.

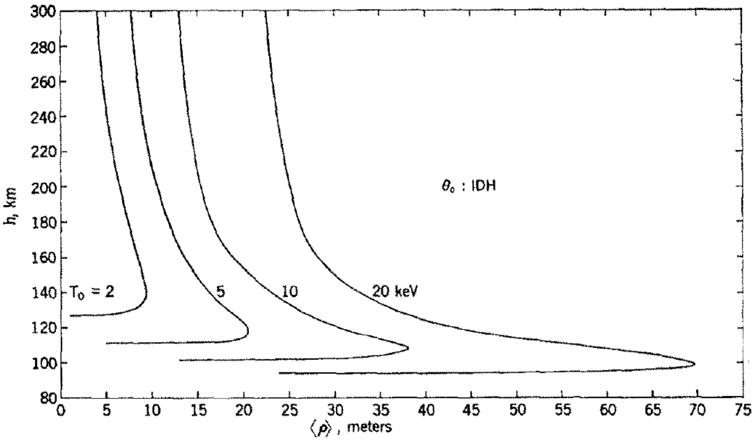

Figure 2.14: Mean value of the radial energy deposition at different electron injection energies using isotropic pitch-angle distribution. The magnetic field strength is $60\ \mu T$. (*Berger et al.*, 1970)

Summary To sum it up, based on an accuracy goal of one horizontal bin, the magnetic field is not necessary for the Monte Carlo simulation. The implementation of a magnetic field, that is: the field strengths and directions, depending on latitude, longitude and altitude, would have increased the number of GEANT4-simulation runs tremendously.

Within the Monte Carlo part of the *Atmosphere Ionization Module OSnabrück* the magnetic field will be replaced by the side condition of a horizontally infinite dimension at each grid point. Therefore, all incident particles deposit their energy in the grid box below their initial point. A possible source of defect might be that a particle can not leave the horizontal grid cell even it should leave it due to scattering or a huge gyration radius. Anyhow, backscattering into space and the corresponding energy loss will be considered.

2.2.3 Detector Construction

The detector construction and therefore the calculation of energy loss/ionization profiles is based on the GEANT4 (GEometry ANd Tracking) toolkit. This is a Monte Carlo based C++ programming toolkit allowing particle simulations in user specific detector layouts. The toolkit was developed by CERN*, the European institution for nuclear research. The benefit of a Monte Carlo method is the potential of simulating zigzag paths of, e.g., electrons, while Bethe-Bloch and range energy-relations can only describe the path of heavy elements. The basic concept is that a particle will interact with matter by a specific probability. Given that the probability is known, the interactions can be simulated along the particle's path through the detector. The path will be divided into small steps. Within each step different interaction processes might occur. The appliance of each process will be determined by a random generator – as well as it determines energy transfer and directions of secondary particles. The interaction probabilities and the skeletal structure is given by the GEANT4 toolkit and was tested and verified at CERN. The main aspects to be solved by a GEANT4 user are: (a) the design of an appropriate detector (atmosphere), (b) the selection of all necessary interaction processes, and (c) the installation of algorithms to extract all required information. Being of minor interest to physics the extraction algorithms will not be discussed here.

Atmospheric Detector

The idea of using Monte Carlo methods (and especially GEANT4) is not new (see, e.g., *Schröter et al.* (2006)). We used this model as our initial point. Various modifications have been applied such as:

- new general detector conception preventing transport errors,
- extended altitude range to cover the energy deposition of magnetospheric particles correctly,
- different primary particle species as electrons and alpha particles have been included,
- extended energy range also to include magnetospheric particles (see Table 2.1),
- and an increased number of incident angles to allow a significantly better altitude resolution (see Section 7.1.2).

As discussed in Section 2.2.2 the atmospheric particle detector will be modeled separately for different horizontal cells. To compensate the missing geomagnetic field we can use the side condition of unlimited horizontal extent at any of these grid points.

The vertical resolution in every horizontal cell is given by 67 logarithmic equidistant pressure levels, ranging from the sea-level to 1.7×10^{-5} Pa. We saw significant variations in atmospheric parameters (see Figure 2.11) for different solar states and different months, and without any doubt there are meridional differences. Therefore we will use parameter sets (priv. comm. Jens Kieser and Hauke Schmidt: temperature, density, composition and altitude is calculated by the GCM HAMMONIA and the MSIS model†) for four months (January, April, July and October), four different latitudes (80°S, 60°S, 60°N and 80°N) as well as three different solar states (solmin: 68 sfu, solmax: 253 sfu and a mean value of them for moderate solar activity).

---

[*] Conseil Européen pour la Recherche Nucléaire

[†] the MSIS-NRLMSISE00 *Picone et al.* (2001) is used for Argon and Helium components

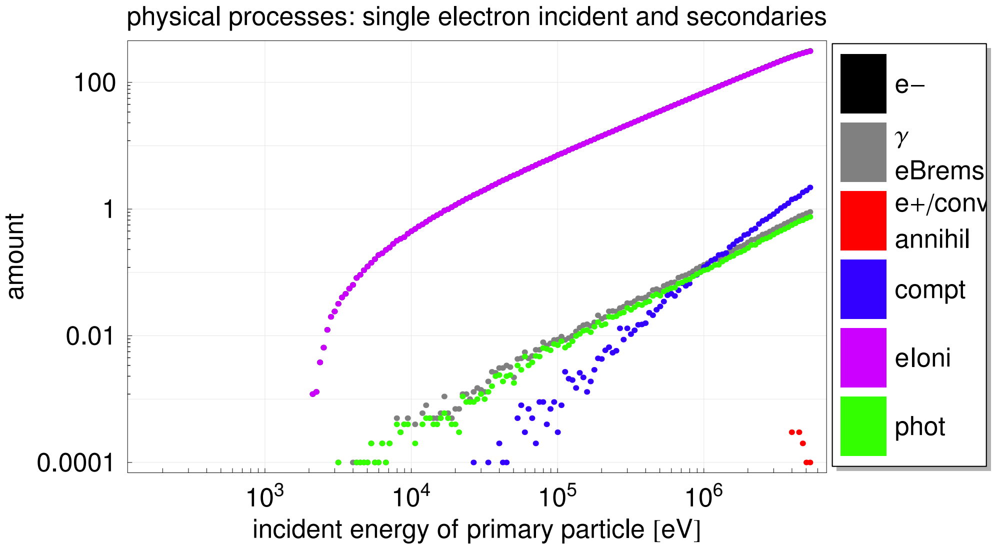

Figure 2.15: Physical processes occurring during vertical electron incidents (October 60°N solmed atmosphere) as a function of initial energy. The result represent a mean of 10000 incident electrons.

To define the ionization thresholds of the atmospheric components the experimental PSTAR/ASTAR data base is used (*National Institute of Standards and Technology* (NIST) *ICRU*, 1993).

In addition we used the most recent GEANT4-version (4.9.1.).

Physical Processes

GEANT4 is able to simulate a large number of different processes. The interacting particles and reactions have to be chosen corresponding to our energy range and detector materials. In AIMOS the detector is a model atmosphere and the energy range covers 150 eV–500 MeV for protons, 150 eV–5 MeV for electrons and 4–500 MeV/(per particle) for alpha particles. According to that the processes are: ionization*, Compton-scattering, γ-generation by electron bremsstrahlung and photo-ionization by γ-rays and, very rare, the generation of positrons (e^+) by γ-conversion and consequently annihilation of positrons. Other processes like pion or myon formation are irrelevant at these energies and have not been observed – even though they are allowed in the physics list. Apart from these discrete processes, GEANT4 is a condensed model, which means it does not e.g. simulate every single collision but the effect of multiple collisions after a specific track length (multiple scattering process).

The occurring processes (apart from multiple scattering) and secondary particles are shown in Figure 2.15 (electron), 2.16 (proton) and 2.17 (alpha particle).

As shown in Figure 2.15 (incident electrons) discrete processes and the production of secondaries is not simulated under a certain threshold. For this reason a large number of secondary electrons is missing in this graph. In more detail the threshold is defined by the energy transfer to a secondary particle and must exceed 1 keV. Ionization is by far the most dominant process, surmounting γ-generation by electron bremsstrahlung (displayed as one curve) and Compton-scattering by two to three orders of magnitude. The photo-effect is more or less alike the amount of γ-rays, considering a small loss into space. Very rare processes are γ-conversion to a electron–positron pair and the following e^+-annihilation.

---

*the exact description in GEANT4 depends on the primary particle: electron, proton or ion (alpha) as well as it's energy.

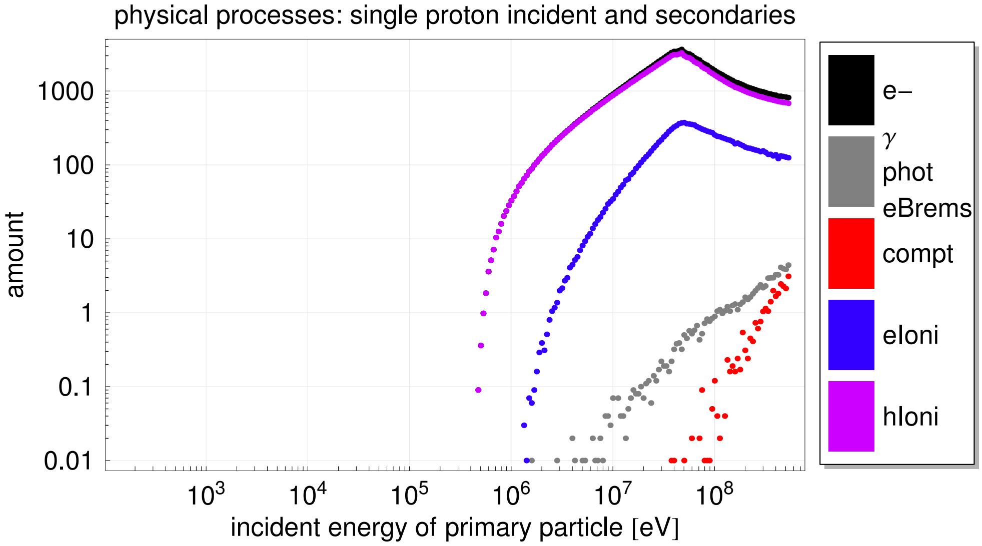

Figure 2.16: Physical processes occurring during vertical proton incidents (October 60°N solmed atmosphere) as a function of initial energy. The result represent a mean of 100 incident protons.

Summing up the dominating process is electron ionization, which even hides the curve of the produced (>1 keV) secondary electrons. As the ionization process is the same for primary electrons and secondary electrons, we can not distinguish between the single fractions.

The occurring processes and secondary particles of incident protons (see Figure 2.16) and incident alphas (see Figure 2.17) are very similar. Most secondary electrons are produced by primary particles (process: ion-ionization or hadron-ionization), while the second dominant process is electron ionization, meaning ionization by secondary particles itself. The generation of electron bremsstrahlung (γ-rays) and the following photo-ionization as well as Compton-scattering does not have a noteworthy influence on the total ionization. As seen and discussed for electrons in Figure 2.15 no secondaries are simulated for incident low energetic protons. In contrast the incident alphas started at higher energies.

Most obvious in Figure 2.16 and 2.17 is the turnover at approximately 40 MeV for protons and 160 MeV/(per particle)* for alpha particles. Given that the simulation of secondaries is time consuming, our aim is to focus on secondaries that might have an effect on the total energy deposition. Hence we introduced a threshold of 1 m. Secondaries that are expected to deposit their energy in a shorter range are not simulated. Our vertical grid is in the range of kilometers at the main energy deposition altitude. At lower altitudes, it is about several meters. Due to the 1 m range threshold we do not expect any significant error. However, as seen in Figure 2.18, the threshold of 1 m is responsible for the decreasing amount of secondaries below layer 29 (approximately 45 km). Layer 29 represents the altitude in which a 1 keV electron is expected to deposit its energy within 1 m. A simulation without the artificial threshold shows no decrease of secondary particles here – but it increases the computing time without a scientific benefit.

Initial particle energies at the right hand side of the turnaround in Figure 2.16 and 2.17 represent a dominant energy deposition below layer 29. As most photons range above 1 m, the mean free path cut-value does not affect bremsstrahlung, photo-effect nor Compton-scattering.

---

*equivalent to 40 MeV/nuc for protons and alphas, meaning that both particles have the same range

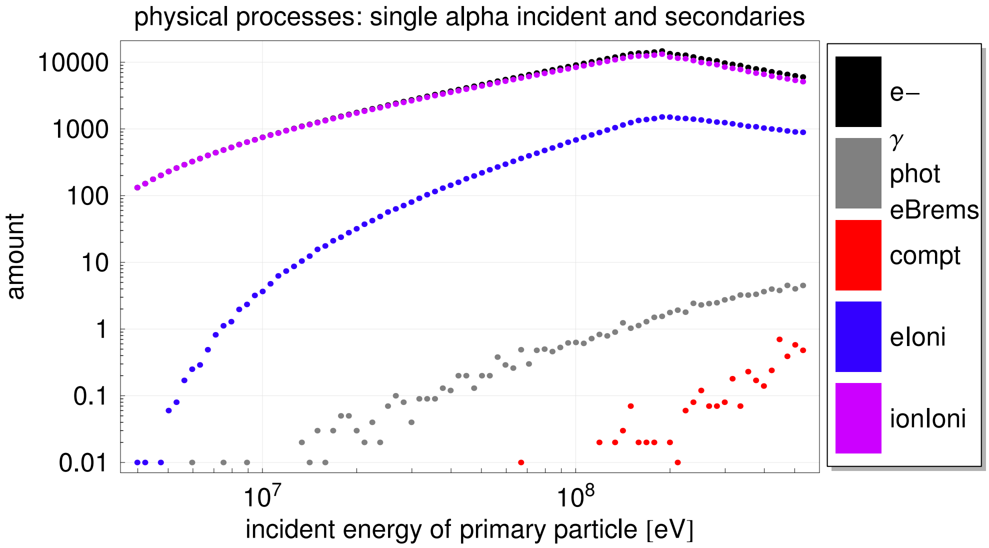

Figure 2.17: Physical processes occurring during vertical alpha incidents (October 60°N solmed atmosphere) as a function of initial energy. The result represent a mean of 100 incident alphas.

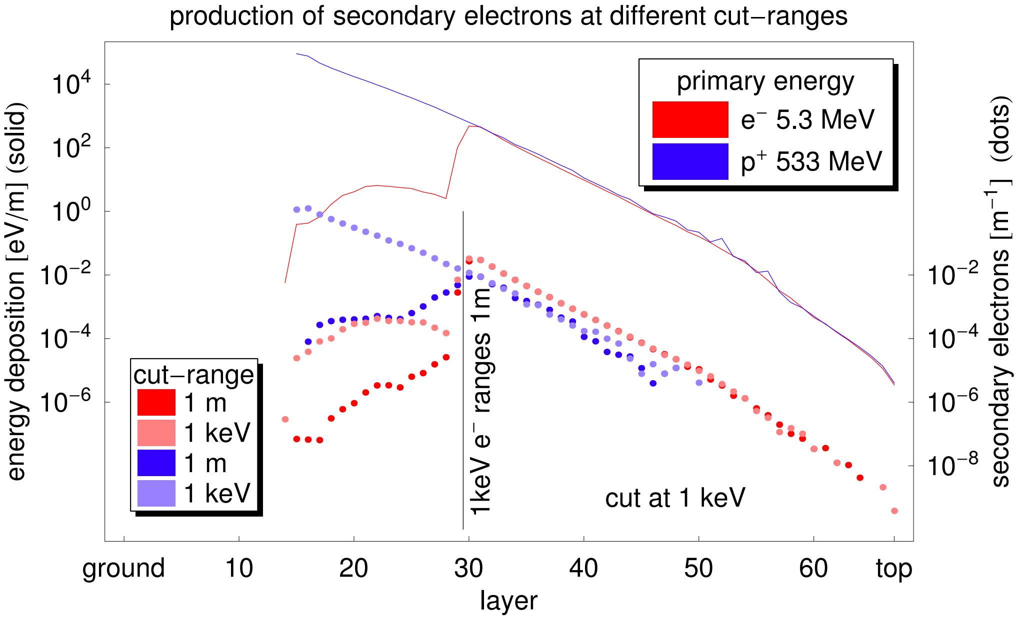

Figure 2.18: Production of secondary (tracked) particles at different threshold set-ups. The solid lines give the energy deposition for a proton (blue) and electron (red). The dotted graphs represent the corresponding production of secondary particles. In light red and light blue the threshold is 1 keV which represents the best (and most time-consuming) set-up. The dark red and dark blue color has two thresholds, 1 keV and 1 m range. In the dense atmosphere (below layer 29) a 1 keV electron ranges less than 1 m and the secondary particle production declines.

2.3 Folding

As details of the energy spectra have been discussed in Section 2.1.1 and the ionization algorithm was topic of Section 2.2, this section will discuss the combination of both.

The total ionization rate at each pressure layer l can be described by the integration of the mean ionization rate of "an" isotropic particle injection of (kinetic) energy E and the particle flux at this particular energy. The average ionization rate at a specific particle energy will be deduced from the GEANT4-based energy deposition algorithm by using a constant factor (see Section 7.2.2). Consequently the aberration $G_l(E)$ represents the GEANT4-based ionization rate at a certain pressure level l and particle energy E.

The 2 h particle flux differs in each of the 56 regions (see Section 4.8) and is given by a stepwise combination of up to five power-laws: $\Phi(E) = \Phi_0 \cdot (E/E_0)^{-\gamma}$. In the following the description will concentrate on one of these regions.

Accordingly the ionization rate I at every pressure layer l can be described by:

$$I_l = \int_{E_1}^{E_2} G_l(E) \cdot \Phi(E)\,\mathrm{d}E, \tag{2.4}$$

while E_1 and E_2 represent the thresholds of the corresponding power-law fits.

As the GEANT4 particle injections are limited to specific energies we have to transform Equation 2.4 by using the injection energies as barycentric energies E_s of a certain interval.

$$I_l = \sum_{E_{s,i}} G_l(E_{s,i}) \cdot \Phi(E_{s,i}) \cdot \Delta E_{s,i}. \tag{2.5}$$

The particle flux is given by:

$$\Phi(E_{s,i}) = \frac{\int_{E_{1,i}}^{E_{2,i}} \Phi(E)\,\mathrm{d}E}{E_{2,i} - E_{1,i}} = \frac{\int_{E_{1,i}}^{E_{2,i}} \Phi(E)\,\mathrm{d}E}{\Delta E_{s,i}}, \tag{2.6}$$

which will be used as substitution in Equation 2.5, resulting in:

$$I_l = \sum_{E_{s,i}} G_l(E_{s,i}) \cdot \int_{E_{1,i}}^{E_{2,i}} \Phi(E)\,\mathrm{d}E. \tag{2.7}$$

The thresholds $E_{1,i}$ and $E_{2,i}$ depend on the slope of the particle spectra. For the sake of simplicity, the thresholds are assumed to be in the mid between to neighboring barycentric energies. In order to limit the uncertainty the GEANT4-spectrum runs at a high energy resolution (262 logarithmically equidistant incident energies in the range of 150 eV to 500 MeV).

In summary the ionization rate at every pressure layer l can be determined by the following equation:

$$I_l \approx \sum_{E_{s,i}} G_l(E_{s,i}) \cdot \int_{(E_{s,i-1}+E_{s,i})/2}^{(E_{s,i}+E_{s,i+1})/2} \Phi(E)\,\mathrm{d}E. \tag{2.8}$$

The particle flux $\Phi(E)$ in this equation represents a stepwise combination of up to 5 power-laws with different slopes.

2.4 Summary

Finally we will briefly recapitulate the main aspects of this chapter and their relevance for AIMOS. The model includes magnetospheric and solar particles while GCRs are mostly omitted. The power-law can be used to describe the particle spectrum. As a wide energy range is covered the description will be based on up to five power-laws. The transitions between them are variable and will be selected by correlation factor. As the number of satellite based particle channels is (always) small in comparison to wide energy range, the fitting function as well as any assumption on transitions, number of fits and the energy range itself will have a significant impact on the estimated particle flux.

The particle detector in AIMOS is based on atmospheric conditions as they are given by the HAMMONIA GCM. This includes heterospheric mixing of constituents which becomes important above 100 km. The atmospheric mixing as well as physical parameters like altitude and temperature at a certain pressure level depend on solar activity and are modeled for solar minimum, maximum and a mean value. The magnetic field is not included in the Monte Carlo energy deposition model. Instead of that a sorting algorithm considers the particle populations on top of the atmosphere and the energy deposition algorithm prevents particle transfer between different grid points in a similar way as a magnetic field does. The energy deposition algorithm is based on the GEANT4 Monte Carlo toolkit. Hence it allows the simulation of proton, alpha and electron incidents. Physical processes like ionization, photo-effect, Compton-scattering, generation of bremsstrahlung and -in rare cases- γ-conversion and annihilation are modeled.

The ionization rates are calculated by a combination of the particle flux on top of the atmosphere and results of the Monte Carlo energy deposition algorithm for “an” isotropic particle injection.

Chapter 3

Variation of energetic Particle Precipitation with local magnetic Time

J.M. Wissing, J.P. Bornebusch and M.-B. Kallenrode

ADVANCES IN SPACE RESEARCH **41** p. 1274–1278, 2008.

3.1 Abstract

The detailed study of the precipitation of magnetospheric particles into the atmosphere is complicated by the rather complex spatial configuration of the precipitation region and its variability with geomagnetic activity. In this paper we will introduce polar oval coordinates and apply them to POES observations of 30 keV to 2.5 MeV electrons and comparable protons to illustrate the dependence of particle precipitation on local time and geomagnetic activity. These coordinates also allow an easy separation of the spatial precipitation patterns of solar and magnetospheric particles. The results indicate that (a) the spatial precipitation pattern of energetic magnetospheric electrons basically follows the pattern of the field parallel Birkeland currents *up to MeV energies* and (b) at least in the mesosphere the influence of magnetospheric electrons is comparable to the one of solar electrons. Implications for modeling of atmospheric chemistry will be sketched.

3.2 Introduction

Ozone depletion in the meso- and stratosphere has been observed following large solar energetic particle (SEP) events (*Heath et al.*, 1977). Precipitating relativistic electrons from the radiation belt were suggested, through the production of NO_x, to lead to local O_3 depletions in the 40- to 80-km region of the middle atmosphere (*Thorne*, 1977). Conventional approaches limit their studies to solar protons (e.g. *Jackman et al.*, 2000) and magnetospheric electrons (e.g. *Callis et al.*, 2001), and compare modeled results to observations. This approach is rather limited for two reasons: (a) both particle populations consist of protons, electrons and αs with different energy spectra and different composition, and (b) at least in solar particle events accompanied by a CME/shock also markedly increased levels of magnetospheric particles can precipitate during the geomagnetic storm. In addition, modeling attempts limit themselves to a rather simple spatial precipitation pattern in a stationary magnetosphere although the polar cap expands with increasing geomagnetic activity leading to particle precipitation at lower latitudes (*Leske et al.*, 1995, 2001).

In this paper we will shed new light on the precipitation of magnetospheric particles. We will introduce a system of polar oval coordinates which allows to order the spatial precipitation patterns of solar and magnetospheric particles and to identify the dependence of magnetospheric particle fluxes on local magnetic time.

The paper is structured as follows: in Section 3.3 the data and data analysis will be introduced, in particular the polar oval coordinates. In Section 3.4 the results are presented while Section 3.5 discusses them in terms of Birkeland currents and atmospheric modeling.

3.3 Data and Data Analysis

This study is based on data of the Medium Energy Proton and Electron Detector (MEPED) as part of the Space Environment Monitor (SEM-2) on board the Polar Orbiting Environmental Satellites (POES); for an instrument description see *Evans and Greer* (2004), the data is available at `http://poes.ngdc.noaa.gov/data/full/`. The instrument measures electrons in the energy range 30 keV–2.5 MeV and protons from 10 keV to more than 150 MeV in two detectors: one is looking backwards along the satellite trajectory, the other has a viewing direction radially outwards. The study is limited to data from the 0° detector because at high latitudes it roughly looks parallel to the magnetic field line and thus detects precipitating particles while most of the particles in the 90° detector will be mirrored back before hitting the atmosphere.

We will use data from the POES satellites NOAA-15 and NOAA-16. Both have roughly polar orbits (98° inclination) at an altitude of about 850 km and differ in the local time of equator crossing: NOAA-15 at LTAN 1900 and NOAA-16 at LTAN 1400. Thus particle populations can be observed simultaneously, meaning within the temporal resolution of one orbit, at different local times: NOAA-15 provides data on the morning and evening sectors while NOAA-16 observes noon and night sectors. The sectors are centered at 0 h, 6 h, 12 h and 18 h local time and spread over six hours each. Figure 3.4 also deals with NOAA-12 data, which is located in an orbit similar to NOAA-15. We have to annotate that the LTAN is not fix during many years, but within the observation period the sector classification is applicable.

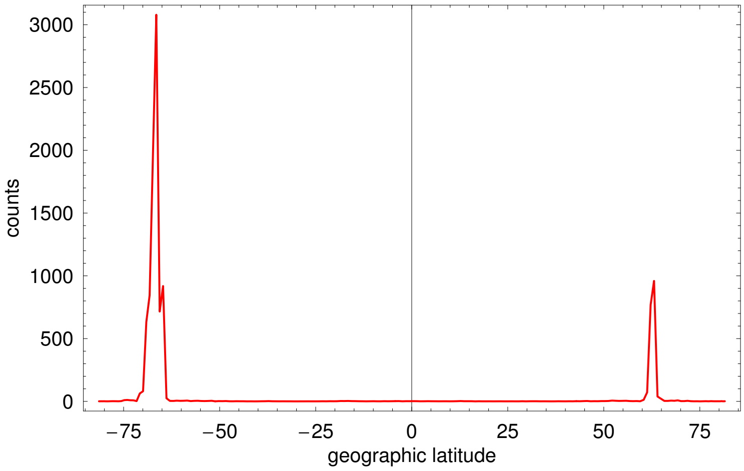

Figure 3.1: Sample for 30–100 keV electron count rates plotted versus geographic latitude at time of measurement for half a POES orbit.

Thus measurements along each orbit can be divided into a morning and an evening (a noon and a night) part. Count rates of 30–100 keV electron for such a half orbit are shown in Fig. 3.1. During quiet times the maximum count rates are observed at the latitude where the satellite orbit intersects the field lines mapping from the radiation belts down to the atmosphere, for short we will call this the auroral/polar oval. Owing to the tilted geomagnetic dipole and the interaction between solar wind and magnetosphere, the polar oval will be encountered at different latitudes for different longitudes and thus for different orbits of the satellite.

For each electron channel of MEPED, the location of the auroral oval during each pass is determined by fitting a Gaussian to the peak in Fig. 3.1 – actually a combination of up to four Gaussians in case the peak suggest a structure of multiple spikes. If one Gaussian is sufficient, the location of its maximum, its half width and the flux at the maximum give a complete description of the particles inside the polar oval. If more than one Gaussian was required for the fit, only the most prominent one (highest count rates and biggest half width) is chosen.

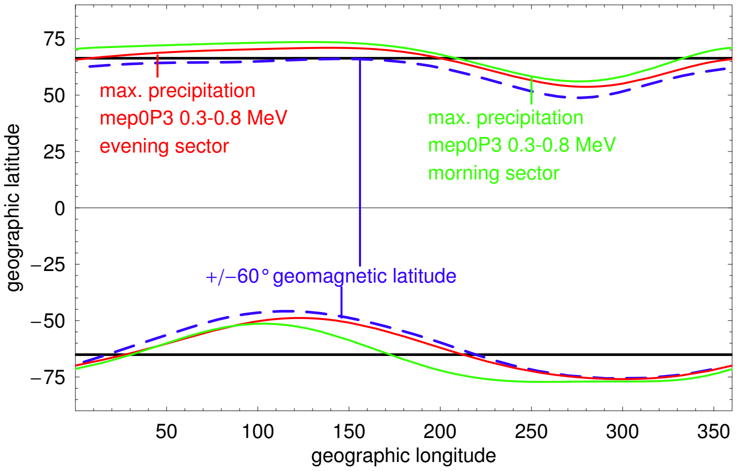

Figure 3.2: Position of the center of the polar oval in geographic coordinates (solid red and green line) and transformed to polar oval coordinates (black line). In comparison a constant geomagnetic latitude is shown (dashed line).

The average location of the polar oval determined from this fit for the geomagnetically quiet period from day 50, 2003, to day 130, 2003, is shown as green (morning sector) and red (evening sector) line in Fig. 3.2 for 0.3–0.8 MeV protons. For comparison, the dashed blue line shows a curve of constant geomagnetic latitude. The wiggle in the location of the maxima and its deviation from the geomagnetic isoline reflects the deviation of magnetospheric features from geographic as well as geomagnetic coordinates. The difference between the hemispheres and especially between the sectors indicates that a simple transformation to geomagnetic coordinates still will produce a wiggled polar oval. To aid the comparison of fluxes during half orbits observed at different geographic longitudes, we introduce polar oval coordinates: the maximum of the observed polar oval is kept at a fixed latitude Λ as indicated by the solid black line in Fig. 3.2. This fixed latitude represents the worldwide mean of the polar oval for that particular energy and is derived by fitting a polynomial up to ninth order in geographic longitude to the latitudes of the observed peak locations.

Since the polar oval coordinates are determined with respect to the center of mass of the particle precipitation, different energy bands lead to slightly different coordinates. As a rule of thumb, the polar oval is closer to the poles in low energies with a difference of the order of 4° between the 30–100 keV and the $>$300 keV electrons.

3.4 Results

The data from each satellite thus can be ordered such that they give the temporal evolution of particle fluxes in two sectors of local time, e.g. morning and evening, in a frame with a fixed position of the quiet time polar oval. Thus the temporal evolution of particle precipitation with respect to the quiet time polar oval can be studied as can be the dependence of particle precipitation on local magnetic time.

3.4.1 Quiet Time Precipitation

Figure 3.3 shows 30–100 keV electron count rates in polar oval coordinates for the morning (left) and evening (right) sectors of the geomagnetically quiet day 51, 2003. The thin white

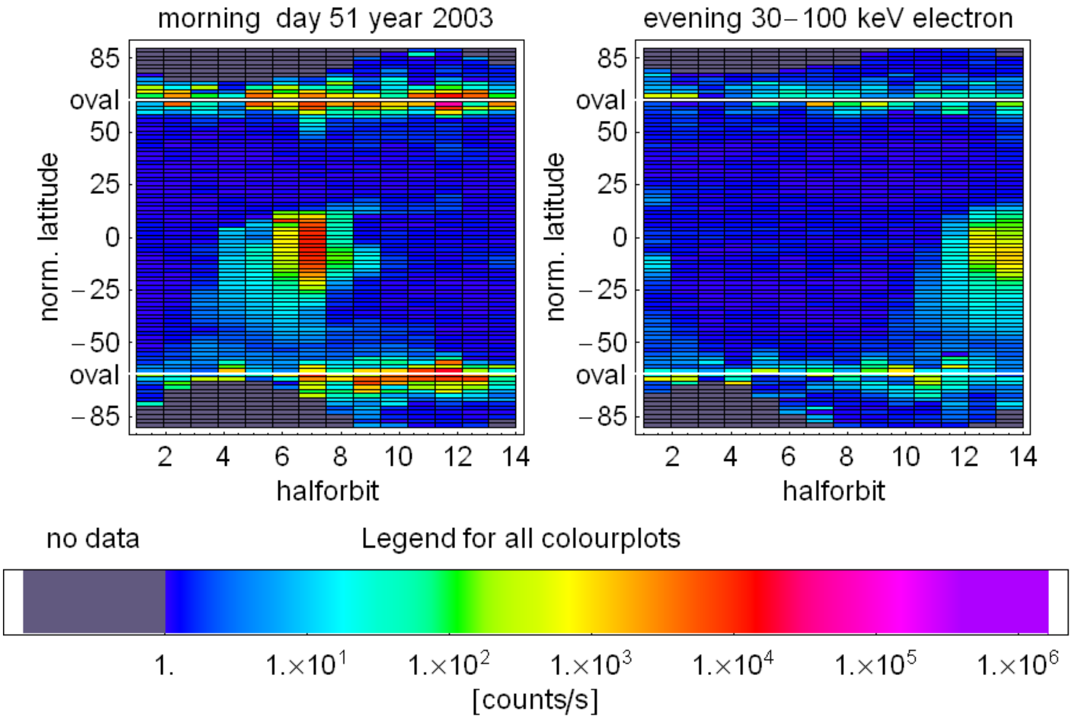

Figure 3.3: Count rates of precipitating 30–100 keV electrons in the morning (left) and evening (right) sector for the geomagnetically quiet day 51, 2003. The orbits are counted consecutively through the day and thus can be read as UT time; the thin white line gives the location of the quiet time polar oval.

line marks the quiet time location of the polar oval and corresponds to the solid lines of maximum precipitation in Fig. 3.2. The pronounced maximum at low latitudes is an artifact from the South Atlantic Anomaly. It does not indicate precipitating particles but a stable radiation belt population because at low geographic latitudes the 0° detector views roughly perpendicular to the magnetic field line and thus these particles will be reflected long before hitting the atmosphere.

From Fig. 3.3 it is noteworthy that fluxes in the morning sector of the polar oval significantly exceed the ones measured in the same orbital period in the evening sector. Figure 3.4 investigates this relation further. The black symbols give daily averages for the count rates in the evening sector versus the ones in the morning sector for all days of the years 1991–2005. Although there is a broad scatter in the data, the electron flux in the morning sector almost always exceeds the one in the evening sector. For a fixed electron flux in the morning sector, the corresponding flux in the evening sector can vary by more than one order of magnitude, occasionally even up to two orders of magnitude. It should be noted that this figure contains not only magnetically quiet periods but also magnetic storms and solar energetic particle events; thus the dominance of electrons in the morning sector (and of protons in the evening sector as will be discussed below) is a persistent feature.

The magnetospheric fluxes in the noon and night sector are in between the ones in the morning and evening sector with slightly higher fluxes in the night than in the noon sector, as can be seen in Fig. 3.5.

This dependence of polar oval particle fluxes on local magnetic time is not limited to electron energies below 100 keV but is still prominent in the energy range 100–300 keV. At energies above 300 keV the intensities of solar energetic particles are comparable or even higher than the ones of magnetospheric particles and thus the polar oval cannot be identified by the fitting procedure sketched above.

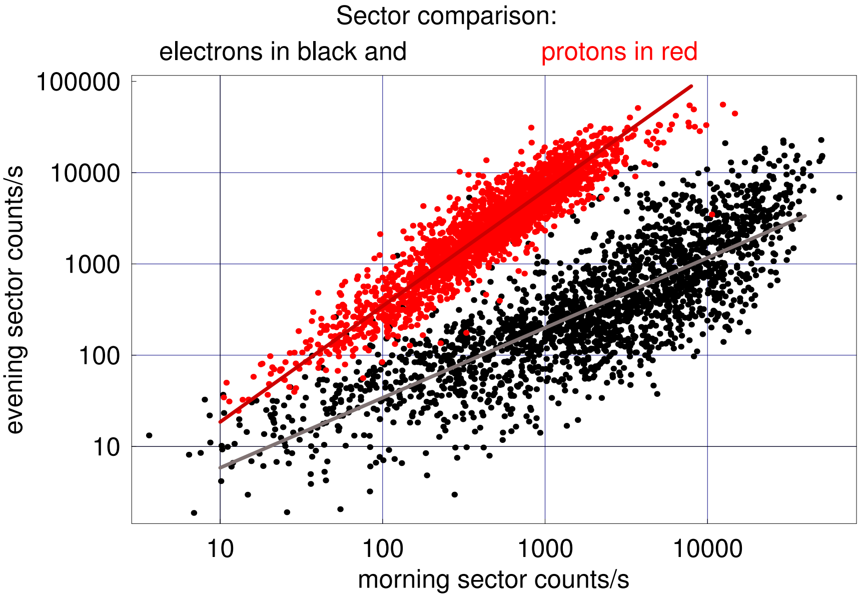

Figure 3.4: Ratio between polar oval counting rates in the evening and in the morning sector for 30–100 keV electrons (black) and 30–80 keV protons (red). Electron data is based on years 1991–2005 and proton data on years 2000–2005. For the period 1999 till 2005 the SEM-2 from NOAA-15 has been used, whereas the electron data before 1999 originates from SEM-1 on NOAA-12. The electron detector from SEM-1 is comparable to the one in SEM-2.

The precipitation of 30–80 keV protons shows the opposite spatial pattern: precipitation is stronger in the evening than in the morning sector as can be seen from Fig. 3.7 and also from Fig. 3.4. This suggests a charge dependent sorting mechanism in the magnetosphere. The day sector lies in between and the night sector plays a different role by having the highest fraction at low and medium count rates and only the second highest portion at the high fluxes. Not considering the night sector, which should intensely affected by the magnetotail the remaining sectors behave opposite to the electrons.

3.4.2 Geomagnetically active Times

From Fig. 3.4 we have already seen that the dependence of electron and proton fluxes in the polar oval on local time is not limited to geomagnetically quiet times but persists throughout storm times as well as during solar energetic particle events. Aside from the dependence on local time polar oval coordinates also offer some insight into the latitudinal variation of particle precipitation during geomagnetically active times.

Figure 3.8 shows in the lower panel the fluxes of 30–80 keV electrons plotted in polar oval coordinates for the period 216–220, 2003; in the upper panel the $\mathrm{K_p}$ index is shown. The injection of radiation belt particles with increasing geomagnetic activity is clearly visible as increase in particle flux (red arrows). The advantage of the polar oval coordinates is visible in the last two periods of increased $\mathrm{K_p}$: not only the increase in flux but also the motion of the polar oval towards lower latitudes is obvious. Both effects are well known and would also be visible in geographic or geomagnetic coordinates, however, polar oval coordinates allow to specify the shift in the spatial precipitation patterns with a single parameter, the shift in Λ.

3.4.3 Particle Precipitation during a Solar Event

Figure 3.9 shows $>$30 keV electron fluxes for the time period 147–152, 2003. The structure is the same as in Fig. 3.8 with an additional bottom panel showing differential intensities

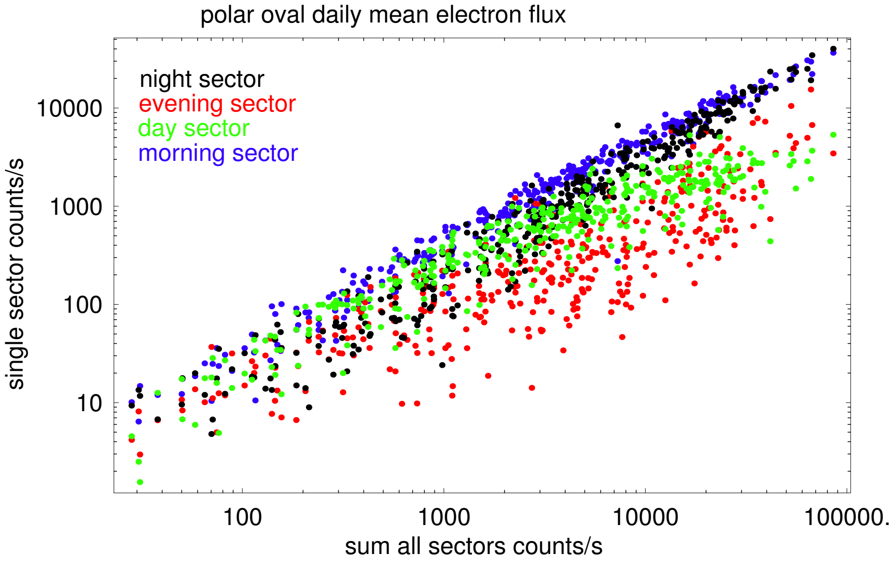

Figure 3.5: Count rates of precipitating 30–100 keV electrons in the different sectors during year 2002, including times of high and low activity.

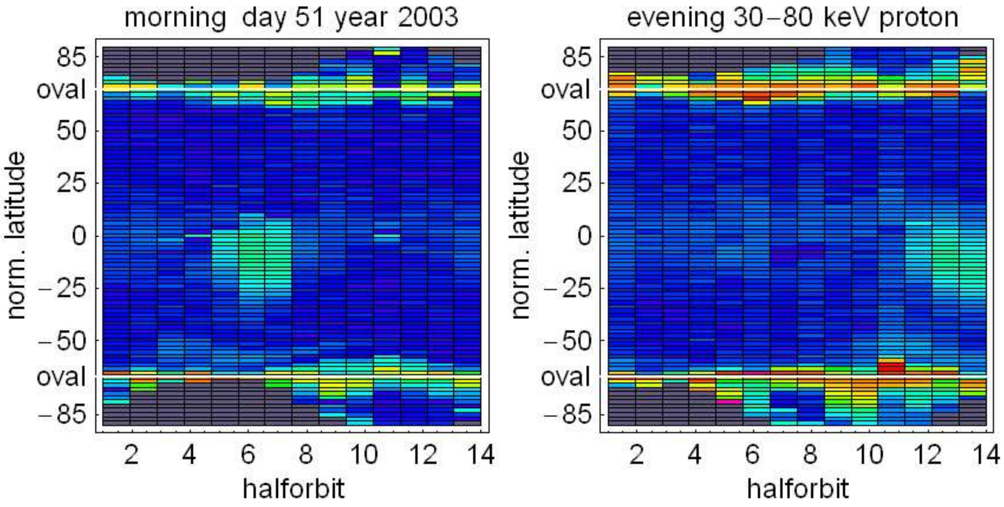

Figure 3.6: Same as Fig. 3.3 but for 30–80 keV protons

of 38–53 keV electrons obtained with the EPAM instrument on board the Advanced Composition Explorer (ACE). Here the power of polar oval coordinates for diagnostic purposes becomes visible: not only the fluxes in the polar oval and its spatial variation with increasing K_p can be identified easily but also the signature of solar energetic particles in the polar cap is obvious at times of increased particle intensities in interplanetary space as marked by the two vertical lines.

In this interplanetary electron event fluxes of about 50 keV magnetospheric electrons released during the geomagnetic storm by far exceed fluxes of the solar electrons in the polar cap by reaching ten or hundred times its value (day 303, 2003). With increasing particle energy the fluxes become more similar, owing to the steeper spectrum of the magnetospheric particles.

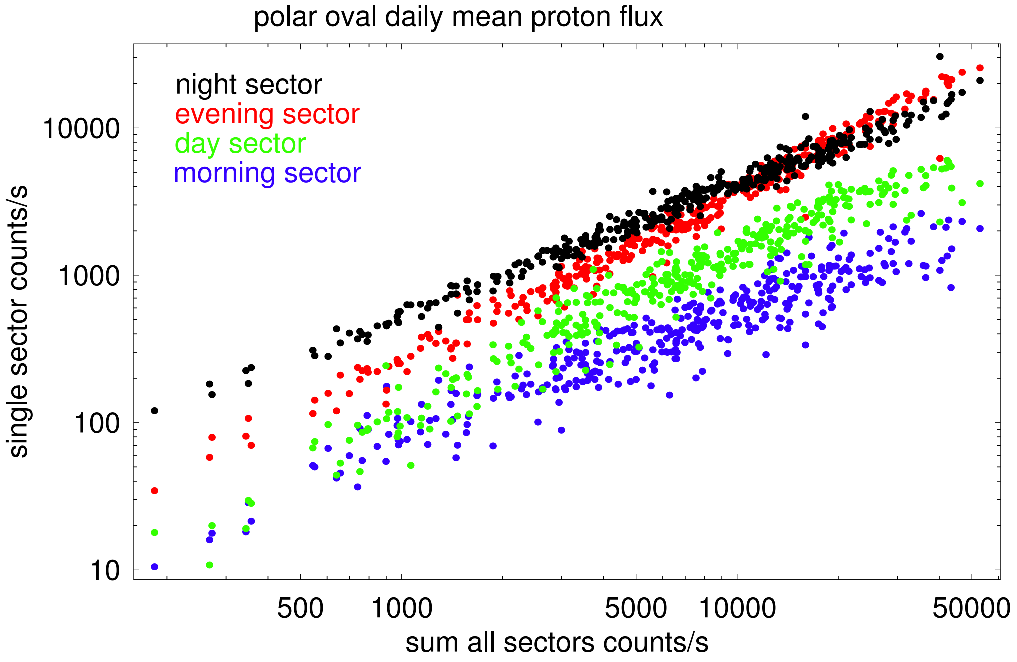

Figure 3.7: Same as Fig. 3.5 but for 30-80 keV protons.

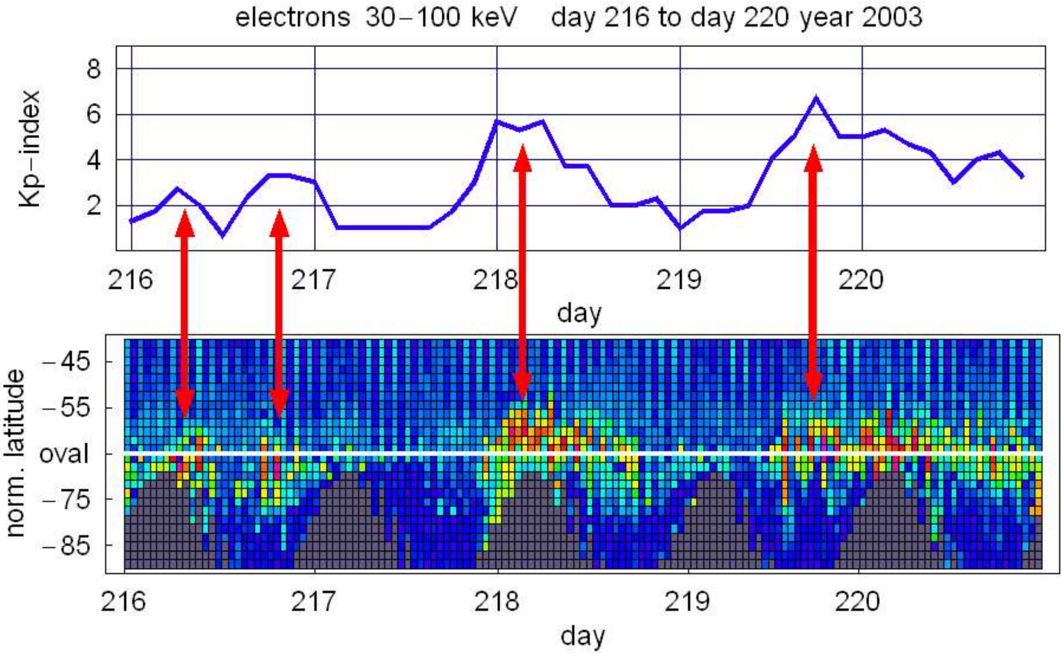

Figure 3.8: Flux of 30–100 keV electrons for doy 216–220, 2003, in polar oval coordinates for the southern hemisphere (lower panel) and K_p index (upper panel)

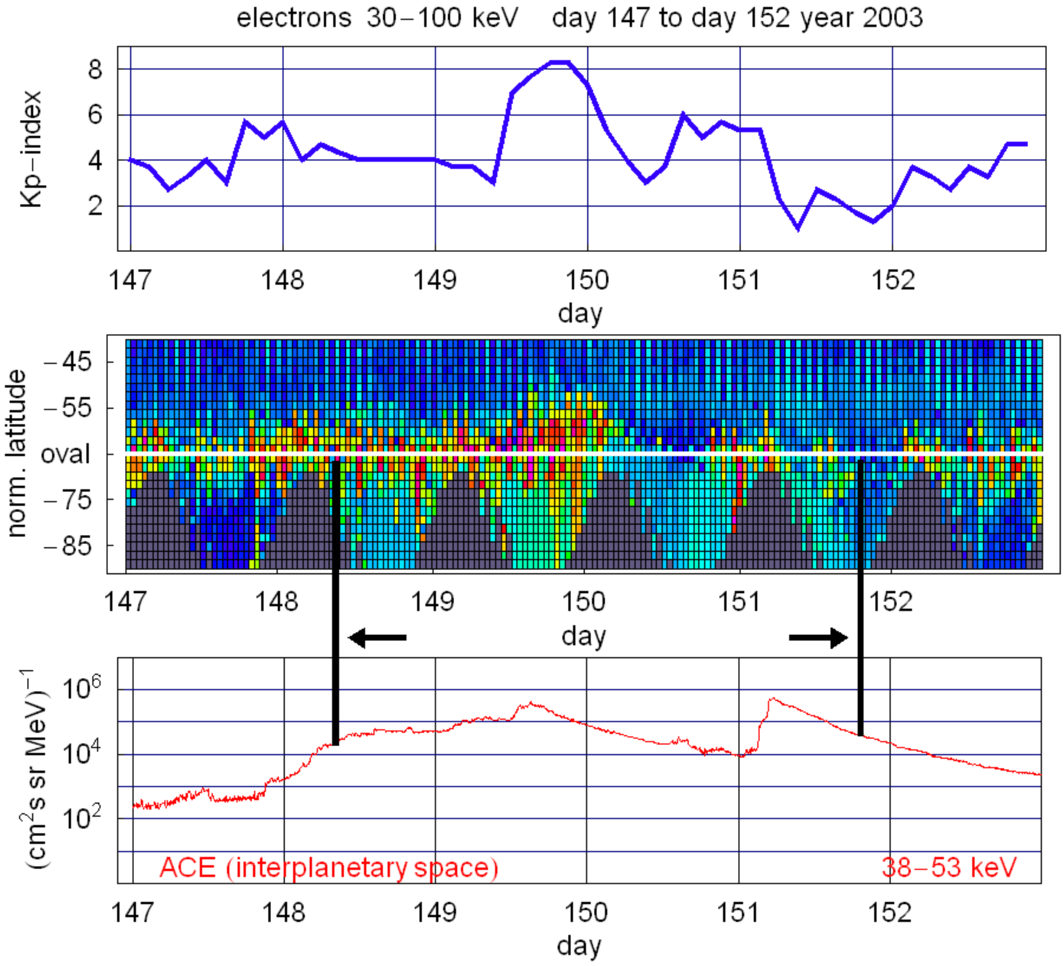

Figure 3.9: As Fig. 3.8 but for the time period 147–152, 2003; the additional lower panel gives the differential intensities of 38–53 keV electrons in interplanetary space as observed by the *Electron, Proton, and Alpha Monitor* (EPAM) on board ACE

3.5 Conclusions

The introduction of polar oval coordinates allows us to order the spatial distribution of particle fluxes observed from a polar orbiting satellite like POES for a more detailed analysis. The main results are:

(1) The flux of precipitating particles depends on local time:
  - At energies around 50 keV electron precipitation dominates in the morning sector while proton precipitation dominates in the evening sector. Similar results relating to lower energies have been presented by *Wedde et al.* (1973).
  - With increasing energy the dependence of electron precipitation on local time is less well-defined; above 300 keV a clear definition of the polar oval is not possible.

(2) The equatorwards motion of electron precipitation at times of increased geomagnetic activity can be quantified by a single spatial parameter $\Delta\Lambda$.

(3) Precipitating solar and magnetospheric particles can be separated easily.

Result (1) is a little bit surprising because it suggests that contrary to our expectations about 100 keV electrons are not individualistic energetic particles. Instead, they appear to be the high energetic tail of the electron distribution forming the magnetospheric current systems, namely the Birkeland current. This view is supported by the observed charge separation with an excess of electrons in the morning sector resulting from the grad B drift in the magnetopause and coupled into the high latitude atmosphere by the region 2 currents. In addition, the relative position of electron and proton precipitation ovals is in agreement with the field parallel currents as described in *Ijima and Potemra* (1976). It should be noted, that the observations presented here only give a first indication that spatial patterns of energetic particles follow the ones of the Birkeland currents. There are some open questions, in particular regarding the night side distributions as well as the behavior of particles with same rigidity. These questions can be addressed only after the analysis of the lower particle energies as measured e.g. with the TED instrument – an analysis, that is beyond the scope of this paper.

For our purposes more interesting are the consequences of this spatial dependence for atmospheric modeling. The most important consequence is the clear separation of the magnetospheric and solar particle populations which allows a quantitative description of their relative contributions at different energies and locations (results 2 and 3). It is well beyond the scope of this paper to derive an indication when and where which component is dominant since this will be highly variable depending on the properties of the solar particle event, the strength of the geomagnetic disturbance and the properties of the magnetospheric particle population. The method presented here will not only be helpful in the study of individual events (*Wissing et al.*, 2010a) but might also help to develop a parametrization of precipitating magnetospheric particle fluxes and locations in terms of geomagnetic indices.

Acknowledgments

We are grateful to the National Oceanic & Atmospheric Administration (NOAA) for providing the POES data, to the Space Radiation Lab at California Institute of Technology for providing ACE data as well as the Danish Meteorological Institute for the initialization of the K_p-index. This work was supported by the Deutsche Forschungsgemeinschaft DFG under contract KA 1297/2-3 and KA 1297/6-1.

Chapter 4

Atmospheric Ionization Module OSnabrück (AIMOS): A 3-D Model to Determine Atmospheric Ionization by Energetic Charged Particles from Different Populations

J.M. Wissing and M.-B. Kallenrode

JOURNAL OF GEOPHYSICAL RESEARCH, VOL. **114**, A06104, doi:10.1029/2008JA013884, 2009.

4.1 Abstract

We present a 3-D numerical model of atmospheric ionization due to precipitating particles with high spatial resolution. The *Atmosphere Ionization Module OSnabrück* (AIMOS) consists of two parts: a GEANT4-based Monte Carlo simulation and a sorting algorithm to assign observations from two polar-orbiting satellites to horizontal precipitation cells, depending on geomagnetic activity. The main results are as follows: (1) the sorting algorithm and thus the 3-D mapping of particle fluxes works reasonably well; (2) ionization rates are in good agreement with the ones from earlier models; (3) during quiet times, the major contribution to ionospheric ionization is from electrons both in the polar cap (solar electrons) as well as in the auroral oval (magnetospheric electrons) with the ionization in the auroral oval exceeding that in the polar cap; (4) during solar particle events the dominant effect in the polar cap in the stratosphere and mesosphere is from solar protons although solar electrons can contribute up to 30% to the ionization; (5) during strong shocks following a solar particle event, in the auroral oval magnetospheric electrons and protons lead to ionization rates of up to some 10% of the ones of solar particles; and (6) independent of particle source and precipitation site, in general, ionization by electrons is more important in the thermosphere.

4.2 Introduction

One link in solar-terrestrial relationships are energetic particles: the precipitation of solar energetic particles into the atmosphere causes ionization, NO_x and HO_x production and eventually the depletion of ozone. An early observation of the role of solar energetic particles (SEPs) in ozone depletion was the large August 1972; its analysis established the role of NO_x in stratospheric ozone chemistry (*Crutzen et al.*, 1975; *Heath et al.*, 1977).

Early modeling attempts focused on stratospheric ozone. The relevant solar particles were protons with energies from a few MeV to a few hundred MeV; contributions from solar electrons and heavier particles were assumed to be negligible (*McPeters and Jackman*, 1985). In addition, particle precipitation is assumed to occur uniformly over a nominal polar cap without considering the equatorward expansion of the cap and thus the particle precipitation area with increasing geomagnetic activity as observed e.g. with SAMPEX (*Kahler and Ling*, 2001; *Leske et al.*, 2001) or POES (*Wissing et al.*, 2008). This conventional approach still is used in modeling precipitating SEPs (see, e.g., *Jackman et al.*, 2001, 2005a; *Randall et al.*, 2007; *Rohen et al.*, 2005; *Verronen et al.*, 2002). In addition, the energy range under study (and thus the height range over which ionization occurs) is limited by the particle instrument considered in the study and thus only is a subset of the total precipitating solar proton inventory during the event. Only in rare cases instruments with different energy ranges are combined to yield a more comprehensive spectrum (*Mewaldt et al.*, 2005) but to our knowledge these combined spectra did not enter into the calculation of atmospheric consequences.

Electron precipitation into the atmosphere also has been analyzed; however, electrons are assumed to be magnetospheric electrons, at its low energetic end also called auroral particles. Here particle fluxes are derived from observations with a polar-orbiting satellite and assumed to be uniform over the auroral oval (e.g., *Callis et al.*, 1996a,b, 1998) or particle fluxes/ionization rates are determined from a parametrization relying on a geomagnetic index (e.g., *Fang et al.*, 2008; *Marsh et al.*, 2007; *Roble and Ridley*, 1987).

Wissing et al. (2008) combined data from two POES spacecraft to analyze in more detail the spatial pattern of precipitating particles. As expected, the authors found a contribution of both electrons and protons in the polar cap (SEPs) as well as in the auroral oval where magnetospheric particles precipitate. Fluxes of these latter particles showed a strong dependence on local magnetic time: measurement of an auroral oval crossing from one satellite does not give a representative particle flux for the entire oval but, depending on local magnetic time, might over- or underestimate the average particle flux inside the oval by a factor of up to five.

The *Atmosphere Ionization Module OSnabrück* (AIMOS) presented in this paper provides a tool to simulate the 3-D ionization effects of almost the total particle inventory on the entire atmosphere depending on geomagnetic activity. This allows (1) for a better comparison between observations and simulations and (2) for a comparison of the relative contributions of the different particle populations to atmospheric chemistry. This is important for long-term studies of atmospheric ionization that rely on proxies such as $\mathrm{K_p}$-index for magnetospheric particles. In addition, the horizontal resolution also provides the necessary quality for local measurements such as the comparison of radar echoes at different locations in the polar cap and polar oval. With time, a long-term database of high-resolution 3-D ion pair production rates in the atmosphere will be made available to the public; a short version spanning the years 2002–2005 already can be found at `http://aimos.physik.uos.de`.

The paper is structured as follows. In Section 4.3 we discuss the flow chart of the model and the submodules for ionization and particle sorting. Section 4.4 describes the data from different satellites that enter into the model while Section 4.5 is concerned with validation. In Section 4.6 the relative contributions of the different particle species and populations to atmospheric ionization will be discussed. Model and results are summarized in Section 4.7.

4.3 Model: AIMOS

The intent of *Atmosphere Ionization Module OSnabrück* (AIMOS) is the consistent modeling of ion pair production due to precipitating particles for the entire particle inventory of energetic solar and magnetospheric particles. The model is designed to convert observations of energetic particles from satellites into a 3-D ionization pattern in the atmosphere.

Figure 4.1 shows the AIMOS scheme, consisting of two parts: (1) the retrieval of energetic particle spectra and the horizontal precipitation pattern from observations and (2) the simulation of particle interaction with the atmosphere using monoenergetic particle beams of

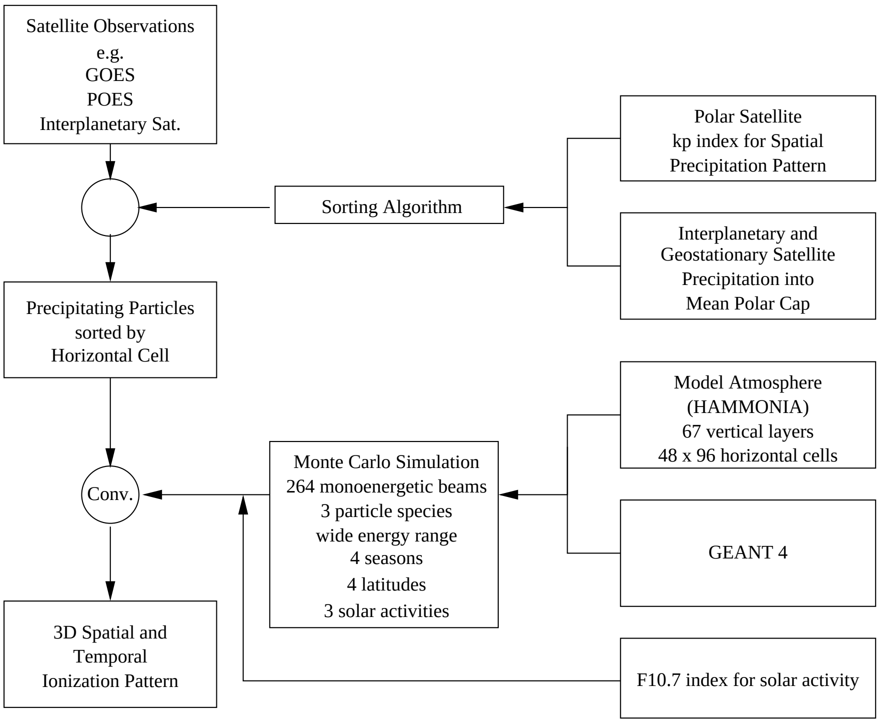

Figure 4.1: AIMOS flow chart.

different energies, angles of incidence and particle species. The latter data set is convoluted with the former to give the 3-D atmospheric ionization (or ion pair production) rates.

A rather complex retrieval mechanism is required because energetic particle measurements are in-situ measurements. Thus it is not possible to obtain some snapshot of particle distributions at the top of the atmosphere. Instead, a combination of data from at least two polar-orbiting spacecraft is required to determine such a precipitation map, as will be described in detail in Section 4.3.2. These maps depend on particle energy, or more accurately rigidity, because the geomagnetic cutoff depends on rigidity. They also depend on geomagnetic activity: with increasing geomagnetic activity the polar cap and the auroral oval expand equatorward. The result is the square "Precipitating Particles sorted by Horizontal Cell" in the middle on the left side in Figure 4.1.

The second part of the model describes the particle interaction with the atmosphere using a Monte Carlo simulation, as described in detail in Section 4.3.1. This part requires an assumption concerning the atmosphere, namely its density and temperature profiles. The latter depends on season, latitude and solar activity. Therefore different runs have been performed for different states of the atmosphere. Thus a given input of precipitating particles yields different ionization profiles for different seasons and/or different levels of solar activity. The atmosphere most adequate for a given day is chosen by date (gives the season) and F10.7 index as a measure for solar activity.

The model's limitations are determined by the spatial resolution of the model atmosphere and by the energy spectrum covered by the particle instruments. The model atmosphere extends from ground up to 1.7×10^{-5} Pa, corresponding to an upper boundary between 250 to 600 km. The spatial grid is $3.6° \times 3.6°$ in the horizontal with 67 logarithmically equidistant height layers. The energy range of precipitating particles is 150 eV to 500 MeV for protons, 4 MeV to 500 MeV for α-particles and 150 eV to 5 MeV for electrons.

4.3.1 Monte Carlo Ionization Module

The interaction between the precipitating particles and the atmosphere is evaluated using a Monte Carlo simulation. Generally speaking, Monte Carlo methods are a class of computational algorithms using repeated random sampling; they are particular useful in modeling systems with many degrees of freedom. The interaction of particles with matter is a process containing a lot of uncertainty: as in radioactive decay, only probabilities in the sense of average lifetime or cross-sections are known. Thus when an incident particle approaches a target atom, it will interact with a certain likelihood. In the Monte Carlo Method this is reflected by using random numbers to choose from the different possible outcomes: interaction or not, kind of interaction with resulting energy loss, deflection from original path and secondary particle(s). This rolling of the dice is repeated along the particle track.

The Monte Carlo simulation has an advantage over a continuous energy loss model: while protons and heavier particles basically follow a straight line, electrons experience multiple scattering. Thus the traveled path is much longer than the penetration depth and consequently results from a Bethe–Bloch or another continuous energy loss model cannot be converted correctly to penetration depth. In addition, the Monte Carlo simulation allows the identification and tracking of secondaries, both particles and electromagnetic radiation. Again, this is of particular importance for electrons since they produce bremsstrahlung which can travel quite a long path before interacting with and ionizing the lower layers of the atmosphere. Bremsstrahlung even can cause ionization at lower heights than the one reached by the primary particle (see, e.g., example in *Schröter et al.*, 2006).

Processes under Consideration

The ionization module is an extended version of the one described in *Schröter et al.* (2006). It is based on the GEANT4 simulation package (*Agostinelli et al.*, 2003) as well, but differs from *Schröter et al.* (2006) in three respects: (1) the extension and composition of the absorber (the atmosphere), (2) the energies of the precipitating particles cover a much broader range, and (3) a more complete range of interaction processes has to be considered to account for the broader energy range.

The processes and cross sections considered in the model reflect the underlying physical processes. The most common process is continuous energy loss due to ionization. This process also can be described by Bethe-Bloch's equation for nuclei or Berger-Seltzer's equation for electrons. For electrons, one important process is multiple scattering: while during ionization nuclei follow more or less a straight line, electrons are deflected because the incident electron interacts with an electron from the atomic shell and both particles have the same mass. Thus electrons follow a zigzag path instead of a straight line. In particular in the low densities of the upper atmosphere, these deviations from a straight line can be quite pronounced, see for instance the example in *Schröter et al.* (2006). Electrons with sufficiently high energy (in the keV range and above) produce bremsstrahlung. This is treated as a secondary generated during the interaction and leads to a shift of ionization into the lower atmosphere, as discussed above. To track the bremsstrahlung photon correctly and to calculate its final energy deposition, its interaction with the atmosphere must be tracked. The interaction processes are, with increasing photon energy, the photoelectric effect in which a photon ionizes a target atom transferring all its energy, the Compton effect (or Compton scattering) in which the photon ionizes a target atom and continues with a lower energy into a different direction, and finally pair production in which a photon of energy above 1.02 MeV decays into an electron and a positron. With the rather low energies of the incident electrons the latter process is rather unlikely. With increasing energy of the incident proton hadronic interaction might play a role: the incident particle interacts with the nucleus instead of the atomic shell, generating lighter nuclei and neutrons. Radiocarbon ^{14}C is a result of such a hadronic interaction.

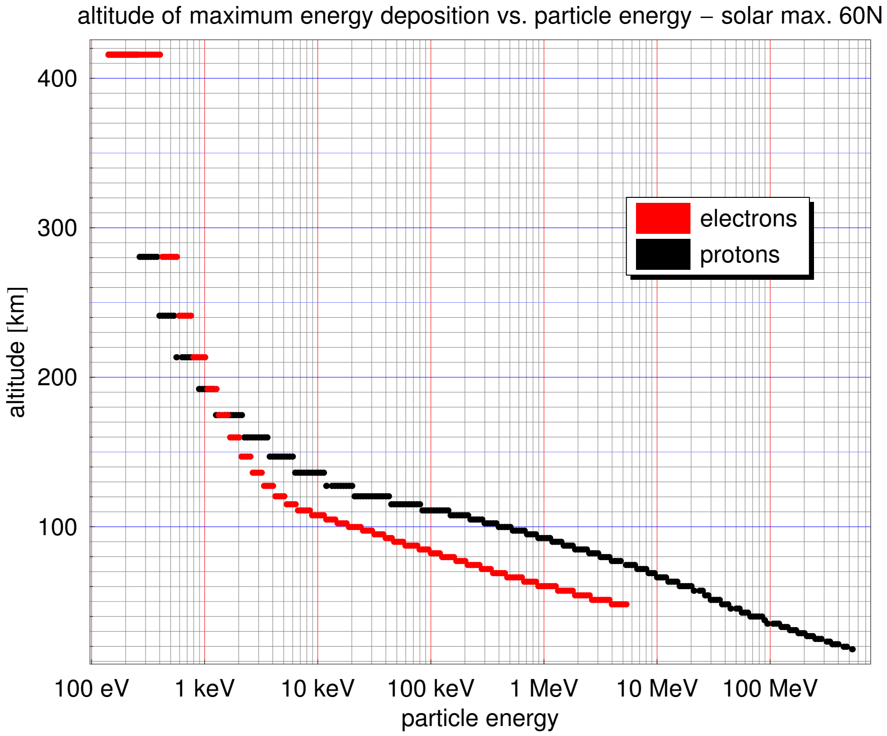

Figure 4.2: Altitude of maximum energy deposition versus energy of the incident particle.

Model Particles

A Monte Carlo simulation is time consuming. Thus simulations are not performed for particle spectra in a given event but for a large number of monoenergetic beams which then are convoluted with the observed particle spectrum. The energy range of precipitating particles considered in the model is 150 eV to 500 MeV for protons, 4 MeV to 500 MeV for α-particles and 150 eV to 5 MeV for electrons. Note that the energy bands are not chosen for physical but for observational reasons: only within these bands a more or less continuous data base can be established while observation at lower or higher energies are less frequent and/or not publicly available. Note that this is not exactly true for the electrons: here the observed spectrum only extends to 2.5 MeV but can be extrapolated up to 5 MeV. SOHO observations in the October 2003 events do not give any indication for a break in the electron spectrum in the MeV range (*Klassen et al.*, 2005). For the error estimate we have to keep in mind that charged particles loose the energy at the end of their track; Figure 4.2 gives the altitudes of maximum energy loss for electrons (red) and protons (black) depending on the energy of the incident particle. Extending the electron spectrum from 2.5 to 5 MeV therefore would mainly affect the lowest two altitude bins of the red curve. Thus in case of a pronounced steepening of the spectrum around 2.5 MeV, the ionization rates would not change in the thermosphere, would change by a few tenth of a percent in the lower mesosphere and at worst case might be strongly overestimated (up to a factor of 2) in the lower two altitude bins, that is around 50 km. Thus in the worst case the error is large in these two bins while owing to the spectrum of the electrons it is small (less than 10^{-4}) if total ionization is considered.

40 logarithmically equidistant monoenergetic beams have been calculated for each order of magnitude in energy, giving a total of 264 monoenergetic beams, depending on particle species. To account for the angular distribution of the incident particles, 9* different

---

[*] The recent AIMOS 1.1 version uses a higher angular resolution, see revisions in Section 4.8 and the discussion

equally spaced directions of incidence with respect to the vertical are considered. To assure statistical accuracy, each monoenergetic beam consists of 10 000 particles for electrons and 100 particles for protons and αs. The higher number of electrons is required because bremsstrahlung is considered.

Absorber

To account for the wide range of particle energies, the atmosphere must extend to heights of several hundred kilometers. For AIMOS we adopted the model atmosphere from HAMMONIA (*Schmidt et al.*, 2006): it extends from the ground up to 1.7×10^{-5} Pa. Depending on season, latitude and solar activity this corresponds to an upper boundary between 250 to 600 km. The spatial grid is $3.6° \times 3.6°$ in the horizontal with 67 logarithmically equidistant geopotential height layers. The spatial resolution of AIMOS is the same as that of the model atmosphere. All monoenergetic beams have been calculated for four latitudes (80°S, 60°S, 60°N, 80°N), the four seasons and three levels of solar activity. For each time interval under study the most suitable atmosphere is selected in AIMOS; the selection criterion for the level of solar activity is not the date but the F10.7 index of solar activity.

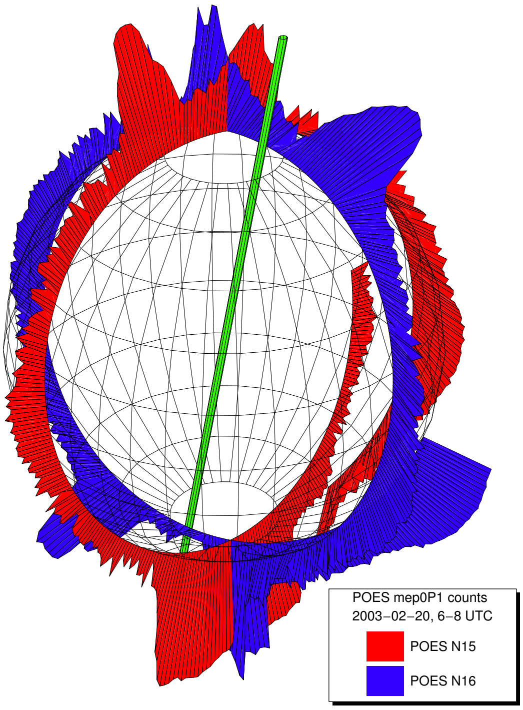

Figure 4.3: The combination of particle fluxes in 30–80 keV protons measured simultaneously by two polar-orbiting satellites with almost perpendicular orbits allows an approximation on the 3-D precipitation pattern, the size of the polar cap and the location of the auroral oval. Fluxes in arbitrary units on a log scale to give a hint on the spatial distributions only.

4.3.2 Sorting Algorithm: Low Particle Energies

The horizontal precipitation pattern depends on local magnetic time and geomagnetic activity. The combination of two polar-orbiting satellites with different equatorial crossing times allows an identification of polar cap and auroral oval as well as an approximation on the fluxes inside the polar cap and the auroral oval. Figure 4.3 shows fluxes of 30–80 keV protons observed simultaneously along the particle orbit for the POES satellites NOAA-15 and NOAA-16. The green line is the geomagnetic dipole axis, polar cap and auroral oval can be distinguished clearly in the northern hemisphere in both satellite orbits. On the southern

---

on statistical errors in Section 7.1.2.

hemisphere, the distinction is obvious in the NOAA-16 data while NOAA-15 only passes through the auroral oval. Owing to the satellite orbit such a figure can be constructed every 2 h.

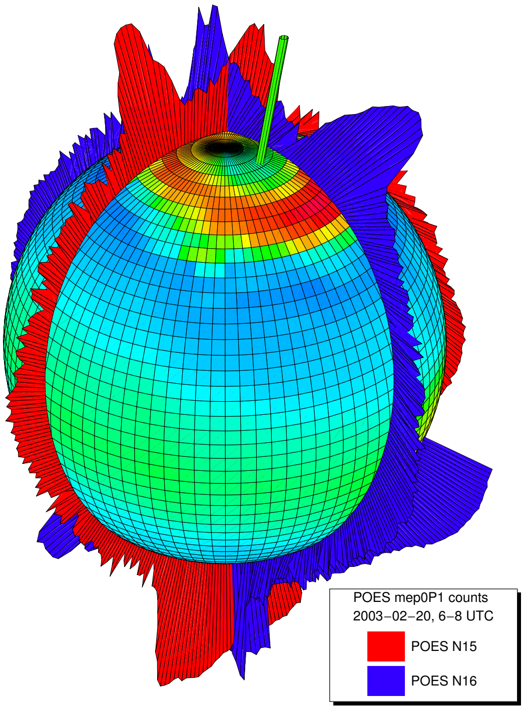

Figure 4.4: Same as Figure 4.3 but with interpolated intensities yields the 2-D map of precipitating particles. Color scheme for the bottom of the image is as in the Figure 4.5 (top).

To derive a map of the horizontal precipitation pattern as shown in Fig. 4.4, the gaps between the orbits have to be filled. These maps depend on local magnetic time, geomagnetic activity, particle energy and the particle fluxes in the magnetosphere and in interplanetary space. To obtain them, the globe is split into 14 regions with similar precipitation patterns (for details, see *Wissing et al.*, 2008). According to daytime-sector affiliation these regions have four subdivisions, depending on local time. The resulting map then gives the relative fluxes in all cells of the globe. The actual flux can be obtained by scaling the flux pattern along the orbit with the corresponding matrix. Scaling on the basis of individual cells is avoided to reduce statistical scatter. Thus the method basically also is an averaging procedure.

Note that these maps must be derived separately for each particle species, each particle energy and different levels of geomagnetic activity. They are only valid for magnetospheric particles, the fluxes of the solar energetic particles inside the polar cap must be obtained separately from direct measurement: fluxes and spectra of solar energetic particles and magnetospheric particles are not (cor)related.

4.3.3 SEPs inside the Polar Cap

The reliable particle instruments/channels on the POES satellites extend to 2.5 MeV for the electrons (with our extrapolation to 5 MeV) and 6.7 MeV for protons. Consequently, the precipitation pattern only can be derived up to these energies. In SEPs significant fluxes of protons at higher energies up to some hundred MeV can be expected; with intensity increases of a few orders of magnitude above background even at 100 MeV. Although their contribution to total energy and therefore total ionization is in the range of a few percent at most, their contribution to the ionization height profiles is marked. Because energetic particles loose most of their energy at the end of their track, the consideration of the high energetic protons does not modify the ionization rates in the thermosphere but extend ionization to lower altitudes according to the height-energy relation in Figure 4.2.

The high energetic solar particles precipitate only inside the polar cap. Particle measurements thus can be taken from an interplanetary satellite, such as IMP or SOHO, or from one of the GOES satellites. The part of the particle spectra above the highest POES energies are determined from these measurement; thus the lowest GOES energy channels are omitted and only energies above 9 MeV are considered. The precipitation area is extrapolated from the polar cap size in the highest proton channel on POES: since the size of the polar cap increases with increasing particle energy, the SEPs with energies above 15 MeV are allowed to precipitate also into the next equatorwards latitude bin. Nonetheless, this is not a completely correct consideration of the decrease in geomagnetic cutoff with rigidity and the total amount of precipitating high energetic protons thus is slightly underestimated; errors in total ionization in the relevant latitude bins depend on the particle spectrum but should not exceed 10% for spectra typically observed in solar energetic particle events. It should be noted that ionization inside the inner part of the polar cap as defined by the POES satellite is not subject to this error. Since the precipitation maps are determined for different values of $\mathrm{K_p}$ separately, the increase of the size of the polar cap during strong geomagnetic storms is taken into account, too. In sum, spectral variation with geomagnetic cutoff is taken into account by allowing a wider polar cap for higher energies and polar cap variation with geomagnetic activity is taken into account by the dependence of the map on a geomagnetic index, in this case $\mathrm{K_p}$.

The shift from POES to GOES does not affect the spatial resolution dramatically: while the precipitation pattern of the lower energies is highly variable (Figure 4.5, top) even the moderate energies in the higher POES channels show only a rather uniformly filled polar cap (Figure 4.5, bottom). Thus the continuation to higher energies only requires the identification of some polar cap extension but no further spatial resolution.

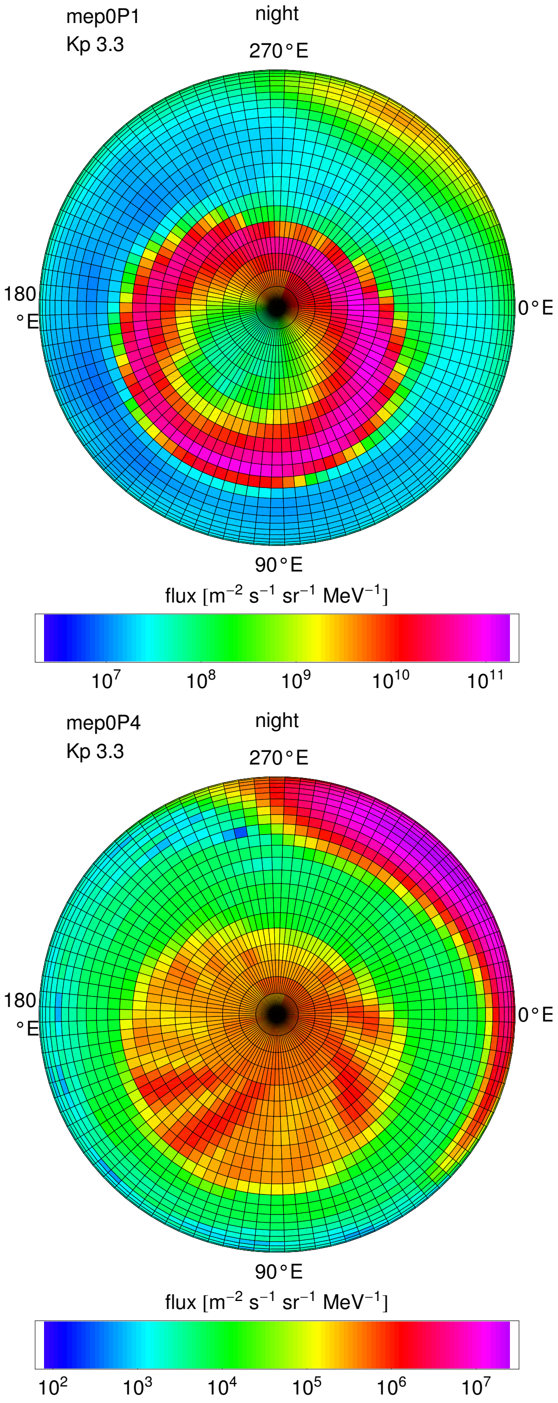

Figure 4.5: (top) Low energetic particles (30–80 keV protons) show a much higher spatial variability at high latitudes than (bottom) higher energetic particles (0.8–2.5 MeV protons). The high ionization patch around 310°E is an artifact of the South Atlantic Anomaly. A view on the south pole is shown.

4.4 Particles

The present data set in the AIMOS data server is limited to the time period 2002–2005 and is based on particle data from the EPS instruments on GOES-10 and GOES-11 and the SEM-2 instruments on board the POES satellites NOAA-15 and -16; the energy ranges and particle species are summarized in Table 4.1. The two POES satellites are the important ones because they are used in the construction of the precipitation maps. As discussed above, the instruments measure electrons up to 2.5 MeV and protons up to 6.7 MeV but no alphas. Protons with higher energies (up to 500 MeV) are taken from the GOES satellite (as discussed in Section 4.3.3).

It should be noted that the ionization module and the sorting algorithm can be applied to any pair of polar orbiting satellites with non-vanishing angular separation of the orbital planes; one example for application to a different satellite in a different orbit (NOAA-17) will be discussed in Section 4.5.3. So far, the model therefore does not contain any specific assumption about the particle data to be processed with it.

4.4.1 Satellites and Instruments

The POES satellites (POES: Polar Orbiting Environmental Satellite) are polar-orbiting satellites in a Sun-synchronous orbit with a height of 850 km and an inclination of 98°. Equatorial crossing in the southward direction nominally occurs at 7:30 UT for NOAA-15 and at 2:00 for NOAA-16. Particle measurements are performed with the Space Environment Monitor SEM-2 (*Evans and Greer*, 2004) which consists of the Total Energy Detector TED measuring low energetic particles and the Medium Energy Proton and Electron Detector MEPED. TED is a cylindrical electrostatic analyzer, MEPED consists of semiconductor detectors with passive shielding to define an aperture. Instruments are flown in pairs with the $0°$-instrument viewing upwards along the radial and thus almost parallel to the magnetic field inside the polar cap, and the other instrument viewing backwards along the satellite's trajectory (MEPED) or at a fixed angle with respect to the $0°$-detector. Since particle precipitation is strongest at high geomagnetic latitudes where the magnetic field is close to radial, AIMOS is limited to the analysis of the $0°$-detector.

The GOES satellites (GOES: geostationary Operational Environmental Satellite) are in geostationary orbit located at 135°W and 104°W. The Energetic Particle Sensor EPS (*GOES I-M DataBook*, 1996) is a telescope for the measurement of protons and α particles. The opening angle is rather wide (70°), in contrast to POES no estimate of particle anisotropies is possible. The dome detector measures the higher energetic end of all particle species, particle identification is made by pulse height analysis.

4.4.2 Particle Energy Spectra

To perform the convolution with the Monte Carlo results we need a handy description of the incident particle spectrum. *Schröter et al.* (2006) assumes for a smaller energy range a power law spectrum $\Phi(E) = \Phi(E_0) \cdot (E/E_0)^{-\gamma}$ fitted to the data with up to three different power law indices in different energy ranges. *Mewaldt et al.* (2005) discuss different spectral shapes which also all go back to the power law spectrum. Therefore we adopt the approach of *Schröter et al.* (2006) but allow for up to five separate segments to account for the wider energy range.

	satellite	channel		energy range
electrons	POES-15/16	TED	electron band 4	0.000154–0.000224 MeV
			electron band 8	0.000688–0.001000 MeV
			electron band 11	0.002115–0.003075 MeV
			electron band 14	0.006503–0.009457 MeV
		MEPED	mep0e1-e2	0.03–0.1 MeV
			mep0e2-e3	0.1–0.3 MeV
			mep0e3	0.3–2.5 MeV
protons	POES-15/16	TED	proton band 4	0.000154–0.000224 MeV
			proton band 8	0.000688–0.001000 MeV
			proton band 11	0.002115–0.003075 MeV
			proton band 14	0.006503–0.009457 MeV
		MEPED	mep0P1	0.03–0.08 MeV
			mep0P2	0.08–0.24 MeV
			mep0P3	0.24–0.8 MeV
			mep0P4	0.8–2.5 MeV
			mep0P5	2.5–6.9 MeV
	GOES-10/11		(telescope) z_p2	4.–9. MeV
			(telescope) z_p3	9.–15. MeV
			(dome) z_p4	15.–40. MeV
			(dome) z_p5	40.–80. MeV
			(dome) z_p6	80.–165. MeV
			(dome) z_p7	165.–500. MeV
alphas	GOES-10/11		(telescope) a_a1	4.–10. MeV/particle
			(telescope) a_a2	10.–21. MeV/particle
			(telescope) a_a3	21.–60. MeV/particle
			(dome) a_a4	60.–150. MeV/particle
			(dome) a_a5	150.–250. MeV/particle
			(dome) a_a6	300.–500. MeV/particle

Table 4.1: Energy ranges and particle species under consideration and the instruments measuring them

4.5 Test of the Model Components

The most elementary test is energy conservation: does all energy deposited inside the atmosphere show up as energy loss and thus leads to ion pair production. This is the case for all particle species and all particle energies. Testing of the model is improved stepwise. We start with the ionization module and compare the Monte Carlo results to analytical solutions. We compare our fits of the energy spectra to other fits using data from different satellites in the same event and finally we test the sorting algorithm.

4.5.1 Ionization Module

The validation of the ionization module is straightforward: here monoenergetic particle beams with fixed direction of incidence are used. The comparison between results from Bethe-Bloch and GEANT4 for protons already have been discussed in *Schröter et al.* (2006). Results from AIMOS differ neither from Bethe-Bloch nor from the results in *Schröter et al.* (2006) for the height/energy range covered in both approaches. For low energetic protons, differences between GEANT4 and Bethe-Bloch can be observed with decreasing density of the absorber, that is with increasing height. Above about 150 km more energy is deposited within an atmospheric layer in the Bethe-Bloch code than in the Monte Carlo model. It should be noted that within one height layer the resulting difference in the ionization rate can be up to 20% although the ‘misplaced’ amount of total energy and therefore also total ionization rate is of the order of 10^{-3} of the total energy/ionization rate.

One physical reason might be energy transport into lower layers by secondaries. Another reason simply are the different corrections and assumptions in different interaction models. Although mathematically the difference exists, it should not be overrated because the main problems in comparisons between model results and observations will be (1) the assumption about atmospheric composition and density in the highly variable thermosphere and (2) the high variability of the ionization due to hard electromagnetic radiation. In addition, owing to the low density of the thermosphere, only a small amount of particle energy is deposited there: for protons with MeV energies less than 10^{-3} of the total energy is deposited in the thermosphere while for protons up to some tens of keV all energy is deposited in the upper thermosphere.

For electrons, the Monte Carlo simulation has been compared to the results in *Berger et al.* (1970): height of maximum ionization and energy deposition agree within a few percent; residual differences partly reflect the different methods and partly differences in the assumption about the model atmosphere. Compared to the results in *Callis et al.* (1998) the ion pair production in the Monte Carlo model is lower by a factor of five in the ionization maximum around 100 km while it is comparable at lower altitudes. The reason could not be identified unambiguously; different assumptions about atmospheric density and the limitation of the atmosphere to lower altitudes in *Callis et al.* (1998) might lead to a cumulated deposition of all energy deposited in the entire thermosphere in a limited height range around the ionization maximum. Since in our Monte Carlo simulation all incident energy (within the accuracy of the computer) is deposited, the latter point might be the appropriate explanation.

4.5.2 Combined Particle Spectrum and Ionization Module

Spectra and resulting ion pair production rates from precipitating solar protons inside the polar cap were calculated with AIMOS. The particle spectra then were compared to the ones in *Mewaldt et al.* (2005) derived for a different data set; the resulting ion pair production rates were compared to the ones in *Jackman et al.* (2005a).

Mewaldt et al. (2005) derived particles spectra for electrons, protons and αs from observations with instruments on the ACE, SAMPEX and GOES-11 satellites for different time periods during the event. For the same time periods, spectra were derived from AIMOS using observations of the TED and MEPED instruments on POES and GOES-10. Agreement of the spectra at the high energy end is not surprising since the instruments on the GOES satellites are similar. Although differing in details, the general spectral shape is the same for electrons and protons below a few MeV in both approaches, although entirely different instruments from satellites in different orbits have been combined. The total energy contained in the different spectra in the energy interval covered by both instruments agrees within a few percent and do not show indications for systematic differences between the two approaches. This agreement supports not only the methods but also suggests that the particle data are reliable.

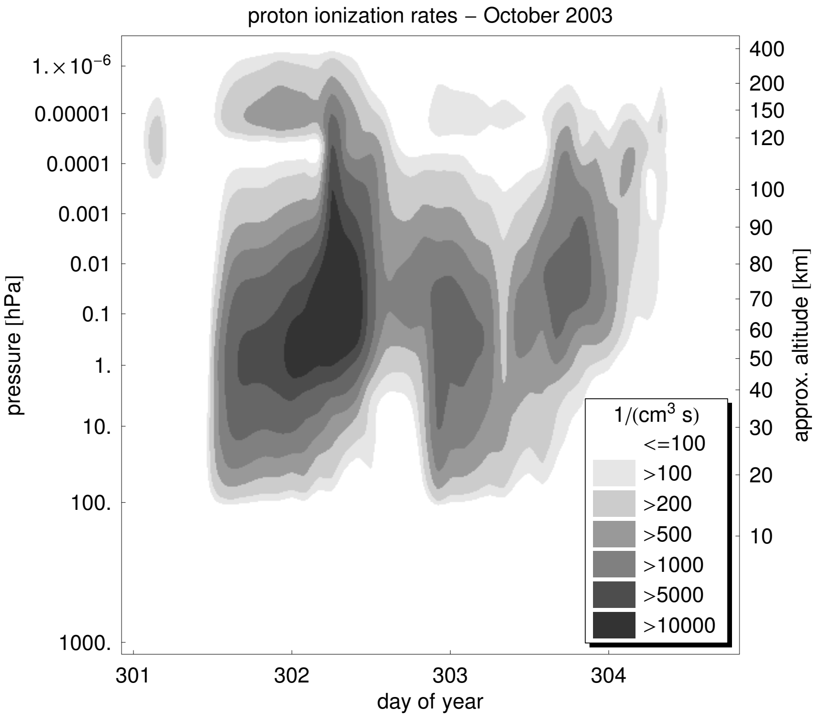

Figure 4.6: Ion pair production rates during the first two events in October/November 2003. Only ion pair production by protons is considered.

Figure 4.6 shows ion pair production rates for the protons calculated with AIMOS from the spectra discussed above for the first four days of the event. The contours are at the same rates as in Figure 3 in *Jackman et al.* (2005a) to allow for an easy comparison. Spatial and temporal ion pair production rates agree quite well with one exception: ion pair production in AIMOS is observed at lower altitudes than in *Jackman et al.* (2005a). This is not a difference in the models but in the data used to calculate the incident particle spectrum: *Jackman et al.* (2005a) consider only protons with energies below 300 MeV while AIMOS considers protons up to 500 MeV. The differences between both models in the height range covered by both models mainly result from differences in timing, the differences in the spectrum calculation (the method is different to the one used in this paper and also in *Mewaldt et al.* (2005)) and in the assumptions regarding the underlying model atmosphere.

4.5.3 Sorting Algorithm

To test the precipitation map we used one of the maps derived from NOAA-15 and NOAA-16 to make predictions for particle fluxes. Figure 4.7 (top) shows predictions for the NOAA-16 satellite (red bars), averaged measurements (black bars) and the actual observations in high resolution (gray dots). The averages agree reasonably well, in particular the steep gradients at the fringes of the polar oval can be reproduced. Since NOAA-16 data were also used in map construction, this test does not support the spatial pattern but only the concept of scaling maps with fluxes.

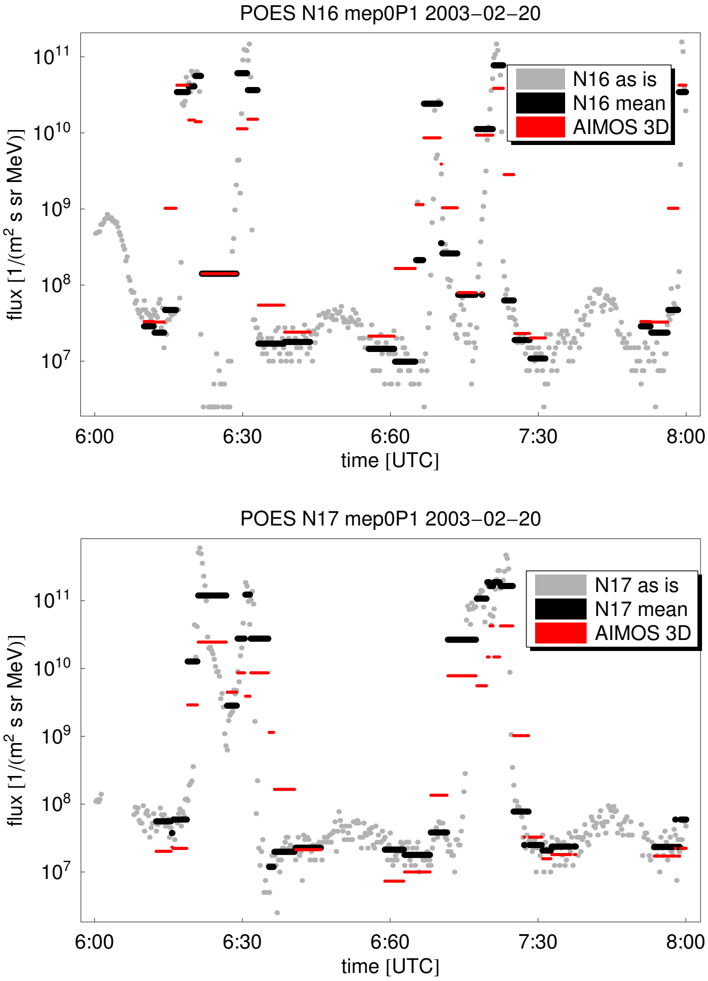

Figure 4.7: Current measurements (gray), averaged measurements (black) and predictions of these averages (red) on the basis of precipitation maps for NOAA-16 (top) and NOAA-17 (bottom).

Figure 4.7 (bottom) shows predictions for the same time period but for the NOAA-17 satellite. Data from NOAA-17 did not enter into the calculation of the precipitation maps and the orbital plane of NOAA-17 lies roughly in the middle between the ones of NOAA-15 and -16. Thus in this case, predictions are made for an entirely different orbit, which shows whether scaling with the interpolated precipitation map gives useful results or not. Again, the general features (radiation belt, polar cap, low latitudes) are predicted quite well; with the exception of one interval around 6:40 even the steep gradients at the fringes of the auroral oval are reproduced.

We conclude from a large number of such comparisons that the sorting algorithm works well. Even when differences between prediction and observation occur, the error is smaller than in case of the simple assumptions of uniform fluxes across the entire polar oval and a nominal auroral oval.

4.6 Relative Contributions of Particle Species and Populations

4.6.1 Quiet Times

Fig. 4.8 (top) shows typical background ionization rates inside the polar cap. All intervals are at geomagnetically quiet times and no increase in particle fluxes in interplanetary medium above background is observed, thus no solar energetic particles are present. The solid lines are for protons, the dashed ones for electrons. The sudden drop in ionization rate around 15 km for protons and around 50 km for electrons is an artifact: we do not have observations of particles with such high energies. Therefore we cannot make a reliable comparison between ionization rates of electrons and protons below 50 km. In the mesosphere ionization by electrons exceeds that by protons by at least an order of magnitude until both become comparable in the lower thermosphere. While ionization rates in the different time intervals are quite similar below the mesopause, in the thermosphere absolute ionization rates are highly variable as is the relative contribution of electrons and protons to ionization.

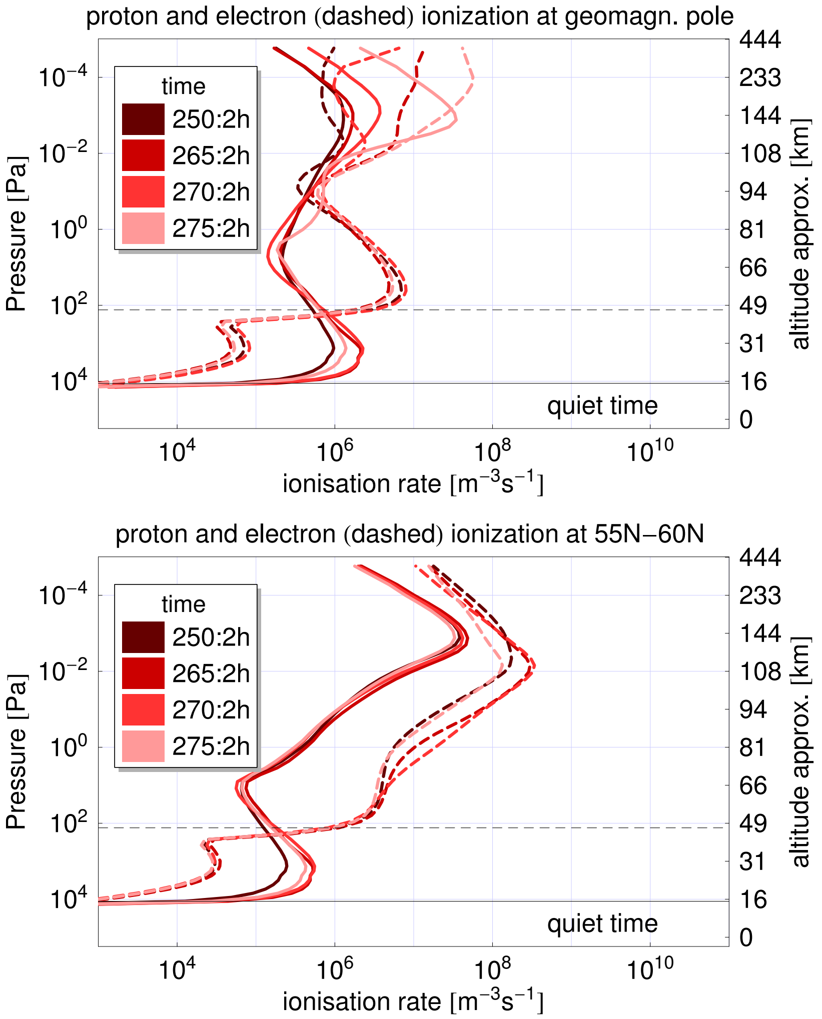

Figure 4.8: Ionization rates during geomagnetically quiet conditions for protons (solid lines) and electrons (dashed lines) for five different time periods in 2003 in the polar cap (top) and at 56°N inside the auroral oval (bottom).

The longitudinally averaged ionization rates for the same time periods are shown in Figure 4.8 (bottom). The maximum of ionization by precipitating particles is in the lower thermosphere; the ionization rates are more than one order of magnitude larger than the ones around the mesopause. Ionization by electrons exceeds that by protons by more than an order of magnitude. Ionization rates in the mesosphere and stratosphere are comparable to the ones in the quiet time polar cop while they are larger in the thermosphere, reflecting the steeper spectrum of the magnetospheric particles.

4.6.2 Solar Energetic Particles

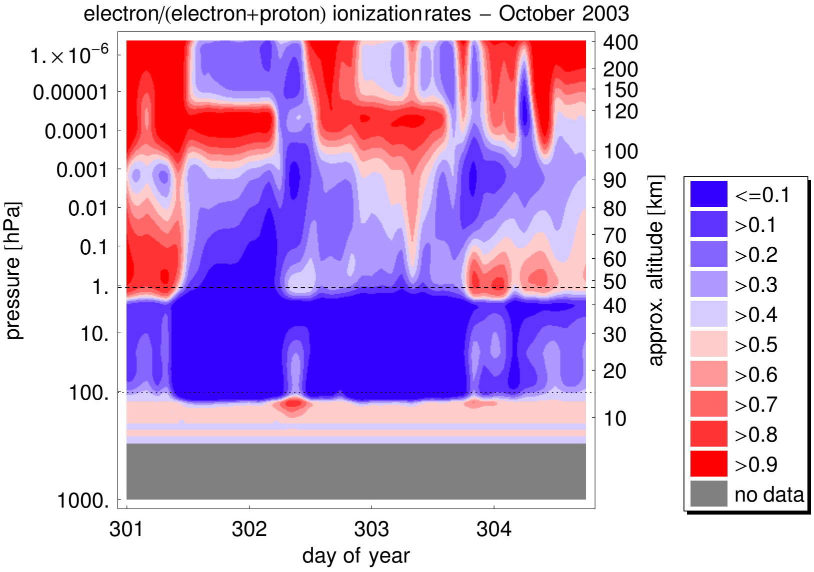

Figure 4.9: Relative contribution of solar electrons to the ionization by solar energetic particles for the first four days in the October/November 2003 event.

Figure 4.9 shows the relative contribution of ionization by solar energetic electrons to the total ionization by solar energetic particles during the first four days in the October/November event; the ionization rates by solar protons have been shown in Fig. 4.6. Figures 4.9 and 4.6 both represent the ionization at the geomagnetic north pole. A value of 0.5 indicates an equal contribution of electrons and protons, electron domination to the ionization rates is shown in red, proton domination in blues. Again, below about 50 km the contribution of electrons is underestimated because of the limited information about the energy spectrum. The ratios below 15 km also result from limited information and must be discarded: the highest proton energy considered is 500 MeV, corresponding to a stopping height of about 15 km. Thus no proton ionization is calculated below that line while small amount of ionization due to electron bremsstrahlung still occurs.

Again, in the lower thermosphere during most of the time ionization by electrons dominates. In the mesosphere, ionization by electrons only is dominant at times of rather low intensities, e.g., before event onset and in the late phase. Early in the event, protons dominate while during the event electrons can contribute more than 30% to the ionization of the mesosphere.

These numbers are not large enough to nullify earlier studies or to change our understanding of the relation between precipitating particles and atmospheric chemistry. However, the numbers are large enough to be considered when model results are compared to observations.

4.6.3 Solar and Magnetospheric Particles

Figure 4.10 shows ionization rates during the October/November 2003 event for protons (solid lines) and electrons (dashed lines) for four different time intervals: early in the event, in the rising phase, at event maximum and in the late phase of the second event. Again, the top panel shows observations inside the polar cap, the bottom panel shows the longitudinally averaged rates inside the auroral oval. The most prominent feature is the persistent ionization maximum due to precipitating electrons in the lower thermosphere. Note that the rates are of the same order of magnitude as during the quiet times shown in Figure 4.8.

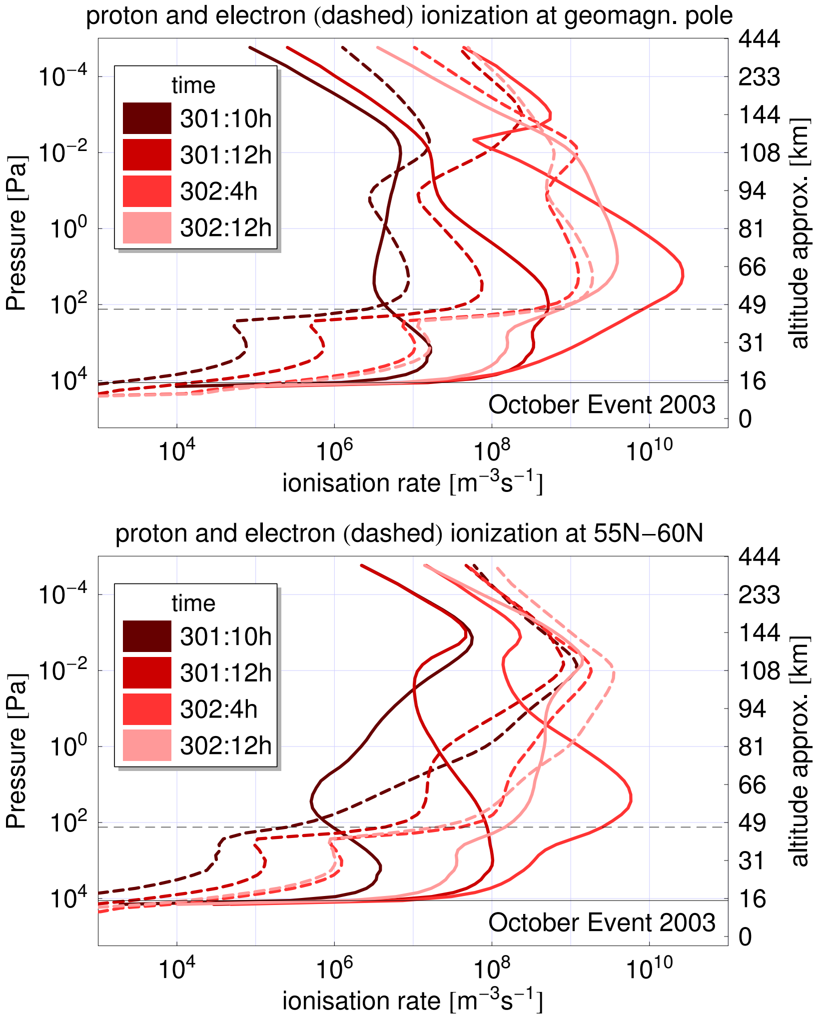

Figure 4.10: Ionization rates during the October/November 2003 event for protons (solid lines) and electrons (dashed lines) for four different time intervals: just early in the event, in the rising phase, at event maximum and in the late phase of the second event.

Much stronger variations in ionization rates by both particle species can be found inside the polar cap, reflecting the development of the particle spectrum during the event. Let us start with the protons: at first only particles with high energies arrive at Earth, leading to an increase in ionization compared to background conditions by more than one order of magnitude in the stratosphere. In the next 2 h time interval, particle intensities at high energies continue to rise while particles with lower energies start to arrive: consequently, the ionization rate continues to increase in the stratosphere and also starts to increase in the mesosphere. Owing to the shape of the spectrum, the height of the ionization maximum increases. During maximum times, the ionization rate inside the polar cap is increased at all altitudes with its maximum in the mesosphere. Late in the event intensities in highest energies already have decreased while intensities in the MeV range and below still are high because these low energetic particles still are accelerated at the interplanetary shock. Thus ionization rates already are low in the stratosphere and have a maximum in the lower thermosphere.

The temporal development of the ionization-height profile for the electrons follows the same pattern, except that we cannot draw any reliable conclusions about ionization in stratosphere. The details of the profiles and the increases in ionization rate of course are different, as has already been discussed in connection with Figure 4.9.

The first three profiles are obtained during geomagnetically quiet conditions, thus the flux of magnetospheric particles is not as high as during a violent geomagnetic storm but it is markedly increased compared to quiet time conditions. Note that certain similarities between the proton ionization profiles of solar and magnetospheric protons are an artifact of the longitudinal averaging in Figure 4.10.

In sum, it appears that during solar particle events the dominant effect in the polar cap in the stratosphere and mesosphere is from solar protons although solar electrons can contribute up to 30% to the ionization. In addition, during strong shocks following a solar particle event, in the auroral oval magnetospheric electrons and protons lead to ionization rates of up to some ten percent of the ones of solar particles. Independent of particle source and precipitation site, in general ionization by electrons is more important in the thermosphere.

4.7 Summary

To our knowledge, AIMOS is the first model to give reliable three dimensional ion pair production rates for precipitating solar and magnetospheric particles with high spatial and temporal resolution. Spectra of precipitating particles and the interaction of these particles with the atmosphere are modeled in a conventional fashion (power law spectra, Monte Carlo simulation for the interaction). The new features of the model are:

(1) The combination of solar and magnetospheric particles.
(2) The consideration of all particle species in both populations.
(3) Last not least the construction of 2-D precipitation maps allows a full 3-D ionization model. The latter allows for comparison with, e.g., electron densities obtained with radio scattering instruments and can be used to validate the model.

The model has been tested by comparison to calculations of spectra and ionization rates in other models and found to be in good agreement with them. A continuous set of ionization rates from 2002–2005 is available at `http://aimos.physik.uos.de`.

The model also has been applied to data during quiet times, a solar particle event and the complex series of SEPs and shocks in October/November 2003. Within the complex temporal and spatial variations in ionization rates, some relevant features can be identified. During a solar particle event the ionization in the mesosphere (and most likely also in the stratosphere) mainly is due to protons while with increasing height the ionization by solar electrons dominates (lower thermosphere). While solar electrons correctly have been neglected in the study of stratospheric effects of precipitating particles they must be considered in atmospheric models extending to greater heights. The situation is different, if particles origin from geomagnetic disturbances, in this case shocks follow solar energetic particle events. Here the relative importance of particle precipitation inside the polar cap and the auroral oval depends on geomagnetic activities and the spectrum of the solar energetic particles. At least in the lower thermosphere, both particle populations can lead to comparable ionization rates. In the mesosphere, ionization by magnetospheric electrons often exceeds that by solar electrons; it also can exceed that by solar protons. Consequently, the consideration of both particle populations with all particle species modifies the estimated ionization rates. These modifications are not large enough to nullify earlier studies but they are large enough to be considered in comparisons between atmospheric models and measurements of atmospheric constituents.

Acknowledgments

This work was supported by the Deutsche Forschungsgemeinschaft DFG under contracts DFG-Ka1297/6-1 and DFG-Ka1297/8-2. We are grateful to many fellow researchers from the CAWSES community who discussed the model and used first results, in particular Jens Kieser, Holger Winkler, Miriam Sinnhuber, and Hauke Schmidt.

4.8 Revision: Scaling of the mean Particle Precipitation

Global precipitation matrices in AIMOS are based on long term particle measurements at different K_p-levels. Precipitation regions (see Figure 4.11) are used to gain a mean particle spectrum for a specific area. As the magnetosphere is affected by the Sun other local time sectors show slight variation of the precipitation regions. Therefore the whole globe will be subdivided into four different local time sectors, consisting of 14 precipitation regions each; seven in the North and the South, respectively. As the magnetospheric particle precipitation depends on the state of the magnetosphere, the maximum of the auroral oval (here green) moves equatorward with rising K_p. The precipitation regions are fix for the same time-sector, but the particle flux distribution therein changes due to K_p, particle energy and species.

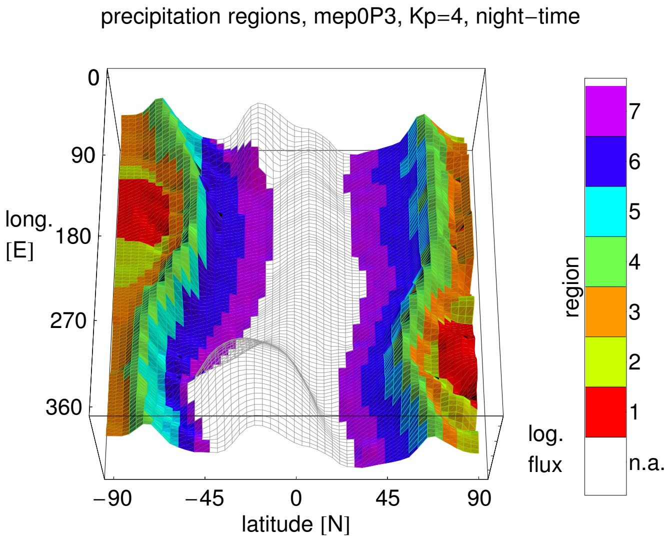
precipitation regions, mep0P3, Kp=4, night−time

Figure 4.11: A mean precipitation matrix for mep0P3, K_p=4 and night-time. The color-shadings represent the precipitation regions in this sector. The colored regions are used to gain an average particle spectrum for that specific area. The equatorial region (transparent shading) is subject to intense geomagnetic shielding. Measured flux in the equatorial region origins from trapped particles therefore it is neglected in the model.

For each 2 h time interval, the global precipitation matrices are scaled with the recent measurements. As the particle precipitation strongly depends on magnetic shielding, some regions of the globe show intense particle flux while other areas do not. During the AIMOS model development the scaling has been refined. In the beginning all regions were used for the scaling (AIMOS 1.0 and first AIMOS-paper, see Section 4), resulting in a strong impact of low-latitude areas which turned out to have no real importance for global particle precipitation. Starting with the second AIMOS paper, see Section 5, the scaling focused on high latitudes (indicated by AIMOS 1.1). The benefit is that the main precipitation zones are characterized in more detail while the low latitudes, where particle impact has a marginal impact on local ionization, are ignored in the scaling. In detail AIMOS 1.1 scales TED particles corresponding to the regions 2–4 and MEPED particles corresponding to regions 3–4 (for regions see Figure 4.11).

In addition, we did not find a smooth flux transition between the polar cap area and the mid latitudes while looking at high energetic particles. Thus the GOES channels have been included to a full extend in regions 1–4, dropping to zero in the equatorward regions 5–7. In AIMOS 1.0 there was a smooth transition resulting in a scaling factor 0.5 in region 4. A summary of the different regions is given in Table 4.2.

Other minor changes from AIMOS 1.0 to AIMOS 1.1 deal with the GEANT4 based particle simulations which now run with a much better angular resolution (see Section 7.1.2 for more details).

	AIMOS 1.0			AIMOS 1.1		
region	TED	MEPED	GOES	TED	MEPED	GOES
1	polar cap mean	polar cap mean	included	polar cap mean	polar cap mean	included
2	mean precipitation maps scaled by regions 2–7			mean precipitation maps scaled by regions 2–4		
3		mean precipitation maps scaled by regions 3–7			mean precipitation maps scaled by regions 3–4	
4			half flux included			
5			not included			not included
6						
7						
else	no simulation of ionization in the equatorial area					

Table 4.2: Properties of the different regions used in AIMOS 1.0 and AIMOS 1.1.

The following will enlarge on the different scaling methods used in AIMOS1.0 and 1.1. A comparison to satellite data will reveal differences of the scaled precipitation matrices and in-situ measures. As the scaling itself depends on real time measurements, the comparison algorithm and its separation from the scaling will be explained first.

The scaling subdivides the earth into 4 local time sectors. All measurements within such a sector are used for the 2 h-scaling as far as it lies inside the scaling regions (see Table 4.2, for differences in AIMOS 1.0 and 1.1 as well as for MEPED and TED detectors). The scaling algorithm compares the in-situ measurement to a mean value at the same grid point originating from the mean precipitation maps. This is not the same as the mean value of the corresponding region, consequently it allows a correct scaling even if the region is passed only partially (in particular at high or low geomagnetic latitude). In high latitudes, the POES satellites pass through different time-sectors, therefore the scaling is always a combination of the two satellites.

In contrast the quantitative error discussion abstains from local time sectors and from the restriction to the scaling regions. Only the enhanced count rates at the equator, which reflect trapped particle population, and the South Atlantic Anomaly are excluded (see transparent area in Figure 4.11). In addition the mean values of the regions (and not every grid point) are used as they will enter the spectra. Both satellites are examined separately.

In summary the scaling tries to describe the precipitation within a sector, considering for the limited satellite data as good as possible. On the other hand, the error discussion uses the modeled precipitation flux at the same resolution as it will enter the ionization algorithm. For this reason it is able to describe variations of the modeled and measured flux along the track as reliable as possible.

Table 4.3 lists a quantitative comparison of model and satellite data considering all areas (AIMOS 1.0), while Table 4.4 lists the comparison based on characteristic regions only (AIMOS 1.1).

The main difference between the two versions is obviously the high energetic proton flux in geomagnetically quiet periods. While the characteristic scaling mostly reproduces the original values (see Table 7.2), the global scaling overrates it by a factor five as a consequence of strong low-latitude impact in AIMOS 1.0 (see Table 4.3). At lower latitudes the particle ionization is by orders of magnitude lower than at high latitudes. Consequently it is not relevant but it still has a strong influence on the global (AIMOS 1.0) scaling algorithm. The aim of *Atmosphere Ionization Module OSnabrück* is to describe the particle induced ionization as exact as possible. Hence we decided to accept a small error within the equatorial

Model version using all regions for scaling AIMOS 1.0		
		geomagnetic quiet
channel	satellite	$\sum AIMOS\ 1.0 / \sum sat$
mep0P4	N15	4.46
	N16	3.58
mep0P5	N15	5.57
	N16	4.76

Table 4.3: Quantitative comparison of the AIMOS 1.0 scaling algorithm (based on all regions) and satellite measurements.

Model version using characteristic regions for scaling AIMOS 1.1			
		$\frac{\sum AIMOS\ 1.1}{\sum sat}$	
channel	satellite	geomagnetic quiet	geomagnetic active
TEDElektronBand4	N15	0.87	1.10
	N16	0.67	0.83
TEDElektronBand8	N15	0.92	1.11
	N16	0.68	0.87
TEDElektronBand11	N15	0.88	1.71
	N16	1.06	0.99
TEDElektronBand14	N15	0.74	1.85
	N16	1.28	1.15
mep0e1-e2	N15	0.98	1.24
	N16	0.91	1.19
mep0e2-e3	N15	1.52	1.37
	N16	0.60	1.32
mep0e3	N15	0.90	0.88
	N16	0.86	0.85
TEDProtonBand4	N15	0.84	1.43
	N16	0.99	1.33
TEDProtonBand8	N15	0.90	1.23
	N16	0.93	1.15
TEDProtonBand11	N15	1.00	0.90
	N16	0.92	1.03
TEDProtonBand14	N15	0.99	0.95
	N16	0.98	1.04
mep0P1	N15	0.94	0.80
	N16	0.98	0.70
mep0P2	N15	0.96	0.66
	N16	1.02	0.65
mep0P3	N15	0.89	0.64
	N16	0.91	0.58
mep0P4	N15	1.08	0.74
	N16	0.98	0.75
mep0P5	N15	0.73	0.75
	N16	0.60	0.75

Table 4.4: Quantitative comparison of the AIMOS 1.1 scaling algorithm (based on characteristic regions only) and satellite measurements.

region, where particle generated ionization tends to zero due to shielding and the ionization is dominated by UV-radiation.

As some figures in this paper are affected, Figures 4.12, 4.13, 4.14, 4.15 and 4.16 represent the current version AIMOS 1.1.

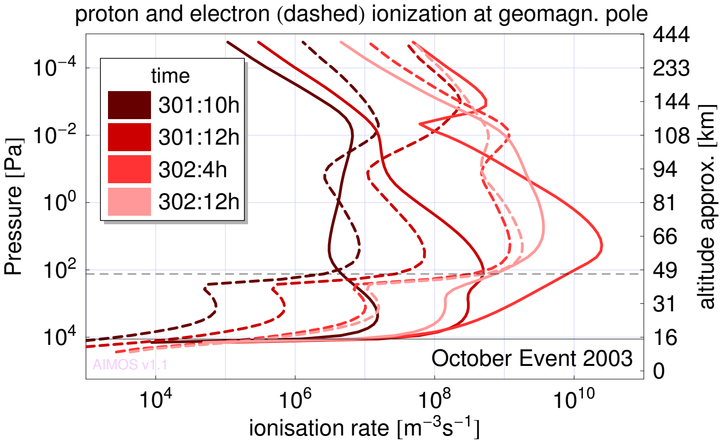

Figure 4.12: Revised ionization profiles for AIMOS 1.1, geomagn. pole during the October event: The polar cap is not affected by changes in the scaling. However, compared to AIMOS 1.0 (see Figure 4.10, top) the proton ionization in the lower atmosphere is smoother. The reason is a better angular resolution in GEANT4 which is used to produce the isotropic energy depositions.

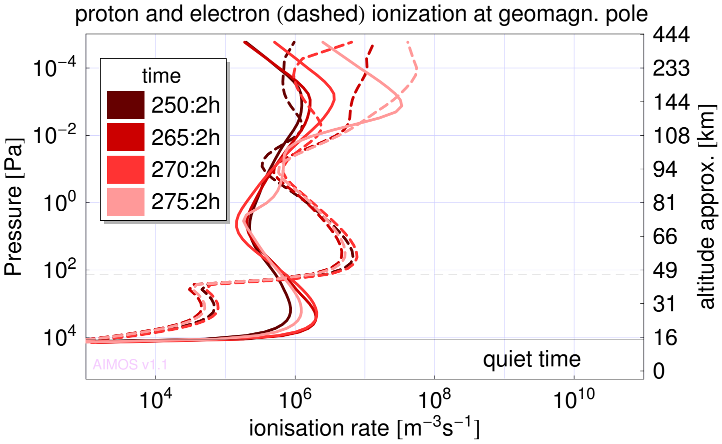

Figure 4.13: Revision of Figure 4.8 (top), quiet time. As described in Figure 4.12 the polar cap area is affected by a revision of the GEANT4 angular resolution only. Since there are no high energetic particles in quiet time no significant difference to AIMOS 1.0 is visible.

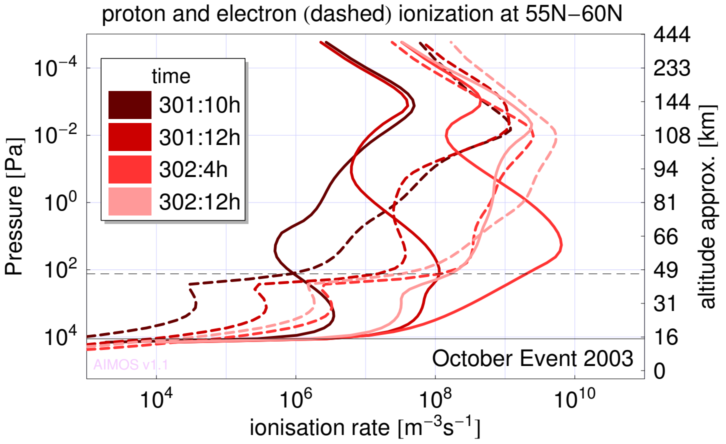

Figure 4.14: Revised ionization profiles for AIMOS 1.1, 55N–60N geomagnetic quiet time: Compared to AIMOS 1.0 (see Figure 4.10, bottom) the proton induced ionization in lower altitude is increased due to the full impact of the GOES channels.

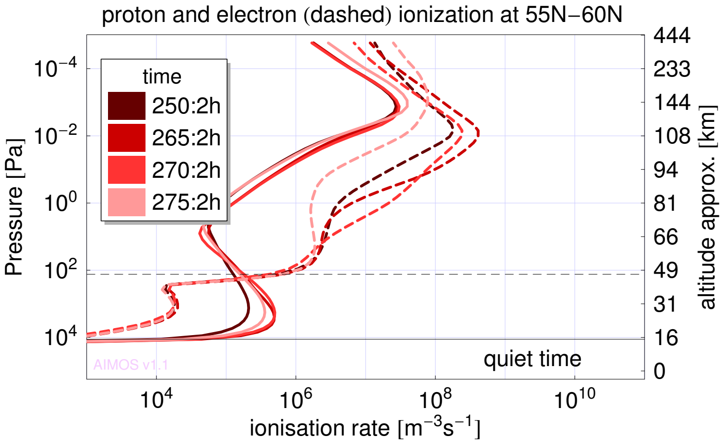

Figure 4.15: Revision of Figure 4.8 (bottom), quiet time. The scaling affects electron and proton induced ionization in the upper atmosphere. Due to the lack of high energetic particles the impact of GOES channels is small. However, the enhanced angular resolution gives a smooth profile in the lower atmosphere.

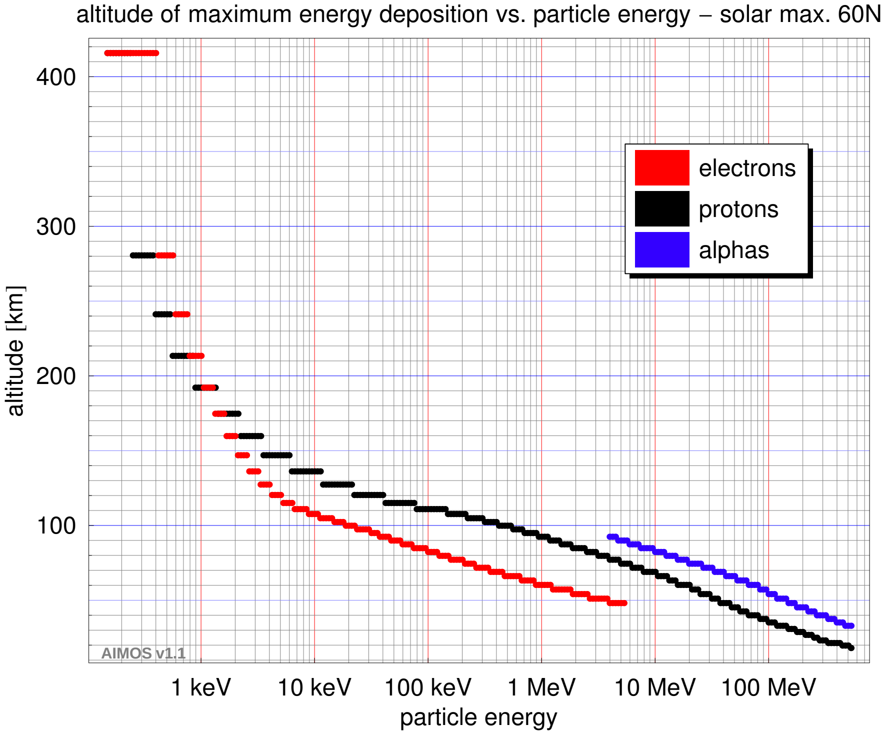

Figure 4.16: Revised figure for AIMOS 1.1: The alpha particles are included to give a more comprehensive picture of the energy-altitude relations.

Chapter 5

Atmospheric Ionisation Module OSnabrück (AIMOS) 2: Total Particle Inventory in the October–November 2003 event and Ozone

J.M. Wissing, M.-B. Kallenrode, N. Wieters, H. Winkler and M. Sinnhuber

JOURNAL OF GEOPHYSICAL RESEARCH, VOL. **115**, A02308, doi:10.1029/2009JA014419, 2011.

5.1 Abstract

Precipitating solar protons contribute to ozone depletion in the atmosphere; α particles and electrons also precipitate during solar energetic particle (SEP) events. If the SEP is accompanied by a shock then magnetospheric particles can also be injected into the atmosphere as the shock hits the magnetosphere. Both particle species in both particle populations show distinct energy spectra (and thus penetration depth in the atmosphere) and precipitate in different regions: the SEP inside the polar cap, the magnetospheric particles inside the auroral oval. In this paper, we re-evaluate the 3-D spatial and temporal precipitation patterns of these particle populations for the October–November 2003 event and compare the results to conventional approaches using only protons in evaluating SEP consequences. The main results are as follows: (1) the 3-D model AIMOS gives a very differentiated picture of the global ionization maps, (2) if only protons are considered, the differences between the 3-D model and the conventional approach of homogeneous precipitation inside the polar cap are small in NO_x production and ozone depletion in the mesosphere and stratosphere; and (3) the consideration of electrons in addition to protons leads to significant increases in atmospheric ionization in the mesosphere, less so in the stratosphere. This is reflected in changes in the chemical composition as shown here for ozone depletion and an increase of NO_x.

5.2 Introduction

Large solar energetic particle events cause ozone destruction (*Crutzen et al.*, 1975; *Heath et al.*, 1977; *Jackman et al.*, 2000; *Randall et al.*, 2005). Conventional modeling of the ozone loss considers solar protons only; for instance the electrons are assumed to contribute less than 10% to the total ionization (*Jackman and McPeters*, 1985). An analysis of the total particle inventory in the October–November 2003 period suggests that depending on the parent flare the relative contributions to ion pair production of protons and electrons can be quite variable (*Wissing and Kallenrode*, 2009). In the study of solar events, often only solar protons are considered, neglecting the contribution of magnetospheric particles. This approach has been justified in some way by the reasonable agreement between model results and measurements, as, e.g., shown for the July 2000 solar event by *Jackman et al.* (2001), or for the October–November 2003 solar event by *Jackman et al.* (2005a, 2008) and *Rohen et al.* (2005). However, there is mounting evidence for a significant influence of magnetospheric electrons on the composition of the middle atmosphere, both from observations (e.g., *Thorne*, 1977; *Randall et al.*, 2005, 2007; *Sinnhuber et al.*, 2006; *Seppälä et al.*, 2007) and from model studies (e.g., *Callis et al.*, 1996a, 2001; *Codrescu et al.*, 1997; *Rozanov et al.*, 2005). As a substantial amount of magnetospheric particles can be injected into the atmosphere if a shock or coronal mass ejection arrives at Earth, both solar and magnetospheric particles might contribute to the observed changes during solar particle events. Both particle populations show distinct spatial and temporal precipitation patterns: solar energetic particles precipitate along open field lines into the polar cap while magnetospheric particles are injected into the polar oval. With increasing geomagnetic activity the polar cap expands and particles are injected at lower latitudes (*Leske et al.*, 1995, 2001).

Wissing and Kallenrode (2009) suggested a combined approach in the *Atmosphere Ionization Module OSnabrück* (AIMOS). AIMOS uses two polar-orbiting satellites complemented by a geostationary one to model atmospheric ionization by protons and electrons of solar and magnetospheric origin. This combination allows the 2-D modeling of the horizontal particle precipitation pattern depending on geomagnetic activity. Thus both particle populations and the spatial variation of their precipitation are modeled. As already shown in *Wissing and Kallenrode* (2009) for the October–November 2003 period, in the solar particle population electron precipitation can exceed 30% at certain heights during certain times of the event. The consideration of atmospheric ionization by the formerly neglected magnetospheric particles will increase total ionization even more. Consequently, also subsequent models for atmospheric chemistry and circulation will yield different results. In this paper we present a case study for the October–November 2003 event to show whether and how these additional particles and ionization show up in the modeling of ozone chemistry.

The paper is structured as follows. In Section 5.3 we describe the data and models. Section 5.4 shows the results: relative contributions of different particle populations to ionization, the consequences of the additional ionization in a conventional chemistry model (Bremen three-dimensional chemistry and transport model) extending well into the mesosphere. The results are summarized and implications for atmospheric modeling are discussed in Section 5.5.

5.3 Data and Models

The modeling chain consists of two parts: (1) the ionization model AIMOS which calculates atmospheric ion pair production rates from particle fluxes observed in space and inside the magnetosphere, and (2) chemistry/circulation models which process these ionization rates to calculate electron densities and ozone depletion, which in turn can be compared to observations.

AIMOS (*Wissing and Kallenrode*, 2009) is a 3-D numerical model of atmospheric ionization due to precipitating particles with high spatial resolution for an atmosphere extending from ground up to 1.7×10^{-5} Pa, corresponding to an upper boundary between 250 to 600 km. The spatial grid is borrowed from HAMMONIA (*Schmidt et al.*, 2006) with $3.6^\circ \times 3.6^\circ$ in the horizontal and 67 logarithmically equidistant height layers. Ionization rates are calculated from the observed particle spectra by a Monte Carlo approach based on the GEANT4 simulation package (*Agostinelli et al.*, 2003).

Particle data to calculate the horizontal precipitation patterns and the low energetic part of the particle spectra for both particle populations are taken from the Polar Orbiting Environmental Satellites (POES) NOAA-15 and NOAA-16; both flying in a Sun-synchronous orbit with a height of 850 km and an inclination of 98°. Equatorial crossing in the southward direction nominally occurs at 730 UT for NOAA-15 and at 200 for NOAA-16. Particle measurements are performed with the Space Environment Monitor SEM-2 (*Evans and Greer*, 2004) which consists of the Total Energy Detector (TED) measuring low energetic particles and the Medium Energy Proton and Electron Detector (MEPED). The combined instruments cover electrons from 150 keV to 2.5 MeV and protons from 150 keV to 6.9 MeV. Protons with higher energies (4–500 MeV) are taken from the Energetic Particle Sensor (EPS) (*GOES I-M DataBook*, 1996) on GOES-10 or 11. For the higher electron energies, AIMOS extends the spectrum to 5 MeV because SOHO/COSTEP (*Klassen et al.*, 2005) and SAMPEX (*Mewaldt et al.*, 2005) observations suggest that the higher electron energies track the lower ones quite well.

AIMOS considers ion pair production rates up to heights of some hundred kilometers; since this study focuses on ozone depletion due to precipitating particles, AIMOS is combined with an atmospheric model with a strong focus on chemistry, the Bremen three-dimensional chemistry and transport model.

The Bremen three-dimensional chemistry and transport model is a combination of the Bremen transport model developed by B.-M. Sinnhuber (*Sinnhuber et al.*, 2003a) with the chemistry code of the Bremen two-dimensional model of the stratosphere and mesosphere (*Sinnhuber et al.*, 2003b; *Winkler et al.*, 2008). The Bremen three-dimensional chemistry and transport model is driven by analyzed wind fields and temperatures from the European Centre for Medium-Range Weather Forecasts (ECMWF). It runs on 28 isentropic surfaces from 330 to 3402 Kelvin (about 10 to 65 km) with a horizontal resolution of 3.75$^\circ \times 2.5^\circ$, and a vertical resolution of about 1 km in the lower stratosphere, increasing to about 4 km at 60 km altitude. The vertical motion perpendicular to the isentropes is described by diabatic heating and cooling. Diabatic heating and cooling rates are calculated using the MIDRAD radiation scheme (*Shine*, 1987). Advection is calculated by using the second order moments scheme of *Prather* (1986). The neutral model chemistry includes about 180 gas phase, photochemical, and heterogeneous reactions and 57 tracers and uses the recent set of recommendations for kinetic and photochemical data of the Jet Propulsion Laboratory (*Sander et al.*, 2006). NO_x and HO_x production due to atmospheric ionization are parameterized in such a way that 1.25 NO_x (55% NO, 45% N) (*Porter et al.*, 1976) and up to 2 HO_x constituents depending on altitude and ionization rate (*Solomon et al.*, 1981) are produced per ion pair, as described, e.g., in *Jackman et al.* (2005a) and *Rohen et al.* (2005).

5.4 Particle Inventory and Ion Pair Production

The period 20 October (doy 293) to 25 November (doy 329) 2003 is dominated by two large solar particle events on 28 October (doy 301) and 31 October (doy 304) and a severe magnetic storm on 20 November (doy 324). It also includes some rather strong flares accelerating highly relativistic particles (*Bieber et al.*, 2005; *Miroshnichenko et al.*, 2005; *Simnett*, 2005) and rather large and fast coronal mass ejections (*Farrugia et al.*, 2005; *Gopalswamy et al.*, 2005; *Zurbuchen et al.*, 2004); the geomagnetic storm on 30 October (doy 303) even led to a daytime aurora as far south as Boston (*Pallamraju and Chakrabarti*, 2005). Figure 5.1 gives an overview over part of the particle event in different energy ranges. Some selected periods which will be discussed in detail in this paper are marked.

Many aspects of particle precipitation during this event already have been modeled: Ozone depletion has been modeled (*Jackman et al.*, 2005a; *Rohen et al.*, 2005; *Verronen et al.*, 2005) and observed by a number of different instruments (*Degenstein et al.*, 2005; *López-Puertas et al.*, 2005; *Rohen et al.*, 2005; *Seppälä et al.*, 2004), as has been the formation of a HNO_3 layer in the upper stratosphere (*Orsolini et al.*, 2005) or the nitric oxide production in a GCM (*Dobbin et al.*, 2006). All these modeling approaches are based on the rather simple assumption of homogeneous proton precipitation inside some nominal polar

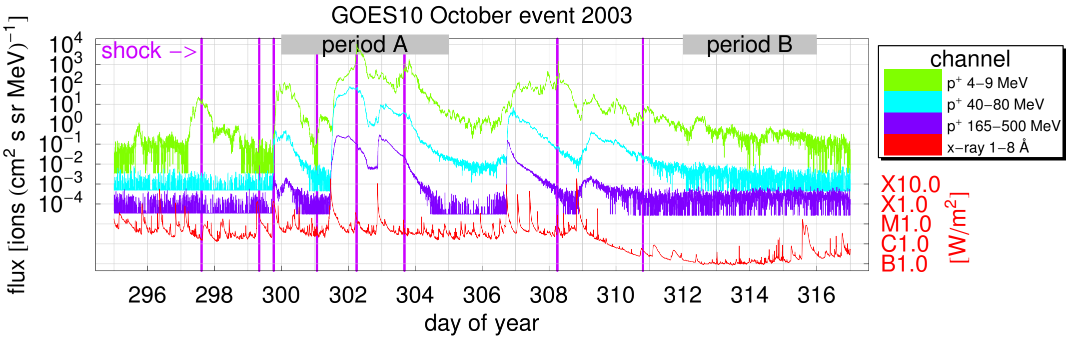

Figure 5.1: Overview of proton fluxes at geostationary orbit (GOES) in different energy ranges from 22 October (doy 295) to 12 November (doy 316) 2003. Marked shocks and X-rays indicate particle events.

cap. In fact, the modeling in *Rohen et al.* (2005) is based on the same ionization model that also underlies AIMOS but is limited to just this simple assumption. Nevertheless *Rohen et al.* (2005) suggest that underestimation of ozone depletion may be caused by a too simple geographic pattern and/or missing electron precipitation.

Some consequences of the 3-D model already have been discussed in *Wissing and Kallenrode* (2009), namely, (1) during quiet times, the major contribution to ionospheric ionization is from electrons in both the polar cap (solar electrons) as well as in the auroral oval (magnetospheric electrons) with the ionization in the auroral oval exceeding that in the polar cap; (2) during solar particle events the dominant effect in the polar cap in the stratosphere and mesosphere is from solar protons although solar electrons can contribute up to 30% to the ionization; (3) during strong shocks following a solar particle event, in the auroral oval magnetospheric electrons and protons lead to ionization rates of up to some 10% of the ones of solar particles; (4) independent of particle source and precipitation site, in general ionization by electrons is more important in the thermosphere.

Figure 5.2 (top) shows the spatial distribution of the total electron production (TEP) rate, that is, the vertically integrated ion pair production rate, for electrons (Figure 5.2, left) and protons (Figure 5.2, right) during 23 October (doy 296). As the K_p index is approximately 1.4, which is very low, particle flux is at background level typical of very quiet times. At (almost) any given point the contribution of electrons to TEP exceeds that of protons with maximum TEP rates around the geomagnetic poles. The sharp separation between a polar cap and an auroral oval in individual energy channels as described in (*Wissing et al.*, 2008) is not visible. TEP is calculated from the entire energy spectrum of each species, and the size and location of polar cap and auroral oval depend on particle energy and species. Thus TEP tends to smear out these features. Nonetheless, the maximum TEP gives some indication of the location of the auroral oval. At slightly higher K_p the sharp separation of oval and cap will be observable.

Please note that the white color within the TEP ionization graphs represents areas where the particle precipitation (within the examined energy range) is assumed to be negligible at any time. Therefore these areas have been excluded in the model. Precipitation in the South Atlantic Anomaly is (at the moment) not covered by the model either. The ionization within the colored area is not calculated continuously but in seven zones for each hemisphere and each local time sector. These zones have been arranged by similar precipitation properties. Hence terrace structure and sudden edges result from binning (*Wissing and Kallenrode*, 2009).

In Figure 5.2 (bottom) the same data are shown for 24 October (doy 297). As shown in Figure 5.1 a shock hits the Earth increasing the TEP rates. Proton induced ionization rises by a factor of ten.

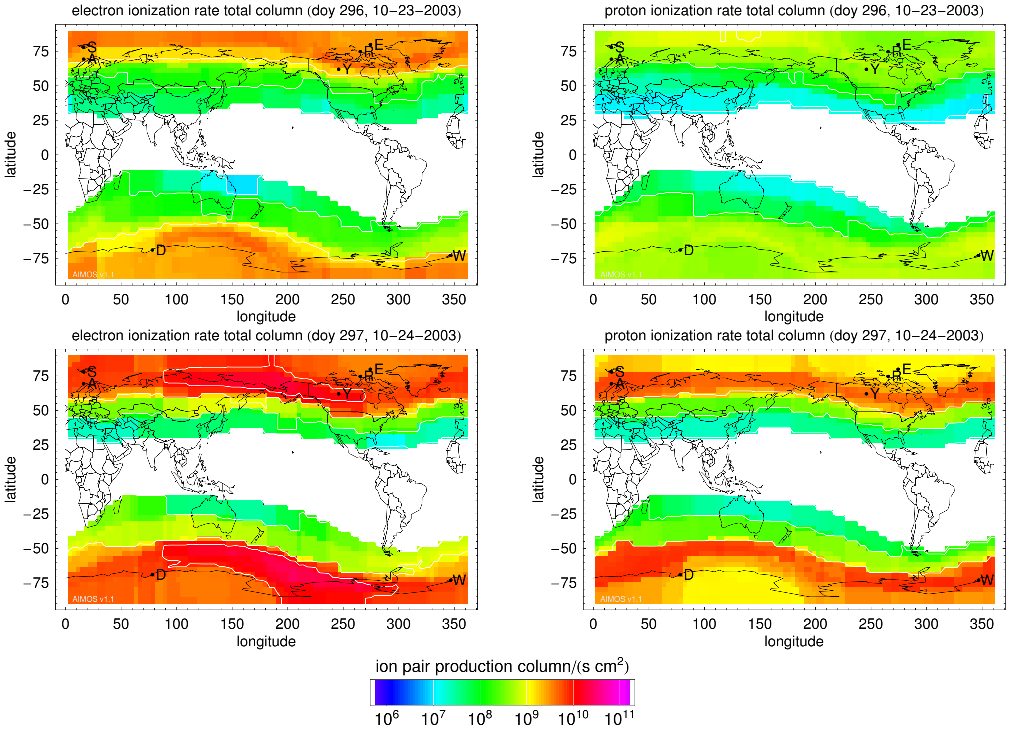

Figure 5.2: Total electron production (TEP) rate, that is, the height integrated ion pair production rate, for a quiet time period (doy 296) and a period with increased geomagnetic activity (doy 297) for electrons and protons. The contribution of electrons to TEP rates exceeds that of protons at (almost) all locations.

The electron domination of TEP in Figure 5.2 should be interpreted with care: as discussed in *Wissing and Kallenrode* (2009), at all times ionization by precipitating electrons is dominant in the thermosphere while this is not necessarily the case in the stratosphere and mesosphere. However, as indicated in their Figure 8, during quiet times ionization by electrons is dominant also in the mesosphere. A c onclusion for the stratosphere cannot be drawn from the model because of the limited energy range of particle observations: electrons with the highest observed energies precipitate only as far as 50 km, thus the model does not give ionization rates for precipitating electrons with higher energies for which no observations are available.

During time period “B” (doy 312 to doy 315) in Figure 5.3 fluxes of solar energetic particles are low but geomagnetic activity increases during day 313 and stays at a rather high level. Figure 5.3 shows the TEP maps for electrons (left) and protons (right). During all four days, the auroral oval is clearly visible in both particle species and precipitating electrons dominate TEP rates. With increasing geomagnetic activity (from the first to the second to the third pair of panels), TEP rates increase and the auroral oval expands. This pattern reflects the typical features expected for the precipitation of magnetospheric particles.

Let us now turn to the two particle events marked by the bar “A” (doy 300 to doy 304) in Figure 5.1. Figure 5.4 shows daily averaged TEP rates for electrons (left) and protons (right) for this time period. TEP rates on doy 300 are dominated by the decay phase of a solar particle event (flare on doy 299) and contributions from a shock originating in an even earlier event. Figure 5.5 (top) displays an ion pair production of $> 10^1\ \mathrm{s}^{-1}\mathrm{cm}^{-3}$ peaking at 70 km and indicating precipitation of high energetic protons due to the former event. However electron ionization dominates upper altitudes; therefore TEP rates are dominated by electrons as well and TEP maximum indicates the energy-averaged location of the auroral

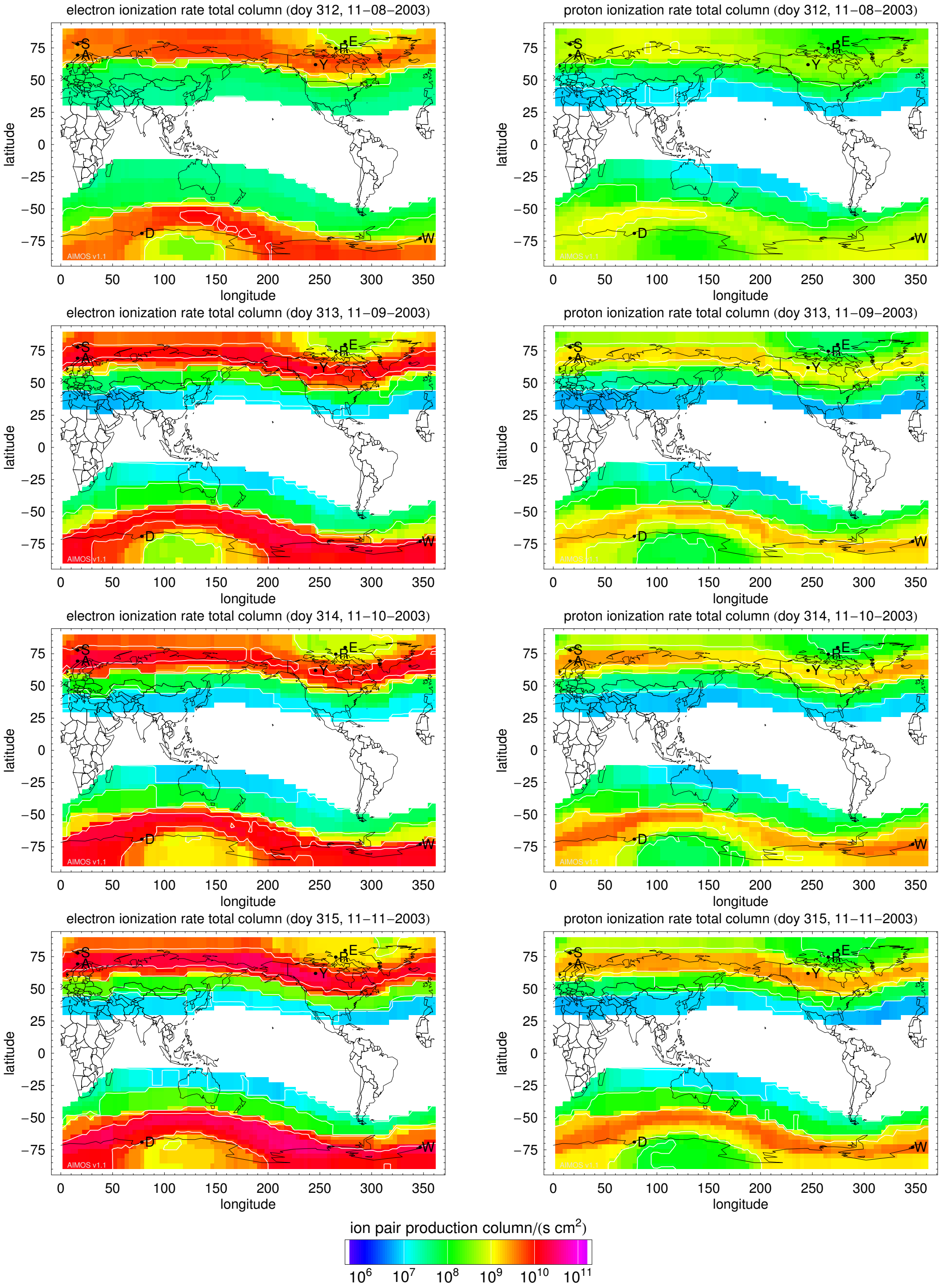

Figure 5.3: Variation of total electron production (TEP) by electrons (left) and protons (right) during four consecutive days in November 2003.

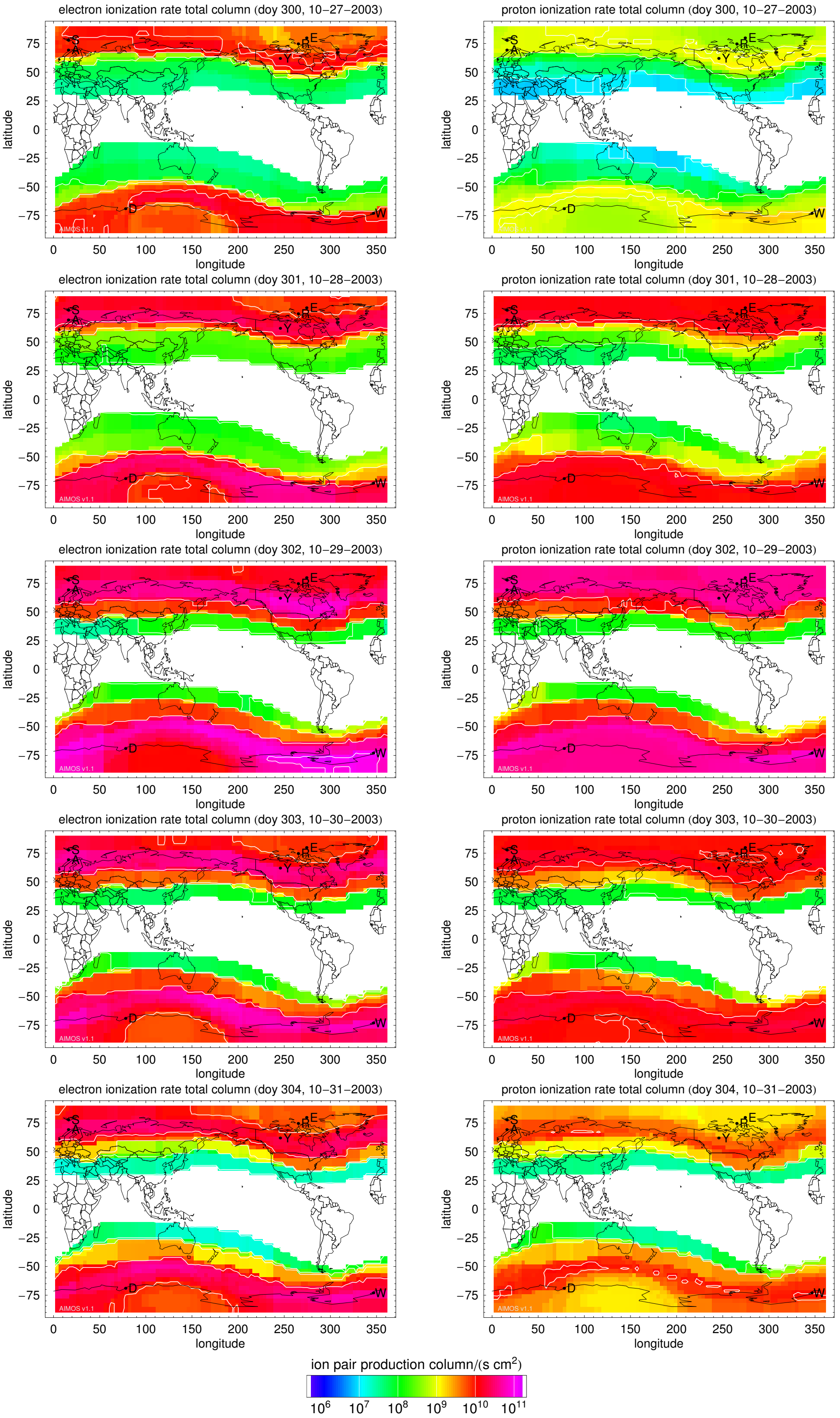

Figure 5.4: Variation of total electron production (TEP) by electrons (left) and protons (right) during five consecutive days in October–November 2003.

oval.

Doy 301 (second row in Figure 5.4) is dominated by a large solar energetic particle event originating in a X17 flare starting at 1215. During this time period, dominant TEP contribution is from protons in the polar cap. The contribution of precipitating electrons to TEP shows the same spatial pattern as on the previous day, indicating a strong magnetospheric contribution.

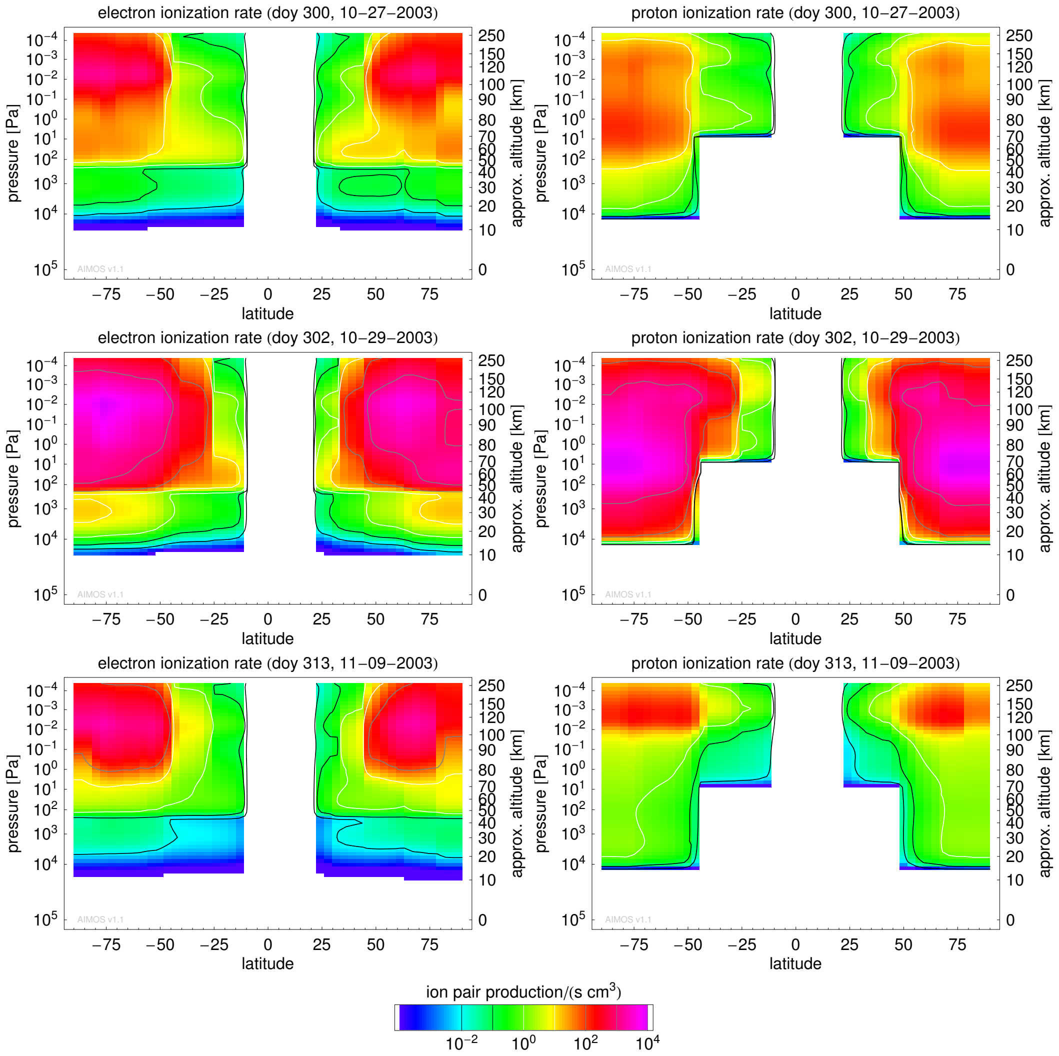

Figure 5.5: Vertical distribution of particle induced ionization at the October event. (top) Doy 300, just before the onset of the main event but affected by decay for an event on the previous day. (middle) Doy 302, the main phase of the October event. (bottom) Doy 313, when ionization profile returned to a rather undisturbed shape.

The shock accompanying the flare of doy 301 arrives in the morning of day 302 (Figure 5.4, third pair of panels, and Figure 5.5, middle). The contribution of precipitating electrons to the TEP map shows (1) a general increase in ion pair production rates and (2) an expansion of the auroral oval toward the equator (expansion is most obvious looking at Northern Russia or Canada) and (3) strong impact on low altitudes. These effects are expected during strong geomagnetic storms. The contribution of precipitating protons to TEP shows a slightly different pattern: compared to the previous day, the ion pair production rate is increased due to the higher particle fluxes and the maximum also expands equatorward as indicated by the 10^{14} contour line. However as ionization in polar cap and aurora can not be distinguished on doy 301 to doy 303 the strong solar particle ionization covers the auroral expansion. While at doy 304 geomagnetic disturbance still is at a high level (K_p=6.3 compared to 3.8 at doy 301, 7.0 at doy 302 and 7.3 at doy 303) a decreasing solar proton flux exposes the expansion.

The strong particle precipitation at doy 302, however, occurs in the polar cap while the auroral oval does not silhouette against the cap. The explanation for the apparently contradictory behavior is obvious from Figure 5.1: later on day 302 a new flare leads to a fresh increase in solar energetic particles which then precipitate deep into an already expanded polar cap (see also Figure 5.5). The maximum ionization moves to lower altitudes and is mostly generated by protons. The entirely different behavior of electrons and protons nicely demonstrates the complexity in the relative contributions of both particle species to TEP.

On doy 303 (Figure 5.4, fourth pair of panels) the situation is much simpler: the fluxes of solar energetic particles decrease but the shock accompanying the flare from the previous day arrives. Consequently, the spatial pattern in both particle species shows a pronounced auroral oval, indicating strong precipitation of magnetospheric particles as expected during a geomagnetic disturbance. The polar cap and auroral oval still are expanded equatorward. On the following day, the pattern continues, also particle fluxes and thus TEP rates are lower.

At the end of the October event the lack of high energetic particles causes an uplift of the zone of maximum ionization. Figure 5.5 (bottom) displays our results for doy 313 showing a maximum ionization at 120 km for protons.

5.5 Atmospheric Consequences

Section 5.4 demonstrated that AIMOS gives a differentiated picture of atmospheric ionization due to precipitating particles. In this section we will demonstrate that this also has consequences for the results of atmospheric modeling. We have incorporated ionization rates produced with AIMOS into the Bremen 3d CTM in three different scenarios: scenario A, the conventional scenario using only averaged proton rates, scenario B, a scenario using only protons but with the 3-D distribution of ionization rates provided by AIMOS; and scenario C, a scenario considering the full AIMOS solution, that is, electrons and protons of both solar and magnetospheric origin. Additionally, a "base" model scenario was carried out for the same time range without atmospheric ionization impacts. This is used as a reference for the particle impacts of model scenarios A, B, and C. In model scenario A, atmospheric ionization is allowed only into regions of geomagnetic latitudes poleward of 60°; in scenarios B and C, the spatial distribution of ionization is determined by the AIMOS model results, i.e., based on measured particle fluxes. Deviations from the "base" model scenario will be given as follows: NO_x: scenario - base; ozone: 100* (scenario-base)/base.

Atmospheric ionization leads primarily to the formation of NO_x and HO_x. Both NO_x and HO_x destroy ozone in catalytic cycles, albeit in different altitudes: NO_x dominates ozone loss in the middle stratosphere, HO_x in the upper stratosphere and mesosphere (*Lary*, 1997). Thus, immediate ozone loss in the mesosphere during a particle precipitation event will be dominated by HO_x, which is short-lived and relaxes to background values immediately with ionization rates. NO_x, however, can be quite long-lived especially during high-latitude winter, when it can be transported down into the middle stratosphere; thus, long-term impacts of the particle events on stratospheric ozone are due mainly to the production of NO_x (e.g., *Jackman et al.*, 2000, 2005b).

Figure 5.6 shows the ozone depletion following particle precipitation for the time interval from Figure 5.2 (doy 296 and 297, correlating to 23 and 24 October, respectively) for the three scenarios described above. As expected due to lack of high energetic protons (see Figure 5.1 in this paper or Figure 8 from *Wissing and Kallenrode* (2009)), ozone depletion due to atmospheric ionization is negligible during this time interval for scenarios considering solar protons only (left for averaged precipitation, middle for precipitation as calculated with

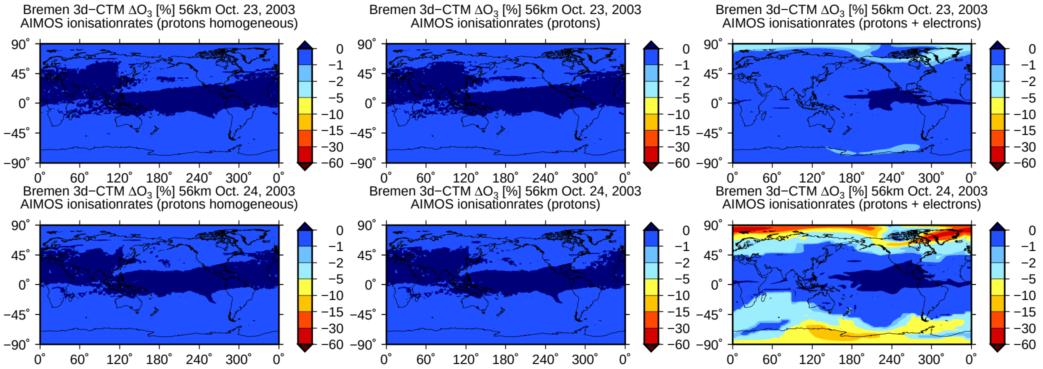

Figure 5.6: Modeled change in O_3 relative to “base” scenario, in % (100* (scenario-base)/base), at 56 km height for the time period from Figure 5.2 for three different scenarios: (left) A, solar proton precipitation averaged over polar cap, (middle) B, solar proton precipitation from 3-D AIMOS; and (right) C, complete AIMOS particle inventory. Here 23 October correlates to doy 296, 24 October to doy 297. Doy 296 was a quiet time day, doy 297 a day with increased geomagnetic activity. Model results are from 1200 UT of the corresponding days.

AIMOS). If electrons and magnetospheric particles are considered (Figure 5.6, right), variations in ozone are observed on both days: Small but significant ozone changes of 2-5% are observed compared to the “base” model run even during geomagnetic quiet times (doy 296) at high northern latitudes. On day 297, which shows increased geomagnetic activity, ozone depletion exceeds 15% in high latitudes. These results suggest that, given the AIMOS ionization rates, even during geomagnetic quiet times electron precipitation has an impact on the ozone budget of the polar mesosphere. This impact is probably restricted to high-latitude winter where ozone recovery is slow. However, these results suggest that at least during polar night, models predicting middle atmosphere ozone need to take electron precipitation into account even during geomagnetically quiet times. This might also explain the large year-to-year variation of middle stratospheric ozone observed during high-latitude polar winter (*Sinnhuber et al.*, 2006).

As ozone loss in this altitude is mainly due to HO_x, whose photochemical lifetime is in the order of minutes in the lower mesosphere and stratosphere, the spatial distribution is mainly due to the precipitation patterns. This is certainly true in the southern hemisphere, where recovery of ozone is very fast. At very high northern latitudes it is already dark enough that ozone recovery, which depends on photolysis of O_2, does not take place, and here the spatial distribution might also be affected by transport of ozone-poor air in regions without solar illumination.

Figure 5.7 shows the longitudinally averaged relative ozone depletion as a function of altitude for the same time period and scenarios as in Figure 5.6. No significant ozone depletion is observed for scenarios A and B (protons only) at any altitude. In scenario C, ozone losses are restricted to altitudes above 45 km and latitudes poleward of 45° N and 30°S, where they exceed 15% on doy 297. That no significant ozone losses are observed below 45 km in scenario C is not surprising because the data set underlying AIMOS only considers electrons up to energies corresponding to a stopping height of about 50 km.

Figure 5.8 shows the same three model scenarios A, B, and C, at an altitude of 56 km for the time period also used in Figure 5.3 (doy 312–315, corresponding to 8 to 11 November) which was geomagnetically active with increased ionization along the auroral oval. Some residual changes in O_3 can be observed in all three scenarios during this time series, especially at northern high latitudes. At this altitude, these are probably due to an incomplete recovery of ozone after the large solar events on 29–30 October and 3–4 November during polar night rather than to a continuing catalytic ozone loss. The overall ozone depletion is largest in scenario C. However, this is probably also a remnant of the solar events and

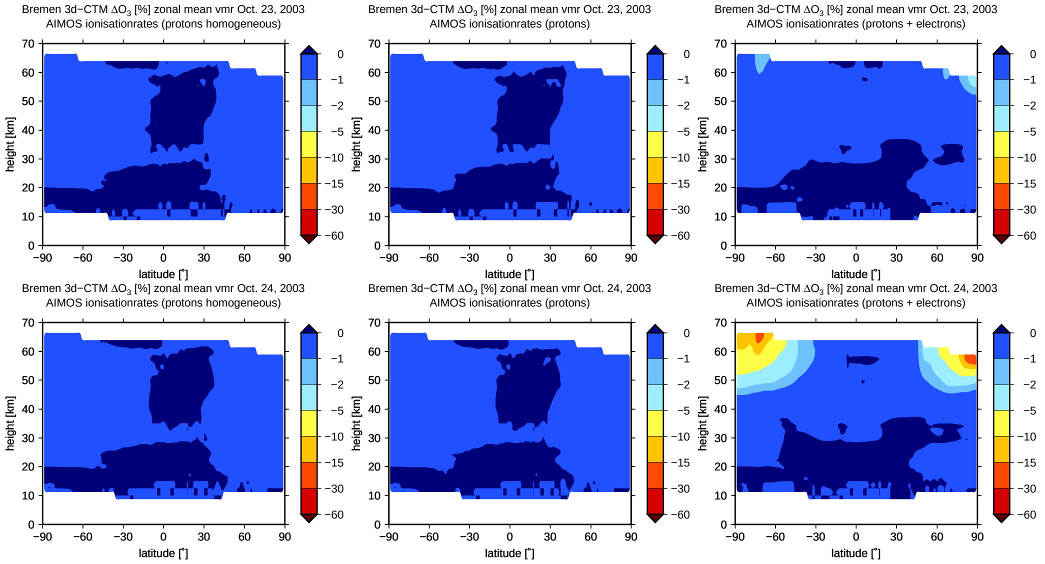

Figure 5.7: Same as Figure 5.6, but as latitude-altitude cross sections. Model results are longitudinally averaged.

not due to the additional precipitating magnetospheric particles during days 312–315, because their particle spectrum is rather steep and consequently most of the TEP is in the thermosphere rather than in the mesosphere.

Figure 5.9 shows the same three model scenarios for the particle events and shocks discussed in Figure 5.4 (doy 300–304, corresponding to 27–31 October). The amount of ozone loss in high latitudes is quite similar in all three scenarios. Model runs A and B also have a very similar spatial pattern, with only small deviations at the edge of the southern polar cap. This shows that the assumption of a homogeneous polar cap with edges defined by 60° geomagnetic latitude is reasonable if only solar particles are considered. In scenario C, ozone losses during the event are quite comparable to scenarios A and B at high latitudes. The spatial distribution of scenario C is different from scenarios A and B insofar as small but significant ozone loss values extend far into mid latitudes compared to scenarios A and B. This is most pronounced on 29 and 30 October, at the east coast of North America, and extending from south Australia to the tip of South America in several regions.

Let us now turn to longer-term consequences of particle precipitation. Outside of polar night, the lifetime of NO_x in the upper stratosphere and lower mesosphere is in the order of days to weeks, the lifetime of ozone in the order of minutes (see Figure 5.11); within polar night, the lifetime of ozone increases to several years. As NO_x does not contribute to catalytic ozone loss above 45 km, ozone is not a good indicator of medium-term atmospheric ionization effects outside polar night. Therefore, in the following we will discuss the medium-term effects of particle precipitation by considering NO_x outside of polar night, and medium to long-term effects by considering NO_x and ozone within polar night. We will limit ourselves to scenarios B and C, that is, the correct spatial pattern for protons only B and for protons and electrons C.

Figure 5.10 shows a global picture of NO_x volume mixing ratios at 56 km for selected time intervals during the event relative to the "base" scenario. The consideration of all particles (Figure 5.10, right) leads to much higher NO_x values at high latitudes. In addition, the latitudinal extension of the region affected by particle precipitation, which has already been discussed for ozone, is occasionally observed in the NO_x production. This can be seen quite clearly, for example, on 29 October, where enhanced NO_x values reach the tip of South America in scenario C, but not in scenario B, or on 4 November, where NO_x enhancements

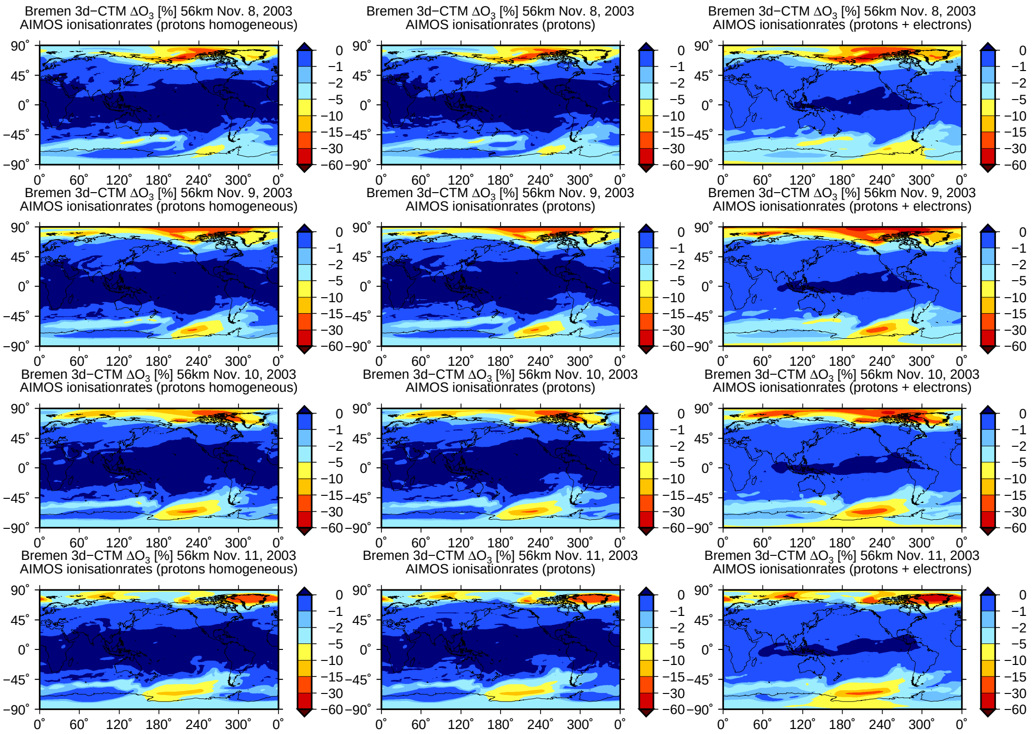

Figure 5.8: Modeled change in O_3 relative to “base” scenario, in % (100* (scenario-base)/base), at 56 km height for the time periods from Fig. 5.3 for three different scenarios: (left) A, solar proton precipitation averaged over polar cap, (middle) B, solar proton precipitation from 3-D AIMOS; and (right) C, complete AIMOS particle inventory. 11 November correlates to doy 312. All days were geomagnetically active. Model results are from 1200 UT of the corresponding days.

reach down into the gulf of Persia in scenario C, but not in scenario B.

However, the spatial distribution of NO_x enhancements into lower latitudes is different to that of ozone loss shown in Figure 5.9. Ozone depletion in this altitude range is driven by HO_x, which is very short-lived. Regarding latitudes southward of 80°N, ozone recovers quickly. Therefore the distribution of ozone depletion directly reflects areas of particle precipitation. However, NO_x is considerably longer lived than ozone everywhere but in polar night (see Figure 5.11), and the spatial distribution of NO_x enhancements also reflects horizontal transport of enhanced NO_x values into lower latitudes.

In Figure 5.12, an example of the evolution of NO_x and ozone over a longer time-series (from 20 October to 31 December) is shown exemplary for the Arctic station of Ny Ålesund (78°55’N, 11°57’E), relative to a model run without atmospheric ionization. A location in high northern latitudes was chosen because there both NO_x and ozone are comparatively long-lived, the lifetime of ozone increasing from several hours in early November (see Figure 5.11) to several years during polar night, and downward transport of NO_x as well as ozone-poor air into the mid-stratosphere is possible during polar winter. As already seen in Figures 5.6 and 5.7, some ozone loss and NO_x production occurs already before the solar events on 29 October in model scenario C due to enhanced geomagnetic activity from 24 October. However, ozone loss and NO_x production during the solar event are actually quite similar in model scenarios B and C. After the event, the lower edge of the significantly affected area descends down from around 40 km altitude to around 28 km; this is observed in both model scenarios, and both for NO_x enhancements and ozone depletion. Both NO_x enhancements and ozone depletion are larger in model scenario C. Ozone loss in model scenario C exceeds this in model scenario B at the end of December by 5–10% at 30 km

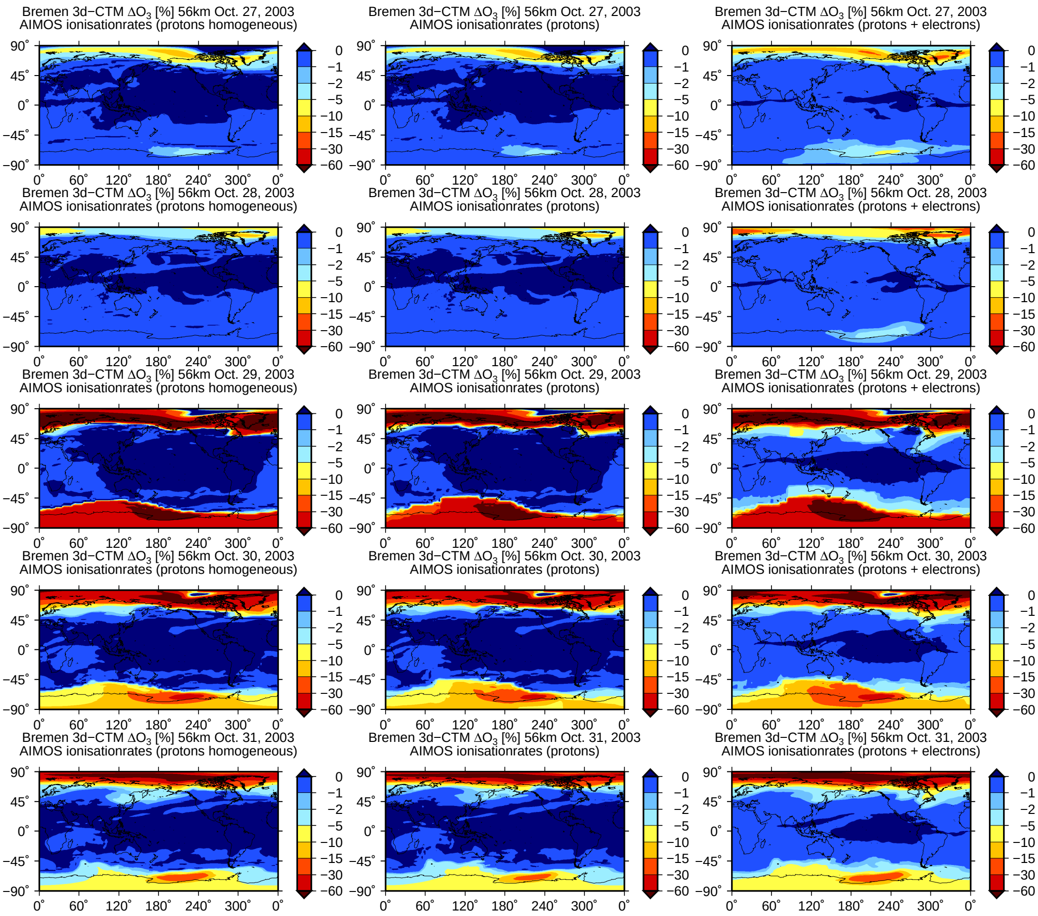

Figure 5.9: Modeled change in O_3 relative to “base” scenario, in % (100* (scenario-base)/base), at 56 km height for the time periods from Figure 5.4 for three different scenarios: (left) A, solar proton precipitation averaged over polar cap, (middle) B, solar proton precipitation from 3-D AIMOS; and (right) C, complete AIMOS particle inventory. 27 October corresponds to doy 300. Due to the solar coronal mass ejection on 28 October, proton fluxes were greatly enhanced during 29 and 30 October (see Figure 5.4). Model results are from 1200 UT of the corresponding days.

altitude, and by more than 10% between 30 and 40 km altitude. However, it is not clear from comparing model scenarios B and C whether this is due to additional ionization at the edge of the polar cap region during the solar events, or due to the additional impact of magnetospheric particle precipitation during the geomagnetically disturbed times before and after the solar event.

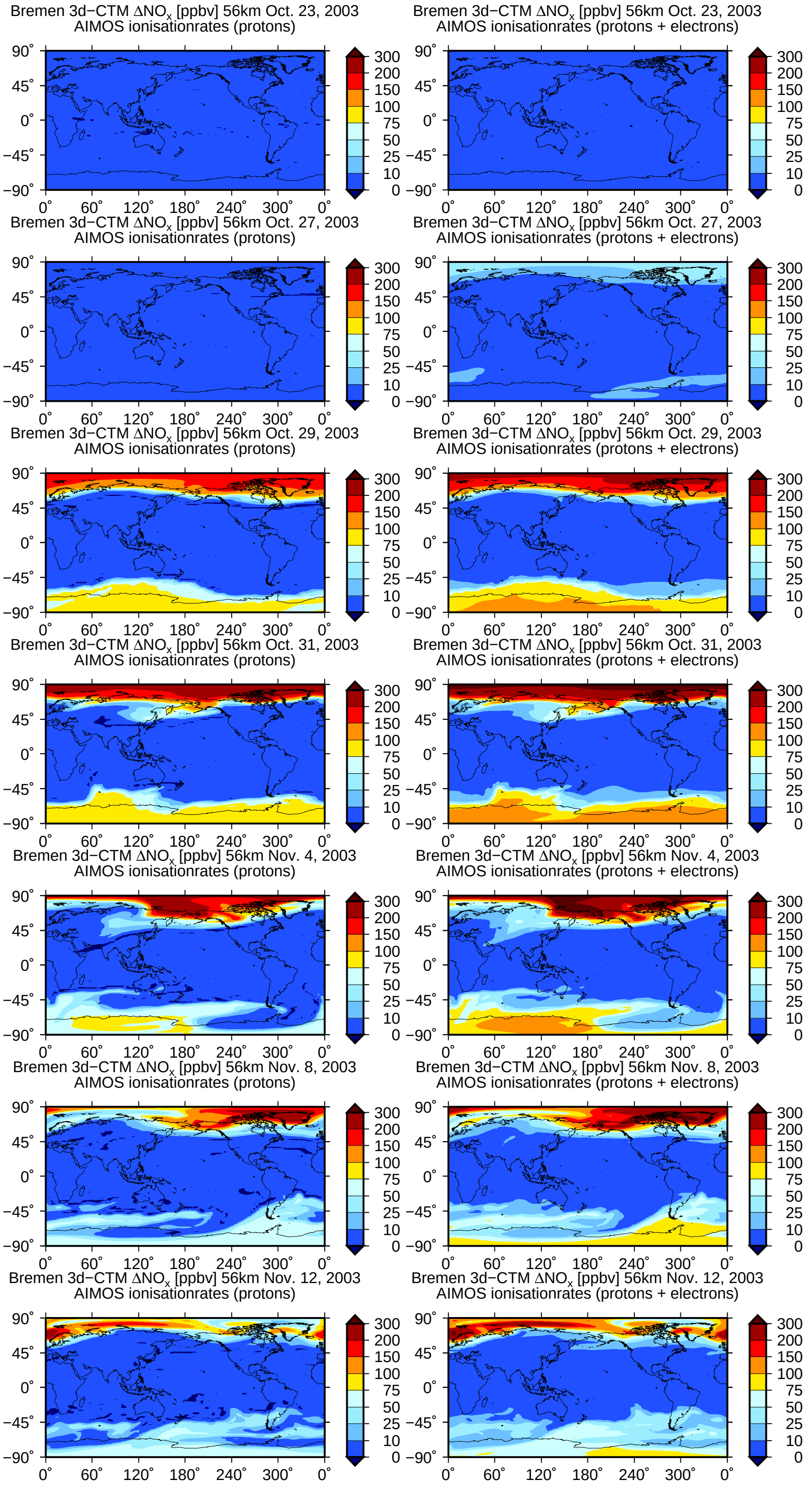

Bremen 3d−CTM ΔNO_x [ppbv] 56km Oct. 23, 2003
AIMOS ionisationrates (protons)

Bremen 3d−CTM ΔNO_x [ppbv] 56km Oct. 23, 2003
AIMOS ionisationrates (protons + electrons)

Bremen 3d−CTM ΔNO_x [ppbv] 56km Oct. 27, 2003
AIMOS ionisationrates (protons)

Bremen 3d−CTM ΔNO_x [ppbv] 56km Oct. 27, 2003
AIMOS ionisationrates (protons + electrons)

Bremen 3d−CTM ΔNO_x [ppbv] 56km Oct. 29, 2003
AIMOS ionisationrates (protons)

Bremen 3d−CTM ΔNO_x [ppbv] 56km Oct. 29, 2003
AIMOS ionisationrates (protons + electrons)

Bremen 3d−CTM ΔNO_x [ppbv] 56km Oct. 31, 2003
AIMOS ionisationrates (protons)

Bremen 3d−CTM ΔNO_x [ppbv] 56km Oct. 31, 2003
AIMOS ionisationrates (protons + electrons)

Bremen 3d−CTM ΔNO_x [ppbv] 56km Nov. 4, 2003
AIMOS ionisationrates (protons)

Bremen 3d−CTM ΔNO_x [ppbv] 56km Nov. 4, 2003
AIMOS ionisationrates (protons + electrons)

Bremen 3d−CTM ΔNO_x [ppbv] 56km Nov. 8, 2003
AIMOS ionisationrates (protons)

Bremen 3d−CTM ΔNO_x [ppbv] 56km Nov. 8, 2003
AIMOS ionisationrates (protons + electrons)

Bremen 3d−CTM ΔNO_x [ppbv] 56km Nov. 12, 2003
AIMOS ionisationrates (protons)

Bremen 3d−CTM ΔNO_x [ppbv] 56km Nov. 12, 2003
AIMOS ionisationrates (protons + electrons)

Figure 5.10: Change in NO_x volume mixing ratio relative to “base” scenario, in ppb (scenario - base), at 56 km height for different time periods during the October–November event for a scenario using 3-D AIMOS (left) proton precipitation and (right) proton plus electron precipitation. The time series covers days from before the solar event (23 and 27 October, during the event (29 and 31 October), and some time after the event (8 and 11 November). On 4 November, a second smaller solar event occurred. All model results represent 1200 UT of the corresponding days.

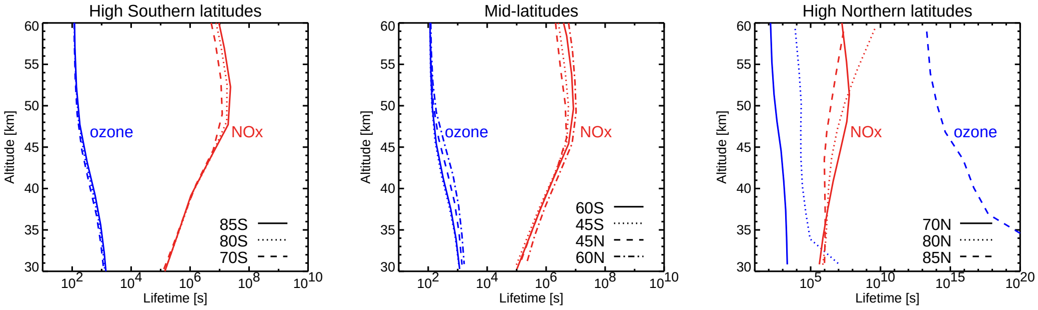

Figure 5.11: Photochemical lifetimes of NO_x (N, NO, NO_2), and ozone for different latitudes from southern high latitudes to midlatitudes to northern high latitudes calculated with a one-dimensional version of our chemistry model for local noon (1200 UT at 0°E) on 5 November, 2003. Note that the lifetime of NO_x is derived from the photochemical loss rate, and reflects the e-fold destruction time; the lifetime of ozone is derived from the photochemical production rate, and reflects an effective doubling time. This was done to reflect the fact that ozone is destroyed during particle precipitation events, NO_x is formed, and we are interested in the time frame of the recovery. In early November, 85°N is already in polar night, 80°N is at the edge of polar night with solar (surface) zenith angles of around 95° at noon.

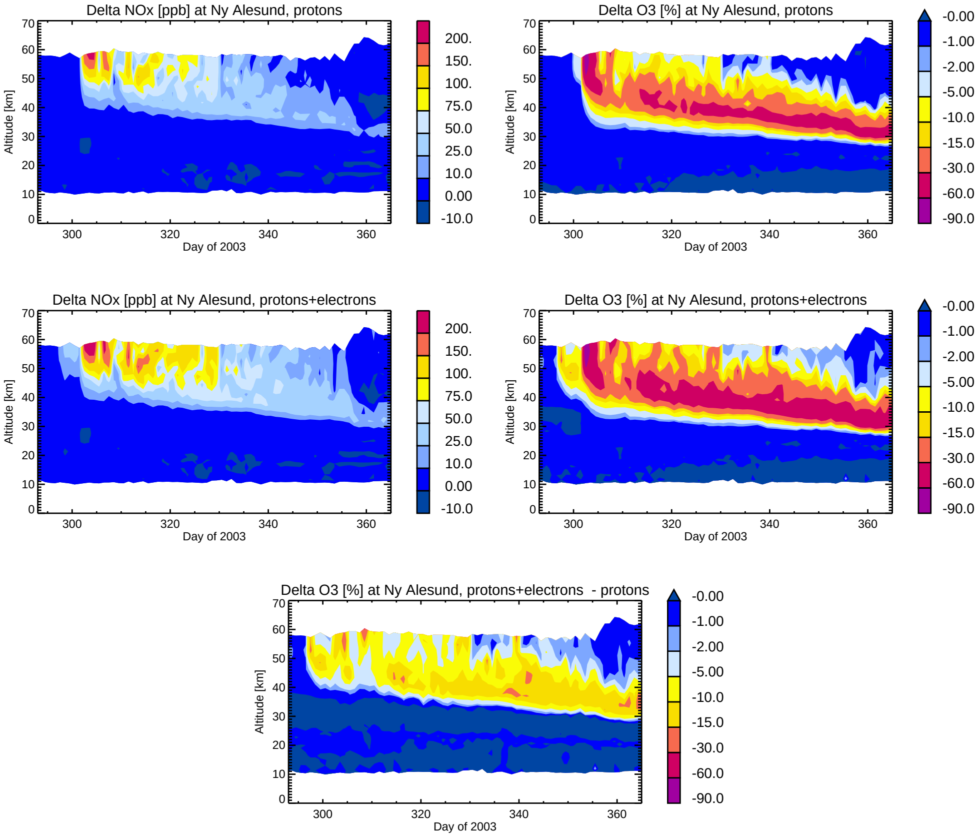

Figure 5.12: Shown is the change in NO_x volume mixing ratio relative to "base" scenario, in ppb (scenario - base) as well as change in ozone relative to "base" scenario, in % (100* (scenario-base)/base). The period covers the end of year 2003 begining with the October event. Ny Ålesund is located at 78°55'N, 11°57'E.

5.6 Summary

In this paper we present different model runs for the October–November 2003 event using the *Atmosphere Ionization Module OSnabrück* in combination with the Bremen three-dimensional chemistry and transport model. First, we examine the relative contributions of electrons and protons to the total electron production (TEP) rates. The results confirm that AIMOS produces the typical features expected from solar and magnetospheric particles and partly already discussed in *Wissing and Kallenrode* (2009). Second, we use the Bremen three-dimensional chemistry and transport model to evaluate whether the use of AIMOS ionization rates influences modeling of NO_x production and ozone depletion compared to the simpler assumption of solar energetic protons only. The main results are:

1. If only proton precipitation is considered, total ozone depletions are almost identical for the assumption of homogeneous precipitation inside the polar cap and the spatial precipitation pattern determined with AIMOS. A minor difference between the spatial pattern of proton induced Ozone depletion is visible in the southern hemisphere on 29 October, the main phase of the event. This might reflect the large aberration of the geomagnetic south pole (79.5°S 108.4°E as given by IGRF-10 model for 2000, and commonly used as central point for the polar cap ionization) compared with the magnetic south pole (64.7°S 138.3°E as measured by *Barton* (2002) for the same year). AIMOS uses satellite measurements only to describe the spatial pattern. Therefore estimations on the central point are not necessary.
2. Our model suggests that total ionization column by electrons almost always exceeds the one of the protons. Exceptions are the polar cap regions within the maximum of the October event. As most of the electron impact concentrates on altitudes above 80 km an increased altitude range may be beneficial for GCM models.
3. During solar particle events, the direct impact of the electrons is small and due to model constraints restricted to altitudes above 50 km. However, considering the electrons as well extends the area affected by particle precipitation somewhat to lower latitudes. This results in a somewhat fuzzy edge of the polar cap, as, e.g., observed by SCIAMACHY during the October–November 2003 SPE (*Rohen et al.*, 2005).
4. Model results suggest that at least at high latitudes during polar winter, mesospheric ozone can be affected significantly by magnetospheric electrons. A small impact of electron precipitation is predicted using the AIMOS ionization rates even during geomagnetic quiet times, increasing to quite significant values of ozone loss during geomagnetically disturbed times even in the absence of solar protons. This might go some way toward explaining the observed variability of ozone in the upper stratosphere and mesosphere at high latitudes during polar winter (*Sinnhuber et al.*, 2006; *Palm et al.*, 2009).
5. It has been shown that considering additional magnetospheric electrons also has a significant (10–15%) impact on stratospheric ozone during polar winter. However, it is not clear whether this is due to additional magnetospheric electron precipitation into the edge of the polar cap during the solar events, or due to magnetospheric electron precipitation during days of enhanced geomagnetic activity before and after the solar events.
6. Our calculations imply that electron ionization strongly affects NO_x concentration and should not be neglected (see Figure 5.10). The computations include electrons up to energies of 2.5 MeV (extrapolated to 5 MeV), which directly produce NO_x above about 45 km. Lower altitudes, which are not directly affected by electron precipitation, also show increased NO_x concentrations (see Figure 5.12).

These results suggest that electron precipitation should be considered in modeling ozone in the stratosphere and mesosphere, not only during large solar events and geomagnetically highly disturbed times, but also during geomagnetically quiet times, at least during polar winter.

Acknowledgments

This work was supported by the Deutsche Forschungsgemeinschaft DFG under contracts DFG-Ka1297/7-1 and DFG-Ka1297/8-1.

Chapter 6

Atmospheric Ionization Module OSnabrück (AIMOS) 3: Comparison of electron density simulations by AIMOS-HAMMONIA and incoherent scatter radar measurements

J.M. Wissing, M.-B. Kallenrode, J. Kieser, H. Schmidt, M.T. Rietveld, A. Strømme, P.J. Erickson

Included as published on August 11, 2011 in JOURNAL OF GEOPHYSICAL RESEARCH, **116**, A08305, doi:10.1029/2010JA016300, 2011. Copyright 2011 American Geophysical Union. Reproduced by permission of American Geophysical Union.

6.1 Abstract

Ionization of the atmosphere due to precipitating solar energetic particles as well as magnetospheric particles is a major source of thermospheric electron density. In this paper we evaluate numerical simulations of the 3-D spatial and temporal electron densities produced by these particle populations through a comparison with incoherent scatter radar observations. The 3-D precipitation patterns are determined with the *Atmosphere Ionization Module OSnabrück* (AIMOS). We use a version of the general circulation and chemistry model *HAMburg MOdel of the Neutral and Ionized Atmosphere* (HAMMONIA) (*Schmidt et al.*, 2006) enhanced by ion chemistry to calculate the impact of particle ionization on the electron density. These modeled data are compared to radar observations from EISCAT Svalbard and Tromsø as well as the ISR stations at Millstone Hill and Sondrestrom. Particle precipitation is severely affected by geomagnetic disturbance and latitude. Therefore different locations (inside the polar cap and at auroral latitudes) and geomagnetic conditions are included in the comparison. The main results of the paper can be summarized as follows: (1) As expected, particle forcing will significantly improve modeled electron density in comparison to results of the radar measurements. (2) In particular night-time comparisons of the electron density are affected; here the particle forcing will account for a boost of two to three orders of magnitude.

6.2 Introduction

The ionospheric E and F layers are primarily created by the Sun's hard electromagnetic radiation. They are also strongly affected by ionization from precipitating particles. The composition and energy spectra of this precipitating particle population strongly depend on solar particle input and its modulation by the magnetosphere. In detail, the effect of the magnetosphere can be characterized by the level of geomagnetic activity and the geomagnetic location. The resulting ionization has a direct impact on chemical reactions (mainly due to the production of NO_x) and therefore affects the composition in the lower thermosphere. As NO_x can be transported downward, ozone destruction in the stratosphere may be affected as well (e.g. *Randall et al.*, 2007).

Ozone destruction due to large solar energetic particle events has been discussed for various SEPs, e.g., August 1972 (*Crutzen et al.*, 1975; *Heath et al.*, 1977; *Jackman et al.*, 2000), October 1989 (*Jackman et al.*, 2000) and October 2003 (*Randall et al.*, 2005; *Rohen et al.*, 2005). In general the effects of solar energetic particles and magnetospheric particles are discussed separately. One model describing the impact of solar energetic protons on atmospheric ionization (and subsequent NO_x production and ozone depletion) was given by *Jackman and McPeters* (1985). The precipitation of magnetospheric particles also affects the ionization of the atmosphere and therefore atmospheric chemistry (*Thorne*, 1977; *Callis et al.*, 1996a, 2001). However, a combined approach to particle induced ionization patterns is given by *Wissing and Kallenrode* (2009): the *Atmosphere Ionization Module OSnabrück* (AIMOS). Results from this model will be used here.

Our aim is to study the particle impact on the lower thermosphere. As NO_x production and ozone destruction are follow-ups of the particle precipitation, both imply the need of a realistic modeling of thermospheric particle forcing. The model chain AIMOS-HAMMONIA has been developed/modified for this purpose.

A comparison of modeled ionization rates and direct measurements is not possible as this would include continuous in-situ measurements at various locations and, in particular, at various altitudes. Alternatively, the electron density is used as an adequate key- and test-value for thermosphere modeling since it is the characteristic physical quantity for ion chemistry.

Incoherent scatter radars (*Gordon*, 1958) allow the determination of altitude-resolved electron densities which can be compared to in-situ rocket measurements (*Friedrich et al.*, 2009). The electron density (calculated from radar measurements) has to be determined by comparison of the radar echo and a best fit theoretical spectrum. As the fit includes various free parameters (electron density, ion and electron temperature, ion composition, and line-of-sight ion drift) it is accompanied by some assumptions e.g. regarding the ion composition. Using EISCAT data from the August 1989 SPE, *Turunen* (1993) computed the electron density and compared it to results from an ion-chemistry model in combination with GOES-7 proton precipitation. The results are restricted to 70–90 km (D region) and focus on the reduction of the degrees of freedom in the incoherent scatter fit. Another EISCAT analysis on the impact of SPEs (November–December 1989) by *Collis* (1996) enlarged the altitude range to 50–90 km. Again starting from incoherent scatter measurements, *Kirkwood et al.* (2001) derived an energy-flux spectrum of precipitating electrons.

Our ambition is similar to *Kirkwood et al.* (2001) but using radar measurements and satellite born particle measurements as starting points. We compare electron densities derived from ISR measurements with simulations by a model chain of AIMOS and HAMMONIA (*Schmidt et al.*, 2006), a general circulation and chemistry model that, for the present study, has been enhanced by the inclusion of ion chemistry. A scheme of the model chain is given in Fig. 6.1.

The ISR measurements in this comparison originate from stations at Sondrestrom, Millstone Hill and from the *European Incoherent SCATter radars* (EISCAT) at Tromsø and on Svalbard.

This paper is the third in a series pertaining to the *Atmosphere Ionization Module OS-*

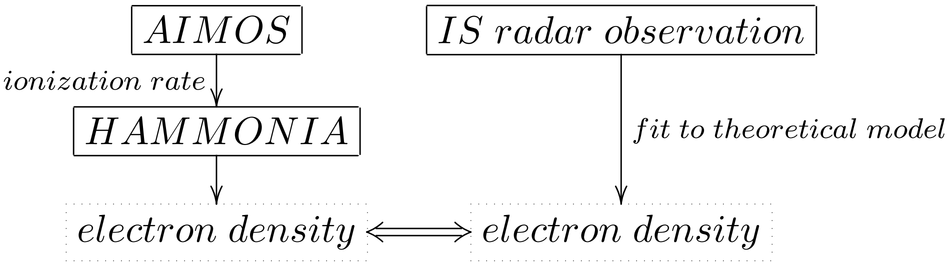

Figure 6.1: Scheme of the model chain. The electron density can be modeled by a combination of a particle-ionization model and a general-circulation model while incoherent scatter radars measurements and post processing by a theoretical model gives the comparative value.

nabrück and intended to validate of the model chain AIMOS-HAMMONIA by means of ISR observations.

The paper is structured as follows. In Section 6.3 we describe the data and models including the assumptions inherent in the interpretation of the data. Section 6.4 describes our results. As the location of precipitation may easily account for strong differences in ionization rate, Section 6.4.1 deals with the model accuracy at different geomagnetic latitudes. Section 6.4.2 will show the comparison of ISR measurements and modeled electron density at geomagnetically active and inactive periods indicated by the $\mathrm{K_p}$ index. Stations within the polar cap and within auroral latitudes will be compared. The congruence of our simulations and ISR at night-time as well as for day-time will be shown in Section 6.4.3. The last Section (6.5) will summarize the results.

6.3 Data and Models

The model chain consists of two parts: (1) the ionization model AIMOS which calculates atmospheric ion pair production rates from particle fluxes observed in space and inside the magnetosphere and (2) the general circulation model HAMMONIA that processes these ionization rates to calculate electron densities, which in turn can be compared to ISR data.

Connecting the model chain to ISR measurements, the preparation of ISR data itself includes some modeling.

6.3.1 AIMOS

AIMOS (*Wissing and Kallenrode*, 2009) is a 3-D model of atmospheric ionization caused by precipitating particles with high spatial resolution for an atmosphere extending from the surface up to 1.7×10^{-5} Pa, corresponding to an upper boundary generally between 250 to 350 km. As the model includes protons in the range of 154 eV to 500 MeV and electrons from 154 eV to 5 MeV the altitude range of this study is well covered. AIMOS uses observations from two polar-orbiting satellites complemented by a geostationary one. This combination allows the determination of atmospheric ionization by protons and electrons of both, solar and magnetospheric origin. Furthermore, it allows to model the 2-D horizontal particle precipitation pattern depending on geomagnetic activity. Ionization rates are calculated from the observed particle spectra by a Monte Carlo approach based on the GEANT4 simulation package (*Agostinelli et al.*, 2003). A detailed model description of AIMOS and additional references are given in *Wissing and Kallenrode* (2009). The ionization data is available at `http://aimos.physik.uos.de` and can be applied to a user specific grid (horizontal and vertical) via web-applet. In our case, the grid is adapted from HAMMONIA and will be described in Section 6.3.2. The temporal resolution of the AIMOS ionization rates is 2 h, which is needed to get a full satellite orbit coverage.

The main source of error in the AIMOS output originates from the spatial distribution (in particular the variable auroral oval), which has to be extrapolated from in-situ measurements of polar-orbiting satellites. Comparing particle flux measurements from another satellite to the extrapolated (modeled) particle flux at the same location reveals the inherent error of the extrapolation algorithm. As mean scaled particle flux maps (*Wissing and Kallenrode*, 2009) are used to quantify the spatial particle precipitation, this error is called 'quantification error'. The maximum observed quantification error is 85% while it is below 20% in most cases. Taking into account that we have a local variation of up to 4 orders of magnitude the error still is small. Please note that the quantification error may just have a small impact on a numerical simulation due to particle transport amongst neighboring bins. However, in a local comparison like this, small displacements of the ionization may show up as significant discrepancies.

One focus of this paper will be the validation of the modeled spatial particle precipitation. As they are not listed in detail in (*Wissing and Kallenrode*, 2009) we will mention other sources of error, even though they are marginal compared with the spatial distribution: (1) The internal mechanism of AIMOS is based on Monte Carlo, therefore the statistical error is in general in the order of 1 to 2%, and of about 10% in the case of electron Bremsstrahlung. (2) With respect to the particle detector, the satellite data suffers from statistical counter reading errors of up to 10% (looking at maximum precipitation areas in the upper atmosphere). (3) Impact of aging and crosstalk of the particle instruments have been negelected.

To sum it up, the expected error in the AIMOS output should be less than a factor of 2 in the most extreme cases and 25% in general.

6.3.2 HAMMONIA

The *HAMburg MOdel of the Neutral and Ionized Atmosphere* (*Schmidt et al.*, 2006) treats atmospheric dynamics and chemistry interactively for the height range from the Earth's surface to 1.7×10^{-5} Pa. HAMMONIA is a superset of the middle atmosphere version of the ECHAM5 general circulation model (GCM) (e.g., *Manzini et al.*, 2006) interactively coupled to the MOZART3 chemistry scheme (*Kinnison et al.*, 2007). The model uses a spectral dynamical core with a triangular truncation at wavenumber 31 (T31) and 67 vertical layers. Chemical reactions and parameterized physics are calculated on a horizontal grid with a resolution of $3.75° \times 3.75°$. The same grid is used by AIMOS. With respect to the model description given by *Schmidt et al.* (2006), HAMMONIA has been expanded to represent the effects of energetic particle precipitation. Some information on the expansion is provided in the following, a more extensive description will follow in a separate manuscript. In the version used here, HAMMONIA considers 216 chemical reactions among 49 neutral species, 5 ions (O^+, O_2^+, N^+, N_2^+, NO^+), and electrons. 54 of the reactions describe photochemical dissociation and ionization (for wavelengths from 0.05 to 121 nm), while six are directly associated with effects of precipitating particles (five ionizations plus one dissociation). The reaction rates are given by the ionization rates from AIMOS combined with branching ratios from *Roble and Ridley* (1987) and *Verronen* (2006). The newly developed ion chemistry module is valid only for the ionospheric E and F regions. In the D region, ion chemistry cannot be described with a simple five ion scheme. Here we use parameterizations of *Jackman et al.* (2005a) which are based on *Porter et al.* (1976) and *Solomon et al.* (1981). Therefore in the lower atmosphere (all height levels with a pressure larger than 10^{-3} hPa), effects of ion chemistry are parameterized and the electron density is not realistic. The effect can be seen in Figure 6.5 where the simulated electron density (solid line) shows an abrupt decrease below an altitude of about 90 km. Consequently, all our comparisons are limited to altitudes above 90 km.

Interactions between the plasma and the neutral gas may strongly affect atmospheric temperature and dynamics. Using the parametrization of *Zhu et al.* (2005) HAMMONIA calculates Joule heating depending on the model-predicted electron densities. Since the effect of Joule heating is usually small in the middle atmosphere and particle-induced ion chemistry is considered only above 10^{-3} hPa, Joule heating is not calculated for altitudes below the thermosphere.

In the simulation used for this study, tropospheric winds and temperature in HAMMONIA are "nudged" towards fields from the European Centre for Medium Range Weather Forecast (ECMWF) operational analyses. However, in the region of our interest, the thermosphere, this tropospheric nudging provides a very weak constraint only. It cannot be expected that the actual thermospheric weather of the analysis period is matched by the model simulation. Please note, in the following we will refer to HAMMONIA as a GCM although this type of GCMs coupled to a chemistry module is sometimes referred to as a CCM (chemistry climate model).

6.3.3 Incoherent Scatter Radars

The GCM-modeled electron densities are compared to 1 h-mean electron densities derived from ISR measurements. In order to cover the spatial and temporal variability we used data from 4 locations: Millstone Hill, Sondrestrom and the EISCAT stations at Tromsø and Svalbard. Further information on these stations is listed in Table 6.1. We used all available ISR data (from the Madrigal data base: `http://www.eiscat.se:8080/madrigal`) during October 2003–April 2004 as far as it covers a suitable altitude range. The periods under study are shown in Figure 6.2 with respect to the recording location. In addition Table 6.2 lists all used ISR data as it appears in the Madrigal data base.

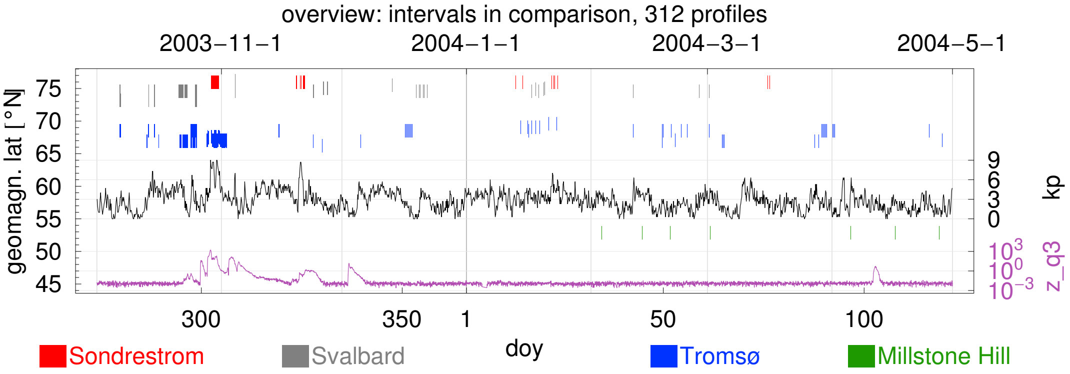

Figure 6.2: All ISR periods which have been used in this comparison are shown by a vertical line. The color represents the respective ISR station. The time indicates the end of the relevant 1 h integration interval. Additionally the geomagnetic activity (K_p) and the geomagnetic latitude of the measurement at 110 km altitude are indicated. Enhanced particle precipitation is indicated by the z_p3 channel on GOES-11 (9–15 MeV protons in units of $\frac{1}{cm^2\,s\,sr\,MeV}$). The ISR stations in the legend below are sorted by decreasing geomagnetic latitude from left to right.

Sondrestrom	Svalbard		Tromsø	Millstone Hill
66°59'12"N 309°03'02"E	78°09'11"N 16°01'44"E	geographic coordinates	69°35'11"N 19°13'38"E	42°37'10"N 288°30'30"E
80°24'	82°3'36"	geomag. dip	77°30'	52°36'
74°11'24"N	75°11'N	invar. lat.	66°12'N	53°24'35"N
177 m	445 m	elevation	86 m	146 m

Table 6.1: Detailed information on the exact ISR location on the ground (*ISR-Factsheet*, 2003).

The European Incoherent Scatter (EISCAT) Radars near Tromsø have center frequencies of 928.4 MHz (UHF) and 224 MHz (VHF) while the EISCAT Svalbard Radar (ESR) is at 500 MHz. The ISR at Sondrestrom operates at 1290 MHz, and that at Millstone Hill at 440 MHz. All these radar frequencies lie far above the plasma frequency. Therefore the signal is not totally reflected but scattered by single electrons in the ionospheric plasma. The plasma theory describing the backscattered signal spectrum in terms of the parameters is extremely accurate, which makes the technique such a powerful one for determining the plasma parameters (*Farley*, 1996). In particular the electron density, electron and ion temperatures and ion velocity are routinely measured by all these radars. The ion composition can also be obtained with certain restrictions that are a factor of many variables. In general, the assumptions used for composition analysis at the various ISRs have a relatively minor effect on the electron density values relevant to this study (*Waldteufel*, 1971).

In the course of signal processing ISR returns to obtain plasma parameters, accurate determination of electron density requires the use of a system constant factor applied to the total backscattered power. This constant is a function of many radar system parameters which are sometimes challenging to track, and which are often time dependent. Each ISR therefore maintains a calibration model for this system constant which provides good accuracy in electron density through inter-comparison with an independent measurement. These measurements can for example be provided by plasma line data from the ISR itself, from ionosonde-derived peak densities, or by tracking to statistical empirical models. However, the inter-comparison process can have difficulties which impose accuracy limitations on full altitude profiles of electron density. In some cases in this study, it was found that separate radar measurements from the same site gave significantly different densities by up to a factor of two, indicating that the calibration was wrong on one of the radars, which was confirmed by subsequent comparisons with ionosonde data.

The EISCAT radars in Tromsø have steerable antennas thereby allowing measurements from 62 to 74°N invariant latitudes. Under quiet magnetic conditions EISCAT is located outside the auroral oval from about 12 h to 15 h magnetic local time (*Roettger*, 1983). The EISCAT Svalbard radar is located in the polar cap, as is the Sondrestrom radar. The Millstone Hill radar measures effects in the subauroral and mid-latitude ionosphere except under very disturbed conditions, which were not the case for the time periods of this study.

ISR Measurements: Reliability and Comparability

The particle precipitation and the electron density caused by it are highly variable in space and time. This variability is, e.g., due to variations in the geomagnetic field like substorms (*Scholer, M.*, 2003) or flux transfer events (*Russell and Elphic*, 1979). These variations show up in a comparison of different locations (see Section 6.4.1) as well as in a temporal analysis of single places. We cover the temporal aspect in Section 6.4.2 by separating the measurements depending on the geomagnetic activity index $\mathrm{K_p}$. A typical ISR variation and the 1 h mean value is shown in Figure 6.3.

The Madrigal database includes some ISR electron density profiles for a redundant setup (time/place). In cases of redundancy (time/place and shape of the profile), the profile with best altitude resolution is used. This has been done to limit the impact of single measurements with many redundant post-processed profiles. In some redundant setups different kind of ISR inconsistencies have been observed:

(1) Different instruments looking at the same time at the same spot of the atmosphere show conflicting electron density profiles. Some of these contradicting values have been explained by the instrument operators, e.g., the calibration of the Tromsø *arcd* program on the VHF radar is wrong. Ionosonde measurements indicate that it shows only half of the expected value for a longer period. In this comparison, the calibration factor for Tromsø *arcd* has been corrected manually (multiplied by 1.9).

(2) Different radar pulse-lengths as well as various post-processing methods are sometimes used for the same instrument. The post-processing is used to infer electron densities from measurements. Different post-processing of the raw data is often done to suit the var-

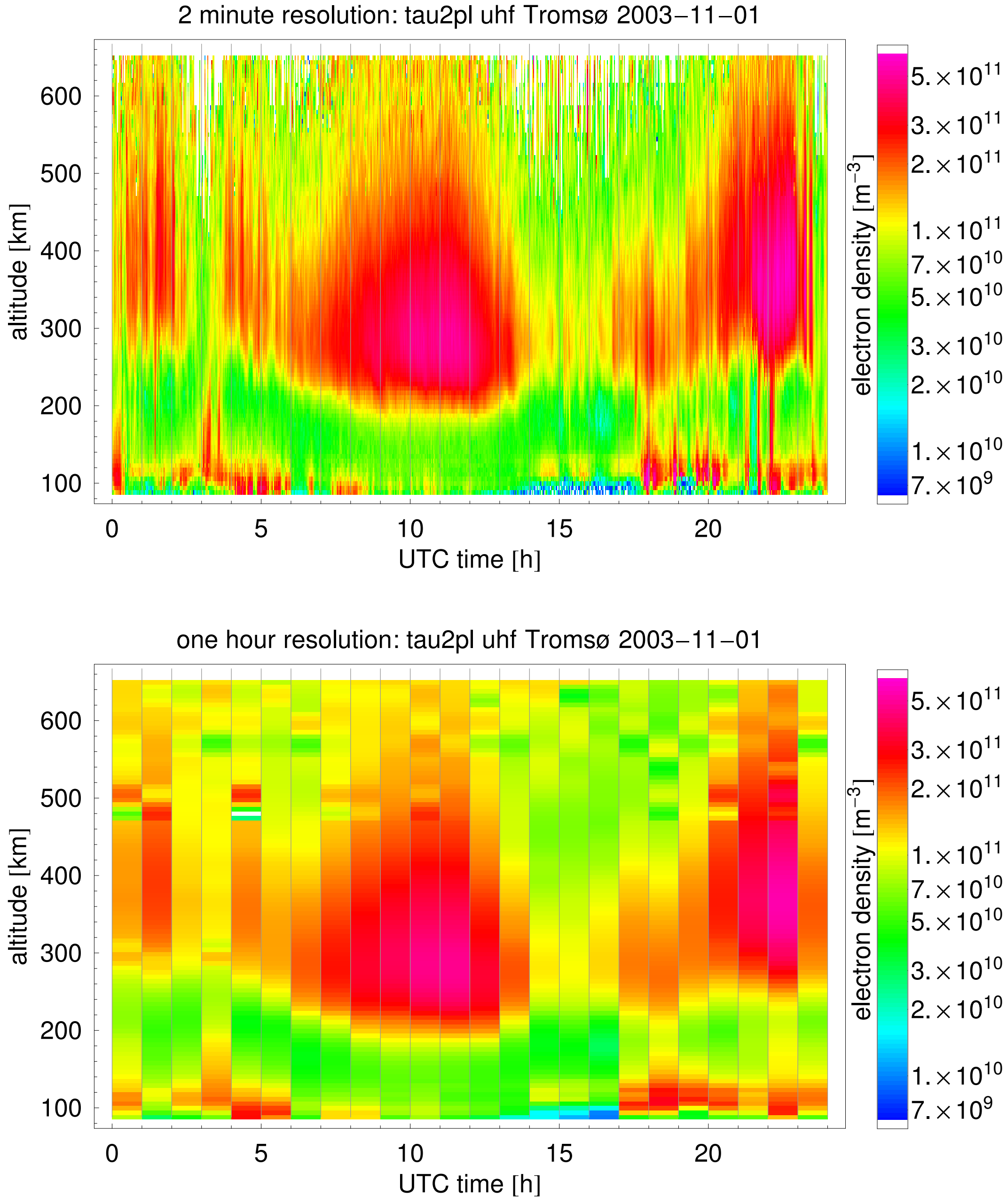

Figure 6.3: A typical ISR (here: EISCAT Tromsø) measurement shown in 2 min and 1 h resolution. The 1 h resolution is needed for comparison with the simulated data.

ious altitude regions, to remove unwanted effects like ground clutter or to focus on some physical aspects, so the same ISR dataset may result in significantly different electron densities if used uncritically. In Figure 6.4 (top) measurements with two pulse-lengths at Sondrestrom have been post-processed in various ways, including different time and altitude resolution and interpolation as well as special emphasis on, e.g., conductivity profiles. The error of the electron density measurements differs significantly (some 1 h averages show relative errors of more than 18000%). Consequently redundant setups have been checked manually in order to select the profile with the smallest error only. In case that the error ranges do not overlap (see Fig. 6.4, bottom) a qualitative selection is not possible. Therefore both profiles will be used in the comparison.

Apart from the qualitative selection of profiles all data points with a relative error of more than 25% are omitted.

(3) In the case of Millstone Hill, we also found some discrepancies, but as they have been identified as radar reflections from a close mountain range, suspicious data has been excluded.

Our chance to detect abnormal profiles is limited to multiple measurements in a redundant setup (time/place). This is just a small fraction of the 312 1 h ISR profiles within the period from October 2003 to April 2004. Therefore some problematic profiles will still remain even though we excluded profiles which are known to be contaminated and corrected wrong calibration factors in the *arcd* profiles.

The impact of problematic ISR measurements on our comparison can be characterized as follows: (1) Faulty calibration may cause a systematic shift in some of the ISR-modeled electron densities. As far as a shift has been identified it was in the order of a factor of 2. (2) Different methods of measurement (e.g. variation of pulse-length) and post-processing result in different electron density profiles even though the announced error bars do not overlap (see Fig. 6.4, bottom). As far as we can compare these profiles in redundant setups the biggest differences are in the order of a factor of 2. (3) Extremely problematic profiles as in Fig. 6.4 (top) showing differences of up to 2 orders of magnitude should be almost completely omitted as they normally have huge relative errors. In this paper we use ISR data points with an announced relative error of less than 25% only.

6.3.4 Integration Time

A comparison based on identical time resolution is not possible. The AIMOS model has a 2 h time resolution; reasoned by a full orbit satellite coverage. Consequently the ionization rates can be considered as a 2 h mean. The numerical time step of HAMMONIA is comparatively small (5 min). However, as the particle forcing applied in the model is constant over 2 h periods, we use snapshots at the end of the 2 h intervals to compare with the observations. In the case of the IS radars the temporal resolution strongly depends on instrument and experiment setup. The viewing direction may change during 2 h and some data may be missing. We analyzed data with a maximum of 10% gaps and 10% differing viewing directions (viewpoint accuracy: $\pm 0.05°$). In the case of Sondrestrom this filtering has been adopted to a different experiment setup: three different viewpoints are adjusted after another, therefore we selected one of them and allowed longer data gaps up to 75%. In this case the filter for the viewpoint accuracy has been reduced to $\pm 1°$ as the accuracy suffers from quick rotation. The electron density from single profiles as given by the Madrigal data base are averaged to the designated integration time. The ISR integration time in our comparison is 1 h, ending at the time of the snapshot. There are two reasons for the different time intervals. First, 2 h intervals without long data gaps and major viewpoint changes would reduce the number of ISR profiles tremendously. And second, the physical motivation is that the satellite data itself does not represent a real “temporal” mean but values from very different locations within a 2 h period (*Wissing and Kallenrode*, 2009). Just a small fraction of them – or in other words just a few minutes – will be used to determine the approximate ionization at one particular location. Fast changes in the particle precipitation will be a problem in ionization modeling

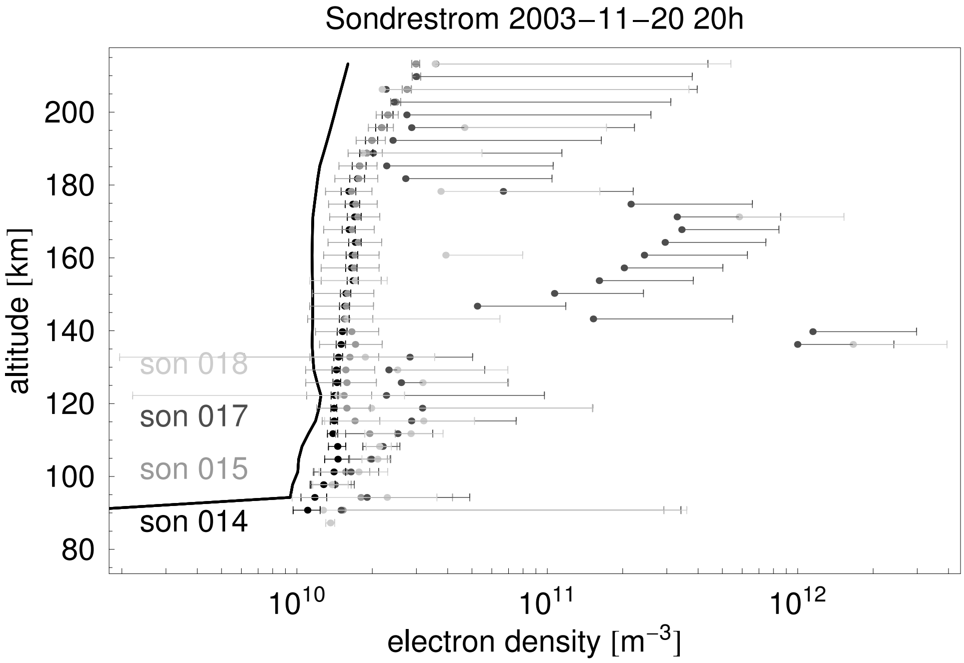

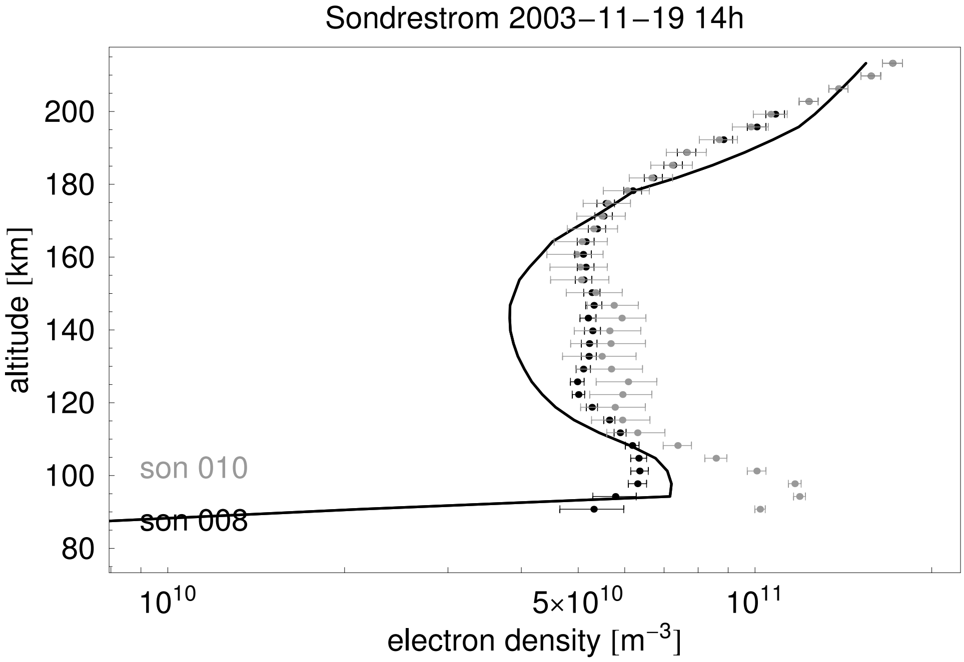

Figure 6.4: The dots represent simultaneous but diverging ISR observations at Sondrestrom. The solid line represents the modeled electron density by AIMOS-HAMMONIA. Detailed information can be found in Section 6.3.3. A missing left side error bar indicates a relative error of more than 100%. (top) The relative error depends on the method of measurement and the post-processing. In case of redundancy the profile with smallest error is used only (here ‘son 014’). (bottom) Non-overlapping error bars do not allow a qualitative selection. In this case both profiles are used in the comparison.

and in the comparison. However, we assume that the results of comparison will be almost the same using ISR data with 1 h or 2 h integration time.

6.4 Results

This section gives an impression of the role of particle induced ionization for the upper atmosphere. A good test value for atmospheric modeling is the determination of the electron density. Figure 6.5 gives a typical example of the GCM-modeled electron density with particle forcing ($\rho_{\mathrm{e}\,\oplus}$, solid line) and without particle forcing ($\rho_{\mathrm{e}\,\oslash}$, dashed line) compared to the electron density derived from ISR measurements ($\rho_{\mathrm{e\,ISR}}$, dots). The difference between $\rho_{\mathrm{e}\,\oslash}$ and $\rho_{\mathrm{e\,ISR}}$ is about three to four orders of magnitude, while $\rho_{\mathrm{e}\,\oplus}$ and $\rho_{\mathrm{e\,ISR}}$ are of the same order. We still have a strong discrepancy below 90 km. The reason is that HAMMONIA uses the full ion chemistry above 90 km, only. As a consequence, the GCM-modeled electron density below 90 km drops by orders of magnitude and we will constrain our comparison to the thermosphere. In the following, we will analyze all available 2 h periods from October 2003 to April 2004. The discrepancy between $\rho_{\mathrm{e}\,\oslash}$ and $\rho_{\mathrm{e\,ISR}}$ is shown in Figure 6.6 (top). Most obvious in Figure 6.6 (top) is the dependence on local time. While calculations at local day (6 h–18 h) show a comparatively good ratio of 0.03 to 1 for $> 50\%$ of the profiles and even better 0.1 to 1 above 135 km, the agreement is poor at night when $> 50\%$ of the ratios are between $3 * 10^{-4}$ and 0.03 ($2 * 10^{-3}$ to 0.03 above 135 km, respectively). The reason is that photo-ionization as the second major source of the ionization is included in HAMMONIA and dominates day-time densities. Please note that 6 h–18 h is not exactly equal to the appearance of sunlight. At noon the $\rho_{\mathrm{e}\,\oslash}$ to $\rho_{\mathrm{e\,ISR}}$ ratios are very close to 1. Thus, most of our comparisons will focus on more interesting night-time data. Generally speaking, the modeled night-time electron density without particle forcing is underestimated by 2 to 3 orders of magnitude.

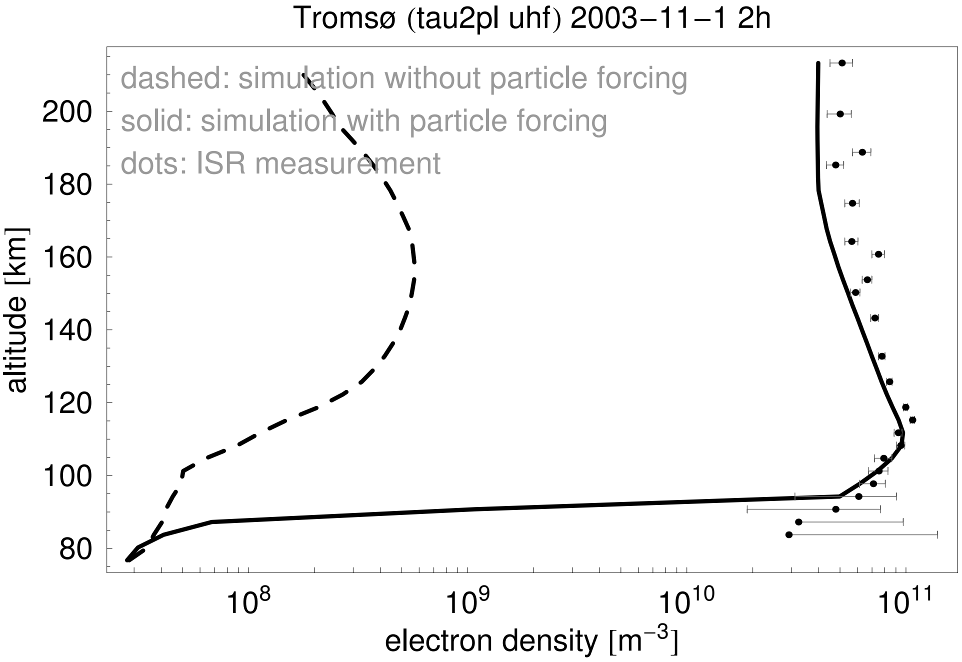

Figure 6.5: A typical auroral night-time comparison of a simulation with and without particle forcing in contrast to the result of incoherent scatter radar measurements is shown. A left missing side error bar indicates a relative error of more than 100%.

Figure 6.6 (bottom) presents the ratio of $\rho_{\mathrm{e}\,\oplus}$ and $\rho_{\mathrm{e\,ISR}}$. Here the distribution is close to a ratio 1 (0.5 to 1.5 for $> 50\%$ of the profiles), which represents agreement with the ISR observations. Additionally the spread of the ratios that include $> 50\%$ of the day and night profiles declines by at least one order of magnitude (below 110 km and above 190 km it is 2 orders of magnitude) through the inclusion of particle induced ionization. The resulting spread for $> 50\%$ of day and night profiles is less than 1 order of magnitude.

These deviations still seem large. The following aspects may help to reclassify that: (1) The ionization model has to hypothesize local particle precipitation (which shows local variations in the order of 4 magnitudes at geomagnetic stable conditions, see Figure 8 in *Wissing and Kallenrode* (2009)) from measurements at other locations. (2) HAMMONIA is not simulating the actually observed thermospheric weather (see above). (3) The integration time of models and ISR observations are not identical (see Section 6.3.4); and (4) different kind of data processing and erroneous calibration in the ISR data may cause variations about a factor of 2 (see Section 6.3.3).

In summary the ionizing impact of electrons and, to some extent, protons and alpha particles gives a significant improvement to the atmospheric electron density modeling.

6.4.1 Comparison sorted by geomagnetic Latitude

For the global comparison of modeled electron densities we use incoherent scatter radar measurements from 4 different locations. As the viewpoint of every profile may vary due to different azimuth and elevation angles we determined the geomagnetic latitude at 110 km altitude in order to bin the profiles into two fractions, one ranging from 66–70° geomagnetic North and the other from 73–76.5° geomagn. N. Figure 6.7 shows the dependence of modeled night-time electron density profiles on geomagnetic latitude. The selection of night-time measurements has been performed by means of the Sunrise/Sunset Calculator by Chris Cornwall, Aaron Horiuchi and Chris Lehman (National Oceanic and Atmospheric Administration, `http://www.srrb.noaa.gov/highlights/sunrise/sunrise.html`). Most obvious is the increased electron density at 66–70° geomagn. N caused by strong electron precipitation in the auroral oval. We only use profiles that can be compared to ISR observations. Therefore no profiles southward of 66° geomagn. N and northward of 76.5° geomagn. N. are shown.

Figure 6.8 (top) shows the corresponding ratio of $\rho_{\mathrm{e}\,\oplus}$ and $\rho_{\mathrm{e\,ISR}}$ for night-time. Please note, that this graph is a scale-up of the night time profiles in Figure 6.6 (bottom) with binning of geomagnetic latitudes.

Regarding Fig. 6.8 (top) the ratio depends on the geomagnetic latitude during night time. While the ratio at 73–76.5° geomagn. N is centered at 1, meaning a good correlation of simulation and measurement, the auroral region (66-70° geomagn. N) shows a slight underestimation. In low latitudes the median is about a factor of 0.5. Figure 6.10 and Section 6.4.2 will go into detail here.

Looking at day-time (see Figure 6.8, bottom vs. top) the ratios at all latitudes show a smaller spread (including $> 50\%$ of the profiles) which can be easily explained by electromagnetic radiation that can be modeled more precisely.

As the 73–76.5° geomagn. N day-time values in Fig. 6.8 (bottom) are based on 32 profiles only, we will not pay too much attention to the underestimation at 120–150 km altitude.

In sum the overall accuracy at day-time is better than at night-time. In the following we will focus on night-time profiles as particle induced ionization does not interfere with forcing from electromagnetic radiation.

6.4.2 Comparison sorted by geomagnetic Activity

The intensity of particle precipitation depends on solar and geomagnetic activity. As the focus of this study is on the thermosphere, the geomagnetic disturbance is of main interest, here. To exclude the variability caused by geomagnetic latitude and sunlight, the impact of geomagnetic disturbance is shown for one distinct place and night-time, only. Figure 6.9 presents modeled electron densities ($\rho_{\mathrm{e}\,\oplus}$) for the location of Tromsø. All periods that are

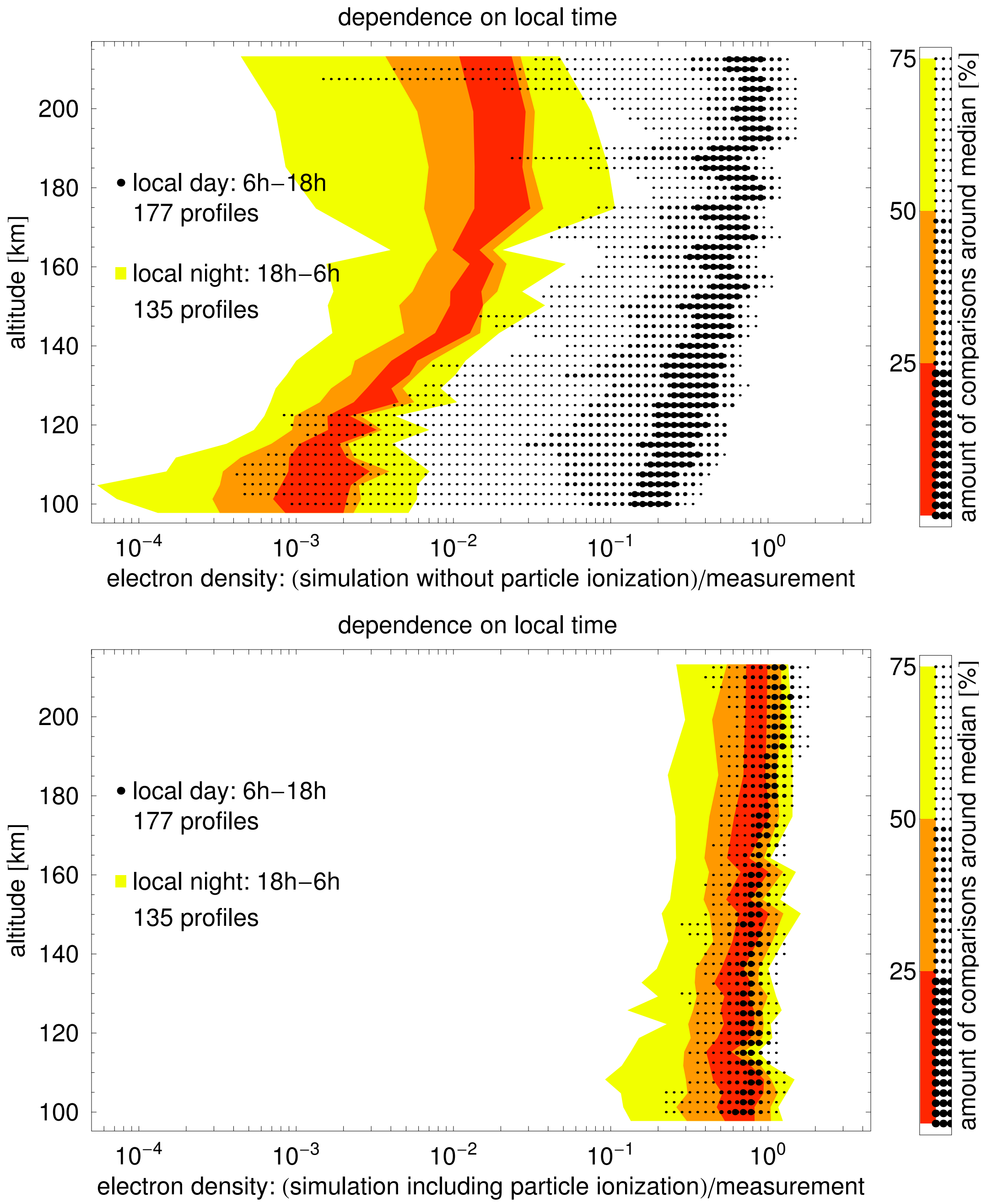

Figure 6.6: Ratios of GCM-modeled electron density and the corresponding electron density derived from ISR measurements ($\rho_{\mathrm{e\,ISR}}$) are shown. The shaded areas include 20%, 50% and 75% of the amount of local day (6 h–18 h) profiles around the median, while the dotted areas indicate the same for night time ratios. Even though the dependency on local time is very obvious, it should be mentioned that the local time is just a rough indicator of daylight since some areas might be affected by polar night. (top) Ratio of $\rho_{\mathrm{e}\oslash}$ and $\rho_{\mathrm{e\,ISR}}$, (bottom) ratio of $\rho_{\mathrm{e}\oplus}$ and $\rho_{\mathrm{e\,ISR}}$.

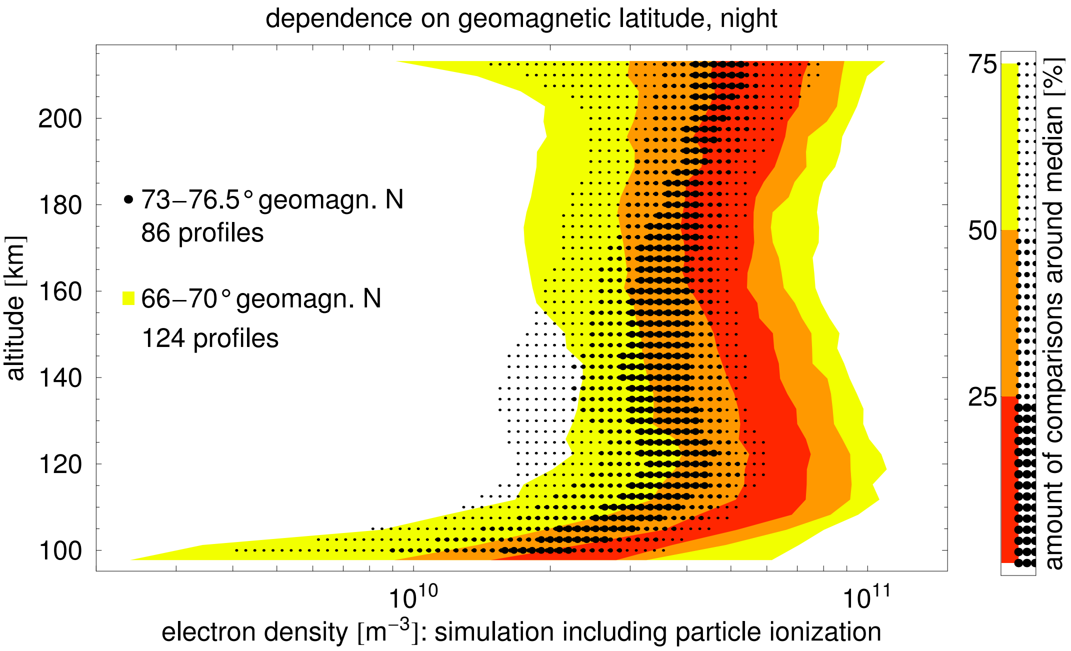

Figure 6.7: Night-time GCM-modeled electron density including particle forcing ($\rho_{e\,\oplus}$) depending on altitude. Colors indicate the corresponding geomagnetic position. The auroral oval leads to a maximum of electron density at approximately 66°N.

covered by measurements are included. As indicated in Figure 6.2 we have a special emphasis on the October event here. Besides the dependency on K_p, the most important information of Figure 6.9 is the variability. Maximum and minimum electron density differ by a factor of 10, which is about the same size as the variation in the ionization rate due to particle forcing above 100 km (see Figure 11, bottom *Wissing and Kallenrode*, 2009).

Figure 6.10 gives an overview of night-time simulations divided by the respective ISR electron density at (top) Svalbard and (bottom) Tromsø, respectively. Again the shaded (dotted) areas indicate a certain percentage of the profiles around the median.

The main difference is that Svalbard is located inside the polar cap while Tromsø allows measurements in the auroral oval. Polar cap and auroral oval are treated completely differently in AIMOS. Polar cap particle precipitation (and therewith the ionization rate) is assumed to be homogeneous within the entire cap. Therefore particle data from polar-orbiting satellites are used directly during polar cap crossing (*Wissing and Kallenrode*, 2009). On average the ratio of $\rho_{e\,\oplus}$ and $\rho_{e\,\mathrm{ISR}}$ is close to one at Svalbard. In detail more than 50% of the ratios at low and high K_p values are between 0.5 and 2.5. While the ratios at low K_p are centered at approximately 1, the ratios at high K_p (K_p=3.5 to 9) show a tendency of overestimation (about a factor of 1.5). However, the amount of profiles which are used at Svalbard is very small. In all these comparisons we should keep in mind that the modeled ionization is a factor 100 to 1000 closer to the measurements than it is without particle forcing (see Figure 6.6).

In the case of Tromsø (see Figure 6.10, bottom) and other locations in the auroral oval, the determination of the ionization rate is more complex. Mean particle precipitation maps at different K_p values are used in combination with recent satellite measurements in order to get global coverage out of two orbits of polar-orbiting satellites. Details are given in *Wissing and Kallenrode* (2009). However, most of the time the ionization has to be estimated from measurements at large distance from Tromsø and the auroral oval is fluctuating in time and space. These aspects complicate simulation and comparison with measurements (see also

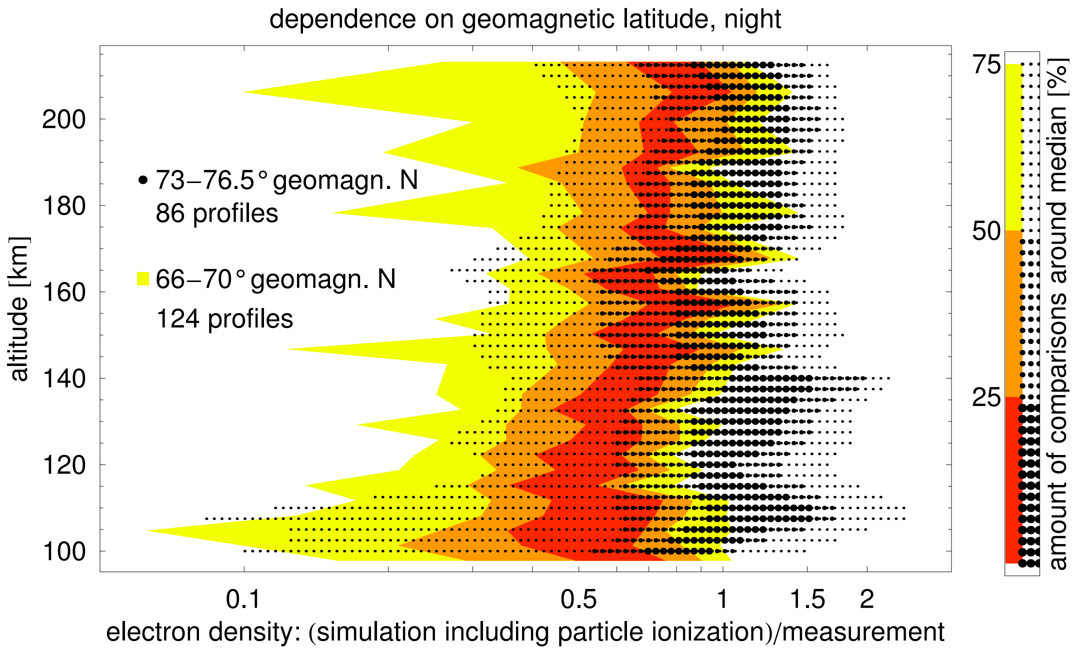

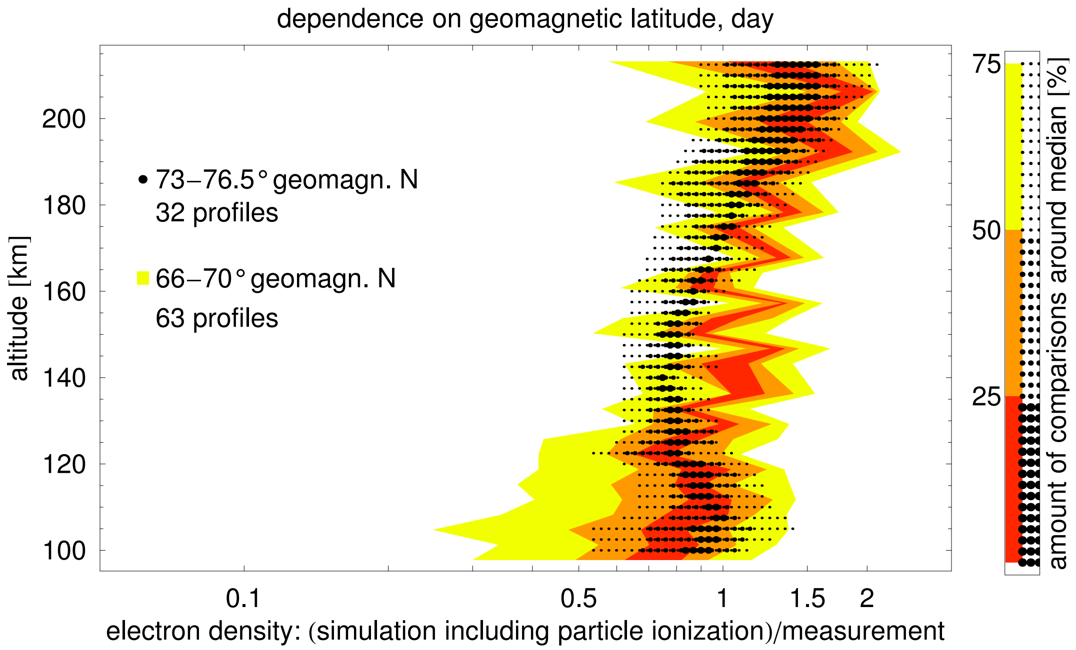

Figure 6.8: Relation of GCM-modeled and ISR-modeled electron density for conditions without and with daylight. “1” indicates a perfect match of $\rho_{\mathrm{e}\,\oplus}$ and $\rho_{\mathrm{e\,ISR}}$.

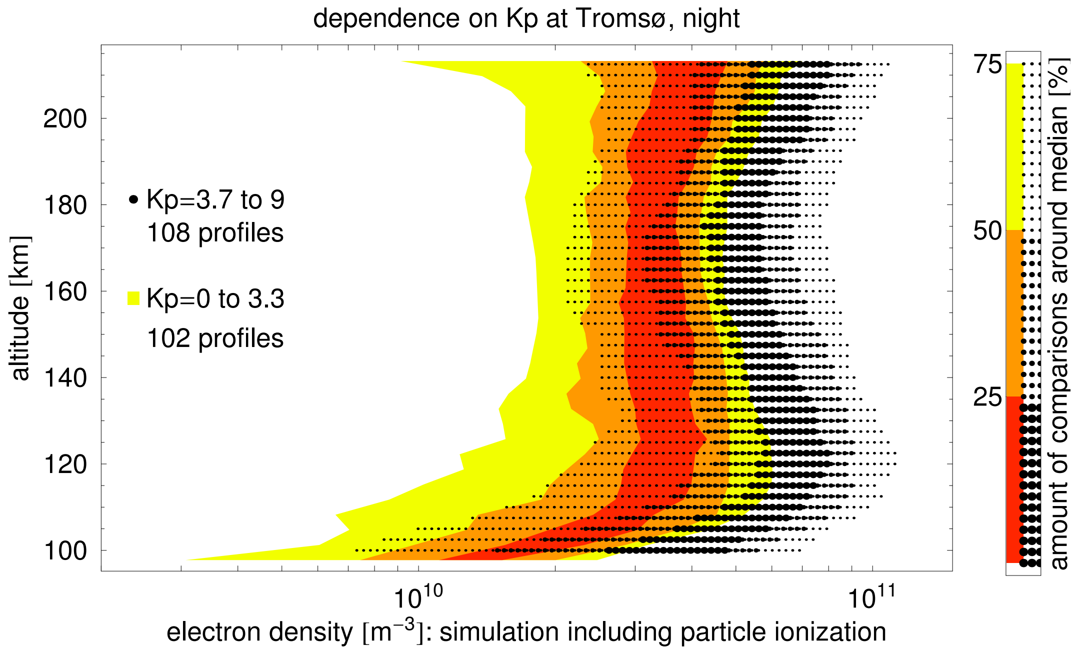

Figure 6.9: Dependence of GCM-modeled electron density on geomagnetic disturbance ($\mathrm{K_p}$-index, indicated by color) at one particular location: Tromsø.

Section 6.3.3 and Figure 6.3, top). In short, we do not expect perfect congruence, here.

The median in Figure 6.10 (bottom) is shifted to a slight underestimation (approximately factor 0.6 to 0.7) while the 50% areas renge from a ratio 0.2 to 1.3. The discrepancy seems to be independent of the $\mathrm{K_p}$ value. Anyway, the congruence is not perfect but compared to simulations without particle forcing it still gives a tremendous improvement in the electron density modeling.

One of the problems for the proper simulation of electron densities is the high temporal variability of geomagnetic activity. It should be expected that the model chain accuracy is better during periods of more or less constant $\mathrm{K_p}$ as the position of the auroral oval remains unchanged in this case. Results for the auroral oval (Tromsø) are shown in Figure 6.12. There appears to be a small dependence of the model accuracy on the change rate of $\mathrm{K_p}$, favoring small/no changes in particular at altitudes above 140 km. However, the tendency is small and the number of profiles is too small to give a definite answer here. In the case of locations other than Tromsø no dependency on the $\mathrm{K_p}$ change rate could be identified.

A plausible reason is that the $\mathrm{K_p}$ is a 3 h mean index while most of the changes are on much smaller time scales (see Figure 6.3). Given that full orbits of satellite data are used in the AIMOS model, using an index with higher temporal resolution is not practicable apart from the fact that there is no suitable one-hour index.

6.4.3 Overall quantitative Agreement

Figure 6.11 shows percentiles of the ratio between $\rho_{\mathrm{e}\oplus}$ and $\rho_{\mathrm{e\,ISR}}$ for night-time only (top), and for day-time only (bottom), respectively. The whole data set is included. At night more than 60% of the profiles have ratios between 0.2 and 1.4. The median shows no significant altitude dependence (approximate ratio 0.7 to 0.8). In contrast, for day-time, the median depends on altitude. Starting at 0.8 at 100 km, it significantly increases above 150 km, reaching a ratio of 1.5 at 205 km. For most altitudes the spread of the ratios is significantly smaller at day-time than at night.

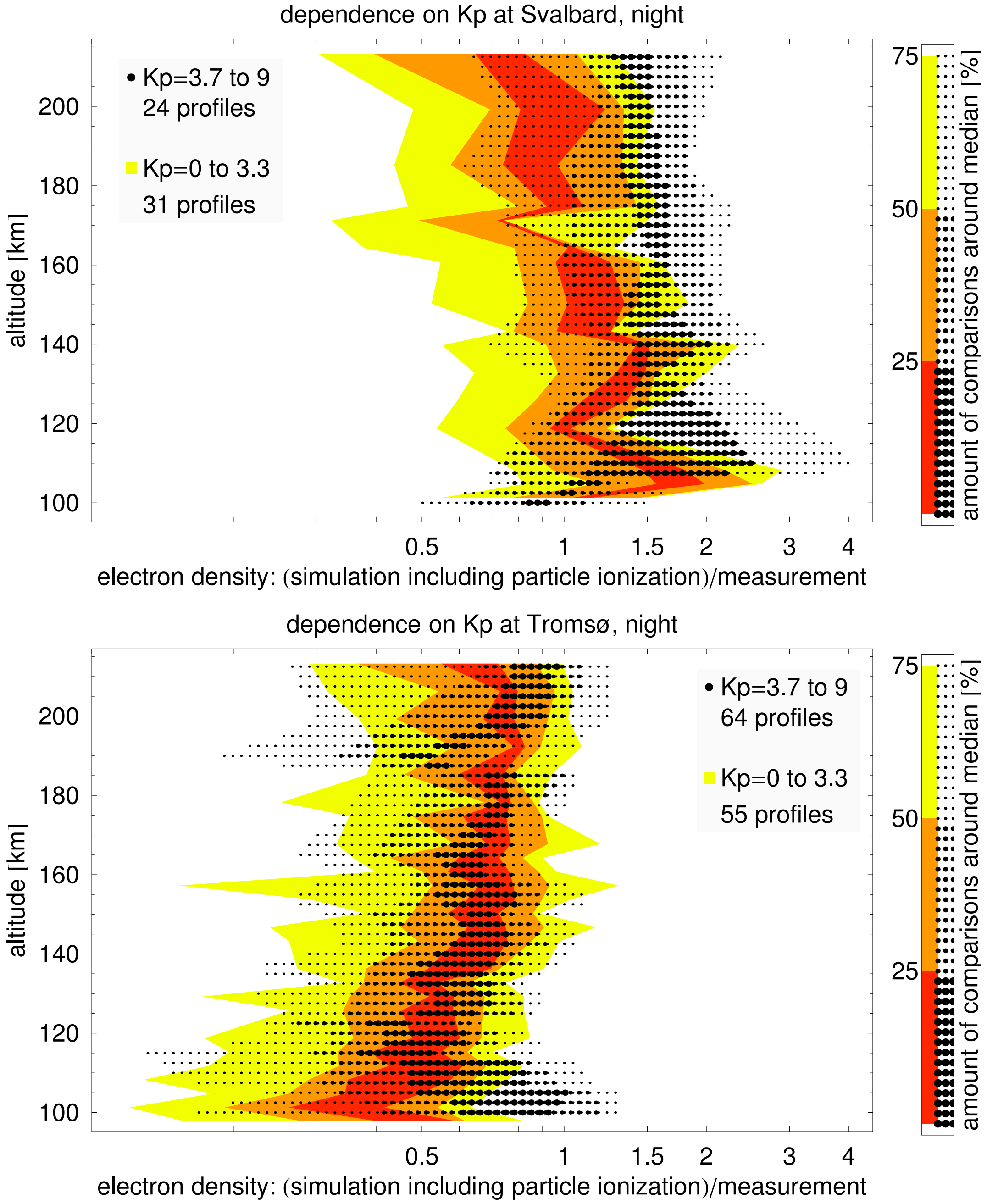

Figure 6.10: Ratio of the $\rho_{\mathrm{e}\oplus}$ and the corresponding $\rho_{\mathrm{e\,ISR}}$ at two different locations: Svalbard (top) and Tromsø (bottom). The dashed line indicates the median of all ratios at the specific location.

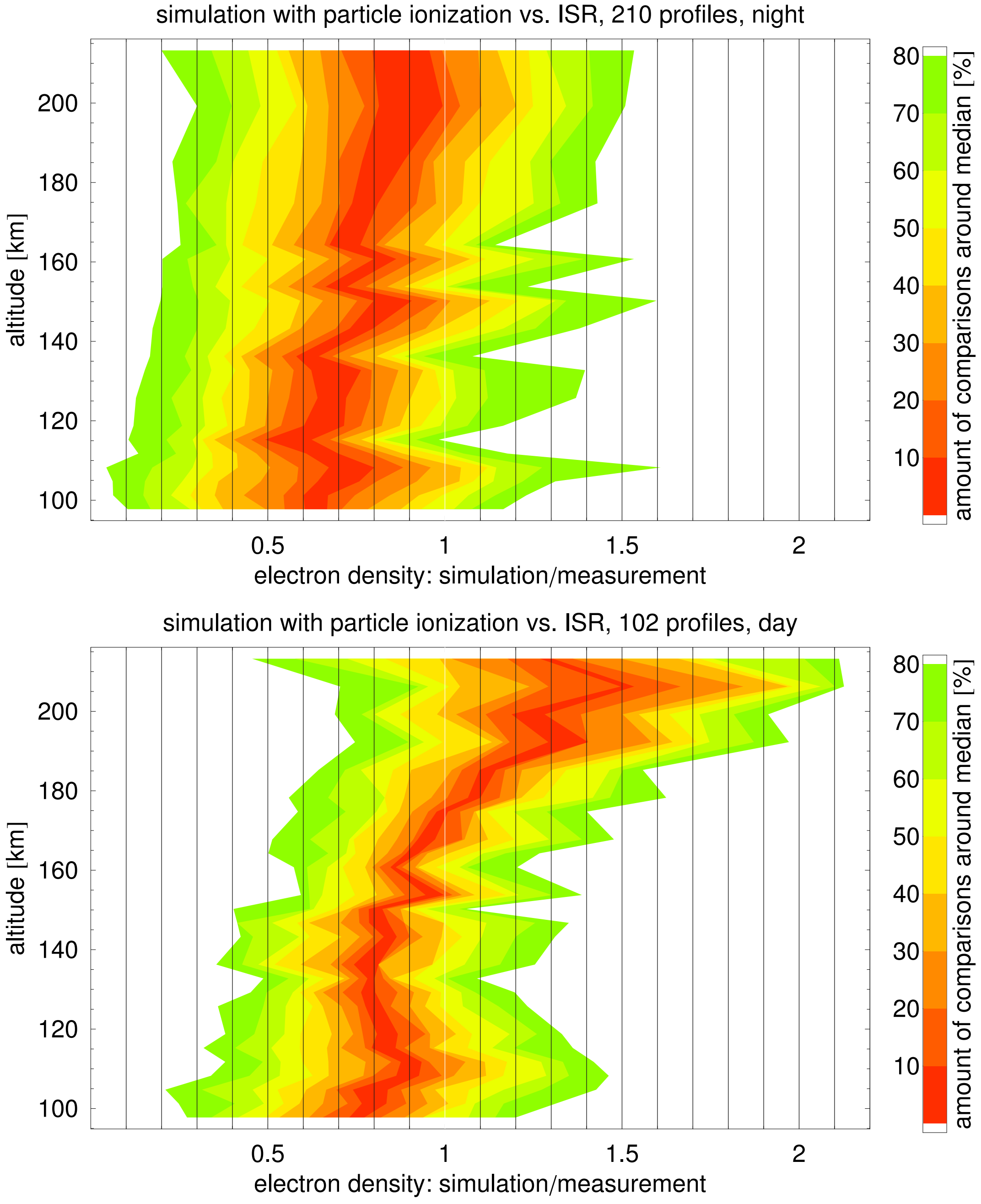

Figure 6.11: Percentiles of the $\rho_{\mathrm{e}\oplus}$ over $\rho_{\mathrm{e\,ISR}}$ ratios around the median values for night (top) and day-time (bottom) profiles. Light gray indicates the median.

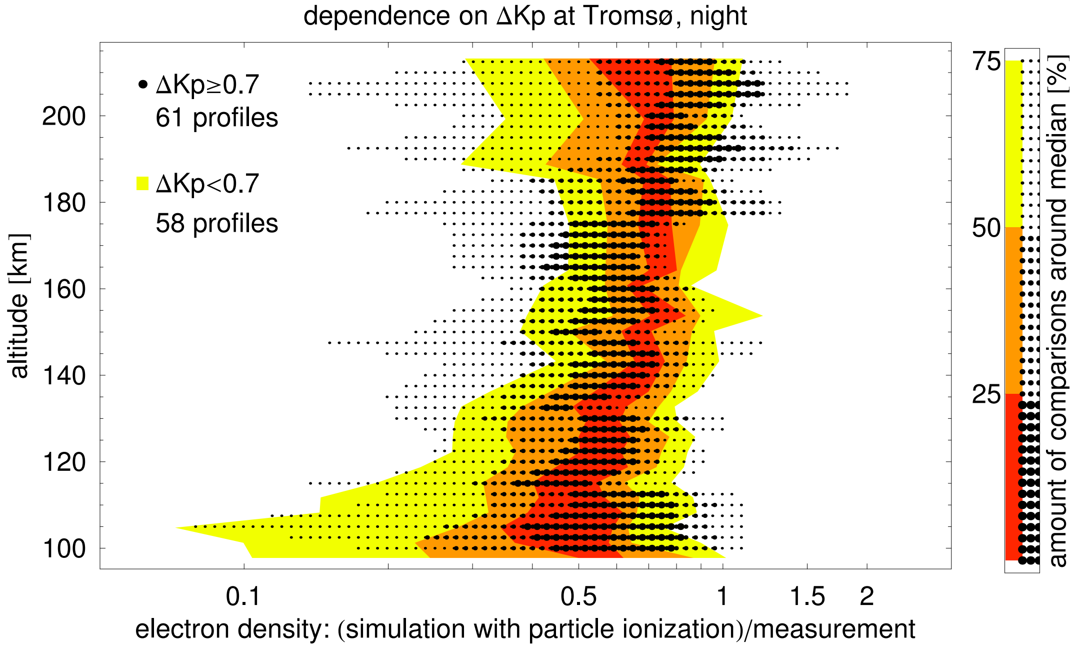

Figure 6.12: Ratio of the profiles at Tromsø are colored corresponding to the change in K_p over 6 h, calculated as $\frac{1}{2}(|\mathrm{Kp}_{-3\mathrm{h}} - \mathrm{Kp}_{current}| + |\mathrm{Kp}_{current} - \mathrm{Kp}_{+3\mathrm{h}}|)$.

6.5 Summary and Conclusions

With the coupling of the AIMOS and HAMMONIA models we have developed a tool to study effects of particle precipitation in the entire atmosphere. In this study, we evaluated the model performance with respect to particle induced ionization in the thermosphere. GCM-simulations without particle forcing (for instance HAMMONIA without AIMOS) are confronted with the following problems: (1) Electron density derived by radar measurements almost always exceeds GCM-modeled electron density. (2) The deviation of GCM-modeled and ISR-modeled electron density is most prominent at night; easily differing by 3 orders of magnitude. Day-time deviations just show deviations of up to one order of magnitude. (3) The ratios between simulated and observation-based electron densities show a spread of more than 3 orders of magnitude, reflecting the different night and day-time behavior.

The model chain AIMOS-HAMMONIA allows the simulation of spatially resolved electron densities corresponding to the local particle precipitation. Different ISR stations are used to compare these results to measurements. The most significant benefit of the model chain is shown in Figure 6.6: (1) The average ratio of ISR-modeled and AIMOS-HAMMONIA-modeled electron density is close to 1 at day and night. (2) The spread of the ratios between $\rho_{\mathrm{e\,ISR}}$ and $\rho_{\mathrm{e}\oplus}$ is an order of magnitude smaller than the spread of $\rho_{\mathrm{e\,ISR}}$ over $\rho_{\mathrm{e}\oslash}$.

In more detail, the main aspects of this paper can be summarized as follows.

6.5.1 Day/Night

Strongest deviations between observation-based and simulated electron densities occur at night but the agreement is much better when particle forcing is included. By doing this, the ratio of $\rho_{\mathrm{e\,ISR}}$ and the electron density derived from the GCM-simulation improved by 2 to 3 orders of magnitude at night. This confirms that during night-time at polar latitudes the largest part of the ionization is caused by particles. In terms of overall quantitative agreement, Fig. 6.11 shows that for all altitudes at least 60% of the night-time ratios

($\rho_{\mathrm{e}\,\oplus}$/$\rho_{\mathrm{e\,ISR}}$) are between 0.2 and 1.4. In contrast to night-time, the median of the day-time ratios ($\rho_{\mathrm{e}\,\oplus}$/$\rho_{\mathrm{e\,ISR}}$) depends on altitude. This may indicate a systematic effect of sunlight.

6.5.2 Different Latitudes

Even though the particle precipitation shows strong latitudinal dependence, followed by a GCM-modeled variation of 1 order of magnitude in electron density in the observed night-time period, the median of the ratio of $\rho_{\mathrm{e\,ISR}}$ and $\rho_{\mathrm{e}\,\oplus}$ is close to 1 in the polar cap and approximately 0.6 to 0.7 (slight underestimation, see Figure 6.8, top) in auroral latitudes, respectively.

6.5.3 Geomagnetic active/inactive Periods

Ratios of $\rho_{\mathrm{e\,ISR}}$ and $\rho_{\mathrm{e}\,\oplus}$ at auroral latitudes (see Figure 6.10, bottom) show no significant dependence on geomagnetic activity, even though the GCM-modeled electron density ($\rho_{\mathrm{e}\,\oplus}$) is modulated by $\mathrm{K_p}$ in the range of 1 order of magnitude. The ratio within the polar cap shows a slight overestimation (in case of the median it is a factor of 1.5) of the GCM-modeled electron density at high $\mathrm{K_p}$-values. The median of the total ratios still is at approximately 1.

6.5.4 Limitations and final Evaluation

The comparison with observation-based data also revealed deficiencies of our approach to simulate electron densities. However, we have to note that (1) the temporal resolution, based on satellite measurements, (2) spatial mapping, as given by the ionization model due to limited satellite data, (3) the omission of actual thermospheric weather conditions in the model, and (4) occasional quality control problems in the ISR measurements complicate the comparison. In addition different theoretical models to derive the ISR-measured electron density (as, e.g., at Sondrestrom) give some range for interpretations.

Overall, it can be stated that the model-chain AIMOS-HAMMONIA is able to produce useful electron density fields in terms of absolute concentrations as well as their dependence on day-time, geomagnetic latitude and activity. We highly recommend the inclusion of such an approach to particle induced ionization in thermospheric modeling in order to avoid problems in chemistry and dynamics resulting from omission or incorrect representation of precipitating particles.

Acknowledgments

This work was supported by the Deutsche Forschungsgemeinschaft DFG under contracts DFG-Ka1297/7-1, DFG-Ka1297/8-1, and DFG-SCHM2158/1-(1-3).

EISCAT is an international association supported by research organizations in China (CRIRP), Finland (SA), Germany (DFG), Japan (NIPR and STEL), Norway (NFR), Sweden (VR), and the United Kingdom (NERC).

The Sondrestrom ISR facility is supported by the US National Science Foundation under Cooperative agreement AGS-0836152.

Radar observations and analysis at Millstone Hill are supported under Cooperative Agreement with the Massachusetts Institute of Technology by the US National Science Foundation.

The numerical simulations have been performed at and with support from the German Climate Computing Centre (DKRZ).

location	period	time [UTC] and Madrigal identification code
Tromsø	2003 Oct	6 18h tau1-vhfa, 6 20h tau1-vhfa, 6 22h tau1-vhfa, 13 10h tau1-uhf, 13 12h tau1-uhf, 13 18h tau1-vhf, 13 20h tau1-vhf, 13 22h tau1-vhf, 15 6h tau1-vhf, 15 8h tau1-vhf, 15 10h tau1-vhf, 16 10h tau1-uhf, 21 14h tau1-uhf, 21 16h tau1-uhf, 21 18h tau1-uhf, 21 20h tau1-uhf, 21 22h tau1-uhf, 22 0h tau1-uhf, 22 8h tau1-uhf, 22 10h tau1-uhf, 22 12h tau1-uhf, 22 14h tau1-uhf, 22 16h tau1-uhf, 22 18h tau1-uhf, 22 20h tau1-uhf, 22 22h tau1-uhf, 23 0h tau1-uhf, 23 2h tau1-uhf, 23 4h tau1-uhf, 23 6h tau1-uhf, 23 8h tau1-uhf, 23 10h tau1-uhf, 23 12h tau1-uhf, 23 14h tau1-uhf, 24 10h tau1-vhf, 24 10h tau2pl-uhf, 24 12h tau1-vhf, 24 12h tau2pl-uhf, 24 14h tau1-vhf, 24 14h tau2pl-uhf, 24 16h tau1-vhf, 24 18h tau1-vhf, 24 22h tau1-vhf, 24 22h tau2pl-uhf, 25 0h tau1-vhf, 25 0h tau2pl-uhf, 25 2h tau1-vhf, 25 2h tau2pl-uhf, 25 4h tau1-vhf, 25 4h tau2pl-uhf, 25 6h tau1-vhf, 25 6h tau2pl-uhf, 25 8h tau1-vhf, 25 8h tau2pl-uhf, 25 10h tau1-vhf, 25 10h tau2pl-uhf, 25 12h tau1-vhf, 25 12h tau2pl-uhf, 25 14h tau1-vhf, 25 16h tau1-vhf, 25 18h tau1-vhf, 25 18h tau2pl-uhf, 25 20h tau1-vhf, 25 20h tau2pl-uhf, 28 10h arcd-vhf, 28 12h arcd-vhf, 28 14h arcd-vhf, 28 16h arcd-vhf, 28 18h arcd-vhf, 28 20h arcd-vhf, 29 12h arcd-vhf, 29 14h arcd-vhf, 29 18h arcd-vhf, 29 20h arcd-vhf, 29 22h arcd-vhf, 30 0h arcd-vhf, 30 2h arcd-vhf, 30 2h tau2pl-uhf, 30 4h arcd-vhf, 30 4h tau2pl-uhf, 30 6h arcd-vhf, 30 6h tau2pl-uhf, 30 8h arcd-vhf, 30 8h tau2pl-uhf, 30 10h arcd-vhf, 30 10h tau2pl-uhf, 30 12h arcd-vhf, 30 12h tau2pl-uhf, 30 14h arcd-vhf, 30 14h tau2pl-uhf, 30 16h arcd-vhf, 30 16h tau2pl-uhf, 30 18h tau2pl-uhf, 30 20h arcd-vhf, 30 20h tau2pl-uhf, 30 22h arcd-vhf, 30 22h tau2pl-uhf, 31 0h arcd-vhf, 31 2h arcd-vhf, 31 4h arcd-vhf, 31 6h arcd-vhf, 31 8h arcd-vhf, 31 10h arcd-vhf, 31 12h arcd-vhf, 31 14h arcd-vhf, 31 18h arcd-vhf, 31 20h arcd-vhf, 31 22h arcd-vhf
	2003 Nov	1 2h arcd-vhf, 1 2h tau2pl-uhf, 1 4h arcd-vhf, 1 4h tau2pl-uhf, 1 6h arcd-vhf, 1 6h tau2pl-uhf, 1 8h arcd-vhf, 1 8h tau2pl-uhf, 1 10h arcd-vhf, 1 10h tau2pl-uhf, 1 12h arcd-vhf, 1 12h tau2pl-uhf, 1 14h arcd-vhf, 1 14h tau2pl-uhf, 1 16h arcd-vhf, 1 16h tau2pl-uhf, 1 18h arcd-vhf, 1 18h tau2pl-uhf, 1 20h arcd-vhf, 1 20h tau2pl-uhf, 1 22h arcd-vhf, 1 22h tau2pl-uhf, 2 0h arcd-vhf, 2 0h tau2pl-uhf, 2 2h arcd-vhf, 2 4h arcd-vhf, 2 4h tau2pl-uhf, 2 6h arcd-vhf, 2 6h tau2pl-uhf, 2 8h arcd-vhf, 2 8h tau2pl-uhf, 15 6h tau1-vhf, 15 10h tau1-vhf, 23 20h tau2pl-uhf, 23 22h tau2pl-uhf, 26 2h tau2pl-uhf, 26 4h tau2pl-uhf
	2003 Dec	5 18h arc1-uhf, 16 18h tau8-vhf, 17 0h tau8-vhf, 17 6h tau8-vhf, 17 12h tau8-vhf, 17 18h tau8-vhf, 18 0h tau8-vhf, 18 6h tau8-vhf, 18 12h tau8-vhf
	2004 Jan	14 12h tau1-uhf, 16 6h tau1-uhf, 16 12h tau8-vhf, 17 6h tau1-uhf, 18 6h tau1-uhf, 19 6h tau1-uhf, 21 12h tau1-uhf, 23 12h tau1-uhf
	2004 Feb	11 12h tau1-vhfa, 18 18h tau2pl-uhf, 18 18h tau8-vhf, 19 0h tau1-vhfa, 21 0h tau8-vhf, 22 0h arcd-vhf, 23 12h tau1-vhfa, 25 0h tau8-vhf
	2004 Mar	1 12h tau8-vhf, 4 18h tau1-uhf, 5 0h tau1-uhf, 5 6h tau2pl-uhf, 27 18h tau2pl-uhf, 28 18h tau2pl-uhf, 29 12h tau8-vhf, 29 18h tau8-vhf, 30 0h tau8-vhf, 30 6h tau8-vhf, 30 12h tau8-vhf, 30 18h tau8-vhf
	2004 Apr	1 6h tau8-vhf, 1 12h tau8-vhf, 1 18h tau8-vhf, 25 6h tau8-vhf, 28 12h tau8-vhf
Svalbard	2003 Oct	6 18h tau0-32m, 6 18h tau0-42m, 6 20h tau0-32m, 6 20h tau0-42m, 6 22h tau0-32m, 13 22h tau0-32m, 13 22h tau0-42m, 15 8h tau0-32m, 15 8h tau0-42m, 15 10h tau0-32m, 15 10h tau0-42m, 21 10h tau0-42m, 21 12h tau0-42m, 21 14h tau0-42m, 21 16h tau0-42m, 21 18h tau0-42m, 21 20h tau0-42m, 21 22h tau0-42m, 22 0h tau0-42m, 22 2h tau0-42m, 22 4h tau0-42m, 22 6h tau0-42m, 22 10h tau0-42m, 22 12h tau0-42m, 22 20h tau0-42m, 22 22h tau0-42m, 23 0h tau0-42m, 23 2h tau0-42m, 23 4h tau0-42m, 23 6h tau0-42m, 23 10h tau0-42m, 23 12h tau0-42m, 25 12h tau0-32m, 25 12h tau0-42m, 25 14h tau0-32m, 25 14h tau0-42m, 25 16h tau0-32m, 25 16h tau0-42m, 25 18h tau0-32m, 25 18h tau0-42m, 25 20h tau0-32m, 25 20h tau0-42m
	2003 Nov	4 12h tau0-32m, 4 12h tau0-42m, 23 22h arc1-42m, 24 0h arc1-42m, 26 10h tau0-32m, 26 12h tau0-32m, 27 8h tau0-32m, 27 10h tau0-32m, 27 12h tau0-32m
	2003 Dec	13 12h tau0-32m, 19 12h tau0-42m, 20 6h tau0-42m, 20 12h tau0-42m, 21 6h tau0-42m, 21 12h tau0-42m, 22 6h tau0-42m
	2004 Jan	17 6h tau0-42m, 18 6h tau0-32m, 19 0h arc1-42m, 20 6h tau0-32m, 20 12h tau0-32m
	2004 Feb	11 12h tau0-42m, 28 0h tau0-42m
	2004 Mar	1 12h tau0-42m
Sondrestrom	2003 Oct	29 12h 009, 29 14h 009, 29 16h 009, 29 18h 009, 29 20h 009, 29 22h 009, 30 0h 009, 30 4h 014, 30 6h 014, 30 8h 014, 30 10h 014, 30 12h 014, 30 14h 014, 30 16h 014, 30 18h 014, 30 20h 014, 30 22h 009, 31 0h 009, 31 2h 009, 31 4h 009, 31 6h 009, 31 8h 009
	2003 Nov	19 14h 008, 19 14h 010, 19 16h 008, 19 16h 010, 19 18h 008, 20 14h 014, 20 14h 015, 20 16h 014, 20 20h 014, 20 22h 014, 21 8h 008, 21 10h 008, 21 12h 008, 21 12h 009, 21 14h 008, 21 14h 009, 21 16h 008, 21 18h 008, 21 18h 009
	2004 Jan	13 6h 003, 15 0h 001, 15 0h 003, 15 0h 005, 15 0h 007, 22 6h 011, 22 18h 015, 23 0h 015, 23 18h 015
	2004 Mar	16 0h 007, 16 12h 007
Millstone Hill	2004 Feb	3 18h 002, 13 18h 002, 20 18h 002
	2004 Mar	1 18h 002
	2004 Apr	5 18h 002, 16 18h 002, 27 18h 002

Table 6.2: List of all used ISR measurements. The time indicates the end of the according 1 h integration interval. All *arcd-uhf* profiles are multiplied by 1.9 to correct the faulty scaling during this period. Note that this table is appended as auxiliary material in *Wissing et al.* (2011).

Chapter 7

Assumptions, Limitations and Errors

This Chapter describes the errors and uncertainties affecting the *Atmosphere Ionization Module OSnabrück* and thus determine its reliability. The AIMOS produces three dimensional output. Errors may concern the total ionization rates itself as well as their spatial (horizontal and vertical) allocation. The model consists of an empirical and a physical subroutine. While statistical errors in the Monte Carlo calculations can be used to describe the accuracy of the physical subroutine, the reliability of the empirical part has to be determined by comparisons to satellite measurements. In combination these errors define the accuracy of the AIMOS model.

However, the ionization rates also depend on input data quality. Due to significant input data limitations (first of all spatial coverage, but also angular distribution and quality in general) the results are affected. In addition we had to make a number of assumptions, most of them in consequence of incomplete data coverage.

	AIMOS	
	`Empirical model`	`Physics`
	Particle data	Input and assumptions
affecting model results	counting statistics, degradation, crosstalk, inter-calibration, orbit, data gaps, smoothing	atmosphere (temperature, composition, density), particle spectrum, isotropic angular distribution, conversion to ionization rates
	Sorting algorithm	Monte Carlo simulation
defining the model accuracy	identification of cell	statistical error

Table 7.1: Overview on assumtions and limitations that affect the accuracy of the AIMOS model.

Table 7.1 lists the main aspects that impact the accuracy of the AIMOS model. The parts that define the accuracy of the model itself will be discussed in Section 7.1. Data limitations and assumptions influencing the results but not the model itself will be discussed in Section 7.2.

7.1 Model Reliability Analysis

Within the scope of this work a model has been developed that consisting of an empirical part, that is a sorting algorithm describing the horizontal pattern of precipitating particles, and a numerical part, that is a Monte Carlo simulation dealing with the interaction of particles and atmosphere. In the first part the accuracy can be estimated by a comparison to satellite measurements while the error of the second part can be determined statistically. The development of both parts is the main aspect of this work. Errors which origin from these parts are relevant for the model.

7.1.1 Sorting Algorithm

Assuming that a sorting algorithm based on mean precipitation maps is capable of describing the spatial pattern of particle precipitation, we can describe the expected error of the sorting algorithm.

Depending on the way the ionization rates will be used there are two different approaches to analyze the expected error. On the one hand we can select a geographic location and look for the relative deviation between model and satellite data. Unfortunately a direct comparison of particle flux at the same position is delicate. A small aberration from the latitudinal bin may cause a variation on four orders of magnitude – even in geomagnetic quiet time. And as this method will always compare mean values of a certain period to direct measurements, the variable magnetosphere will never be in the same state. Accordingly the relative error will be in any order and the significance is exiguous. Using ground based radar measurements the temporal variation can be reduced but other aspects, such as the transformation of the ionization rates into electron density by a GCM and the radar measurements itself, limit the accuracy of that kind of comparison. As Chapter 6 discusses this topic in detail, we will focus on the second approach, which is a comparison of satellite data and modeled AIMOS particle flux along the satellite track. This kind of analysis gives information on the positions of precipitation zones and it allows a quantitative comparison.

Detection of Oval Positions

The most delicate aspect in modeling spatial particle precipitation is the variable position of the auroral oval. In this model the position is given by the empirically determined mean precipitation maps that are selected corresponding to the recent K_p-value. Therefore the recent position of the auroral oval (and the spatial particle distribution outside the polar caps in general) is defined by the K_p-index. As recent NOAA POES-15 and 16 measurements are used for the scaling, but not in order to locate the precipitation zones, we can use them to compare the auroral oval position. The position depends on particle species and energy. Consequently this comparison will be done for every spatially resolved (TED and MEPED) channel.

In more detail, we compare the positions where the intensity jumps up as the satellite enters the oval and, respectively, drops down while leaving it. Without making a qualitative extract the comparison can be simplified by using orbits with polar cap crossing* only. The increase in intensity can be a successive rise extending over some latitudinal bins or a sudden boost between two adjacent bins containing (more or less) the total increase. We will focus on the sudden jump as the expected deviations are most serious here. A second reason to look for sudden rise is, that its position can be checked more easily, whereas the position of a gradual rise comprehends new sources of error. Multiplying the maximum flux increase in satellite data and the maximum flux increase in the model during each auroral oval crossing, the orbits have been sorted corresponding to sudden jump and successive rise. We selected two-thirds of the orbits, starting from the most intense sudden jump. As

---

*orbit inclination as well as the shifted position of the magnetic poles allow for some orbits without polar cap crossing

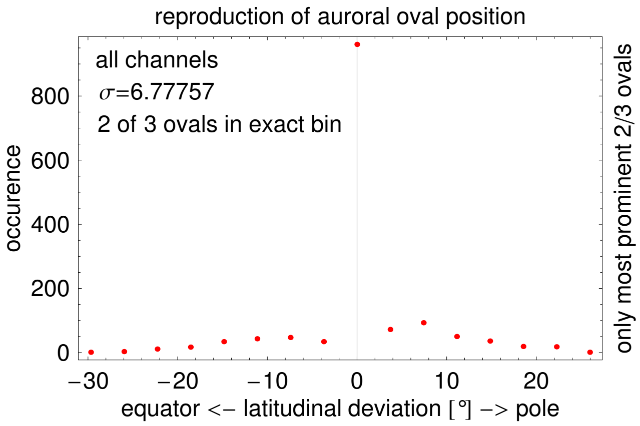

Figure 7.1: Comparison of the auroral oval positions in AIMOS and in the N15 and N16 satellite data. In 2/3rd of the comparisons we found no latitudinal deviation of the auroral position. (Further explanation in corresponding paragraph.)

shown in Figure 7.1 the entry into and the exit of the auroral oval will be reproduced in the correct bin in two of three cases. This result is based on one day within a geomagnetically quiet period (doy 51, 2003) as well as on one day in an active period (doy 302, 2003).

In some cases very huge position discrepancies were detected. We assume that the detection algorithm of the error analysis was not able to find the correct positions here. This may be reasoned by strong fluctuations of the satellite particle flux.

Given that the satellite's oval position represents a 16 s mean and the AIMOS position is based on longer time-scales, we do not expect a much better accuracy.

Correlation along Satellite Track

Very similar to the approach in Section 7.1.1, we use the particle flux along a satellite's track for a linear (Pearson) correlation to the modeled particle flux. As the satellites will pass over various precipitation regions of the model, all flux measurements within a region will be transformed into a mean, allowing a better comparison to the modeled value of this area. This correlation will describe the quality of the modeled precipitation pattern. (A quantitative comparison of the total flux along the track and the modeled particle flux has also been done. As the quantitative comparison was used to improve the model, it can be found in Section 4.8.) The correlation is based on one day of geomagnetical quiet times (doy 51, 2003) and on one day within the main particle event (doy 302, 2003). For both settings, all TED and MEPED channels on the satellites NOAA POES-15 and 16 have been used.

In general, we expect that precipitation pattern during geomagnetically quiet (and thus more constant) circumstances can be described more accurately by AIMOS. The reason is that auroral latitudes at quiet conditions are not associated with high temporal flux variability. That is why the 3 hourly K_p-index and the 2 h AIMOS time-resolution, which is needed for a full orbit, cover the same (and stable) geomagnetic condition.

Please note that precipitation of high-energetic SEPs (arriving at Earth prior to the geomagnetic shock) is located at the polar cap and is determined by current measurements only. These periods definitely show strong flux variances in the polar cap but as they are treated differently in AIMOS their precipitation will not affect this comparison. However, the modeled particle precipitation at the boundary of the polar cap is determined by the mean precipitation maps and therewith depends on K_p. An increased particle flux in this area can be interpreted as an increased size of the polar cap. Consequently the modeled particle flux in the extended polar cap may differ from measured polar cap values, in particular in the period prior to the geomagnetic shock. As the amount of latitudinal bins inside the extended polar cap is limited (1 to 3) the effect on the comparison is negligible.

Results of the comparison are listed in Table 7.2. Some of the results stand out from the general tendency of good correlation in quiet periods. Focusing on the MEPED high energy electrons (especially mep0e3) and the most energetic spatial-resolved proton channels mep0P4 and mep0P5, the correlation in disturbed conditions clearly surmounts quite time

		correlation	
channel	satellite	geomagnetic quiet	geomagnetic active
TEDElectronBand4	N15	0.77	0.47
	N16	0.83	0.60
TEDElectronBand8	N15	0.71	0.50
	N16	0.75	0.59
TEDElectronBand11	N15	0.60	0.45
	N16	0.30	0.34
TEDElectronBand14	N15	0.81	0.56
	N16	0.50	0.34
mep0e1-e2	N15	0.68	0.76
	N16	0.31	0.59
mep0e2-e3	N15	0.48	0.64
	N16	0.70	0.69
mep0e3	N15	0.55	0.83
	N16	0.75	0.82
TEDProtonBand4	N15	0.76	0.58
	N16	0.65	0.55
TEDProtonBand8	N15	0.66	0.41
	N16	0.71	0.70
TEDProtonBand11	N15	0.64	0.86
	N16	0.71	0.80
TEDProtonBand14	N15	0.78	0.85
	N16	0.81	0.83
mep0P1	N15	0.82	0.52
	N16	0.78	0.71
mep0P2	N15	0.82	0.61
	N16	0.75	0.60
mep0P3	N15	0.81	0.69
	N16	0.86	0.63
mep0P4	N15	0.66	0.91
	N16	0.66	0.93
mep0P5	N15	0.28	0.92
	N16	0.22	0.94

Table 7.2: Linear correlation of the AIMOS sorting-algorithm and satellite measurements along the track for 24 h within geomagnetical quiet and active periods, respectively. As POES-15 and 16 are used separately, a significant difference between the two correlation factors may indicate accidental correlation, e.g. noisy mep0e3 data during geomagnetically quiet times.

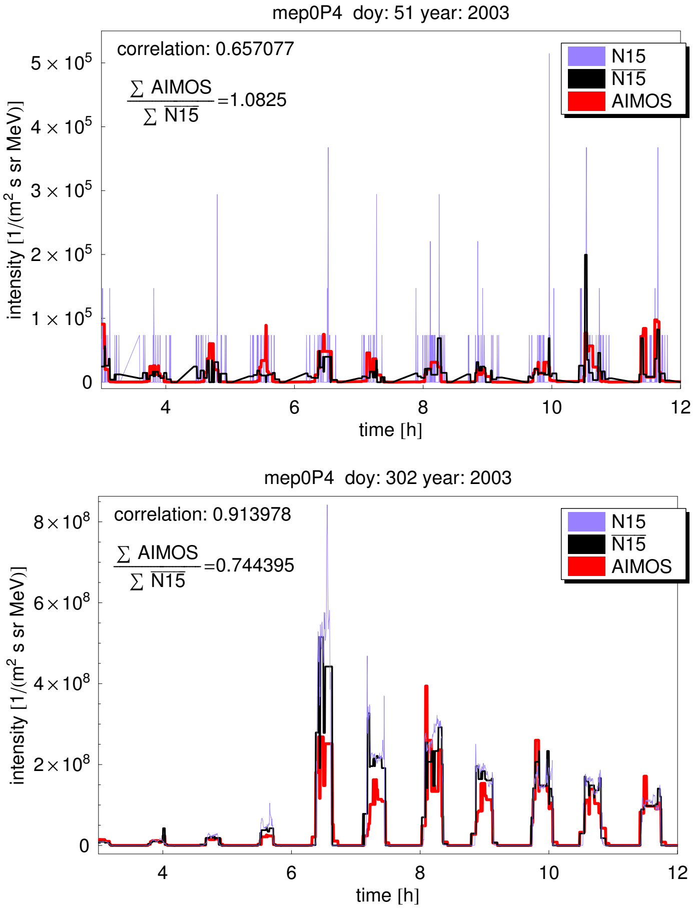

Figure 7.2: NOAA-15 high energy proton channel mep0P4. The green curve shows satellite particle flux at 16 s resolution. The black line is a mean value for satellite data within characteristic precipitation areas while the red curve shows the AIMOS simulation results for these areas. (top) geomagnetic quiet period (doy 51, 2003): the 16 s satellite data (green) has rather bad statistics – and therefore bad correlation with simulated values. (bottom) particle event (doy 302, 2003): 16 s satellite data (green) shows better statistics – due to increased count rates as well as more simple precipitation pattern – followed by good correlation.

correlation. Reasons are twofold: (1) temporal averaging in geomagnetic quiet periods is too short to gain statistically reasonable values for the high energies (see Figure 7.2, top, noisy data), while the significantly increased particle flux within a particle event gives much better statistics (see Figure 7.2, bottom). Noisy data will decline the correlation tremendously. (2) High energetic solar particles precipitate homogeneously within the polar cap which can be reproduced easier (see also Figure 7.2, bottom) than the complex structure of the auroral oval which results in a narrow double-peak pattern in the data (see Figure 7.3).

Some of the correlations in the TED channels have to be treated with care: an unexpected good correlation in Table 7.2 has been observed for TEDProtonBand11 and 14 in geomagnetic active period. This correlation is artificial as these channels are contaminated by crosstalk of high energetic electrons (private communication David Evans, NOAA). The correlation factors of the high energetic electron channel mep0e3 are very much the same and, due to the more simple precipitation pattern of high energetic particles, followed by high correlation factors. Given by low mep0e3 particle flux in geomagnetic quiet times (noisy data, as shown for protons in Figure 7.2, top), this effect is mostly limited to particle events.

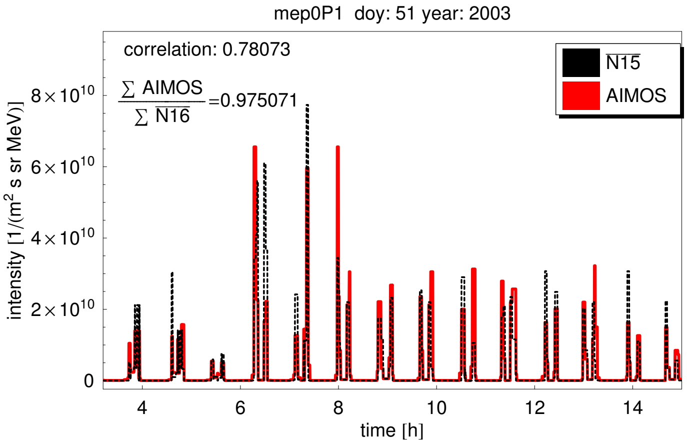

Figure 7.3: Typical temporal pattern of low-energy channels: The double-peak structure indicates auroral oval crossings. The exact position of the peaks is subject to small variations. This variation has the decisive role in correlating satellite data and AIMOS.

However, quite time contamination can not be excluded completely. Since we have no better particle instruments and there are no corrections for electron contamination, we have to use these channels as-is. More information on crosstalk can be found in Section 7.3.3.

The reason for the bad correlation for TEDElectronBand11 and mep0e1-e2 from NOAA-16 for this period is still unknown.

7.1.2 Monte Carlo Simulation

The atmospheric ionization rate is given by the energy deposition of a GEANT4-based Monte Carlo model and its conversion into ion pair production with a constant factor (see Section 7.2.2). We will concentrate on the Monte Carlo model first. While the physical aspects e.g. accuracy of interaction cross-sections are handled by GEANT4 (*Agostinelli et al.*, 2003) and are checked against empirical data, our main concern are statistics: “Can we generate statistical relevant results based on the number of injected particles?”

In theory, the amount of particles which is needed for a statistical relevant result should increase with the number of possible processes. The number depends on the probability of rare processes.

At first the statistical error of mono-energetic particle beams will be discussed. As a total particle spectrum is a composition of mono-energetic beams with a special energy-specific weighting they will be discussed accordingly. Given that a particle spectrum includes various incident angles, the simulation has to cover these with a certain angular resolution. Since a high incident angle (0° indicates vertical) shifts the energy deposition to higher altitudes, the statistical accuracy of different angular resolutions will be discussed in this Section (see below).

Statistical Error: mono-energetic Beams

The Monte Carlo model results are based on a specific number of injections (protons and alpha particles: 100, electrons: 10000) at each energy and direction. Sample tests will show the statistical relevance of these mono-energetic beams. The generation of bremsstrahlung will be considered in electron interactions. Since bremsstrahlung has a small interaction cross-section the increased number of particles reduces statistical effects. The species-specific injection number represents an ensemble. We are interested in the standard deviation using 1000 different ensembles with same energy and direction.

As anticipated the probability of interaction dominates the variation. Typical aspects defining the probability of an interaction are: the density of the atmosphere and therewith the amount of possible collision partners, the speed of the particle which defines the time span during which the energetic particle may interact with matter and the kind of interaction process itself. A more detailed description follows.

Even though the impact on a combined particle spectrum is very limited the most obvious statistical errors occur below the primary particle's range. Given that these altitudes are affected by rare secondary processes, e.g. bremsstrahlung or limited numbers of secondary electrons, the total amount of energy deposition in these altitudes is small and the statistical error is high (see e.g., Figure 7.5d for a 100% relative error below the primary particle's range). As the total amount of energy deposition in these altitudes is very low compared to the deposition in the main deposition altitude of that particle energy (6 orders of magnitude difference for 500 MeV protons), a combined spectrum of various energies will almost eliminate this statistical error (see below in this Section).

Density and therefore the number of interaction partners decreases with increasing altitude. For this reason the chance of an interaction is smaller in the upper atmosphere (see increasing error bars with increasing layer in Figure 7.5e and 7.5c). Concerning high energetic particles the area of enhanced energy deposition is in the lower atmosphere and it exceeds the deposition in upper layers by orders of magnitude. Figures 7.5d and 7.5f show the corresponding relative deviations. In contrast, low energetic particles deposit a dominant part of their energy in the upper atmosphere, compensating the smaller probability of an interaction due to low density. As a particle spectrum always includes various energies the combined effect will be discussed in this Section (see below).

Particle speed determines the time span during which the energetic particle may interact with matter. Low particle speed increases this period and raises the probability of an interaction. The result is shown for low energetic protons (Figure 7.4b, almost no error bar) in contrast to high energetic protons (Figure 7.5c, significant error bar at high altitudes). Hence, high energetic particles (e.g., 500 MeV protons in this simulation) exemplify the maximum expected errors.

Physical processes with small interaction cross-sections cause poor statistics. For example, energy deposition due to bremsstrahlung is less likely than due to particle collision. The high energetic electron beams include some altitude layers which are affected by bremsstrahlung only (see Figure 7.5a, layer 31 and below), while the primary particle's range is limited to layer 32. Hence this leads to poor statistics of the ionization in layer 31 and below. Layers which are dominated by bremsstrahlung (and cause a relevant part of the total energy deposition) show an error of less than 1% (see Figure 7.5a and Figure 7.5b). Layer 19 and below show a decrease in energy deposition of several orders of magnitude. These layers are considered as being non-relevant for the total energy deposition. Apart from that the relative error in this altitude is significantly increased (see Figure 7.5b).

To sum it up, the expected statistical error in monoenergetic particle beams does not exceed 3% for protons and alpha particles and 1% for electrons – as far as only relevant layers for the specific particle energy are considered. Statistical errors as seen at the end of the primary partile's range and in the upper atmosphere will be greatly reduced while folding the complete spectrum as we will see in the following paragraph.

Statistical Error of a total Particle Spectrum

A total particle spectrum consists of a sum of various single energy beams that will be weighted corresponding to the slope of the particle spectrum. The slope is described by the spectral index γ and will be discussed for four different levels ranging from -1 to -4. This includes all realistic and even some extreme spectra. Due to limited computing capacity, ensemble runs of the total particle spectrum have a reduced energy resolution. The number of discreet particle energies has been diminished by a factor of 10 compared to the resolution used in AIMOS[*]. All other parameters, e.g. the angular resolution (will be discussed in

---

[*] The standard energy resolution in AIMOS divides every order of magnitude into 40 logarithmic equidistant incident particle energies.

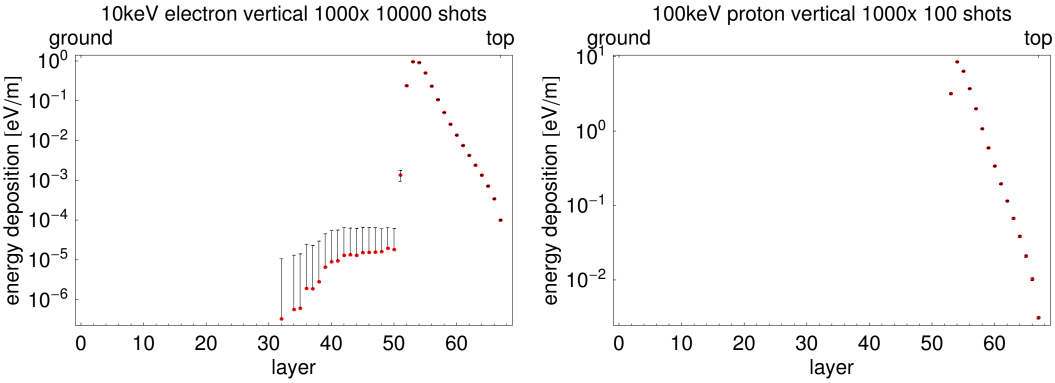

(a) each containing 10000 injections of 10 keV electrons (b) each containing 100 injections of 100 keV protons

Figure 7.4: Mean energy deposition per layer, based on 1000 ensembles and the corresponding standard deviation, indicated by error bars. Vertical injections are considered only. A missing lower error bar indicates that some ensembles show no interaction/energy deposition in that layer.

this Section, see below) and the number of injections at each energy are the same. As a consequence of the reduced energy resolution, the ensemble run will show an upper limit of the expected statistical error. Each ensemble run consists of 100 members.

particle	γ (slope of spectra)	statistical error	lower border	stat. error at layer 31-19 due to bremsstrahlung
protons	-1	$< 0.2\%$	layer 22	-
protons	-2	$< 0.2\%$	layer 22	-
protons	-3	$< 0.4\%$	layer 22	-
protons	-4	$< 0.6\%$	layer 22	-
αs	-1	$< 1.1\%$	layer 30	-
αs	-2	$< 1.1\%$	layer 30	-
αs	-3	$< 1.3\%$	layer 30	-
αs	-4	$< 1.4\%$	layer 30	-
electrons	-1	$< 0.2\%$	layer 32	$< 2\%$
electrons	-2	$< 0.2\%$	layer 32	$< 2\%$
electrons	-3	$< 0.8\%$	layer 32	$< 3\%$
electrons	-4	$< 8.2\%$	layer 32	$< 10\%$

Table 7.3: Statistical error of the energy deposition per layer for the total spectrum. The lower border is given by the used (highest) particle energies. Therefore it indicates the lowest layer which can be accurately described by the model while using the described input data set. In fact, the Monte Carlo simulation itself is not restricted to an upper energy border. Errors noted for mono-energetic particle injections in Section 7.1.2 are already included here.

As can be seen in Table 7.3 and in Figures 7.6b, 7.6c and 7.6a folding of spectra leads to reduced statistical error compared to monoenergetic runs. High statistical deviations due to rare energy deposition in some mono-energetic particle beams will be compensated by other mono-energetic particle beams which deposit most of their energy at that specific altitude.

The statistical error can be described as follows: (a) as the upper energy is restricted, high but not relevant statistical errors will persist below the range of particles with highest energy (see also above in this Section). A similar aspect can be seen for altitudes that are

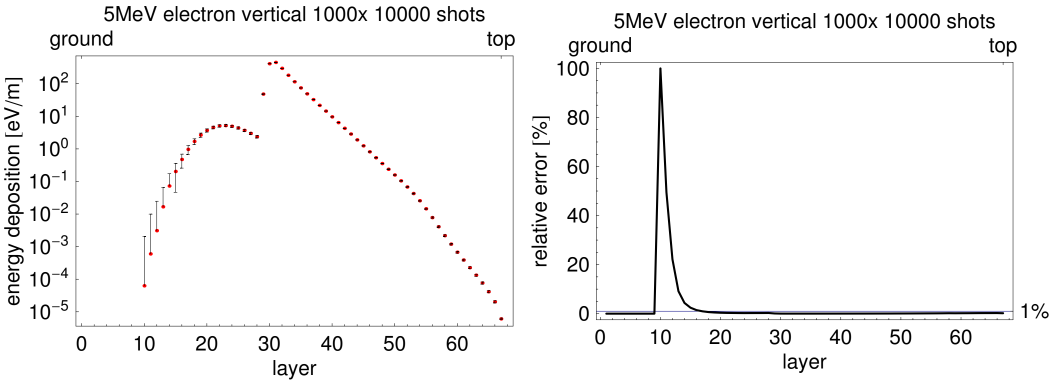

(a) mean and standard deviation: ensemble containing 10000 injections of 5 MeV electrons each

(b) relative error for scenario (a)

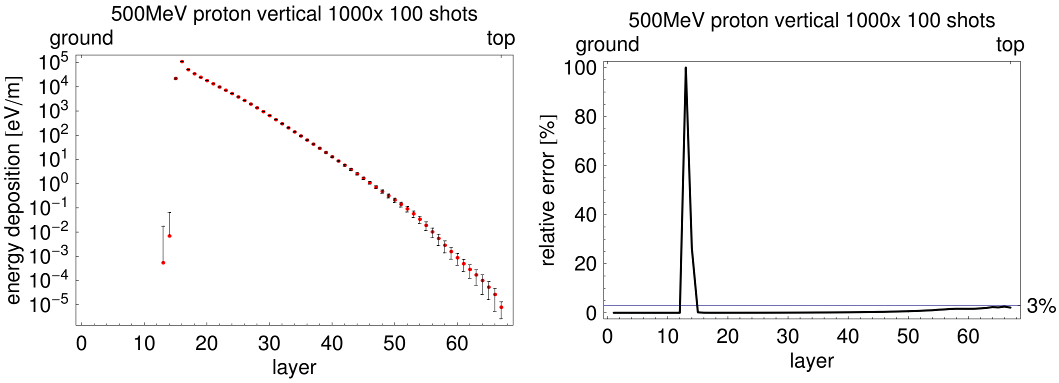

(c) mean and standard deviation: ensemble containing 100 injections of 500 MeV protons each

(d) relative error for scenario (c)

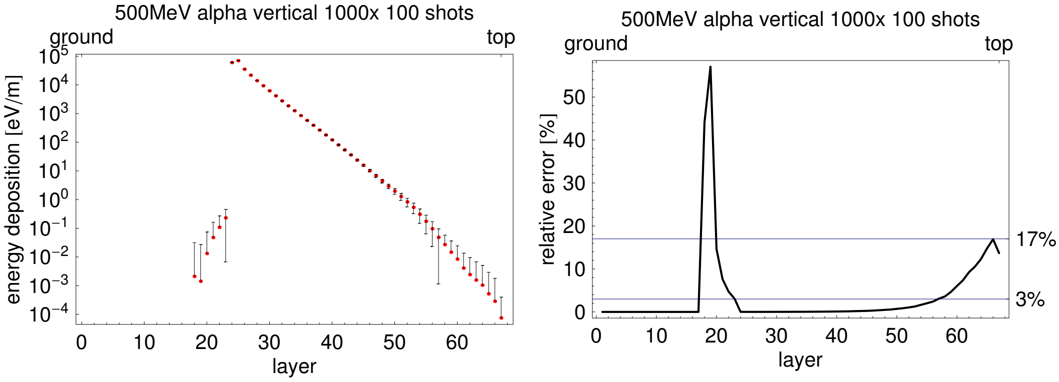

(e) mean and standard deviation: ensemble containing 100 injections of 500 MeV alphas each

(f) relative error for scenario (e)

Figure 7.5: Left hand figures (a), (c) and (e) show the mean energy deposition per layer, based on 1000 ensembles and the corresponding standard deviation, indicated by error bars. Vertical injections are considered only. A missing lower error bar indicates that some ensembles show no interaction/energy deposition in that layer. Right hand figures (b), (d) and (f) show the corresponding relative error of the energy deposition per layer. The maximum relative error (apart of that one at the end of the primary particle's range) is indicated at the right hand frame label.

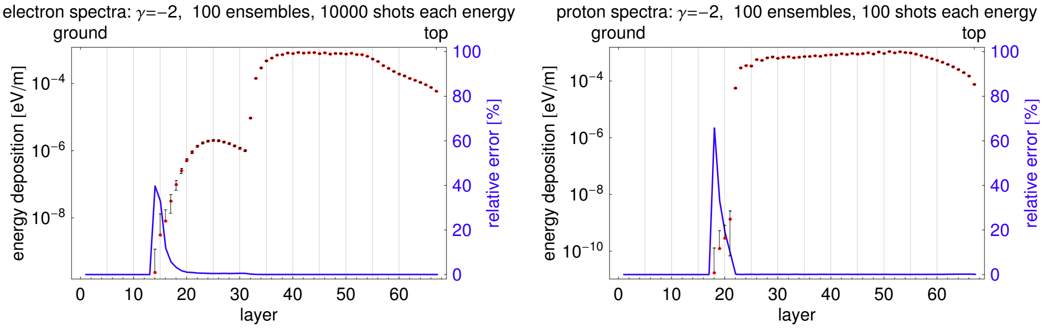

(a) electrons: 10000 injections

(b) protons: 100 injections

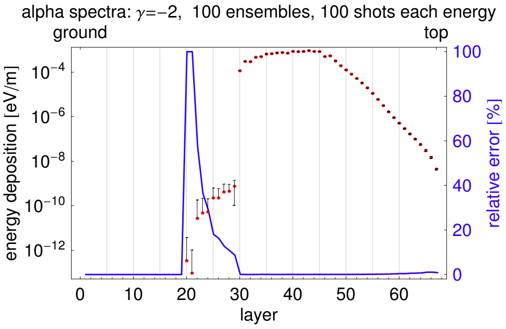

(c) alphas 100 injections

Figure 7.6: Mean, standard deviation and relative error of the energy deposition per layer for a folded particle ensemble. The spectral index is $\gamma = -2$.

affected by rare processes. Statistical errors of electron spectra are increased beyond the range of the primary particle as the energy deposition results from bremsstrahlung only. (b) The statistical error increases at high altitude, resulting from reduced density and therewith interaction probability. (c) It increases with increasing steepness of the spectrum (especially for $\gamma = -4$). This mostly affects lower altitudes due to a reduced number of high energetic particles.

Statistical Error in different angular Resolutions

This paragraph will discuss the statistical error for different angular resolutions. Once an angular resolution has been chosen, 144 different atmospheric conditions have to be simulated (three solar conditions, four geographic latitudes, four seasons and three particle species). While each simulation includes 100 to 10000 repetitions at each energy and incident angle, the angular resolution should be limited to a reasonable specification.

Figures in 7.7 and 7.8 display the deviation of different angular resolutions compared to a 0.5° reference resolution at different spectral indices ($\gamma =$ -1 to -4).

Results are: (a) very hard spectra (γ=-1, see Figure 7.7, top) show strongest aberrations of the energy deposition using different angular resolutions against the reference resolution. Due to the high number of high-energetic particles that penetrate deep into the atmosphere the injection angle has a huge impact on the deposition altitude. (b) Weak angular resolutions have a tendency to local maxima. We assume an isotropic angular distribution, therefore bigger beam angles have higher weighting factors. These factors result in local maxima if the angular resolution is too poor (e.g., a 10° resolution produces an energy deposition maxima which is separated into two parts, one can be related to injections with incident angles of 0°–70° and the other one relates to the 80° injections).

In order to avoid artificial local maxima and at the same time limit calculation time, the model will use a variable angular resolution: 0° to 60° using steps of 5°, 60° to 70° using steps of 2° and 70° to 89° using steps of 1°. Particles with an injection angle of 90°would pass the model atmosphere without interaction therefore maximum angle will be 89°.

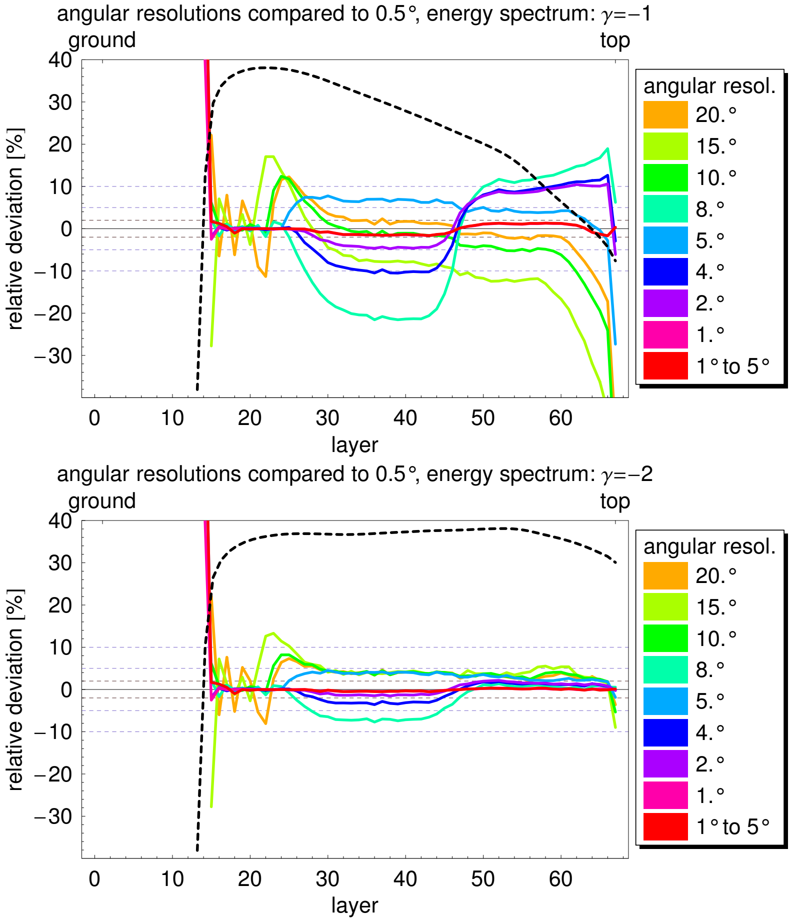

Figure 7.7: Comparison of spectra with different angular resolutions using a spectral index of γ =-1 (top) and -2 (bottom). The red curve indicates the relative error of the variable angular resolution as specified in the paragraph compared to 0.5° reference. The dashed black line shows the shape of the energy deposition for the corresponding spectrum – in this connection the ordinate represents a logarithmic energy deposition.

The variable angular resolution has a statistical deviation of less than 2% compared to 0.5° reference energy deposition at all spectral indices ($\gamma = -1$ to -4).*

Summary

While the mono-energetic beams show a significant statistical error at specific altitudes, folding of angular distribution and energy spectra evens out most of the statistical error. In general the statistical error of electron and proton spectra will be below 1%, the alpha spectra below 2%. Another 2% uncertainty results from the angular resolution. Taking into account bremsstrahlung of a soft electron spectrum, the resulting total statistical error rises up to 10% at altitudes below the range of the incident particle and for electrons only.

---

*Total computing time with variable angular resolution sums up to three weeks using as far as 18 PCs equipped with 2 to 4 CPUs. The simulation of a specific atmospheric condition for one particle species takes up to 2 days on a usual computer.

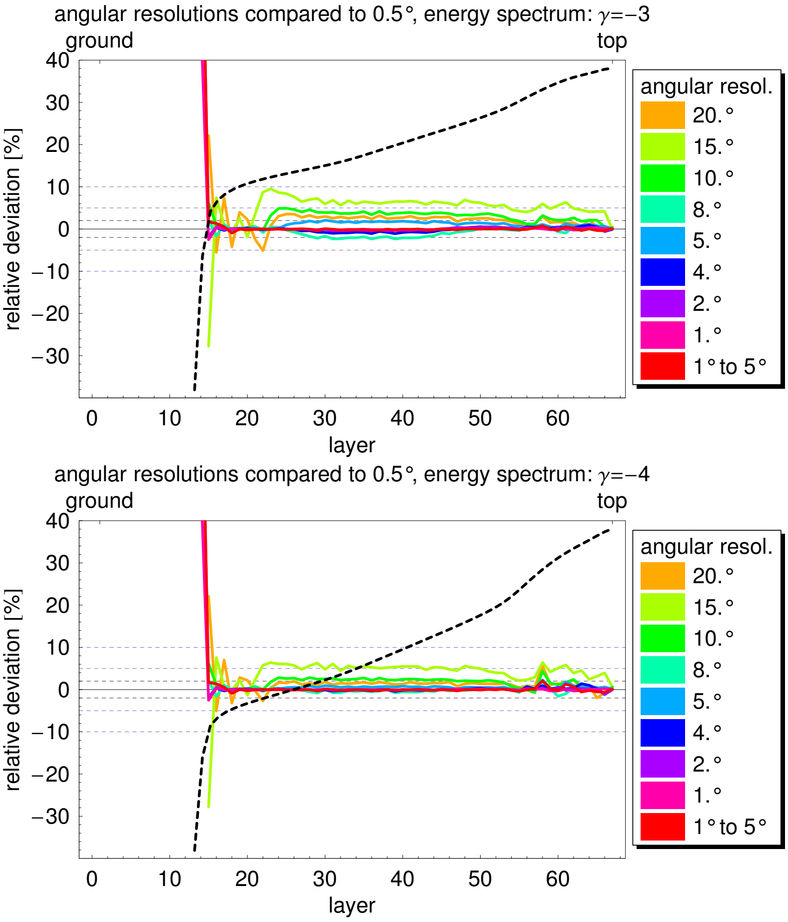

Figure 7.8: Same as Figure 7.7 for γ =-3 (top) and -4 (bottom).

7.2 Assumptions and Limitations affecting the Model Results

This Section will discuss the assumptions and limitations that affect the results of AIMOS. Most assumptions and limitations are given by the input data, e.g. data gaps (see Section 7.2.1) and inherent errors like crosstalk (see Section 7.3). Another assumption is needed since the GEANT4 simulation toolkit does not allow direct counting of ionization processes. Thus the ionization rate has to be determined by conversion of the energy deposition (see Section 7.2.2). It should be noted that this limitation would also hold for energy loss calculations using Bethe-Bloch or some other continuous energy loss approach.

7.2.1 Data Gaps in Satellite Measurements

One of the main problems in this global ionization model is the limited spatial data coverage. As all spatial information is derived from in-situ measurements of two polar orbiting satellites, data gaps in these measurements have to be treated with care. Data for polar cap passages, for example, is regularly missing as the geomagnetic poles are not covered during every satellite orbit. AIMOS tries to compensate these periods as good as possible. In addition some rare periods suffer from satellite and even ground station blackouts. Thence we will discuss an attempt to compensate periods without satellite data. Another aspect is the limited angular resolution of precipitating particles. These topics will be discussed in this Section.

Polar Cap

The particle flux inside the polar cap region is described by direct measurements only. Due to the orbit inclination or data gaps it may happen that data for one pole is missing. In order to avoid data gaps in the AIMOS results we try to compensate these gaps by using values from the other pole. The justification is as follows:

A comparison of MEPED mean values (2002 till the end of 2004) for northern and southern polar cap shows excellent agreement, as listed in Table 7.4. In more detail the discrepancies belong to solar energetic particle events. Considering that events always include a disturbed magnetosphere and therewith a high variable particle flux, the temporal offset of the northern and southern half orbit measurements foreclose a direct comparison. So Table 7.4 also presents the ratio of northern and southern polar flux lacking the most intense 2%, respectively 10% flux values.

channel	$\frac{\bar{x}_{\mathrm{north}}}{\bar{x}_{\mathrm{south}}}$	$\frac{\bar{x}_{\mathrm{north},2\%}}{\bar{x}_{\mathrm{south},2\%}}$	$\frac{\bar{x}_{\mathrm{north},10\%}}{\bar{x}_{\mathrm{south},10\%}}$
mep0e1_e2	1.02	0.79	0.89
mep0e2_e3	1.42	0.95	0.96
mep0e3	1.16	0.99	0.99
mep0P1	0.93	0.97	1.09
mep0P2	0.96	0.89	0.98
mep0P3	1.01	0.96	0.96
mep0P4	1.43	0.97	0.98
mep0P5	1.21	1.00	1.01

Table 7.4: Comparison of northern and southern polar cap flux in POES MEPED channels. Leaving out the most intense 2%, respectively 10% of the flux data, these columns do not suffer from strong short-term flux differences during particle events. The comparison allows to use one pole as proxy for the other one in case of missing data.

In combination with the flux evolution (see Figures in 7.9) we state no significant north-south flux difference in the upper TED and all MEPED channels. For this reason AIMOS uses values from the other polar cap as backup.

In case of missing data at both polar caps the flux of the previous and the following 2 h interval is being used. Longer periods of missing polar cap data are not compensated but flagged. For a recent list of missing data see `README` at `http://aimos.physik.uos.de`.

Please note that the correlation between particle fluxes at north and south polar caps breaks down at low particle energies. Figure 7.9 shows the time series of particle fluxes ordered by the particle energy, starting with the highest spatial channels for protons and electrons in the top row and ending with one of the low energetic (TED) channels in the bottom.

A closer look at the lowest channels in AIMOS, the TED band 4 and 8 for protons and electrons, reveals a seasonal dependence for TEDprotonBand4 and 8 (see Figure 7.10) and a 27-day Sun's rotation period for TEDelectronBand4 and 8 (see Figure 7.11) which are both anti-correlated among the hemispheres.

The reason for the seasonal period in the low energetic polar cap proton flux is not known for sure. It might be the different tilt angle of the Earth's rotation axis in relation to the Sun (and therefore also a different geomagnetic adjustment), followed by a shift of the precipitation zones. Another explanation might be the impact of increased sunlight in the local summer as this effect can also be detected in different day-time sectors (see Figure 7.20). In contrast the reason for the 27 day period in the electron flux can only be given by the solar rotation. As the interplanetary magnetic field is linked to the Sun the interplanetary B_z-component, which is of main interest for magnetic reconnection to the magnetosphere, as well as a possible link to active regions on the Sun will change with a 27 day period (see also *Williams*, 1966).

Given that there is no additional low energetic polar cap data available (e.g., ACE has no low particle instrument at this energy range), polar cap data gaps will be treated in the same manner as it is done for high energetic channels.

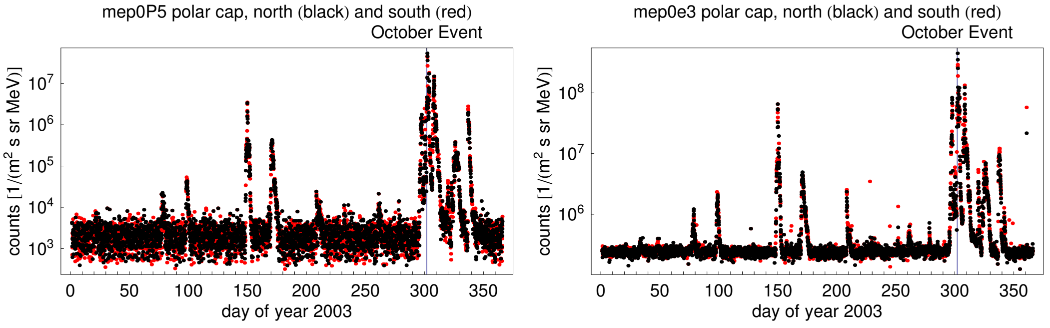

(a) MEPED mep0P5

(b) MEPED mep0e3

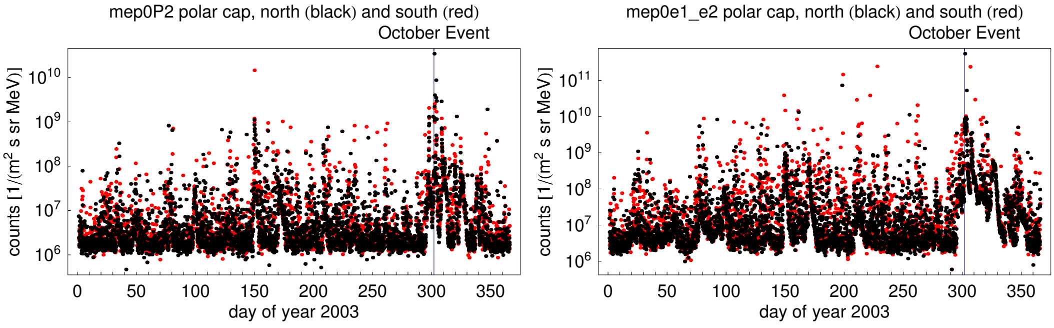

(c) MEPED mep0P2

(d) MEPED mep0e1-e2

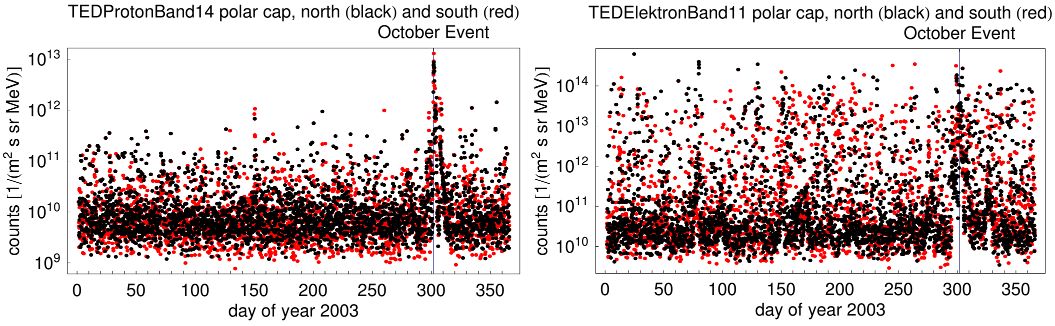

(e) TED proton band 14

(f) TED electron band 11

Figure 7.9: Time series of particle flux in northern and southern polar cap in 2003: High energetic channels (top) show a good agreement of the polar caps. However, at low particle energies (bottom) the correlation decreases.

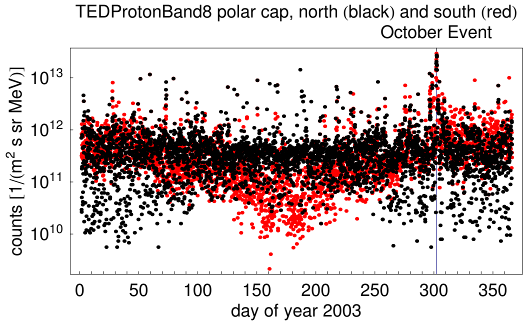

Figure 7.10: Polar cap particle flux for low energetic protons (TEDprotonBand8). A dependence on season is supposable. The particle flux is at maximum in local summer.

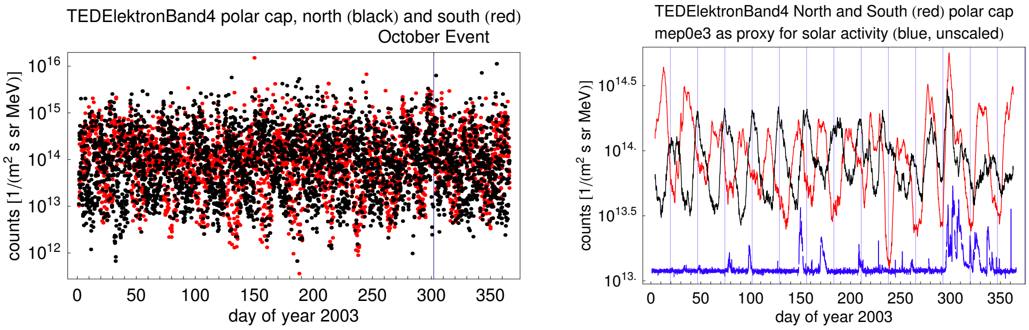

(a) original (b) 5 day running mean

Figure 7.11: Polar cap data for low energetic electrons (TEDelectronBand4) using (a) all 2 h mean values in 2003 and (b) a 5 day running mean. The impact of the October event is limited. In contrast polar cap flux shows an approximate 27 day period with antipodal effect on north and south in quiet time.

Lower Latitudes (auroral and equatorward)

The description of global particle population in AIMOS is based on mean precipitation maps (except for the particles inside the polar cap). As these maps are derived from in-situ measurements, inclination of the satellites' orbit lead to blank areas surrounding the geographic poles (see Figure 7.12), including some parts of the auroral oval. Unfortunately, this region is important for particle induced ionization, therefore the model should appraise missing values.

Mean precipitation patterns originate from four years of satellite data sorted by the geomagnetic K_p-index. At a first guess, the patterns should be quite smooth. However, considering that the K_p-index is a 3 h mean and the magnetosphere (and the particle population within) can be highly variable on shorter time-scales the mean precipitation matrices are still bumpy.

Both implies the need for a smoothing and interpolating algorithm. The spatial pattern of particle precipitation is organized by the geomagnetic field, which means that a neighboring region on the same geomagnetical latitude is supposed to have more weight on the smoothing and interpolating algorithm than one on the same geomagnetic longitude. Figure 7.13 shows the result of a geomagnetic smoothing/interpolation algorithm in contrast to a geographic one. As expected the auroral oval in the geographic smoothing suffers from broadening while the result of geomagnetic algorithm is close to the original pattern.That is why the geomagnetic algorithm is used in AIMOS. Additionally the smoothing/interpolation uses weighting factors that consider the number of measurements at every grid point. Hence the influence of poor statistics due to grid points based on just few measurements is reduced.

While the first part described (spatial) data gaps in the mean precipitation maps, we will now turn to temporal data gaps in the measurements. Normally the lower latitudes in the ionization model do not suffer from data gaps. These regions are covered in every satellite orbit and short-term data gaps, as they appear e.g. during instrument calibrations, are compensated by data from the second satellite or from the same satellite during the second half of the orbit (ascending/descending). However, in some rare cases both POES satellites or even the ground station had a blackout. For a recent list of missing data, see `README` at `http://aimos.physik.uos.de`.

In this rare cases the low latitude particle data is derived from the mean precipitation maps without any scaling while the polar cap region will be blanked. Figure 7.14 shows a comparison of a simulation with particle measurements to a simulation based on the K_p-mean precipitation maps. During a particle event the simulation without particle data is very

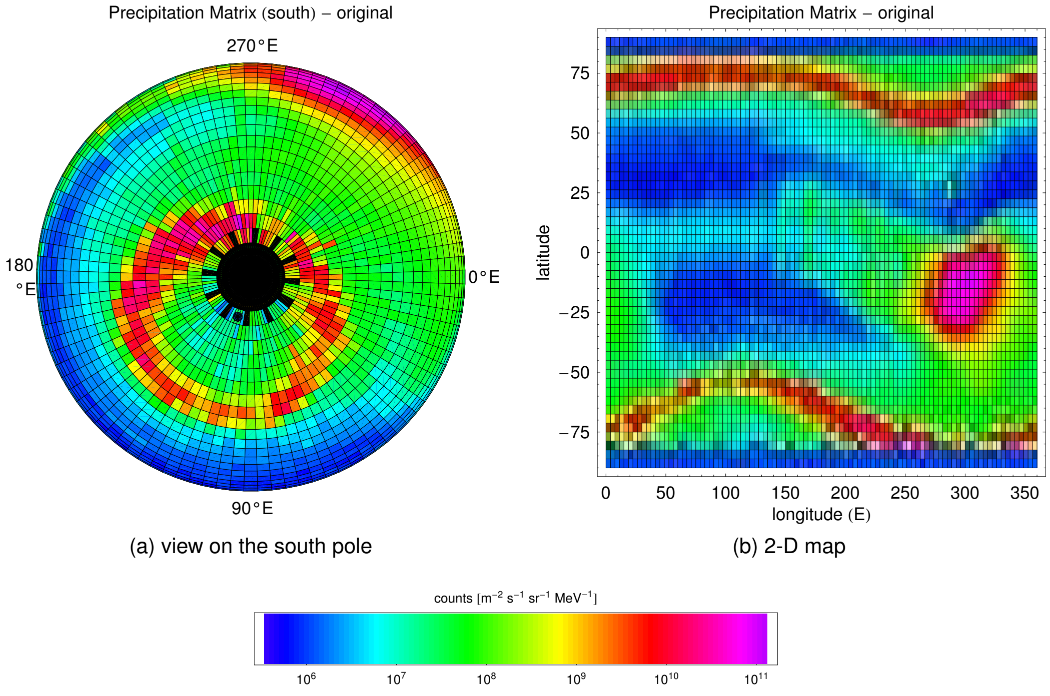

(a) view on the south pole

(b) 2-D map

(c) legend

Figure 7.12: Systematic gaps (black) in the original mean precipitation matrix due to inclination of the POES orbit.

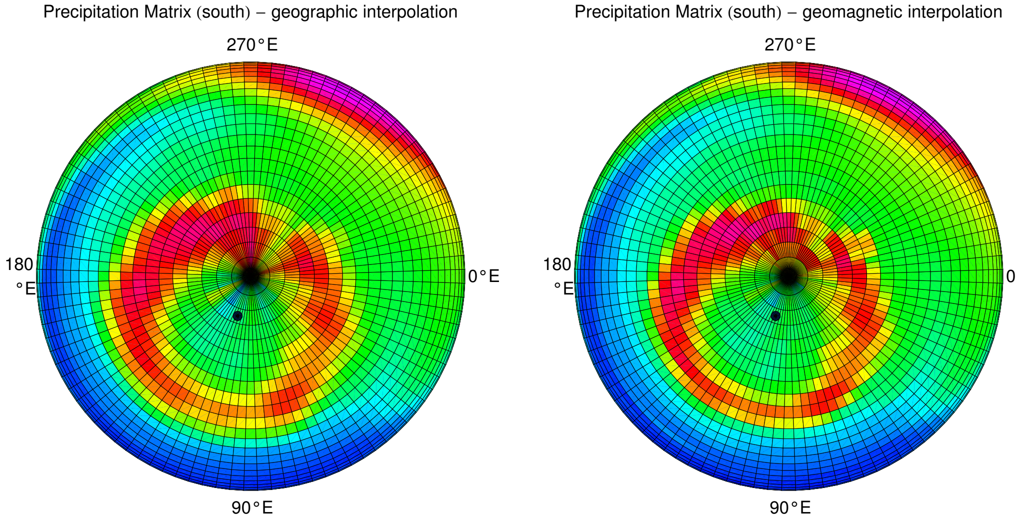

(a) geographic interpolation/smoothing

(b) geomagnetic interpolation/smoothing

Figure 7.13: Geographic smoothing/interpolation is shown opposed to the geomagnetic one. The blue dot indicates the geomagnetic pole. As charged particles stick to their guiding field line the geomagnetic interpolation is used for AIMOS. The most obvious difference is that the auroral oval is smeared out due to the geographic algorithm while the geomagnetic algorithm reproduces the original width (see Figure 7.12c). Legend is the same as in Figure 7.12c.

close to the simulation with particle measurements. The ionization in the main precipiation region of magnetospheric particles lies between 31% underestimation and 200% overestimation of the original AIMOS ionization. For geomagnetic quiet time the absolute deviations are bigger but still between 21% underestimation and some hundered percent overestimation. We will not go into details here as there are just three days affected in the period January 2002 to December 2008.

Missing angular Resolution

The angular distribution of the precipitating particles is not measured. Even though POES particle instruments are installed with a vertical and a horizontal viewing direction, the horizontal instruments just detect mirrored particles (at the main precipitation regions). So the current angular distribution of the precipitating population is unknown. Likewise to all other precipitation models in Table 1.1, a isotropic distribution is assumed. However, a different angular distribution will affect the main ionization altitude of a specific particle energy since particles with a vertical incident angle deposit their energy deeper in the atmosphere. In fact AIMOS can work with any angular distribution. The limitation to an isotropic one is based on the availability of data (or the lack thereof).

7.2.2 Conversion of Energy Deposition into Ionization Rate

Direct counting of ionization processes in GEANT4 is restricted to energetic particles. Below a certain energy threshold (1 keV, see *Geant4 Physics Reference Manual* (2007, page 102)), GEANT4 switches from production of secondaries (due to ionization processes) to a continuous energy loss model. Thus the total number of ionizations has to be derived from the total energy deposition. This implies the need of a conversion from energy loss/deposition to the number of ionization processes. This section will enlarge on the conversion factor.

Incident Electrons

The mean energy loss by an electron producing an ionization pair has been determined to be 32.6 eV (*Eisl*, 1929) for the particle energy range 9–59 keV. *Freund* (1935) and *Breunig* (1936) presented a constant conversion factor of 30 eV/ioniz.-pair (Freund, using particle energies of 30–300 eV) and 34 eV/ioniz.-pair (Breuning, for the energy range 70–160 eV), respectively. Below the lower threshold a slight increase of the energy loss per ionization has been detected.

Valentine and Curran (1958) published values for the conversion factor generated by β-radiation. In air it was 35.0 ±0.5 eV/ioniz.-pair and stayed constant in the range of 3 keV until the upper measurement boundary of 1 MeV. The measuring accuracy allowed deviations of 2%. At lower particle energies (down to 240 eV) the measurement accurency declined, allowing deviation of 10%. Based on this measurement *Valentine and Curran* (1958) concluded that the variation of the conversion factor (as function of particle energy) was small – it may not even be present. Looking at the ionization by X-ray (bremsstrahlung), the conversion factor is 35 ±5 eV/ioniz.-pair as determined by *Kulenkampff* (1926). *Gaertner* (1935) supported this value (35.15 eV/ioniz.-pair).

To sum up the conversion factor is the same (35 eV/ioniz.-pair) for electron ionization as well as for bremsstrahlung. For this reason the total ionization of incident electrons can be deduced from the total energy deposition by using a constant conversion factor.

Incident Alphas

In contrast to the electron conversion factor, the conversion factor for ionization by α-particles definitely shows a dependence on the primary particle energy. Summing up *Valentine and Curran* (1958)'s results, the energy loss per ion pair in air increases at low particle speed/energy while it converges to a constant value for high particle energy. *Gray* (1944)

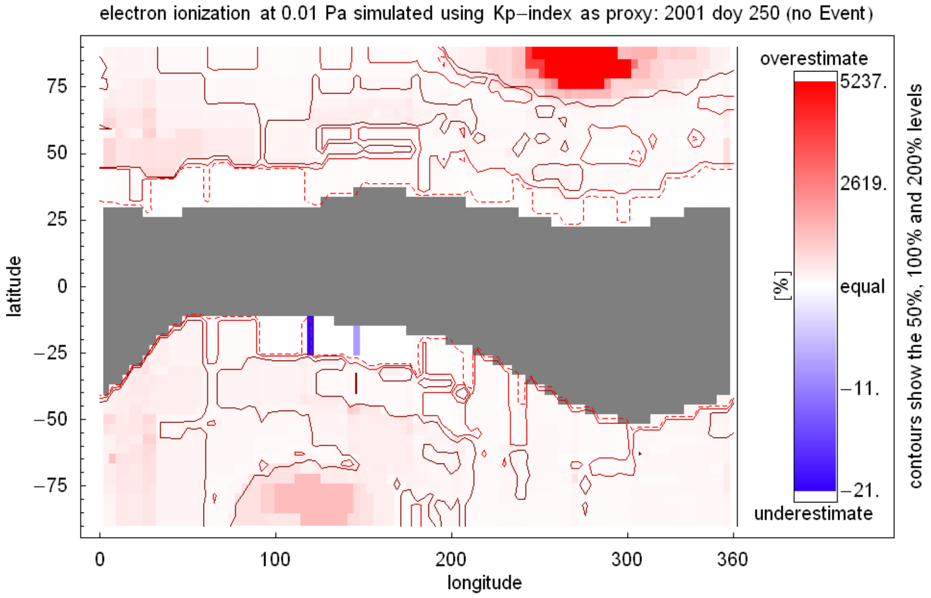

(a) quiet time

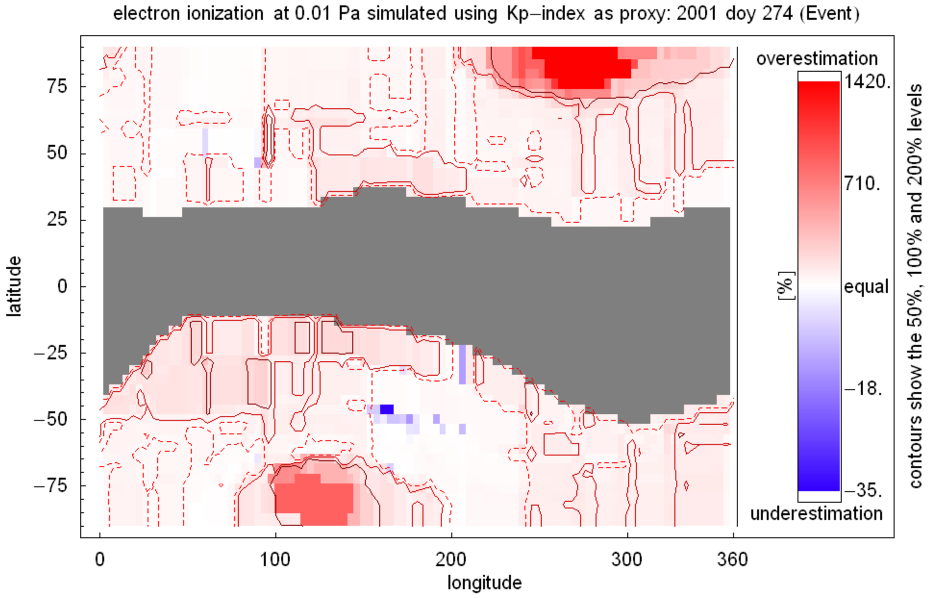

(b) event

Figure 7.14: Comparison of the ionization rate by precipitating electrons derived by satellite data and by using mean precipitation maps only. The pressure level of 0.01 Pa (approximately 110 km) is shown, representing the altitude of maximum ionization due to auroral particles. (a) is for quiet time while (b) shows a particle event. The ionization inside the polar cap can not be estimated by the K_p-index. In this case both polar caps show intense overestimations. As far as the unscaled precipitation maps are used the polar cap region will be blanked in AIMOS.

reports a variance above 1 MeV of about 1 to 2%. Measurements from *Schmieder* (1939) at 7.683 MeV[*] give a conversion factor of 34.8 eV/ioniz.-pair.

Within this work alpha particles with a primary energy of 4–500 MeV will be used. Considering that the major part of the energy deposition will take place before the conversion factor increases at low particle speed and a dominant part of the ionization will be produced by secondaries (in general electrons), it is reasonable to use the constant conversion factor of 35 eV/ioniz.-pair here as well.

Incident Protons

Larson (1958) stated the mean ionization energy per ion pair for dry-air as being 35.18 ±0.42 eV based on 1.826 MeV protons. Based on 7.56 MeV protons, one of the first measurements of the conversion factor for protons was given by *Gray* (1944) with 35.1 eV/ioniz.-pair. For high proton energies (340 MeV) measurements from *Bakker and Segrè* (1951) result in 33.3 eV/ioniz.-pair. Likewise the α-particles, a significant part of the ionization, will be produced by secondary electrons.

Summary: Conversion Factor in AIMOS

A theoretical derivation of the conversion factor is given by *Porter et al.* (1976). It is based on plausibilities of specific excitation- and ionization processes of N_2 and O_2, considering the energy of the primary particle. For electrons the calculated 34.5 eV/ioniz.-pair cover the experimental results. The conversion factor stays constant down to 150 eV. Concerning energetic protons the theoretical conversion factor from *Porter et al.* (1976) is 35.8 eV/ioniz.-pair, which is also in good agreement with the experimental results. The lower boundary of this constant value is not explicitly given but according to the figures in *Porter et al.* (1976) it at least stays constant from 10 keV to 1 GeV. In agreement with other ionization models (e.g., *Jackman et al.*, 1990; *Schröter et al.*, 2006), we will ignore the energy dependence of low energetic particles in the conversion.

Another small constraint is that the conversion deals with the air composition at ground level. Considering a heterosphere and atomic constituents the mean energy loss per ionization pair may vary. As there are no measurements (in particular with atomic oxygen/nitrogen composition) known to the author, the conversion factor of 35 eV/ioniz.-pair will be used universally at all heights, particle species and energies.

7.3 Inherent Errors in the Particle Measurements

This Section will discuss the inherent errors of the satellite data. Some errors can be described statistically such as the counter reading errors. Others like the conversion error resulting from compressed transmission from satellite to ground station can even be neglected. However, satellite measurements can also be significantly affected by the satellite's environment. Particle instruments in space are often influenced by e.g. crosstalk, physical defects (aging) due to mechanical, electromagnetic and thermal stress as well as ionizing radiation. In addition the local environment is not necessarily identical with the assumed structure of the magnetosphere, e.g. parts of a geostationary orbit may suddenly be situated inside the magnetosheath or even in the interplanetary space. An exact error analysis on these influences is not possible. Normally these influences exceed the limits described by the statistical error analysis.

As the errors in this Section are linked with quality of the input data, although they cause errors in the model output, they do not represent a problem of the model but the use of inaccurate data sets.

---

[*] alpha decay of RaC

species	energy	channel name	maximum at condition: geomagnetic quiet			maximum at condition: particle event		
e$^-$	154–224 eV	TED band 4	10000	±100	(1%)	100000	±316	(0.32%)
e$^-$	6.5–9.5 keV	TED band 14	500	±22	(4.4%)	1000	±32	(3.2%)
e$^-$	30–100 keV	mep0e1-e2	10000	±100	(1%)	100000	±316	(0.32%)
e$^-$	0.3–2.5 MeV	mep0e3	10	±3	(30%)	4000	±63	(1.8%)
p$^+$	154–224 eV	TED band 4	100	±10	(10%)	1000	±32	(3.2%)
p$^+$	6.5–9.5 keV	TED band 14	50	±7	(14%)	300	±17	(5.7%)
p$^+$	30–80 keV	mep0P1	10000	±100	(1%)	100000	±316	(0.32%)
p$^+$	2.5–6.9 MeV	mep0P5	10	±3	(30%)	400	±20	(5%)

Table 7.5: Typical statistic counter reading errors for particle instruments.

7.3.1 Counting Statistics of an Ideal Particle Instrument

An ideal particle instrument is a device whose sensitivity for particles in a definite channel – which means a particle of specific species s, a specific energy range ΔE and a specific incidence angle $\Delta\Omega$ – is accurately one $(A(\Delta E, s, \Delta\Omega) = 1)$. Thus an ideal particle instrument has no crosstalk neither in energy, between species nor in the angle of incidence.

The measuring error ΔZ belonging to the counter reading of an ideal particle instrument is characterized by Poisson-statistics:

$$\Delta Z = \sqrt{Z}\,.$$

The corresponding relative error is described by:

$$(\Delta Z)_{\mathrm{rel}} = \frac{1}{\sqrt{Z}}\,.$$

Counter readings of different energy channels vary by orders of magnitude, corresponding to the energy spectra of the particle population, temporal averaging and geometry factors. Typical counter readings and the relative errors for maxima in the auroral oval and maxima within a particle event are listed in Table 7.5. An analysis of the counter reading error at minimum particle flux suffers from the following problem. Background values are treated as non-existent since zero count rates were detected in all particle instruments. However, values outlying the regions of intense particle precipitation are irrelevant for ionization (see Figures 7.2, bottom, and 7.3). Hence a description of the relative error at minimal counter readings will not be given.

The particle count rates arise from counter readings divided by the temporal averaging interval. The relative error persists, therefore I will use the term “count rate error” which is the more common physical denotation.

Table 7.5 lists a relative statistical error of less than 6% within an event. At geomagnetically quiet condition the relative error increases to 14%. Looking at the highest electron and proton channels the relative error is approximately 30% since particles at these energies are very rare outside an event. Considering that the dynamic range incorporates several orders of magnitude the resulting errors are still small.

7.3.2 Conversion Error

In order to reduce the data volume to be transferred between satellite and ground control the count rate transmission is compressed (*Evans and Greer*, 2004, page 79). The compression uses a conversion table, replacing counts above 32 by approximated values of an exponential function. Hence values above 32 include a conversion error as shown in Figure 7.15. The relative error due to conversion is smaller than 3%.

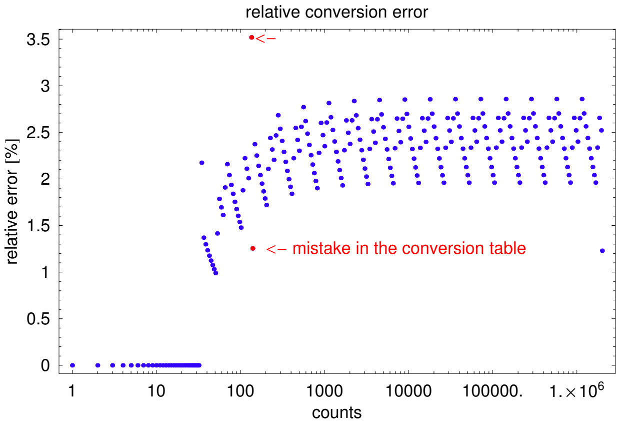

Figure 7.15: Relative conversion error resulting from compressed transmission. Red dots show a mistake in the conversion table.

Apart from the conversion error there seems to be a mistake in the conversion table (indicated by red dots). The mistake leads back to a single count rate threshold, therefore we consider it as negligible.

7.3.3 Real Detector Response and Crosstalk

Ideal and real measuring instruments can be classified by their response. Real response (see Figure 7.16, blue) differs from an ideal response $A(\Delta E, s, \Delta\Omega)$ (red) due to the following effects:

1. Even under the assumption that only particles from the correct species s will be detected, a real channel Z(s, E_{up}–E_{low}, $\Delta\Omega$) will:
   (a) not detect all particles (sensitivity $A < 1$),
   (b) detect some particles from upper and lower energy range ($E > E_{\text{up}}$ and/or $E < E_{\text{low}}$).
   Therefore the response represents a more or less smeared out rectangle (indicated a trapezoid in Figure 7.16). And it is not necessarily symmetric.
2. Particles with higher and lower energies can cause crosstalk into the target channel.
   (a) At small energy difference: the reason is the trapezoid shape of the response.
   (b) At lager energy difference: the reason might be that long temporal averaging (e.g., MEPED: 80 ns) allows a lager amount of low energetic particles to produce a similar pulse as a particle within the desired detector range (coincidence). E.g. *Evans* (2008) noted that $>$30keV and $>$100keV electron channels might be affected by intense flux of auroral (low energetic) particles.
3. Another source of unintentional counts is crosstalk between different particle species.
   (a) Protons can be detected as electrons if only part of the energy is recorded (detector defects, problems concerning charge accumulation, ambiguity of sensitivity at detector borders).
   (b) The same is true for α-particles which can be recorded as protons or even as electrons.
   (c) Electrons can be identified as protons if the energy deposition exceeds a certain threshold, mainly due to multiple scattering and/or coincidence.
   (d) Crosstalk of electrons and/or protons into α-channels is unlikely since the kinetic energy of light particles is normally not sufficient to exceed the threshold of an α-detector.
   Please note that crosstalk in a multi-channel detector (like e.g., MEPED) always includes a second kind of error since a ”crosstalking” particle will not be detected in its designated channel.
4. The aperture in high energy channels is sometimes ambiguous, in particular when the detector is equipped with passive incident angle limitation only.

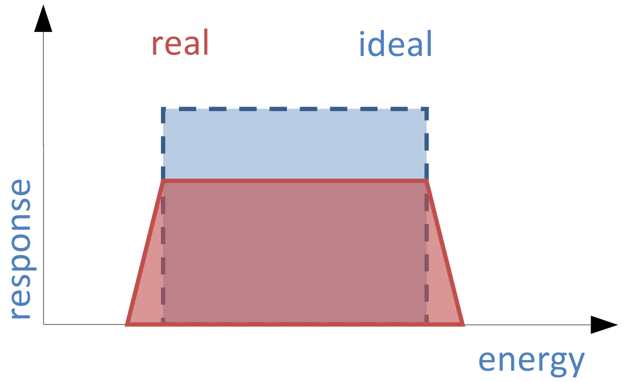

Figure 7.16: Sensitivity of an ideal (blue) and a real (red) particle detector.

Quantification of these processes can hardly be done as all effects depend on composition and spectra of the particle population.

Within the scope of this work some effects have been identified:

- crosstalk of protons into electron channels,
- crosstalk of high energetic electrons into low energetic (TED) channels and
- crosstalk of high energetic electrons into proton channels.

These effects will be described in the following paragraphs.

Crosstalk of Protons into Electron Channels

The electron detector (in contrast to the proton detector) is not equipped with a magnetic shielding, repelling particles incident outside the viewing angle. A magnetic shielding deflects lightweight particles due to their smaller gyro radii in a magnetic field. Thus, it can not be applied (in this manner) to electron channels. Table 7.6 lists the electron channels that may be affected by protons. The table also lists the corresponding proton energy ranges that can generate misplaced counts.

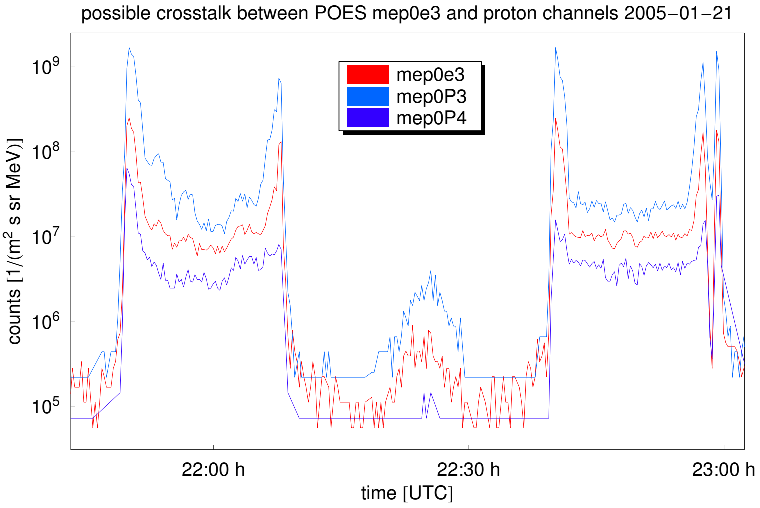

Figure 7.17: Proton and electron flux during the January 2005 event. Similar behavior might indicate crosstalk.

Kalicinsky (2008) gives strong indication that this sensitivity for protons might affect the electron counts. He describes a very connatural behavior of the electron channel mep0e3 and the proton channels mep0P3 and mep0P4 during the January 2005 event (see Figure 7.17 for an extract of this period). He concludes that it results from crosstalk by enhanced proton flux.

electron channel	possibly affected by protons at
mep0e1	210–2700 keV
mep0e2	280–2700 keV
mep0e3	440–2700 keV

Table 7.6: Sensitivity of MEPED electron channels to protons (*Evans*, 2008).

Please take note that the flux evolution of protons and electrons is also very similar in periods when significant impact of crosstalk can be foreclosed. Nevertheless as the detector construction allows crosstalk, the electron channels may be contaminated (private communication, Janet Green, NOAA) – even though the exact amount is not known for sure.

Crosstalk of high energetic Electrons into TED Channels (“additional” Auroral Oval)

In particular TED proton channels show a feature that can be misunderstood as a second auroral oval (see Figure 7.18, left). A comparison of both oval locations to the oval position of the lowest MEPED channel (mep0P1) indicates that the poleward flux maximum is the correct one. In contrast the equatorward oval was unanticipated. David Evans (NOAA, private communication) notes that high energetic electrons can penetrate the shielding.

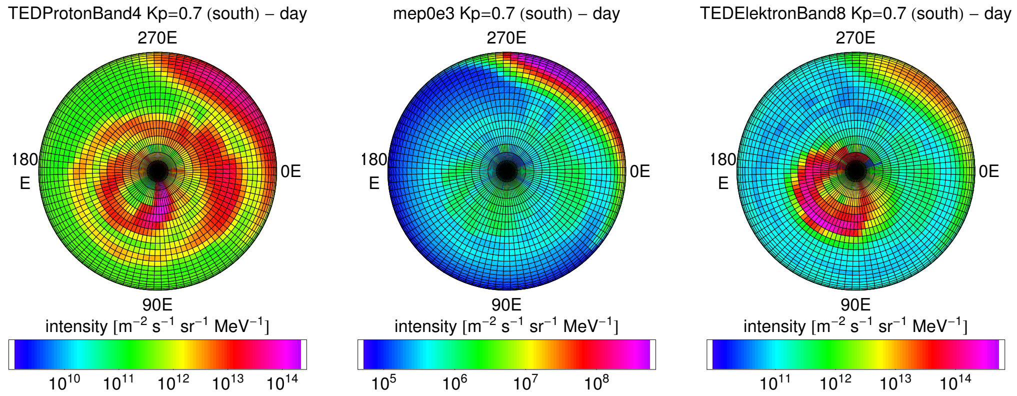

Figure 7.18: (left) TED proton flux (TEDProtonBand4) reveals an “additional” auroral oval. (middle) High energetic electron flux (mep0e3) covers the same region as the equatorward oval. (right) The TED electron detector (TEDElectonBand8) shows just little impact of crosstalk due to energetic electrons. All figures show the day sector on the southern hemisphere at very low K_p (0.7).

In fact the main precipitation area of high energetic electrons (mep0e3, 0.3–2.5 MeV, see Figure 7.18, middle) agrees with the “additional oval”. The *NASA Virtual Ionosphere, Thermosphere, Mesosphere Observatory*[*] allows a determination of the L-values depending on the geographic position. Consequently the poleward oval in Figure 7.18 (left) is linked to an L-value of $>$5.4, while the second oval is located at approximately L=3.7–4.7. As shown in a AE-8 MAX (SPENVIS) simulation by *Vette* (1991) (Figure 7.19) the equatorward oval is connected to the high energy electron belt.

Hence the second oval will be generated by MeV-electrons penetrating the TED detector shielding. The upper TED electron channels show the alike behavior (see Figure 7.18, right) and endorse this assumption. As the TED electron count rates in every energy band exceed the proton rates of the same energy range tremendously the second oval is less pronounced in the TED electron channels. In the case of TEDElectronBand4 the low energy electron flux hides the potential impact of crosstalking energetic electron completely.

---

[*] *NASA Virtual Ionosphere, Thermosphere, Mesosphere Observatory* (VITMO) `http://omniweb.gsfc.nasa.gov/vitmo/cgm_vitmo.html`

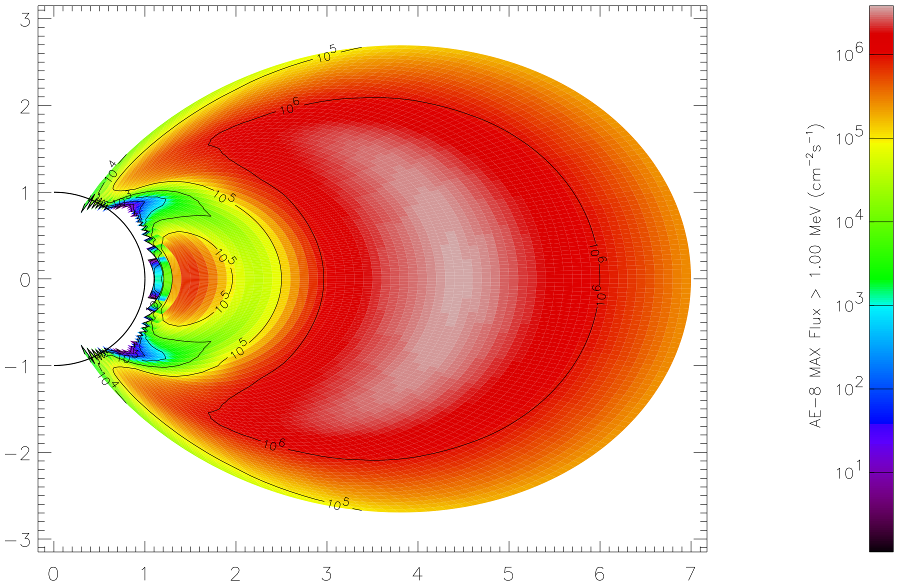

Figure 7.19: Integral electron flux >1 MeV as given by the AE-8 MAX (SPENVIS) simulation (*Vette*, 1991). The axis ticks are given in earth radii, therefore the horizontal axis represents the L-value.

Crosstalk of high energetic Electrons into Proton Channel mep0P6

Channels mep0P1 till mep0P5 are not known to be susceptible to electron contamination. However, mep0P6 suffers from contamination. This is one* reason why mep0P6 is not used in the model. *Evans* (2008) explains the contamination of proton channels by high energetic electrons as follows: While electrons below 0.8 MeV are deflected by the magnetic shielding of the detector, more energetic electrons may penetrate the magnetic shielding. These penetrating electrons do not affect the proton channels mep0P4 (0.8–2.5 MeV) and mep0P5 (2.5–6.9 MeV) since the energy deposition within the first detector layer is very rare. In contrast the energy deposition of these electrons is most intense at the end of the track and interfere with P6 (>6.3 MeV) proton energy deposition. Thence channel mep0P6 may display higher values than mep0P4 and mep0P5.

7.3.4 Influence due to Sunlight

As shown in Figure 7.20 the background of the TED proton channels during morning, day and evening is raised compared to the background at night. The reason for this boost is unsettled. Indeed, the NOAA operators *Evans and Greer* (2004, page 151) hypothesize spacecraft charging due to sunlight being accountable.

7.3.5 Instrument Inter-Calibration

In order to get a wide energy spectra data from several instruments have to be combined.

- Determination of the precipitation maps needs combined data from two satellites (POES) originating from two different sets of identical instruments.
- Additionally subjoining high energetic particles affords data from a third satellite (GOES) with unlike set of instruments.
- Each measurement of the particle population at one certain place is based on a combination of different instruments (varying e.g. in field of view, energy range, particle species).

---

*mep0P6 has no upper energy border, so it can not be used in AIMOS without further assumptions.

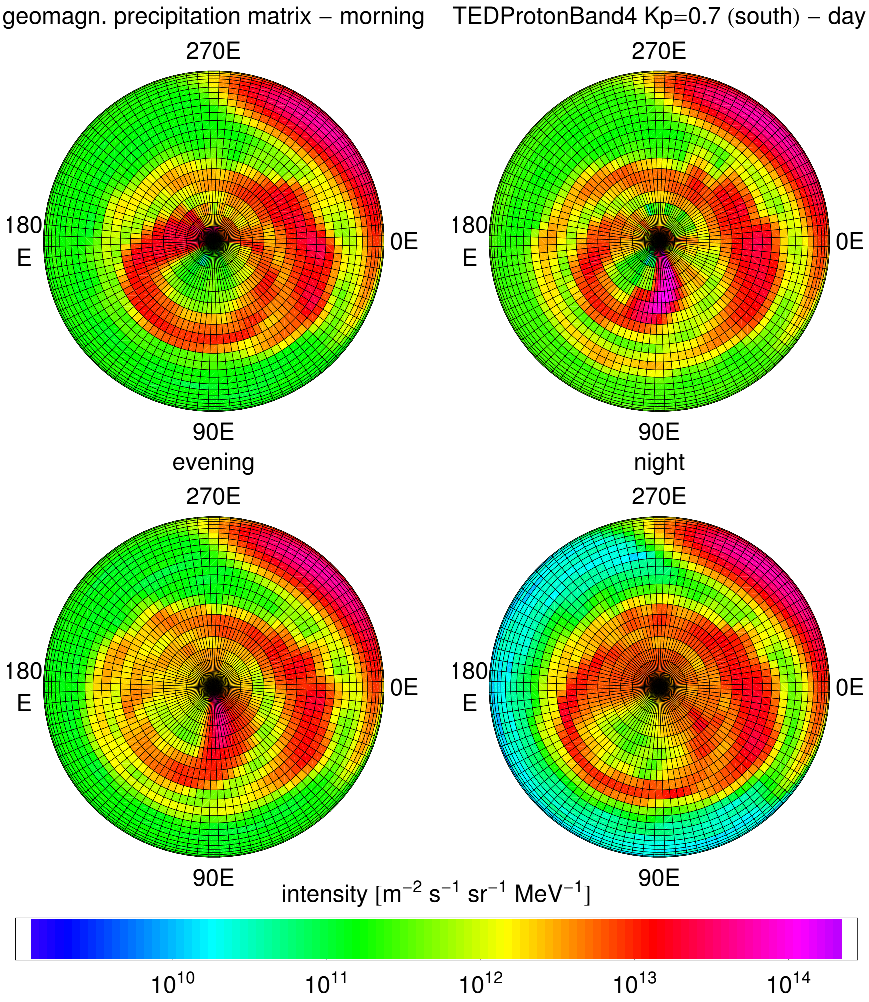

Figure 7.20: TED proton background flux seems to depend on sunlight. Apart from that, the “additional” auroral oval as described in Figure 7.18 is visible for all local time sectors. A view on the southern hemisphere is shown.

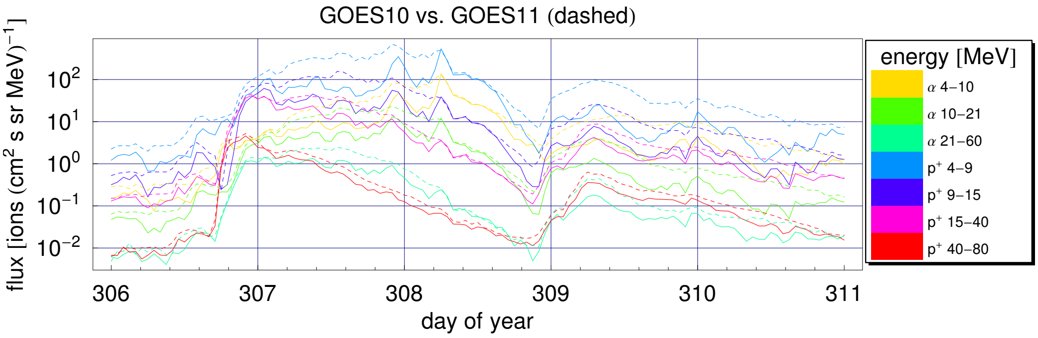

Figure 7.21: Diverging flux values from GOES-10 vs. GOES-11 during the October event 2003.

Satellites/instruments are calibrated after construction. However, as the environmental satellites are part of a long term data base inter-calibration of instruments is an important task. Two methods are used: (a) Different instruments on the same satellite can be inter-calibrated corresponding to the spectrum using an overlap between instruments. This kind of inter-calibration takes place in space as no appropriate particle sources with spectra and composition are available on the ground. (b) Inter-calibration between one instrument and its successor on a later spacecraft is possible as far as both fly simultaneously and the orbits are more or less identical. It involves a simple comparison of measured data. Discrepancies have to be treated with care since the older instrument suffers from non-linear aging effects.

Apart from the method inter-calibration results in a redefinition of the geometry factor, sometimes even a redefinition of the energy range. Concerning our input data the inter-calibration has been done by the satellite operators: GOES-SEM and POES-MEPED data was adjusted by NOAA directly while POES-TED can be corrected manually by documented geometry factors. Inter-calibration of satellites in different orbits (e.g., GOES and POES) is difficult since distant measurements inside the magnetosphere always involve different particle populations. To sum up inter-calibration took place, but it is impossible (at least for us) to evaluate its quality. We have to trust the operators. Indeed we found no irregularity or systematic differences that give reason to question the inter-calibration.

Aging effects as known for the MEPED proton detectors and described in Section 7.3.8 are not corrected, neither by us nor by the operators.

7.3.6 Long-term GOES-10/11 Differences: Detector Orientation

Occasionally GOES-10 and GOES-11 show flux differences for periods of severals days.

Figure 7.21 indicates that the differences are not negligible for the October 2003 period. Richard Mewaldt (private communication) suggest that the orientation of the detectors is responsible for the flux differences. Consequently some periods show a non-isotropic particle population. Apart from that, both satellites measure existing particles, thus a qualitative selection of a specific satellite is not possible. Anyhow the differences in the ionization rates may be large e.g., within the October event 2003, the choice of the GOES satellite makes a flux difference of an order of magnitude. This implies ionization rate variations of the same order. The GOES-10/11 satellites were selected because they provide the most complete data base, in detail we use GOES-10 for 2002 and 2003 and GOES-11 for 2004 and later.

The flux variation reveals that the data input selection may have a stronger impact on ionization rates than the kind of ionization model itself. For this reason an inter-comparison of ionization models should include an identical input data set (e.g. as it has been done in Section 2.1.1).

7.3.7 Short-term GOES-10/11 Differences: Measurement inside the Magnetosheath

In addition to long-term variations, GOES-10 and 11 also show short-term (minutes to hours) flux differences.

A change in the GOES particle flux does not automatically imply an increase or a reduction of the particle population. On the one hand magnetospheric field experiences compression due to solar wind and on the other hand the variable ring current also induces a superimposing magnetic field. Thus particle drift orbits are affected. In extreme cases, strong solar wind pressure as a consequence of shock waves forces a compression of the magnetosphere so that (part of) the GOES orbit is not inside the magnetosphere any more but in the magnetosheath*. Since the particle population is different in the magnetosheath it is not possible to infer fluxes of precipitating particles at that time. More information is given in *Kalicinsky* (2008) who observed significant flux differences for electrons depending

---

*The magnetosheath contains solar wind plasma; modified by the bow shock. A shift into the solar wind is unrealistic as the solar wind pressure is not strong enough (see *Kalicinsky*, 2008, page 51).

on the position of two GOES satellites. While AIMOS only uses protons and alphas from GOES, which have a higher rigidity, the effect is less intense.

At the moment no method is known to correct these periods. Cutting out GOES data at high solar wind pressure is not a solution as this erases the particle events at times of strong geomagnetic activity and therewith the most interesting periods. However GOES count rates (in particular the lower channels) may be affected by strong shocks. Therefore we do not use the lower proton channel. This channel has been replaced by the POES mep0P5 channel.

7.3.8 Aging

Constant penetration of charged particles causes radiation damage that accumulates over time to noticeable variations of detector sensitivity. Consequently an incident particle does not produce the same amount of charges, resulting in a displacement of the energy thresholds, e.g., a proton of given energy might be classified into different energy channels corresponding to the level of degradation. More specific, during the early stages of a satellite mission a proton might be counted for a higher channel as it will later in the mission. The process of degradation is non-linear in time as it depends on the proton flux. A strong event can easily produce a fluence comparable to one year at quiet condition.

Further information on detector degradation is given by *Evans* (2008, pages 2-6) who describes the energy displacement of the lower threshold of the mep0P1 proton channel as follows: beginning of mission in mid 1998 it was 30 keV. Comparison with NOAA-16 at the end of 2000 yields 35-40 keV. A comparison with NOAA-17 in late 2002 gives 40 keV. Compared with NOAA-18 in mid 2005 it is 55 keV and in early 2007 comparison with MetOp-02 adds up to 60 keV. The thresholds at 80 keV and 240 keV should misalign by similar factors.

A more detailed description on the degradation of the MEPED proton channels mep0P1, mep0P2 and mep0P3 can be found in *Asikainen and Mursula* (2010). Again the detectors are compared to the newest satellite resulting in a scaling factor of 1.64, 1.62 and 1.23 for NOAA-15 in mid 2003, respectively 1.36, 1.48 and 1.51 for the same channels on NOAA-16. However, it should be noted that a (constant) scaling factor can not correct the data completely. As both energy boundaries are affected in the degradation process, the energy range ΔE is enlarged and, even more important, the detector is sensible for particles with higher energies. Consequently a correction has to depend on the steepness of the particle spectrum.[*]

The most accurate measurements can be expected during the first years of the satellite mission while later the threshold displacement leads to a misinterpretation of the proton flux. For the observed period beginning with the liftoff of NOAA-16 the POES satellites NOAA-15 and NOAA-16 are the most adequate choice. For this reason the energy displacement is not considered in the model yet. For long-term analysis the degradation has to be corrected or, even better, the satellites used in a model such as AIMOS should be replaced as soon as a new ones are available on the same orbit. *Evans* (2008) shows that the degeneration is limited to the MEPED proton detectors whereas the electron channels and TED data[†] do not suffer from degradation and threshold displacement. Since the reader would expect degradation in these detectors, too, it should be noted that the TED detectors are regularly calibrated on board. The MEPED electron channels have a negligible degradation.

7.3.9 Electrostatic Charging due to high Particle Fluxes

Another effect that reduces the data quality is the enhanced background due to electrostatic charging during periods of intense particle flux. However, this aspect can not be assigned as "real instrument" problem as the background particles exist – even though they would

---

[*] In theory this may lead to under- or overestimation depending on the steepness of the spectrum.

[†] as well as the –not used– omni-directional proton channels

not appear without a changed satellite affecting the local environment. *Evans* (2008) stated that intense auroral electron flux (>10 keV) may generate negative charging of up to -1 kV of the POES satellite. This charging accelerates surrounding plasma ions and leads to contamination of the TED proton detectors. The effect of particle acceleration concentrates on the channel that represents the spacecraft charging. As soon as the satellite leaves the area of intense electron flux, the charge will be compensated by cold ionospheric ions. *Evans* (2008) also states that this charging effect occurs in the night sector only.

7.4 Summary

Errors in the *Atmosphere Ionization Module OSnabrück* can be summarized as follows:

1. The statistical error resulting from the Monte Carlo simulation benefits from a high number of particle injections. Additionally the superposition of different energies in a spectrum reduces the error below 1%. Uncertainness of the angular resolution gives an extra 2% error. In layers which are mainly affected by electron bremsstrahlung (that is the stratosphere below the direct reach of electrons), the statistical error may reach 10% at maximum for a soft spectra.
2. The error discussion of the sorting algorithm can be subdivided into a quantification error comparing the total precipitation along a satellite track[*] and a qualification error correlating the evolution of count rates along the track and in particular the position of the auroral oval.
   - Quantification: The quantification has been discussed in Section 4.8 since the first results showed the necessity of modificating the model. As shown in Table 4.4 the quantity of AIMOS precipitation in quiet time matches very good with the measured values indicated by the factors close to 1. In most cases the relative error is less than 10%, in rare cases an error of 52% has been noticed. During an event the count rates suffer from strong variations in time and space. Therefore, a higher quantification error is expected. Half of the flux ratios (modeled/measured) show an error less than 20%. The maximum error is 85% – considering that an event causes a flux increase of many orders of magnitude a difference of less than a factor of two is not that bad. In addition a characteristic underestimation of the high energetic proton and electron channels indicates some space for further fine tuning (e.g. in the size of the region which is used for scaling).
   - Qualification: The main aspect of qualifying is the detection of the auroral oval position. This shows whether the K_p-dependent precipitation maps are useful. The entry to the oval is linked with a strong increase in precipitation, therefore the accurateness is needed in particular for the spatial analysis of ionization. Figure 7.1 shows that two of three oval positions are in the correct bin.

     The quality of simulated values along a satellite track is listed in Table 7.2 and has been explained in the corresponding paragraph. In a quiet period the low energetic particles are of special interest for the ionization and precipitate along a relatively stable and determinable oval, resulting in acceptable correlation factors. During an event high energetic particles take over the main interest and show a rather simple precipitation pattern (just polar cap). As a consequence the correlation factor, e.g. for mep0P4 and mep0P5, exceeds 0.9.

---

[*] This must not be misunderstood for the scaling (as described in Section 4.8), which uses the values along the satellite's track, too. The scaling subdivides the earth into four local time sectors. All local measurements within such a sector are used for the 2 h-scaling as far as it lies inside auroral oval. Therefore the scaling is always a combination of the two satellites. In contrast the error discussion abstains from local time sectors and from the auroral oval restriction. Only the enhanced count rates at the equator which reflect trapped particle population and the South Atlantic Anomaly are excluded. Additionally the satellites are examined separately. As a consequence the scaling tries to describe the precipitation within a sector as good as possible while the error discussion simply uses uncut values to compare the local phenomena along the track as good as possible.

Assumptions and limitations: The conversion factor of the ionization rates can be assumed to be exact within a range of less than ±10%. The accuracy of other assumptions and limitations in this section can not be quantified easily. Data gaps and their temporal or spatial interpolation may account for any error. However, it seems to be reasonable to work with interpolations. Otherwise, e.g. the strong benefit of a spatial resolution would not be possible. The assumption of an isotropic pitch-angle resolution may account for a shift in the ionization altitude and, to a limited extend as the particle detectors do not cover the full pitch-angle range, for the total amount of energy deposition. As we expect variations in the pitch-angle distribution, short-term effects may occur, but we expect them to level out on the long run.

The inherent errors in the input data can be subdivided into statistical and conversion errors which are in the range of a few ten percent. An exact determination of inherent errors in in-situ particle measurements is not possible. Some uncertainties like the long-term flux differences in the GOES satellites due to a different detector orientation, may be responsible for one magnitude flux difference (and therewith ionization) at the corresponding altitude. In a brief summary, the different aspects are:

- The statistical error of the count rates (and therefore ionization) will be listed for the maxima of auroral oval/polar cap only. At quiet time they range from 1% to 30%. During a particle event they reduce to 0.4% to 6%, depending on the energy channel. As ionization in geomagnetic quiet time is mainly produced by low energetic particles, the statistical error will reduce to 1–14%. Areas outlying auroral oval and polar cap have larger statistical deviation.
- The error due to conversion is smaller than 3%.
- The error due to crosstalk and aging is potentially higher – however, in many cases it's impossible to optimize third-party instruments. A corrected input data set would be desirable. As long as no corrected data set is available, the count rates are used in the same pragmatic way as many other research groups do. Thus quantitative changes might happen even when the qualitative results persist.

The total error is frightening from the point of view of a laboratory-physicist – looking at an astrophysical or geophysical background, considering that assumptions or measuring limitations may be responsible for even bigger errors, the total error of the model is acceptable.

Goal of this study is the development of a model describing the 3-D ionization based on particle precipitation. Does the sensitivity of a real instrument have an impact on the model results? The answer is a clear "Jein"[*]:

- **No**, because the sorting algorithm uses "doubtful" values, but using an artificial, corrected or even ideal data base would be possible as well. Therefore the development of the model is independent of the behavior of the real instrument.
- **Yes**, the computed ionization rates depend on the quality of the data base. An analysis based on these results has always to keep in mind real instrument effects.

An ideal data set is not available hence we used a pragmatic approach. (1) We did not design these instruments. (2) A correction of instruments of other scientists is not our business. (3) This data is used by various groups as input for 1-D precipitation models (*Jackman et al.*, 2001, 2005a; *Schröter et al.*, 2006). (4) As pointed out in Chapter 6 a correlation with EISCAT and other incoherent scatter radars shows good results and consistent findings on precipitating particles. So even the less than perfect input data can be used to improve our understanding on particle induced ionization and its consequences.

---

[*] German for "yes and no"

7.5 Impact of AIMOS’ Assumptions, Limitations and Errors on Climate Modeling

In addition to EISCAT, the MIPAS satellite allows a verification of the model. AIMOS was part of the HEPPA-MIPAS model inter-comparison. In order to provide a similar and realistic forcing, the AIMOS ionization rates have been adopted to the grids of the following Global Chemistry Models (CTMs) and Global Circulation Models (GCMs): B2dCTM/B3dCTM (*Sinnhuber et al.*, 2003a), *Central Aerological Observatory* model (CAO) (*Krivolutsky and Vyushkova*, 2002), FinROSE (*Damski et al.*, 2007), HAMMONIA (*Schmidt et al.*, 2006), *Karlsruhe Simulation Model of the Middle Atmosphere* (KASIMA) (*Kouker*, 1999), *ECHAM5/MESSy Atmospheric Chemistry model* (EMAC) (*Jöckel et al.*, 2005), *SOlar Climate Ozone Link studies* (SOCOL/SOCOLi) (*Egorova et al.*, 2005; *Schraner et al.*, 2008) and *Whole Atmosphere Community Climate Model* (WACCM) 4 (*Garcia et al.*, 2007).

All climate models convert the ionization rates into NO_y production which then is used as catalyst for atmospheric reactions*. Consequently the total NO_y content is the best test-value for the ionization model, in particular as it is measured by the MIPAS satellite.

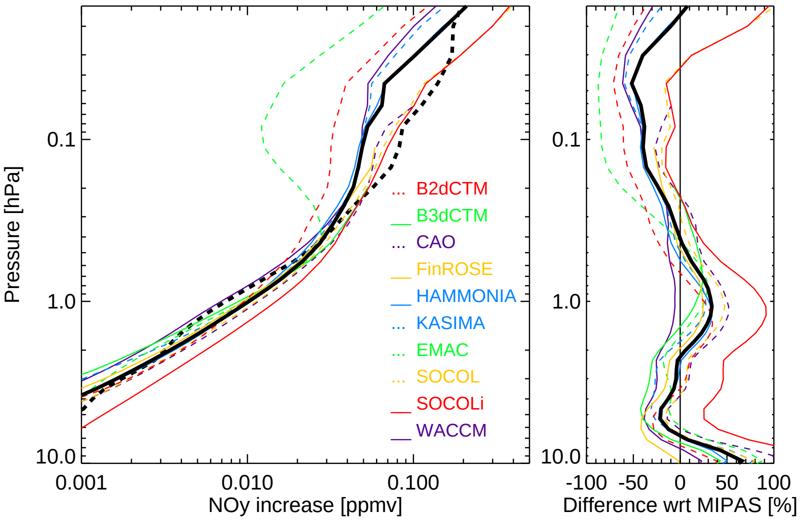

Figure 7.22: Area conserving averages (40°–90°N) of observed and modeled NO_y enhancements during 30 October – 1 November (October event period) with respect to 26 October (left) and relative deviations of modeled averages from MIPAS observations (right). Thick solid and dashed lines represent model mean average and MIPAS observations, respectively (*Funke et al.*, 2010).

The results are shown in Figure 7.22. Assuming that the particle forcing of AIMOS is represented by the mean of the 10 participating climate and chemistry models, we can estimate the errors in comparison to MIPAS measurements. In general model results and MIPAS measurements are in good agreement, which means that the estimated error is less than ±50%. Compared to the variations among the GCMs and CTMs which is –depending on altitude– 50% to more than 150%, the estimated deviation due to AIMOS is small. Nevertheless Figure 7.22 shows a limitation of the ionization model. The pressure level of 0.1 hPa indicates a systematic underestimation while the 1.0 hPa layer is affected by a systematic overestimation in (almost) all models.

Based on a more detailed analysis of the ionization rates (see Figure 7.23), the main area of overestimated flux has been identified as electrons of the mep0e3 channel, ionizing at 1 hPa. Most prominent is the effect at 40–50°N, as this area is almost devoid from ionization of other channels. The ionization rate at a pressure range of 0.1–1 hPa is given by electron precipitation at 300 keV to 5 MeV only. As the highest electron channel on POES does not provide data up to 5 MeV, the energy spectra was extended according

---

*All models use the same conversion factors to transform ionization rate into nitric oxides except for MESSy (*Baumgaertner*, 2010).

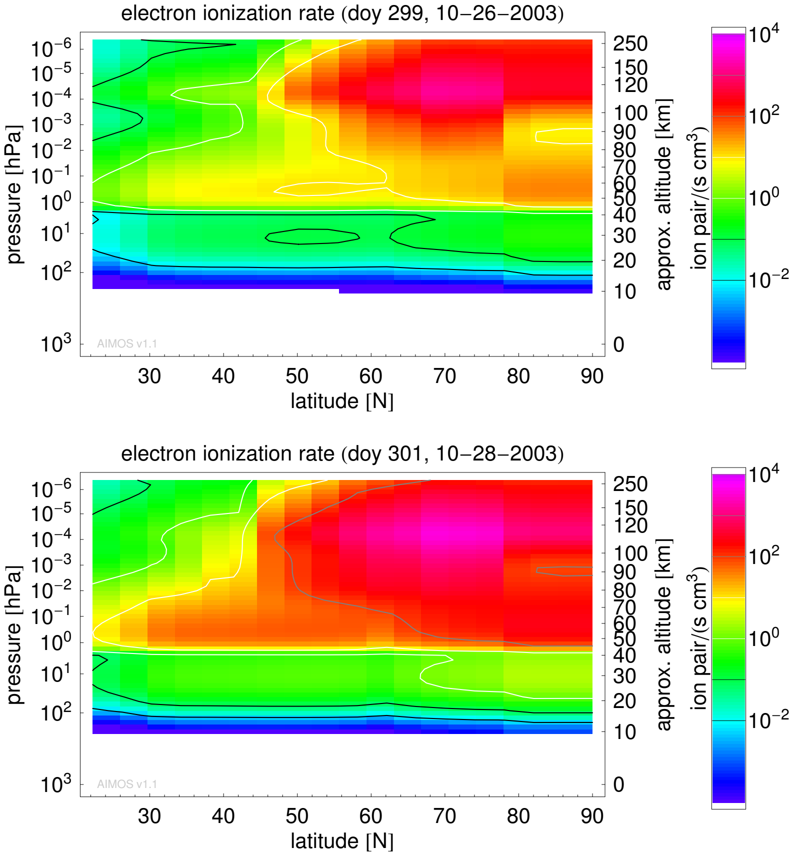

Figure 7.23: Electron ionization rate at doy 299 (top) and 301 (bottom), 2003. The pressure at 1 hPa and slightly above shows unexpected high rates due to faulty flux values from the mep0e3 channel. The most prominent anomaly is located at 40–50°N as this area is devoid of forcing from the other electron channels. In periods of increased high energetic particle flux (day 301) the anomaly is more pronounced.

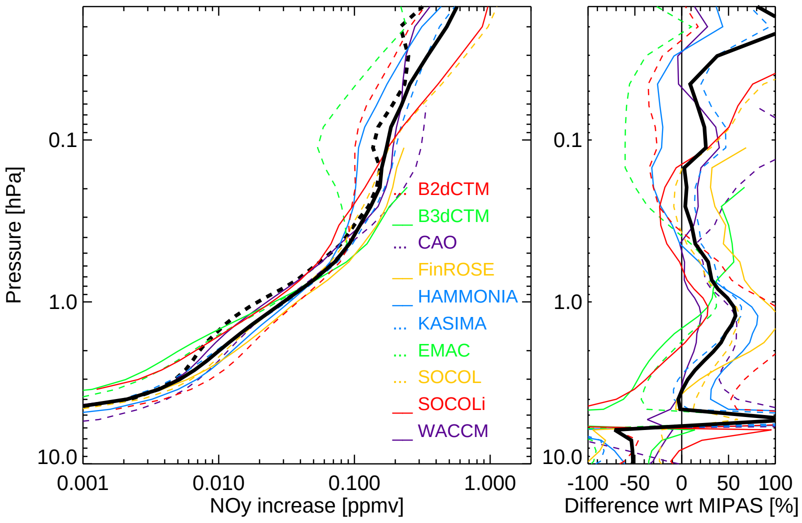

Figure 7.24: Same as Figure 7.22 for 80°–90°N, (private communication Bernd Funke, Instituto de Astrofísica de Andalucía).

to *Klassen et al.* (2005). However, the increased $\mathrm{NO_y}$ at 1 hPa questions the validity of our approach. In addition the energy range of the highest electron channel mep0e3 is not known for sure (privat communication Susan Greer, NOAA) and it might be smaller than the published 300 keV–2.5 MeV (*Evans and Greer*, 2004). A smaller energy range would give an increase to $\mathrm{NO_y}$ production at 0.1 hPa. Anyhow please take note the ionization rate at this altitude varies by four orders of magnitude during the observed period and other sources of error can not be excluded totally.

Apart from the systematic discrepancy, one main concern is the $\mathrm{NO_y}$ spread at a certain location. While Figure 7.22 covers a wide range of latitudes, transportation by atmospheric wind can be almost neglected. Within a smaller latitude range (see Figure 7.24 for 80°–90°N) different dynamics seem to have a major impact. Consequently Figure 7.24 shows the typical uncertainties of climate models that will affect comparisons with local measurements like e.g. EISCAT (see Chapter 6).

Chapter 8

Final Remarks and Outlook

This chapter gives a short summary of the main aspects of this work as they were discussed in the included papers. Since the model is unique in deriving spatial (and temporal) impact of proton, electron and alpha particles on a wide energy range, it is used as ionization module in numerous simulations in combination with various climate and chemistry models. Section 8.2 lists some examples. The ionization rates have to be adopted to different model grids, therefore a web-page has been developed, allowing easy transformations to user specific grids as well as online access of the AIMOS data in general. There is always some space for further development, so the outlook (see Section 8.3) lists some future aspects that might give a benefit to the model as well as it lists tasks that might be approached with the help of the model.

8.1 Main Aspects of this Thesis

Wissing et al. (2008) sets the basis of the model conception. Results as flux differences and variations of the spatial particle precipitation corresponding to local time sectors (in particular below 300 keV) give a clear indication that an ionization model should deal with different local time sectors. The equatorward motion of the auroral particle precipitation area with geomagnetic activity leads to a K_p-based description by mean precipitation maps. And last but not least, the different precipitation areas of solar and magnetospheric particles as well as their independent occurrence are the reason for the partially separate internal handling of these particles in AIMOS.

The first AIMOS paper (*Wissing and Kallenrode*, 2009), like all three AIMOS papers published in *Journal of Geophysical Research*, provides the model description. The model includes precipitating magnetospheric and solar particles (electrons, protons and alpha particles) in a full 3-D ionization model due to a combination of 2-D precipitation maps and a Monte Carlo ionization algorithm. First results show that during solar particle events ionization in the strato- and mesosphere is mainly due to protons while electron ionization dominates with increasing height of the atmosphere and in particular in the lower thermosphere.

In the second AIMOS paper (*Wissing et al.*, 2010a) the ionization rates are used as forcing for the Bremen three-dimensional chemistry and transport model (B3dCTM) in order to compare the more complex spatial pattern to a simple geomagnetic 60° polar cap precipitation pattern as it is used in many other studies (see Table 1.1). In addition the benefit of electron ionization in addition to (solar) proton forcing is discussed and compared to common ionization models that are limited to protons or electrons. Main results are, comparing proton precipitation only, that there is no significant difference in the precipitation area in the north while the southern hemisphere shows differences. The location of the geomagnetic south pole is not identical to the center of the main precipitation area as given by satellite measurements (and empirically used in AIMOS). Concerning the additional impact of electrons the total ionization column by electron exceeds the one of protons, except for the polar cap during the main phase of a particle event. As most of the electron impact concentrates above 80 km, an increased altitude range may be beneficial for GCM models. Mesospheric ozone can be significantly affected by magnetospheric electrons precipitating at high latitudes during polar winter. And as the electron precipitation is not restricted to highly disturbed times, quite time electron precipitation may affect stratospheric and mesospheric ozone – at least during polar winter. The additional impact of magnetospheric electrons induce 10–15% of the stratospheric ozone depletion during polar winter. In addition evidence for downward $\mathrm{NO_x}$ transport is shown, implying indirect electron impact below the threshold of 45 km altitude, which is given by the highest electron energy channel.

The third AIMOS paper (*Wissing et al.*, 2011) describes the thermospheric electron density as determined by the HAMMONIA model using AIMOS data as input. Results of this model chain are compared to incoherent scatter radar (ISR) measurements. Therefore this paper is an important part of the model verification at high altitudes; in particular as different geographic locations are compared. It allows a test of the spatial precipitation pattern. The most important results are that the average ratio of ISR measurements and AIMOS/HAMMONIA-modeled electron densities is close to 1 at day and night, while night-time simulations without particle forcing underestimate electron densities by 2 to 3 orders of magnitude. Consequently during night-time the largest part of the ionization at polar latitudes is caused by particles. In terms of overall quantitative agreement at least 60% of the night-time ratios (modeled/measured) are between 0.2 and 1.4 if particle precipitation is considered. As the ionization model has a spatial resolution, emphasis is on the simulation at different locations. Even though the particle precipitation shows strong latitudinal dependence, followed by a modeled variation of 1 order of magnitude in electron density in the observed night-time period, the median of the ratio of measured and modeled electron density is close to 1 in the polar cap and approximately 0.7 (slight underestimation) at auroral latitudes, respectively. The accuracy of the model chain's electron density does not significantly depend on the geomagnetic disturbance – which lends a strong support to the sorting algorithm.

AIMOS data are also used for the inter-comparison of different atmospheric models. *Funke et al.* (2010) discusses the effect of particle induced ionization on the lower atmosphere. AIMOS data are used in combination with 10 different CTMs and GCMs and compared to MIPAS measurements of certain atmospheric constituents. This paper gives an estimation of the combined model accuracy in the lower atmosphere. The main aspects concerning AIMOS are summarized in Section 7.5. First, the mean of all models' $\mathrm{NO_y}$ simulations is close to the MIPAS measurements. Second, at 1 hPa a faulty description of the highest electron channel leads to an overestimation of the AIMOS electron ionization.

Model acronym	description
B2dCTM	Bremen 2-D Chemistry-Transport-Model, CTM, *Sinnhuber et al.* (2003a)
B3dCTM	Bremen 3-D Chemistry-Transport-Model, CTM, *Sinnhuber et al.* (2003a) and see publication *Wissing et al.* (2010a)
CAO	Central Aerological Observatory model, *Krivolutsky and Vyushkova* (2002)
EMAC	ECHAM5/MESSy Atmospheric Chemistry model, GCM, *Jöckel et al.* (2005)
FinROSE	middle atmospheric CTM, *Damski et al.* (2007)
HAMMONIA	HAMburg MOdel of the Neutral and Ionized Atmosphere, GCM, *Schmidt et al.* (2006) and see publication *Wissing et al.* (2011)
KASIMA	KArlsruhe SImulation Model of the middle Atmosphere, CTM, *Kouker* (1999)
SOCOL/ SOCOLi	SOlar Climate Ozone Link studies, GCM *Egorova et al.* (2005); *Schraner et al.* (2008)
WACCM4	Whole Atmosphere Community Climate Model (4), GCM, *Garcia et al.* (2007)

Table 8.1: Overview on climate models that use AIMOS ionization data. All these models participate is the HEPPA-MIPAS model inter-comparison. Some of them are used in additional collaborations.

8.2 Benefit of the Model

The main benefit of the model is the most comprehensive (see Table 1.1) coverage of particle species and energy in combination with a high spatial resolution and altitude range. So it can be used to simulate the natural climate variability due to particle forcing in combination with a GCM. In the same way as NO_y and ozone changes can be estimated, the impact on global circulation can be modeled.

8.2.1 International Collaborations using AIMOS Data

Originally the AIMOS model was designed to provide ionization data for the HAMMONIA model. During the model development, it became evident that particle induced ionization data was needed by various CTMs and GCMs worldwide. In particular as the altitude range of climate model increases compared to older models to consider vertical coupling, the impact of particle precipitation becomes more important. Consequently, the AIMOS model project has been modified in order to provide ionization data for different user specifications. All ionization data is available online and can be adopted to almost any user specific grid (see Section 8.2.2).

The tasks that are under examination with the help of AIMOS ionization data range from the occurrence of noctilucent clouds (cooperation with W. Singer), production and destruction of trace gases as e.g. NO_y, Ozone and Chlorine (different cooperations with e.g. M. Sinnhuber, J. Kieser, N. Wieters, H. Winkler, S. Kazeminejad and A. Krivolutsky) to the inter-comparison of climate models (10 participating GCMs and CTMs allowing inter-comparison of the chemistry module and comparison to MIPAS measurements at the same time, see *Funke et al.* (2010)).

Table 8.1 gives a list of the models using AIMOS data. Apart from that the fruitful collaborations in terms of publications and presentations are listed in Section 9.2 and 9.3.

8.2.2 Web-Applet

In most cases the AIMOS ionization rates are used in combination with a second model e.g. a GCM or CTM. However, the secondary model grids normally differ (in pressure levels, latitudinal or horizontal spacing, geographic/geomagnetic grid system and time) compared to the internal resolution of AIMOS. For this reason the primary AIMOS output as to be adopted to the secondary grid, which can be done interactively on `http://aimos.physik.uos.de`. A more scientific aspect is that different particle forcing can be simulated as e.g. a 1-D polar cap forcing similar to *Schröter et al.* (2006); *Jackman et al.* (2001, 2005a) which has been done in *Wissing et al.* (2010a). In addition, it might be useful to access ionization rates over a certain location e.g. a radar site, as it has been done in collaboration with W. Singer (see presentations at IAGA and in London, Ontario in 2009, Section 9.3). And last but not least, the ionization rate at a specific pressure, longitude or latitude cross section can easily be extracted via web-applet (see Figure 8.1).

Within all grid transformations the original cells are weighted corresponding to their spatial fraction included in the secondary cells.

A test account including all functions can be accessed by login: `guest`, password: `guest`. As this account can be accessed and modified by everyone, we recommend long-lasting grid transformations to be run on an individual account.

8.3 Outlook

In this Section I will list some aspects still being under development or part of recent discussion. We will start with technical features that might give a benefit to the model, while scientific questions, that might be approached with the help of AIMOS, will be discussed afterwards.

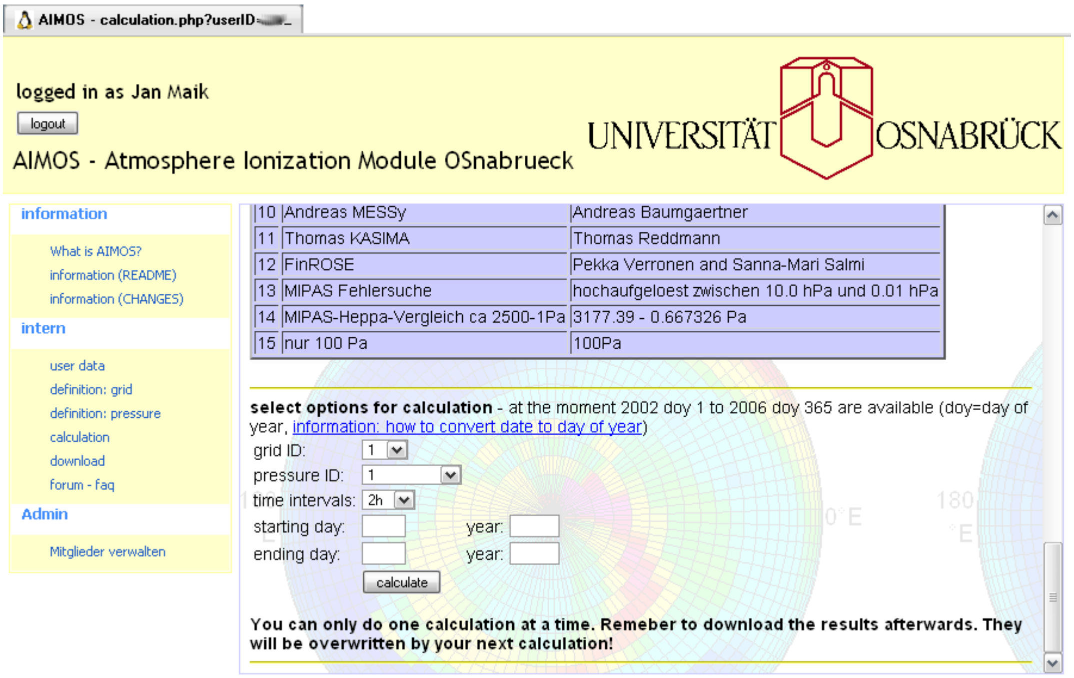

AIMOS - calculation.php?userID=[redacted]

logged in as Jan Maik

AIMOS - Atmosphere Ionization Module OSnabrueck

10	Andreas MESSy	Andreas Baumgaertner
11	Thomas KASIMA	Thomas Reddmann
12	FinROSE	Pekka Verronen and Sanna-Mari Salmi
13	MIPAS Fehlersuche	hochaufgeloest zwischen 10.0 hPa und 0.01 hPa
14	MIPAS-Heppa-Vergleich ca 2500-1Pa	3177.39 - 0.667326 Pa
15	nur 100 Pa	100Pa

select options for calculation - at the moment 2002 doy 1 to 2006 doy 365 are available (doy=day of year, information: how to convert date to day of year)

grid ID: 1
pressure ID: 1
time intervals: 2h
starting day: year:
ending day: year:

You can only do one calculation at a time. Remeber to download the results afterwards. They will be overwritten by your next calculation!

Figure 8.1: AIMOS homepage `http://aimos.physik.uos.de`

The quality of the input data set seems to have the most significant impact on AIMOS results. In particular including the highest electron channel is questionable (see Section 7.5

and *Funke et al.* (2010)). Recent comparisons to MIPAS measurements indicate that this channel has a faulty description of the upper energy threshold. According to Susan Greer (privat communication, NOAA) the upper energy threshold is not known for sure, even though is was given in *Evans and Greer* (2004). Consequently it might be a benefit for the model to ignore this channel completely. This would result in an uplift of the lower altitude range of the electron ionization to 70 km.

A second problem is the quality of the GOES data while the satellite is in the magnetosheath (see Section 7.3.7). At the moment no correction method is known. First attempts of a detection of these periods are presented in *Badorreck* (2010). Using a night-side GOES satellite during periods of an impacting shock might solve this problem.

Apart from changes in the model or the input data set, the temporal coverage will be enlarged by using recent satellites.

The Monte Carlo model, which is part of the energy deposition algorithm, runs without a magnetic field. In general we assume that this is not a major limitation of the model as the condition of unlimited lateral extend at every grid point compensates it. However, a simulation of particle precipitation inside the South Atlantic Anomaly as well as modeling the lateral shift of ionization at auroral latitudes need a magnetic field. A comparison to the model of *Fang et al.* (2007) might be helpful here.

From the scientific/physical point of view AIMOS can be used for simulations of (natural changes in) global circulation. The spatial distribution of precipitation particles and the linked changes in atmospheric composition will induce temperature changes (by direct heating as well as changes in the electromagnetic absorption) and therefore it has an impact on winds and the circulation itself.

Another interesting topic is the recent solar minimum which is almost devoid of solar particle events. Given that AIMOS is capable of modeling magnetospheric particle precipitation, the ionizing effect of these low energetic particles can be described and their impact on the atmosphere can be evaluated without superposing high-energetic particles. Apart from that, changes of the precipitation patterns, as described in *Spamer* (2010), may be analyzed and compared to other periods.

Chapter 9

Appendix

This Chapter will provide some information on the satellites NOAA-POES and -GOES and the particle instruments used in this study. In addition, Section 9.4 lists the acronyms including a brief description.

9.1 Satellites

Choosing an appropriate particle data base the following aspects have to be considered:

- The satellite has to be equipped with suitable particle detectors.
- The detector's energy range and its viewing direction should be applicable.
- The satellite's orbit is to cover the precipitation areas.
- In addition the availability of the data has to be considered.

In order to use a long data base satellite programs like NOAA-POES or NOAA-GOES are a good choice as old satellites will be replaced by new ones equipped with similar instruments.

9.1.1 POES

The spatial resolved count rates originate from the **P***olar* **O***perational* **E***nvironmental* **S***atellites* from NOAA[*]. The POES' orbit is at 850 km altitude (*Schätzing*, 2005, see page 498), having an inclination of 98°. Therefore, the POES satellites in-situ measurements cover the area from 82°S to 82°N. A minimal precession assures sun-synchronous equator crossing at a constant local time. The southbound equator crossing of NOAA-15 is at 7:30, respectively 19:30 in northbound direction. NOAA-16 crosses the equator at 2:00h in southbound direction and 14:00 in northbound direction resulting in a night-midday orbit. As the initial local time setup may alter during operation, the exact position has to be clarified for every satellite and year. Concerning NOAA-15/16 the local time position can be considered as constant during 2002 to 2005. One orbit takes 102 min – equivalent to 14.1 orbits a day.

Particle Detector (SEM/2)

POES is equipped with the **S***pace* **E***nvironment* **M***onitor*/2 particle detector. The SEM/2 subdivides into a Data Processing Unit (DPU) and 2 detector units, the Total Energy Detector (TED) and the Medium Energy Proton and Electron Detector (MEPED). Both detectors are installed in pairs having different viewing directions. The viewing directions of the MEPED instrument are horizontally backward to the direction of motion (marked with index 90) and

---

[*] National Oceanic and Atmospheric Administration

vertically looking away from the Earth (marked with 0)*. Regarding the TED detectors, one is looking radially outward (index 0) and the other is tilted by 30° to the outward direction (*Evans and Greer*, 2004). As no ion mass separation is provided in the POES-SEM/2 we can only assume that the majority of the detector response follows proton injections. GOES is equipped with proton and alpha detectors and shows significant proton domination. Therefore, we do not expect a considerable mistake for this reason.

TED

The **T***otal* **E***nergy* **D***etector* measures low energetic proton and electron flux ranging from 0.05 to 20 keV divided into 16 channels. TED contains 8 detector systems based on different cylindrically shaped electrostatic charged plates. Only particles with appropriate charge and energy may pass the analyzer. At the outlet, a **C***ontinuous* **D***ynode* **E***lectron* **M***ultiplier* produces an impulse for every particle. Detailed information on the TED can be found in *Evans and Greer* (2004).

In AIMOS we concentrated on the energy channels that are provided in the free available data set. These are the energy bands 4, 8, 11 and 14. The corresponding energy ranges are listed in Table 9.1.

energy band	lower energy border	center of energy	upper energy border	energy bandwidth
4	154 eV	189 eV	224 eV	70 eV
8	688 eV	844 eV	1000 eV	312 eV
11	2115 eV	2595 eV	3075 eV	961 eV
14	6503 eV	7980 eV	9457 eV	2954 eV

Table 9.1: TED energy bands (protons as well as electrons)

Calibration The Total Energy Detectors vary due to production. Therefore, every detector has to be calibrated. The calibration factors are given in *Evans and Greer* (2004) based on measurements prior to the launch (see Table 9.2).

channel	TED S/N 011 (NOAA-15) calibration factor	TED S/N 010 (NOAA-16) calibration factor
electron band 4	2.167×10^6	3.568×10^6
electron band 8	5.013×10^5	8.229×10^5
electron band 11	3.305×10^5	4.043×10^5
electron band 14	1.521×10^5	2.041×10^5
proton band 4	1.060×10^6	1.218×10^6
proton band 8	1.971×10^5	1.907×10^5
proton band 11	4.064×10^5	5.524×10^5
proton band 14	9.763×10^4	1.260×10^5

Table 9.2: Calibration factors belonging to the radially outward looking (0°) TED detector on NOAA-15/16. In order to get [particles/(m^2 s sr MeV)] a factor of 10^6 has to be used in addition to the calibration.

---

[*] Being precise, the real direction is shifted by 9° to these values as these positions are blocked by other instrumentation. However, the viewing angle of 30° allows to ignore the slight shifting.

MEPED

The **M***edium* **E***nergy* **P***roton and* **E***lectron* **D***etektor* (see Figure 9.1) consists of a detector for electrons and one for protons.

Electron Detector The detector opening is 30°.The semiconductor detector consists of a 700 μm silicon surface barrier detector having an area of 25 mm^2. The upper side of the detector is laminated with an aluminum foil, reducing the sensitivity to light. In addition, a nickel foil of 0.76 μm is located upon the sensitive layer, reducing the sensitivity to light and low energetic protons. The wrapper shield consists of aluminum and tungsten inhibiting lateral impact of electrons below 6 MeV and protons below 90 MeV. The energy deposition inside the detector is analyzed corresponding to the pulse level – levels above 2.5 MeV are subducted giving the upper energy bound of the highest electron channel. The electron channels on POES are integral channels. As the energy-intensity spectra needs differential channels, these are produced by subtraction. The differential channels are called: mep0e1_e2 representing mep0e1-mep0e2 and mep0e2_e3 representing mep0e2-mep0e3. The resulting energy borders for all channels are listed in Table 4.1.

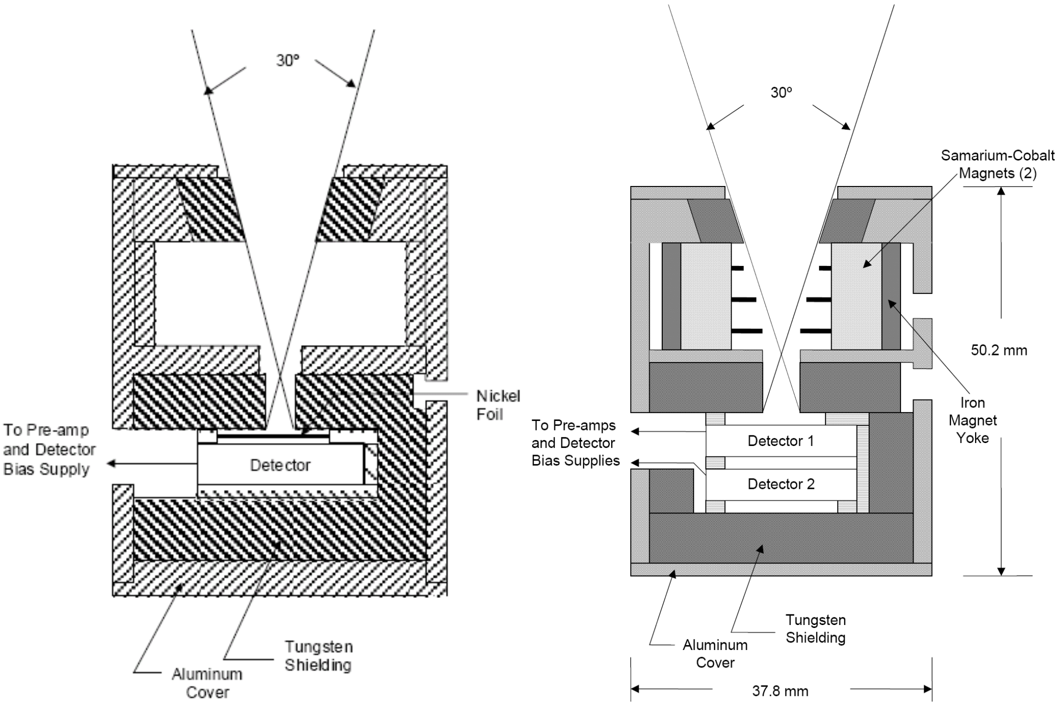

Figure 9.1: POES MEPED detectors for electrons (left) and protons (right), from *Evans and Greer* (2004).

Proton Detector The MEPED proton detector is, likewise the electron detector, designed as a telescope construction and it also has a 30° opening. As for the electron detector, the wrapper shielding consists of aluminum and tungsten repelling lateral impact of electrons below 6 MeV and protons below 90 MeV. Behind the entry, the proton detector is equipped with a 0.2 T magnetic field deflecting electrons with energies below 1 MeV. Additionally, an aluminum foil protects the detector against sunlight. The sensitive core of the detector is based on 2 silicon surface barrier detectors, arranged one behind another. The energy deposition in the upper detector is assigned to the 5 energy channels ranging from 30 keV to 6.9 MeV corresponding to the pulse level. Particles entering the second detector and producing a coincident response in the front detector are assigned to the sixth energy channel. As this channel has no upper energy border we will not use it.

9.1.2 GOES

The **G***eostationary* **O***perational* **E***nvironmental* **S***atellite Programm* is a combined project of the **N***ational* **A***eronautics and* **S***pace* **A***dministration* and **N***ational* **O***ceanic and* **A***tmospheric* **A***dministration*. Main tasks are meteorological measurements as weather forecast or hurricane warnings. Additionally, GOES contains the satellite rescue system SARSAT and, concerning our topic, the **E***nergetic* **P***article* **S***ensor*. As indicated in the name, GOES orbits at 36000 km altitude on a fixed longitude above the equator.

Energetic Particle Sensor (EPS)

The **E***nergetic* **P***article* **S***ensor* on board GOES subdivides into a telescope detector and a dome detector. The EPS looks backward to the direction of motion (or in other words: it looks westward). As GOES-11 spins, is has no constant viewing direction.

Telescope Detector The telescope detector is equipped with a 70° opening and measures protons and alphas. An aluminum foil protects the detector from light contamination. To avoid lateral particle contamination, the detector is shielded by a tungsten wrapper. Electrons below 100 keV can not enter the opening as a deflector magnet is placed beyond the mouthpiece. The sensitive core consists of 2 silicon surface barrier detectors, the first 50 μm thick with 100 mm^2 area and the one underneath having twice the surface area and a thickness of 500 μm. The telescope detector counts protons of 0.8 to 15 MeV. Nominally, the detector is sensible to 3.2 to 60 MeV/particle alphas[*]. Within the GOES handbook it reads 4–60 MeV. Since it is not mentioned if the proton or the alpha energy range is exact, I will use the value as given in the GOES handbook. The electric charge resulting from a particle incident is classified as channels P1, P2, P3, A1, A2 or A3 corresponding to the pulse height level.

Dome Detector The dome detector measures electrons, protons and alphas. It has an opening of 95° and consists of three pairs of silicon surface barrier detectors – having a thickness of 1500 μm and an expanse of 25 mm^2 each. These detector pairs are surrounded by different decelerating materials. The division into particle species and energy is again done by pulse level height. The detector covers a range of 15–500 MeV for protons (in 4 subdivisions), 60–500 MeV for alphas in 3 subdivisions and $\leq$0.6 MeV to ≤ 4 MeV for electrons (in 3 subdivisions). The exact energy borders are given in Table 4.1.

---

[*] The official technical handbooks disagree whether the energy borders for alpha particles are given in 'per particle' or 'per nucleon'. Therefore I used the Bethe-Bloch equation to figure out that it is 'per particle' and Dan Wilkinson from NOAA (private communication) confirmed it.

9.2 Publications

2008

- Wissing, J.M., J.P. Bornebusch and M.-B. Kallenrode: Variation of Energetic Particle Precipitation with Local Magnetic Time, *Adv. Space Res.* **41** (8) 1274–1278, doi:10.1016/j.asr.2007.05.063, **young scientist's paper award**

2009

- Wissing, J.M. and M.-B. Kallenrode: Atmospheric Ionization Module OSnabrück (AIMOS): A 3-D model to determine atmospheric ionization by energetic charged particles from different populations, *J. Geophys. Res.*, **114**, A06104, doi:10.1029/2008JA013884
- Bornebusch, J.P., J.M. Wissing and M.-B. Kallenrode: Solar Particle Precipitation into the Polar Atmosphere and their Dependence on Hemisphere and Local Time, *Adv. Space Res.*, Volume **45** (5), available online 15 November 2009, p. 632–637, doi:10.1016/j.asr.2009.11.008

2010

- Wissing, J.M., M.-B. Kallenrode, N. Wieters, H. Winkler and M. Sinnhuber, Atmospheric Ionization Module Osnabrück (AIMOS): 2. Total particle inventory in the October/November 2003 event and ozone, *J. Geophys. Res.*, **115**, A02308, doi:10.1029/2009JA014419
- Sinnhuber, M., S. Kazeminejad, and J.M. Wissing, Interannual variation of NO_x from the lower thermosphere to the upper stratosphere in the years 1991–2005, *J. Geophys. Res.*, **in press**, doi:10.1029/2010JA015825
- Wissing, J.M., M.-B. Kallenrode, J. Kieser, H. Schmidt, M.T. Rietveld, A. Strømme and P.J. Erickson, Atmospheric Ionization Module OSnabrück (AIMOS) 3: Comparison of electron density simulations by AIMOS/HAMMONIA and incoherent scatter radar measurements, **submitted**[*] **to** *J. Geophys. Res.*
- Funke, B., A. Baumgärtner, M. Calisto, C.H. Jackman, J. Kieser, A. Krivolutsky, M. López-Puertas, T. Reddmann, E. Rozanov, S.-M. Salmi, M. Sinnhuber, G.P. Stiller, P.T. Verronen, S. Versick, T. von Clarmann, N. Wieters and J.M. Wissing, Composition changes induced by the "Halloween" solar proton event: the HEPPA model versus MIPAS data intercomparison study, **in preparation for** *Atmos. Chem. Phys.*, 2010

As my contribution to *Sinnhuber et al.* (2010), *Bornebusch et al.* (2010) and *Funke et al.* (2010) was not as first author, these papers are not included in the thesis.

---

[*] The published version of the dissertation includes the final version of the AIMOS-3 paper as published on August 11, 2011.

9.3 Presentations/Posters

2006

EGU Vienna

- Wissing, J.M., J.P. Bornebusch and M.-B. Kallenrode: Spatial Precipitation Patterns of Energetic Particles, oral
- Bornebusch, J.P., J.M. Wissing and M.-B. Kallenrode: Particle precipitation at the poles, poster

COSPAR Beijing

- Wissing, J.M., J.P. Bornebusch and M.-B. Kallenrode: Variation of Energetic Particle Precipitation with Special Focus on Local Magnetic Time, poster
- Bornebusch, J.P., J.M. Wissing and M.-B. Kallenrode: Influences on Polar Particle Precipitation, poster

2007

Second International Conference on Earth System Modelling - Hamburg

- Wissing, J.M., M.-B. Kallenrode, H. Winkler, M. Sinnhuber, J. Kieser and H. Schmidt: Spatial Ozone Depletion resulting from total Particle Inventory, poster

DACH Meteorologentagung Hamburg

- Kieser, J., H. Schmidt, M.-B. Kallenrode and J.M. Wissing: Der Einfluss solarer und magnetosphärischer Partikel auf die mittlere und obere Atmosphäre - Simulationen mit einem Allgemeinen Zirkulations- und Chemiemodell

2008

CAWSES Berlin

- Wissing, J.M., M.-B. Kallenrode, J. Kieser and H. Schmidt: Impact of solar and magnetospheric particles on the entire atmosphere - Introduction to the 3D ionization model AIMOS, oral

DPG-Frühjahrstagung Freiburg

- Wissing, J.M., M.-B. Kallenrode, J. Kieser and H. Schmidt: Verteilung und Auswirkung ionisierenden Teilcheneinfalls am Beispiel des Oktoberereignisses 2003, oral

EGU Vienna

- Wissing, J.M. and M.-B. Kallenrode: Impact of solar and magnetospheric particles on the entire atmosphere, poster

1st HEPPA Helsinki

- Wissing, J.M., M.-B. Kallenrode, J. Kieser and H. Schmidt: Impact of solar and magnetospheric particles on the entire atmosphere - a view on global ionization with ARTOS, poster
- Kieser, J., H. Schmidt, J.M. Wissing and M.-B. Kallenrode: The influence of precipitating solar and magnetospheric particles on the entire atmosphere - Simulations with HAMMONIA
- Winkler, H., M. Sinnhuber, J.P. Burrows, J. Notholt, M. Scharringhausen, J.M. Wissing and M.-B. Kallenrode: The Mg/Mg+ system during the solar particle events in October/November 2003, poster

MIPAS Karlsruhe

- Wissing, J.M. and M.-B. Kallenrode: Impact of solar and magnetospheric particles on the entire atmosphere - a view on global ionization with AIMOS, oral

2009

CAWSES Bonn

- Wissing, J.M. and M.-B. Kallenrode: The Atmospheric Response to Solar Variability - Simulations with a 3D Particle Precipitation Model for the Entire Atmosphere, oral
- Wissing, J.M. and M.-B. Kallenrode: The Atmospheric Response to Solar Variability ARTOS-AIMOS - Simulations with a 3D Particle Precipitation Model for the Entire Atmosphere, poster

EGU Vienna

- Kieser J., H. Schmidt, J. M. Wissing and M.-B. Kallenrode: The influence of precipitating solar and magnetospheric particles on the entire atmosphere - Simulations with HAMMONIA
- Sinnhuber M., H. Winkler, N. Wieters, S. Kazeminejad, J.M. Wissing, M.-B. Kallenrode, G.P. Stiller and T. von Clarmann: Middle atmospheric ion chemistry during energetic particle events, and impacts on the neutral chemistry, poster

Saariselkä, Finland

- Wissing, J.M. and M.-B. Kallenrode: Energetic Particle Precipitation into the Atmosphere, oral

2nd HEPPA Boulder

- Wissing, J.M., M.-B. Kallenrode, M. Sinnhuber, N. Wieters and H. Winkler: Variation of particle induced ionization due to different models and boundary conditions, oral
- Winkler, H., S. Kazeminejad, N. Wieters, J.M. Wissing, M.-B. Kallenrode, M. Sinnhuber and J. Notholt: Chlorine activation due to solar proton events
- Kieser, J., H. Schmidt, J.M. Wissing and M.-B. Kallenrode: The influence of precipitating solar and magnetospheric particles on the entire atmosphere - Simulations with HAMMONIA
- Sinnhuber, M., M.-B. Kallenrode, S. Kazeminejad, N. Wieters and J.M. Wissing: The contribution of electron precipitation to middle atmosphere composition
- Wieters, N., M. Sinnhuber, G. Stiller, J.M. Wissing and J. Notholt: Modeled impact of atmospheric ionization by solar protons and magnetospheric electrons on upper stratospheric constituents compared with MIPAS measurements

IAGA Sopron

- Singer, W., N. Swarnalingam, J.M. Wissing, R. Latteck, M.-B. Kallenrode, C. Meek, A.H. Manson, J. Drummond and W.K. Hocking: Longitudinal Differences of the PMSE strength at high arctic latitudes

London Ontario

- Singer, W., N. Swarnalingam, J.M. Wissing, R. Latteck, C. Meek, A.H. Manson, W.K. Hocking and W. Ward: Longitudinal differences of PMSE strength at high Arctic latitudes and their relation to precipitating particles

2010

COSPAR Bremen

- Wieters, N., M. Sinnhuber, H. Winkler, U. Berger, J.M. Wissing, G. Stiller, B. Funke and J. Notholt: Model simulations of the impact of energetic particle precipitation onto the upper and middle atmosphere
- Krivolutsky, A., J.M. Wissing, T. Vyushkova and L. Cherepanova: Motions in the MLT polar regions induced by energetic particles as simulated by GCM

- Winkler, H., N. Rahpoe, C. von Savigny, J.P. Burrows, J.M. Wissing and M.-B. Kallenrode: Ion-chemical impacts of solar particle events on noctilucent clouds
- Krivolutsky, A., M. Banin, J.M. Wissing and T. Vyushkova: Simulations with CAO-3D model of photochemical response caused by precipitating electrons and solar protons at both polar regions during geomagnetic storms in October-November 2003 (preliminary comparison with MIPAS data)
- Winkler, H., M. Sinnhuber, J. Notholt, J.M. Wissing, M.-B. Kallenrode and M. Santee: Impacts of the January 2005 solar particle events on middle atmospheric chlorine species

SCOSTEP Berlin

- Wissing, J.M., M.-B. Kallenrode, J. Kieser, H. Schmidt, M. Rietveld, M. McCready and P. Erickson: Modeling electron density in E- and F-layer: Comparison of the model chain AIMOS-HAMMONIA and ISR measurements, oral
- Engler N., J. Röttger, I. Strelnikova, Q. Li, M. Rapp, J. Kieser, H. Schmidt, J.M. Wissing, M.-B. Kallenrode, S. Marker, H. Lühr and P. Hoffmann: Summary of German observational results obtained with EISCAT in the frame of the CAWSES priority program, oral
- Kieser J., H. Schmidt, Wissing, J.M. and M.-B. Kallenrode: The influence of precipitating solar and magnetospheric particles on the entire atmosphere - Simulations with HAMMONIA, oral
- Sinnhuber M., B. Funke, M.-B. Kallenrode, S. Kazeminejad, G. Stiller, N. Wieters and J.M. Wissing: The contribution of electron precipitation to middle atmosphere composition, oral
- Wieters N., H. Winkler, M. Sinnhuber, J. Notholt, J.M. Wissing, U. Berger, G. Stiller, T. Von Clarmann and B. Funke: Three dimensional model simulations of the impact of ion-chemistry induced by solar particle precipitation onto chlorine species, poster
- Winkler H., S. Kazeminejad, N. Wieters, M. Sinnhuber, J.M. Wissing, M.-B. Kallenrode, G. Stiller, T. Von Clarmann, B. Funke, M. Santee and J.M. Russell III: Effects of solar particle events on the middle atmosphere's chlorine chemistry, oral

EGU Vienna

- Winkler, H., M. Sinnhuber, J.M. Wissing, M.-B. Kallenrode, G. Stiller and T.v.Clarmann: Impacts of solar particle events on middle atmospheric chlorine compounds, poster
- Latteck, R., W. Singer, N. Swarnalingam, J.M. Wissing, C. Meek, A.H. Manson, J. Drummond and W.K. Hocking: Longitudinal differences of the PMSE strength at high Arctic latitudes, poster

For abstracts, see `http://sun.physik.uos.de/~maik/publications/`.

9.4 Acronyms

acronym	description
ACE (EPAM/-SWEPAM/MAG)	Advanced Composition Explorer and instruments, for detailed information, see `http://www.srl.caltech.edu/ACE/`
AIMOS	*Atmosphere Ionization Module OSnabrück*, see all Sections...
A_p	geomagnetic index, `http://www.ngdc.noaa.gov/stp/geomag/kp_ap.html`
AU	Astronomical Unit, 149.598 Gm
B2dCTM	Bremen 2-D Chemistry-Transport-Model, CTM, amongst others participating in the HEPPA-MIPAS model inter-comparison, *Sinnhuber et al.* (2003a)
B3dCTM	Bremen 3-D Chemistry-Transport-Model, CTM, amongst others participating in the HEPPA-MIPAS model inter-comparison, *Sinnhuber et al.* (2003a)
CAO	Central Aerological Observatory model, participating in the HEPPA-MIPAS model inter-comparison, *Krivolutsky and Vyushkova* (2002)
CME	Coronal Mass Ejection, see Section 1.2.2
CTM	Global Chemistry Model, sometimes also called General Chemistry Model
DMSP	Defense Meteorological Satellite Program, `http://www.ngdc.noaa.gov/dmsp/index.html`
EISCAT	European Incoherent SCATter radar
doy	day of year, starting with 1 at January 1st, conversion table at: `http://daac.gsfc.nasa.gov/julian_calendar.shtml`
DST	Disturbance Storm Time index, geomagnetic index, *Koskinen and Huttunen* (2006)
EMAC	ECHAM5/MESSy Atmospheric Chemistry model, GCM, participating in the HEPPA-MIPAS model inter-comparison, *Jöckel et al.* (2005)
EPS	Energetic Particle Sensor on GOES, see Section 9.1.2
F10.7	10.7 cm solar flux used as an index for solar activity, see Section 2.2.1, `http://modelweb.gsfc.nasa.gov/solar/ottawa.html`
FinROSE	middle atmospheric CTM, participating in the HEPPA-MIPAS model inter-comparison, *Damski et al.* (2007)
GCM	Global Circulation Model, sometimes also called General Circulation Model
GCR	Galactic Cosmic Rays, see Section 1.2 and Section 2.1
GEANT4	GEometry ANd Tracking, C++ Monte Carlo Toolkit for particle simulations, provided by the CERN, see Section 2.2.3
GOES	Geostationary Operational Environmental Satellite, see Section 9.1.2
HAMMONIA	HAMburg MOdel of the Neutral and Ionized Atmosphere, GCM, amongst others participating in the HEPPA-MIPAS model inter-comparison, *Schmidt et al.* (2006)
HEPPA-MIPAS	Inter-comparison of different GCMs and CTMs using AIMOS ionization rates and including a comparison to MIPAS measurements, paper in preparation
IGRF	International Geomagnetic Reference Field (IGRF-10), `http://wdc.kugi.kyoto-u.ac.jp/igrf/index.html`
IMP	Interplanetary Monitoring Platform on board some of the Explorer satellites
ISEE	International Sun-Earth Explorer Satellite
ISR	Incoherent Scatter Radar

continued on next page

continued from previous page

acronym	description
KASIMA	KArlsruhe SImulation Model of the middle Atmosphere, CTM, participating in the HEPPA-MIPAS model intercomparison, *Kouker* (1999)
K_p	Planetare Kennziffer, geomagnetic index, `http://swdcwww.kugi.kyoto-u.ac.jp/kp/`, *Bartels et al.* (1939); *Gonzalez et al.* (1994)
LTAN	Local Time Ascending Node (at equator-crossing)
MEPED	Medium Energy Proton and Electron Detector on POES, see Section 9.1.1
MIPAS	Michelson Interferometer for Passive Atmospheric Sounding on ENVISAT, allowing spectral analysis of the atmosphere by limb sounding, `http://envisat.esa.int/instruments/mipas/`, part of the HEPPA-MIPAS model inter-comparison
MLT	Magnetic Local Time
MPI	Max-Planck-Institut
NIST (PSTAR/-ASTAR)	National Institute of Standards and Technology, Excitation energy, stopping-power and range tables for protons/alphas, `http://physics.nist.gov/cgi-bin/Star/compos.pl`, `http://physics.nist.gov/PhysRefData/Star/Text/programs.html`, *ICRU* (1993)
NOAA	National Oceanic and Atmospheric Administration, operating the POES and GOES satellites, `http://www.noaa.gov`
N-15/16	NOAA POES-15/16 satellite, see Section 9.1.1
POES	Polar Operational Environmental Satellites, see Section 9.1.1
R_E	Earth radius, approximately 6370 km
SAA	South Atlantic Anomaly, a region of weak geomagnetic field
SAMPEX	Solar Anomalous and Magnetospheric Particle Explorer, `http://sunland.gsfc.nasa.gov/smex/sampex/`
SBUV/2	Solid Backscatter UltraViolet radiometer on POES, `http://goespoes.gsfc.nasa.gov/poes/instruments/sbuv.html`
SCIAMACHY	Scanning Imaging Absorption Spectrometer for Atmospheric CHartographY on ENVISAT, allowing detection of trace gases in the atmosphere, `http://envisat.esa.int/earth/www/object/index.cfm?fobjectid=1671`
SEM/1	Space Environment Monitor/1 on NOAA POES-14 and earlier. The electron detector is similar to the SEM/2 electron detector. The energy ranges of the proton detector are different, see `http://www.ngdc.noaa.gov/stp/satellite/poes/documentation.html`
SEM/2	Space Environment Monitor/2, see Section 9.1.1
SEP	Solar Energetic Particles, see Section 1.2.2
SOCOL(i)	SOlar Climate Ozone Link studies, GCM, participating in the HEPPA-MIPAS model inter-comparison, *Egorova et al.* (2005); *Schraner et al.* (2008)
SOHO	Solar and Heliospheric Observatory, `http://sohowww.nascom.nasa.gov`
SPE	Solar Proton Event: as particle events also include other species, Solar Energetic Particle (SEP) event is used in most cases
TED	Total Energy Detector on POES, see Section 9.1.1
TEP	Total Electron Production rate, vertically integrated ion pair production rate
UT and UTC	Universal Time and Universal Time Coordinated, as both do not differ by more than 0.9 s, they are used as one.
WACCM4	Whole Atmosphere Community Climate Model (4), GCM, participating in the HEPPA-MIPAS model inter-comparison, *Garcia et al.* (2007)

Bibliography

Agostinelli, S. et al., GEANT4-a simulation toolkit, *Nucl. Instr. Meth.* **506**, p. 250–303, 2003 60, 82, 101, 124

Alfven, H. and C.-G. Faelthammar, Cosmical electrodynamics: fundamental principles, *Clarendon Press*, 1963 16

Anderson, K.A. and J.R. Winckler, Solar Flare X-Ray Burst on September 28, 1961 *J. Geophys. Res.*, Vol. **67**, No. 11, p. 4103–4117, 1962 15

Asikainen, T. and K. Mursula, Recalibration of long-term NOAA/MEPED energetic proton measurements, submitted to *J. of Atmos. and Sol.-Terr. Phys.*, 2010 145

Badorreck, H., Identifizierung des Aufenthaltes der GOES-Satelliten bezüglich der Magnetopause, Bachelor thesis, University of Osnabrück, 2010 155

Baker, D.N., What is space waether?, *Adv. Space Res*, **22**, p. 7–16, 1998 16

Bakker, C.J. and E. Segrè, Stopping Power and Energy Loss for Ion Pair Production for 340-MeV Protons, *Phys. Rev.*, **81**, p. 489–492, 1951 137

Banks, P.M., Joule heating in the high-latitude mesosphere, *J. Geophys. Res.*, **84**, p. 6709–6712, 1979 13

Bartels, J., N.H. Heck and H.F. Johnston, The three-hour-range index measuring geomagnetic activity, *J. Geophys. Res.*, **44**, p. 411–454, 1939 16, 166

Barton, C., Survey Tracks Current Position of South Magnetic pole, *EOS*, **83**(27), p. 291, 2002 96

Baumgaertner, A.J.G., Jöckel, P., Riede, H., Stiller, G. and B. Funke, Energetic particle precipitation in ECHAM5/MESSy Part 2: Solar Proton Events, *Atmos Chem. Phys. Discuss.*, **10**, p. 4501–4542, `http://www.atmos-chem-phys-discuss.net/10/4501/2010/`, 2010 148

Bazilevskaya, G.A., Observations of variability in cosmic rays, *Space Sci. Rev.*, **94**, p. 25–38, 2000 25

Berger, M.J., S.M. Seltzer and K. Maeda, Energy deposition by auroral electrons in the atmosphere, *J. Atm. Solar-Terr. Phys.* **32**, p. 1015–1045, 1970 19, 39, 68

Bieber, J.W., J. Clem, P. Evenson, R. Pyle, D. Ruffolo and A. Sáiz, Relativistic solar neutrons and protons on 28 October 2003, *Geophys. Res. Lett.*, **32**, L03S02, doi:10.1029/2004GL021492, 2005 83

Bornebusch, J.P., J.M. Wissing and M.-B. Kallenrode, Solar particle precipitation into the polar atmosphere and their dependence on hemisphere and local time, *Adv. Space Res.*, Vol. **45** (5), p. 632–637, doi:10.1016/j.asr.2009.11.008, 2010 36, 161

Breunig, E., Die totale Trägerbildung langsamer Kathodenstrahlen in der Nähe der Trägerbildungsspannung, *Annalen der Physik*, 5. Folge, Band 25, p. 467–480, 1936 135

Brueckner, G.E., J.-P. Delaboudiniere, R.A. Howard, S.E. Paswaters, O.C.St. Cyr, R. Schwenn, P. Lamy, G.M. Simnett, B. Thompson and D. Wang, Geomagnetic storms caused by coronal mass ejections (CMEs): March 1996 through June 1997 *Geophys. Res. Lett.*, **25** (15), p. 3019–3022, doi:10.1029/98GL00704, 1998 15

Callis, L.B, R.E. Boughner, D.N. Baker, R.A. Mewaldt, J.B. Blake, R.S. Selesnick, J.R. Cummings, M. Natarajan, G.M. Mason and J.E. Mazur, Precipitating electrons: evidence for effects on mesospheric odd nitrogen, *Geophys. Res. Lett.* **23**, p. 1901–1904, 1996 11, 17, 58, 82, 100

Callis, L.B., D.N. Baker, M. Natarajan, J.B. Blake, R.A. Mewaldt, R.S. Selesnick and J.R Cummings, A 2-D model simulation of downward transport of NO_y into the stratosphere: effects on the austral spring O_3 and NO_y, *Geophys. Res. Lett* **23**, p. 1905, 1996 3, 4, 17, 58

Callis, L.B., Odd nitrogen formed by energetic electron precipitation as calculated from TIROS data, *Geophys. Res. Letters*, vol 24, No 24, p. 3237–3240, 1997 19

Callis, L.B., M. Natarajan, D. S. Evans and J. D, Lambeth, Solar atmospheric coupling by electrons (SOLACE) 1. Effects of the May 12, 1997 solar event on the middle atmosphere, *J. Geophys. Res.* **103**, p. 28 405–28 419, 1998 17, 19, 58, 68

Callis, L.B. and J. D, Lambeth, $\mathrm{NO_y}$ formed by precipitating electron events in 1991 and 1992: Descent into the stratosphere as observed by ISAMS, *Geophys. Res. Let.*, Vol. **25**, No. 11, p. 1875–1878, 1998. 19

Callis, L.B., M. Natarajan and J.D. Lambeth, Solar atmospheric coupling by electrons (SOLACE), 3. Comparison of simulations and observations, 1979–1997, issues and implications, *J. Geophys. Res.* **106**, p. 7523–7539, 2001 3, 4, 17, 47, 82, 100

Chian, A.C.-L. and Y. Kamide, An Overview of Solar-Terrestrial Environment, in: Handbook of the Solar-Terrestrial Environment, *Springer Verlag*, doi:10.1007/11367758_1, 2007 14

Cliver, E.W., B. Klecker, M.-B. Kallenrode and H.V. Cane, Researchers discuss role of flares and shocks in SEP events, *EOS Trans. AGU*, 8̲3, p. 132, 2002 15

Codrescu, M.V., T.J. Fuller-Rowell, R.G. Roble and D.S. Evans, Medium energy particle precipitation influences on the mesosphere and lower thermosphere, *J. Geophys. Res.*, **102**, p. 19 977–19 987, 1997 82

Collis, P.N., The high latitude D-region and mesosphere revealed by the EISCAT incoherent scatter radars during solar proton events, *Adv. Space Res.* Vol. **18**, No. 3, p. (3)83–(3)92, 1996 100

Crutzen, P.J., I.S.A. Isaksen and G.C. Reid, Solar proton events: stratospheric sources of nitric oxide, *Science*, **189**, p. 457, 1975 3, 4, 11, 14, 57, 81, 100

Daglis, I.A., W.I. Axford, E.T. Sarris, S. Livi and B. Wilken, Particle acceleration in geospace and its association with solar events, *Sol. Phys.*, **172**, p. 287–296, 1997 15

Damski, J., L. Thlix, L. Backman, P. Taalas and M. Kulmala, FinROSE - middle atmospheric chemistry transport model, *Boreal Env. Res.*, **12**, p. 535–550, 2007. 148, 153, 165

Datlowe, D., Relativistic Electrons in Solar Particle Events, *Solar Phys.*, **17**, p. 436–458, 1971 17

Degenstein, D.A., N.D. Lloyd, A.E. Bourassa, R.L. Gattinger and E.J. Llewellyn, Observations of mesospheric ozone depletion during the October 28, 2003 solar proton event by OSIRIS, *Geophys. Res. Lett.*, **32**, L03S11, doi:10.1029/2004GL021521, 2005 83

Dobbin, A.L., E.M. Griffin, A.D. Aylward and G.H. Millward, 3-D GCM modelling of thermospheric nitric oxide during the 2003 Halloween storm, *Annales Geophys.*, **24**, p. 2403–2412, 2006 83

Dungey, J.W., Interplaneary magnetic field and the auroral zones, *Phys. Rev. Lett.*, **6**, p. 47–48, 1961 15

Egorova, T., E. Rozanov, V. Zubov, E. Manzini, W. Schmutz and T. Peter, Chemistry-climate model SOCOL: a validation of the present-day climatology, *Atmos. Chem. Phys.*, **5**, p. 1557–1576, doi:1680-7324/acp/2005-5-1557, 2005 148, 153, 166

EISCAT-Group, Printable summary sheet giving the principal parameters of the high latitude incoherent scatter radars (EISCAT VHF, UHF, EISCAT Svalbard Radar, AMISR, and the Sondrestrom Radar), `http://e7.eiscat.se/groups/Documentation/BasicInfo/ISRfactsheet.pdf`, 2003 103

Eisl, A., Über die Ionisierung von Luft durch Kathodenstrahlen von 10-60 kV, *Ann. Phys.*, **3**, p. 277–313, 1929 135

Evans, D.S. and M.S. Greer, NOAA Technical Memorandum, Polar Orbiting Environmental Satellite Space Environment Monitor - 2 Instrument Descriptions and Archive Data Documentation, `www.ngdc.noaa.gov/stp/NOAA/docs/SEM2v1.4b.pdf`, 2004 48, 66, 83, 138, 142, 150, 155, 158, 159

Evans, D.S., General update: SEM-2 performance on the operating satellites during 2007, `http://poes.ngdc.noaa.gov/docs/status_2008_01_10.pdf`, 2008 139, 141, 142, 145, 146

Fang, X., M.W. Liemohn, J.U. Kozyra and S.C. Solomon, Quantification of the spreading effect of auroral proton precipitation, *J. Geophys. Res.*, **109**, A04309, doi:10.1029/2003JA010119, 2004 39

Fang, X., M.W. Liemohn, J.U. Kozyra and S.C. Solomon, Study of the proton arc spreading effect on primary ionization rates, *J. Geophys. Res.*, **110**, A07302, doi:10.1029/2004JA010915, 2005 38

Fang, X., M.W. Liemohn, J.U. Kozyra, D.S. Evans, A.D. DeJong and B.A. Emery, Global 30-240 keV proton precipitation in the 17-18 April 2002 geomagnetic storms: 1. Patterns, *J. Geophys. Res.*, **112**, A05301, doi:10.1029/2006JA011867, 2007 17, 18, 19, 155

Fang, X., C.E. Randall, D. Lummerzheim, S.C. Solomon, M.J. Mills, D.R. Marsh, C.H. Jackman, W. Wang and G. Lu, Electron impact ionization: A new parameterization for 100 eV to 1 MeV electrons, *J. Geophys. Res.*, **113**, A09311, doi:10.1029/2008JA013384, 2008 19, 26, 58

Farley, D.T., Incoherent Scatter radar Probing, in Modern Ionospheric, *Science*, (Kohl, H., Ruster, R. and Schlegel, K., eds), EGS Publications, Katlenburg-Lindau, p. 415–439, 1996 104

Farrugia, C.J., H. Matsui, H. Kucharek, R.B. Torbert, C.W. Smith, V.K. Jordanova, K.W. Ogilvie, R.P. Lepping, D.B. Berdichevsky, T. Terasawa, J. Kasper, T. Mukai, Y. Saito and R. Skoug, Interplanetary coronal mass ejection and ambient interplanetary magnetic field correlations during the Sun-Earth connection events of October–November 2003, *J. Geophys. Res.*, **110**, A09S13, doi:10.1029/2004JA010968, 2005 83

Fermi, E., On the Origin of the Cosmic Radiation, *Physics Review*, **75**, p. 1169–1174, 1949 26

Forbush, S.E., Three unusual cosmic-ray increases possibly due to charged particles from the Sun, *Phys. Rev.*, **70**, p. 771–772, 1946 15

Freund, L., Die totale Trägerbildung langsamer Kathodenstrahlen in Luft, *Annalen der Physik*, 5. Folge, Band 22., p. 748–760, 1935 135

Friedrich, M., K.M. Torkar, W. Singer, I. Strelnikova, M. Rapp and S. Robertson, Signatures of mesospheric particles in ionospheric data, *Ann. Geophys.*, **27**, p. 823–829, 2009 100

Funke, B., A. Baumgaertner, M. Calisto, C.H. Jackman, J. Kieser, A. Krivolutsky, M. López-Puertas, T. Reddmann, E. Rozanov, S.-M. Salmi, M. Sinnhuber, G.P. Stiller, P.T. Verronen, S. Versick, T. von Clarmann, N. Wieters and J.M. Wissing, Composition changes induced by the "Halloween" solar proton event: the HEPPA model versus MIPAS data intercomparison study, *in preparation for Atmos. Chem. Phys.*, 2010 20, 148, 152, 153, 155, 161

Gaertner, O., Relative Ionisierung der schweren Edelgase sowie von N, O, Luft, CO2, CH4, C2H4, C2H2 und Propan, gemessen mit der Kα-Linie von Kupfer, *Annalen der Physik*, Volume **415**, Issue 3, p. 255–258, 1935 135

Garcia, R.R., D.R. Marsh, D.E. Kinnison, B.A. Boville and F. Sassi, Simulation of secular trends in the middle atmosphere, *J. Geophys. Res.*, **112**, D09301, doi:10.1029/2006JD007485, 2007 148, 153, 166

Gonzalez, W.D., J.A. Joselyn, Y. Kamide, H.W. Kroehl, G. Rostoker, B.T. Tsurutani and V.M. Vasyliunas, What is a geomagnetic storm?, *J. Geophys. Res.*, **99**, p. 5771–5792, 1994 16, 166

Gonzalez, W.D., B.T. Tsurutani and A.L. Clúa de Gonzalez, Interplanetary origin of geomagnetic storms, *Space Sci. Rev.*, **88**, p. 529–562, 1999 15

Gopalswamy, N., S. Yashiro, Y. Liu, G. Michalek, A. Vourlidas, M.L. Kaiser and R.A. Howard, Coronal mass ejections and other extreme characteristics of the 2003 October–November solar eruptions, *J. Geophys. Res.*, **110**, A09S15, doi:10.1029/2004JA010958, 2005 83

Gordon, W.E., Incoherent scattering of radio waves by free electrons with applications to space exploration by radar, *Proc. IRE*, **46**, p. 1824, 1958 100

Gosling, J., J.R. Asbridge, S.J. Bame, W.C. Feldman, R.D. Zwickl, G. Paschmann, N. Sckopke and R.J. Hynds, Interplanetary ions during an energetic storm particle event - The distribution function from solar-wind thermal energies to 1.6 MeV, *J. Geophys. Res.*, **86**, p. 547, 1981 26

Gray, L.H., Ionization method of measuring neutron energy, *Proc. Camb. Phil. Soc.*, **40**, p. 72, 1944 135, 137

Hardy, D.A., M.S. Gussenhoven and D. Brautigam, A statistical model of the auroral ion precipitation, *J. Geophys. Res.*, **94**, p. 370, 1989 17, 18, 19

Heath, D.F., A.J. Krüger and P.J. Crutzen, Solar proton event: influence in stratospheric ozone, *Science*, **197**, p. 886–889, 1977 11, 47, 57, 81, 100

Iijima, T. and T.A. Potemra, The amplitude distribution of field-aligned currents at northern high latitudes observed by Triad, *J. Geophys. Res.*, **81**, p. 2165–2174, 1976 55

International Commission on Radiation Units and Measurements (ICRU), Stopping Powers and Ranges for Protons and Alpha Particles, *ICRU Report* **49**, 1993 33, 41, 166

Jackman, C.H., J.E. Frederick and R.S. Stolarski, Production of odd nitrogen in the stratosphere and mesosphere: An intercomparison of source strengths, *J. Geophys. Res.*, **85**, p. 7495–7505, 1980 26

Jackman, C.H. and R.D. McPeters, The response of ozone to solar proton events during solar cycle 21: a theoretical interpretation, *J. Geophys. Res.* **90**, p. 7955–7966, 1985 17, 82, 100

Jackman, C.H., A.R. Douglass, R.B. Rood, R.D. McPeters, P.E. Meade, Effect of solar proton events on the middle atmosphere during the past two solar cycles as computed using a two-dimentional model, *J. Geophys. Res.*, **95** (D6), p. 7417–7428, 1990 11, 137

Jackman, C.H., E.L. Fleming and F.M. Vitt: Influence of extremely large solar proton events in a changing stratosphere, *J. Geophys. Res.*, **105**, p. 11 659–11 670, 2000 3, 4, 47, 81, 89, 100

Jackman, C.H., R.D. McPeters, G.J. Labow, E.L. Fleming, C.J. Praderas and J.M. Russell, Northern hemisphere atmospheric effects due to the July 2000 Solar Proton Event, *Geophys. Res. Lett.*, **28**(15), p. 2883–2886, 2001 12, 17, 18, 19, 20, 58, 82, 147, 154

Jackman, C.H., M.T. DeLand, G.J. Labow, E.L. Fleming, D.K. Weisenstein, M.K.W. Ko, M. Sinnhuber, and J.M. Russell, Neutral atmospheric influences of the solar proton events in October–November 2003, *J. Geophys. Res.*, **110**, A09S27, doi:10.1029/2004JA010888, 2005a 17, 19, 58, 68, 69, 82, 83, 102, 147, 154

Jackman, C.H., M.T. DeLand, G.J. Labow, E.L. Fleming, D.K. Weisenstein, M.K.W. Ko, M. Sinnhuber, J. Anderson and J.M. Russell, The influence of the several very large solar proton events in years 2000–2003 on the neutral middle atmosphere, *Adv. Space Res.*, **35**, p. 445–450. doi:10.1016/j.asr.2004.09.006, 2005b 26, 33, 89

Jackman, C.H., D.R. Marsh, F.M. Vitt, R.R. Garcia, E.L. Fleming, G.J. Labow, C.E. Randall, M. López-Puertas, B. Funke, T. von Clarmann and G.P. Stiller, Short- and medium-term atmospheric constituent effects of very large solar proton events, *Atmos. Chem. Phys.*, **8**, p. 765–785, 2008 82

Jöckel, P., R. Sander, A. Kerkweg, H. Tost and J. Lelieveld, Technical Note: The Modular Earth Submodel System (MESSy) – a new approach towards Earth System Modeling, *Atmos. Chem. Phys.*, **5**, p. 433–444, 2005 148, 153, 165

Kahler, S. and A. Ling, Comparison of E > 20 MeV proton geomagnetic cutoffs observed on SAMPEX with predictions based on the SEPTR model, *Proc. 27th Int. Cosmic Ray Conf.*, p. 4060, 2001 17, 58

Kalicinsky, C., Prezipierende magnetosphärische Teilchen und die Zuverlässigkeit der Satellitenmessungen, Diploma Thesis, Universität Osnabrück, 2008 140, 144

Kallenrode, M.-B., Current views on impulsive and gradual solar energetic particle events, *J. Geophys. G. Nucl. Part. Phys.*, **29**, p. 965–981, 2003 15, 17

Kallenrode, M.-B., Space Physics, *Springer*, 3. Auflage, 2004 26

Kamide, Y. and Y.P. Maltser, Geomagnetic Storms, in Y. Kamide and A. Chian; Handbook of the solar Terrestrial Environment, *Springer*, p. 356–374, 2007 15

Kinnison, D.E., G.P. Brasseur, S. Walters, R.R. Garcia, D.R. Marsh, F. Sassi, V.L. Harvey, C.E. Randall, L. Emmons, J.F. Lamarque, P. Hess, J.J. Orlando, X.X. Tie, W. Randel, L.L. Pan, A. Gettelman, C. Granier, T. Diehl, U. Niemeier, A.J. Simmons, Sensitivity of chemical tracers to meteorological parameters in the MOZART-3 chemical transport model, *J. Geophys. Res.*, **112**(D20), doi:10.1029/2006JD007879, 2007 102

Kirkwood, S., A. Osepian and N. Smirnova, Quantitative description of electron precipitation during auroral absorption events in the morning/noon local-time sector, *Journal of Atmospheric and Solar-Terrestrial Physics*, **63**, (18), p. 1907–1921, doi:10.1016/S1364-6826(01)00070-0, 2001 100

Klassen, A., V. Bothmer, G. Mann, M.J. Reiner, S. Krucker, A. Vourlidas and H. Kunow, Solar energetic electron events and coronal shocks, *Astronomy and Astrophysics*, Vol. **385**, No. 3, p. 1078–1088, DOI: 10.1051/0004-6361:20020205, 2002 17

Klassen, A., S. Krucker, H. Kunow, R. Müller-Mellin, R. Wimmer-Schweingruber, G. Mann and A. Posner, Solar energetic electrons related to the 28 October 2003 flare, *J. Geophys. Res.*, **110**, A09S04, doi:10.1029/2004JA010910, 2005 61, 83, 150

Koskinen, H.E.J. and K.E. Huttunen, Space Weather: From Solar Eruptions to Magnetospheric Storms, in: Solar Eruptions and Energetic Particles, *Geophysical Monograph Series*, **165**, AGU, 2006 15, 16, 165

Kouker, W., D. Offermann, V. Küll, T. Reddmann, R. Ruhnke and A. Franzen, Streamers observed by the CRISTA experiment and simulated in the KASIMA model, *J. Geophys. Res.*, **104** (D13), p. 16 405–16 418, 1999 148, 153, 166

Krivolutsky, A.A. and T.Y. Vyushkova, Three-dimensional photochemical transport model for the middle atmosphere (Basic variant), *Scientific Report* **1.3.2.15**, Central Aerological Observatory, Russian Service for Hydrometeorology and EnvironmentalMonitoring, 2002 148, 153, 165

Kulenkampff, H., Über die Ionisierung von Luft durch Röntgen- und Kathodenstrahlen, *Annalen der Physik*, Volume **385**, Issue 11, p. 261–278, 1926 135

Larson, H.V., Energy Loss Per Ion Pair for Protons in Various Gases, *Phys. Rev.*, **112**, 6, p. 1927–1928, 1958 137

Lary, D.J., Catalytic destruction of stratospheric ozone, *J. Geophys. Res.*, **102** (D17), p. 21 515–21 526, 1997 89

Leske, R.A., M.A. Mewaldt, E.C. Stone and T.T. von Rosenvinge, Geomagnetic cutoff variations during solar energetic particle events – implications for the space station, *Proc. 25th Int. Cosmic Ray Conf.,* **2**, p. 381–384, 1995 17, 47, 82

Leske, R.A., R.A. Mewaldt, E.C. Stone and T.T. von Rosenvinge: Observations of geomagnetic cutoff variations during solar energetic particle events and implications for the radiation environment at the Space Station, *J. Geophys. Res. 106*, p. 30 011–30 022, 2001 15, 17, 47, 58, 82

López-Puertas, M., B. Funke, S. Gil-López, T. von Clarmann, G.P. Stiller, M. Höpfner, S. Kellmann, H. Fischer and C.H. Jackman, Observation of NO_x enhancement and ozone depletion in the Northern and Southern Hemispheres after the October–November 2003 solar proton events, *J. Geophys. Res.*, **110**, A09S43, doi:10.1029/2005JA011050, 2005 83

Maire, M., D.H. Wright, H. Kurashige, L. Urban, V. Ivantchenko, H. Burkhardt, V. Grichine, P. Gumplinger, R. Kokoulin, A. Rybin, S. Kelner, H. Araujo, A. Forti, V. Lefebure, P. Nieminen, M.G. Pia, G. Depaola, F. Longo, A. Trindade, P. Rodrigues, L. Peralta, A. Mantero, L. Pandola, J. Weng, M. Takahata, H.P. Wellisch, T. Koi, P. Truscott, N. Starkov, N. Kanaya, N.V. Mokhov, M.V. Mossov, A. Heikkinen, N. Stepanov and V. Lara, GEANT4 - Physics Reference Manual, Dez. 2007, for GEANT4-version 4.9.1. 135

Manzini, E., M.A. Giorgetta, M. Esch, L. Kornblueh and E. Roeckner, The influence of sea surface temperatures on the northern winter stratosphere: Ensemble simulations with the MAECHAM5 model, *J. Climate*, **19**(16), p. 3863–3881, 2006 102

Marsh, D.R., R.R. Garcia, D.E. Kinnison, B.A. Boville, F. Sassi, S.C. Solomon and K. Matthes, Modeling the whole atmosphere response to solar cycle changes in radiative and geomagnetic forcing, *J. Geophys. Res.*, **112**, doi:10.1029/2006JD008306, 2007 18, 58

McPeters, R.D. and C.H. Jackman, The response of ozone to solar proton events during solar cycle 21: the observations, *J. Geophys. Res. 90*, p. 7945, 1985 17, 58

Mewaldt, R.A., C.M.S. Cohen, A.W. Labrador, R.A. Leske, G.M. Mason, M.I. Desai, M.D. Looper, J.E. Mazur, R.S. Selesnick and D.K. Haggerty, Proton, helium, and electron spectra during the large solar particle events of October–November 2003, *J. Geophys. Res.*, **110**, A09S18, doi:10.1029/2005JA011038, 2005 18, 26, 58, 66, 68, 69, 83

Miroshnichenko, L.I., K.-L. Klein, G. Trottet, P. Lantos, E.V. Vashenyuk, Y.V. Balabin and B.B. Gvozdevsky, Relativistic nucleon and electron production in the 2003 October 28 solar event, *J. Geophys. Res.*, **110**, A09S08, doi:10.1029/2004JA010936, 2005 83

National Aeronautics and Space Administration, *GOES I-M DataBook*, *DRL 101-08*, Goddard Space Flight Cent., Greenbelt, Md. (available at `http://goes.gsfc.nasa.gov/text/databook/databook.pdf`), 1996 66, 83

Orsolini, Y.J., G.L. Manney, M.L. Santee and C.E. Randall, An upper stratospheric layer of enhanced HNO_3 following exceptional solar storms, *Geophys. Res. Lett.*, **32**, L12S01, doi:10.1029/2004GL021588, 2005 83

Pallamraju, D. and S. Chakrabarti, First ground-based measurements of OI 6300 Å; daytime aurora over Boston in response to the 30 October 2003 geomagnetic storm, *Geophys. Res. Lett.*, **32**, L03S10, doi:10.1029/2004GL021417, 2005 83

Palm, M., N. Wieters, M. Sinnhuber, S.H.W. Golchert, C.G. Hoffmann, J. Notholt and G. Hochschild, Stratospheric and Mesospheric O3 above Spitsbergen modeled by a 3D chemical transport model and measured by ground-based millimeter wave radiometry, submitted to *J. Geophys. Res.*, 2009 96

Picone, M., A.E. Hedin and D. Drob, Neutral densities and temperature from ground to thermosphere, NRLMSIS-00 empirical atmosphere model, `http://nssdcftp.gsfc.nasa.gov/models/atmospheric/msis/nrlmsise00` 40

Porter, H.S., C.H. Jackman and A.E.S. Green, Efficiencies for production of atomic nitrogen and oxygen by relativistic proton impact in air, *Journal of Chem. Phys.*, **65**, p. 154–167, doi 10.1063/1.432812, 1976 83, 102, 137

Prather, M., Numerical Advection by Conservation of Second-Order Moments, *Journal of Geophysical Research*, **91**, p. 6671–6681, 1986 83

Randall, C.E., V.L. Harvey, G.L. Manney, Y. Orsolini, M. Codrescu, C. Sioris, S. Brohede, C.S. Haley, L.L. Gordley, J.M. Zawodny and J.M. Russell, Stratospheric effects of energetic particle precipitation in 2003–2004, *Geophys. Res. Lett.* **32**, L05802, doi:10.1029/2004GL022003, 2005 3, 4, 12, 81, 82, 100

Randall, C.E., V.L. Harvey, C.S. Singleton, P.F Bernath, C.D. Boone and J.U. Kozyra, Enhanced NO_x in 2006 linked to stronger upper stratospheric Arctic vortex, *Geophys. Res. Lett.*, **33**, doi:10.1029/2006GL027160, 2006 3, 4, 12

Randall, C.E., V.L. Harvey, C.S. Singleton, S.M. Bailey, P.F. Bernath, M. Codrescu, H. Nakajima and J.M. Russell III, Energetic particle precipitation effects on the Southern Hemisphere stratosphere in 1992–2005, *J. Geophys. Res.*, **112**, D08308, doi:10.1029/2006JD007696, 2007 58, 82, 100

Randel, W.J. and J.B. Cobb, Coherent variations of monthly mean total ozone and lower stratosphere temperature, *J. Geophys. Res.*, **99**, D3, p. 5433–5447, 1994 13

Reagan, J.B., R.E. Meyerott, R.W. Nightingale, R.C. Gunton, R.G. Johnson, J.E. Evans, W.L. Imhof, D.F. Heath and A.J. Krueger, Effects of the August 1972 solar particle events on stratospheric ozone, *J. Geophys. Res.*, **86**, p. 1473–1494, 1981 13

Reames, D.V., Particle acceleration at the Sun and in the heliosphere, *Space Sci. Rev.*, **90**, p. 413–491, 1999 15, 17, 24, 25

Reid, G.C., S. Solomon and R.R. Garcia, Response of the middle atmosphere to the solar proton events of August-December 1989, *Geophysical Research Letters*, **18**, 6, p. 1019–1022, 1991 3, 4

Roble, R.G. and E.C. Ridley, An auroral model for the NCAR thermospheric general circulation model (TGCM), *Ann. Geophys.*, **5A**, p. 369–382, 1987 18, 19, 26, 58, 102

Roettger, J., EISCAT – The European incoherent scatter radar for studying the polar atmosphere, *Mitteilungen der Astronomischen Gesellschaft Hamburg*, **58**, p.67–79, `http://adsabs.harvard.edu/abs/1983MitAG..58...67R`, 1983 104

Rohen, G., C. von Savigny, M. Sinnhuber, E.J. Llewellyn, J.W. Kaiser, C.H. Jackman, M.-B. Kallenrode, J. Schröter, K.-U. Eichmann, H. Bovensmann and J.P. Burrows, Ozone depletion during the solar proton events of October/November 2003 as seen by SCIAMACHY, *J. Geophys. Res.* **110**, A09S39, doi:10.1029/2004JA010984, 2005 17, 58, 82, 83, 84, 96, 100

Rozanov, E., L. Callis, M. Schlesinger, F. Yang, N. Andronova and V. Zubov, Atmospheric response to NO_y source due to energetic electron precipitation, *Geophys. Res. Lett.*, **32**, L14811, doi:10.1029/1005GL023041, 2005 82

Russell, C.T. and R.C. Elphic, ISEE observations of flux transfer events at the dayside magnetopause, *Geophys. Res. Lett.*, **6**, p. 33, 1979 104

Sander, S.P., B.J. Finlayson-Pitts, R.R. Friedl, D.M. Golden, R.E. Huie, H. Keller-Rudek, C.E. Kolb, M.J. Kurylo, M.J. Molina, G.K. Moortgat, V.L. Orkin, A.R. Ravishankara, P.W. Wine, Chemical Kinetics and Photochemical Data for Use in Atmospheric Studies, Evaluation Number 15, *JPL Publication*, **06-2**, Jet Propulsion Laboratory, 2006 83

Schätzing, F., Der Schwarm, *Fischer Verlag*, **3**. Auflage, 2005 157

Schmieder, K., Bremsvermögen und Trägerbildung der α-Strahlen in Gasen, *Annalen der Physik*, **427**, issue 5, p. 445–464, 1939 137

Schmidt, H., G.P. Brasseur, M. Charron, E. Manzini, M.A. Giorgetta and T. Diehl, The HAMMONIA chemistry climate model: sensitivity of the mesopause region to the 11-year solar cycle and CO_2 doubling, *J. Climate* **19**, p. 3902–3931, 2006 18, 33, 62, 82, 99, 100, 102, 148, 153, 165

Scholer, M., Reconnection on the Sun and in the magnetosphere, in: Klein, L., Energy conversation and particle acceleration in the solar corona, *Lecture notes in Physics*, **612**, Springer, Berlin, Heidelberg, 2003 104

Schraner, M., E. Rozanov, C.S. Poberaj, P. Kenzelmann, A.M. Fischer, V. Zubov, B.P. Luo, C.R. Hoyle, T. Egorova, S. Fueglistaler, S. Broennimann, W. Schmutz and T. Peter, Technical Note: Chemistry-climate model SOCOL: version 2.0 with improved transport and chemistry/microphysics schemes, *Atmos. Chem. Phys.*, **8**, p. 5957–5974, 2008 148, 153, 166

Schröter J., B. Heber, F. Steinhilber and M.-B. Kallenrode, Energetic particles in the atmosphere: a Monte Carlo approach, *Adv. Space Res.* **37**, (8), p. 1597–1601, 2006. 18, 19, 24, 33, 40, 60, 66, 68, 137, 147, 154

Schulz, M., Magnetosphere in: Handbook of the Solar-Terrestrial Environment, *Springer Verlag*, doi:10.1007/11367758_1, 2007 14

Seppälä, A., P.T. Verronen, E. Kyrölä, S. Hassinen, L. Backman, A. Hauchecorne, J.L. Bertaux and D. Fussen, Solar proton events of October–November 2003: Ozone depletion in the Northern Hemisphere polar winter as seen by GOMOS/Envisat, *Geophys. Res. Lett.* **31**, 31, L19107, doi:10.1029/2004GL021042, 2004 83

Seppälä, A., P.T. Verronen, M.A. Clilverd, C.E. Randall, J. Tamminen, V. Sofieva, L. Backman and E. Kyrölä, Arctic and Antarctic polar winter NO_x and energetic particle precipitation in 2002–2006, *Geophys. Res. Lett.*, **34**, L12810, doi:10.1029/2007GL029733, 2007 82

Seppälä, A., C.E. Randall, M.A. Clilverd, E. Rozanov and C.J. Rodger, Geomagnetic activity and polar surface air temperature variability, *J. Geophys. Res.* **114**, A10312, doi:10.1029/2008JA014029, 2009 13

Shaviv, Nir J., Racah Institute of Physics, Hebrew University of Jerusalem, photography from the aurora taken in northern Finland, 2009 16

Shine, K., The middle atmosphere in the absence of dynamical heat fluxes, *Quarterly Journal of the Royal Meteorological Society*, **113**, p. 603–633, 1987 83

Simnett, G.M., Near-relativistic electron emission following the 28 October 2003 X17 flare, *J. Geophys. Res.*, **110**, A09S01, doi:10.1029/2004JA010789, 2005 83

Sinnhuber, B.-M., M. Weber, A. Amankwah and J.P. Burrows, Total ozone during the unusual Antarctic winter of 2002, *Geophys. Res. Lett.*, **30**, p. 1580, doi:10.1029/2002GL016798, 2003 83, 148, 153, 165

Sinnhuber, B.-M, O. von der Gathen, M. Sinnhuber, M. Rex, G. König-Langlo and S.J. Oltmans, Large decadal scale changes of polar ozone suggest solar influence, *ACP*, p. 1835–1841. SRef-ID: 1680–7324/acp/2006-6-1835, 2006 82, 90, 96

Sinnhuber, M., J.P. Burrows, M.P. Chipperfield, C.H. Jackman, M.-B. Kallenrode, K.F. Künzi and M. Quack, A model study of the impact of magnetic field structure on atmospheric composition during solar proton events, *Geophys. Res. Lett.*, **30** (15), p. 1818, doi:10.1029/2003GL017265, 2003 3, 4, 12, 83

Sinnhuber, M., S. Kazeminejad and J.M. Wissing, Interannual variation of NO_x from the lower thermosphere to the upper stratosphere in the years 1991–2005, *J. Geophys. Res.*, doi:10.1029/2010JA015825, in press. 161

Solomon, S. and P.J. Crutzen, Analysis of the August 1972 Solar Proton Event Including Chlorine Chemistry, *J. Geophys. Res.*, **86** (C2), p. 1140–1146, 1981 11

Solomon, S., D. Rusch, J. Gerard, G. Reid and P. Crutzen, The Effect of Particle-Precipitation Events on the neutral and Ion Chemistry of the middle Atmosphere. II - Odd Hydrogen, *Planetary and Space Science*, **29**, p. 885–892, 1981 3, 4, 83, 102

Spamer, T., Quiet Time Precipitation Patterns of Energetic Particles, Bachelor thesis, University of Osnabrück, 2010 155

Tapping, K.F. and B. DeTracey, The origin of the 10.7 cm flux, *Solar Physics*, **127**, p. 312–332, 1990 34

Thorne, R.M., Energetic radiation belt electron precipitation: a natural depletion mechanism for stratospheric ozone, *Science*, **197**, p. 287–289, 1977 17, 47, 82, 100

Tohmatsu, T., Compendium of Aeronomy, translated and revised by Ogawa T., *Terra Sci. Publ. Comp.*, 1990 18

Turunen, E., EISCAT incoherent scatter radar observations and model studies of day to twilight variations in the D-region during the PCA event of August 1989, *Journal of Atmospheric and Terrestrial Physics*, Vol. **55**, No 4/5, p. 767–781, 1993 100

Valentine, J.M. and S.C. Curran, Average energy expenditure per ion pair in gases and gas mixtures, *Repts. Progr. in Phys.*, **21**, doi:10.1088/0034-4995/21/1/301, 1958 135

Vampola, A.L. and D.J. Gorney, Electron Energy Deposition in the Middle Atmosphere, *Journal of Geophysical Res.*, **88**, No. A8, p. 6267–6274, 1983 36

Verronen, P.T., E. Turunen, T. Ulich and E. Kyrölä, Modelling the effects of the October 1989 solar proton event on mesospheric odd nitrogen using a detailed ion and neutral chemistry model, *Ann. Gepophys.* **20**, p. 1967–1976, 2002 17, 58

Verronen, P.T., A. Seppälä, M.A. Clilverd, C.J. Rodger, E. Kyrölä, C.-F. Enell, T. Ulich and E. Turunen, Diurnal variation of ozone depletion during the October–November 2003 solar proton events, *J. Geophys. Res.*, **110**, A09S32, doi:10.1029/2004JA010932, 2005 83

Verronen, P.T., Ionosphere-atmosphere interaction during solar proton events, Doctoral dissertation, *University of Helsinki*, May 2006 102

Vette, J.I., The AE-8 Trapped Electron Model Environment, *NSSDC/WDC-A-R&S* **91-24**, 1991 141, 142

Waldteufel, P., Combined Incoherent-Scatter F1-Region Observations, *J. Geophys. Res.*, **76**(28), p. 6995-–6999, doi:10.1029/JA076i028p06995, 1971 104

Walt, M., W.M. McDonald and W.E. Francis, Penetration of auroral electrons into the atmosphere, in Physics of the Magnetosphere, edited by R.L. Caravillano, J.F. McClay, and H.R. Radoski, p. 534, D. Reidel, Norwell, Mass., 1968 19

Wedde, T. , G. Skovli, R. Amundsen, K. Aarsnes, H.R. Lindalen and F.Söraas, High latitude electron and proton precipitation at different local times and magnetic activity, *J. Atmos. Terr. Phys.* **35**, p. 2191–2203, 1973 55

Weeks, L.H., R.S. CuiKay and J.R. Corbin, Ozone measurements in the mesosphere during the solar proton event of 2 November 1969, *J. Aimos. Sci.*, **29**, p. 1138–1142, 1972 11

Wilkinson, D.C., NOAA GOES-Webside, `http://www.ngdc.noaa.gov/stp/satellite/goes/index.html` at date: 2010-10-22 26

Williams, D.J., A 27-Day Periodicity in Outer Zone Trapped Electron Intensities, *J. Geophys. Res.*, **71**, No. 7, p. 1815–1826, doi:10.1029/JZ071i007p01815, 1966 131

Winkler, H., M. Sinnhuber, J. Notholt, M.-B. Kallenrode, F. Steinhilber, J. Vogt, B. Zieger, K.-H. Glassmeier and A. Stadelmann, Modeling impacts of geomagnetic field variations on middle atmospheric ozone responses to solar proton events on long timescales, *J. Geophys. Res.*, **113**, D02302, doi:10.1029/2007JD008574, 2008 83

Wissing, J.M., J.P. Bornebusch and M.-B. Kallenrode, Variation of energetic particle precipitation with local magnetic time, *Adv. Space Res.* **41**, p. 1274–1278, 2008 17, 18, 58, 63, 84, 151

Wissing, J.M. and M.-B. Kallenrode, Atmospheric Ionization Module OSnabrück (AIMOS) 1: A 3-D model to determine atmospheric ionization by energetic charged particles from different populations, *J. Geophys. Res.*, **114**, A06104, doi:10.1029/2008JA013884, 2009 82, 84, 85, 89, 96, 100, 101, 102, 106, 109, 111, 151

Wissing, J.M., M.-B. Kallenrode, N. Wieters, H. Winkler and M. Sinnhuber, Atmospheric Ionization Module Osnabrück (AIMOS): 2. Total particle inventory in the October/November 2003 event and ozone, *J. Geophys. Res.*, **115**, A02308, doi:10.1029/2009JA014419, 2010 55, 151, 153, 154

Wissing, J.M., M.-B. Kallenrode, J. Kieser, H. Schmidt, M.T. Rietveld, A. Strømme and P.J. Erickson, Atmospheric Ionization Module OSnabrück (AIMOS) 3: Comparison of electron density simulations by AIMOS-HAMMONIA and incoherent scatter radar measurements, *J. Geophys. Res.* **116**, A08305, doi:10.1029/2010JA016300, 2011 118, 152, 153

Zhu, X. and Talaat, E.R. and Baker, J.B.H. and Yee, J.H., A self-consistent derivation of ion drag and Joule heating for atmospheric dynamics in the thermosphere, *Annales Geophysicae*, Vol. **23**, Issue 10, p. 3313–3322, 2005 102

Zurbuchen, T.H., G. Gloeckler, F. Ipavich, J. Raines, C.W. Smith and L.A. Fisk, On the fast coronal mass ejections in October/November 2003: ACE-SWICS results, *Geophys. Res. Lett.* **31**, L11805, doi:10.1029/2004GL019461, 2004 83

Erklärung über die Eigenständigkeit der erbrachten wissenschaftlichen Leistung

Ich erkläre hiermit, dass ich die vorliegende Arbeit ohne unzulässige Hilfe Dritter und ohne Benutzung anderer als der angegebenen Hilfsmittel angefertigt habe. Die aus anderen Quellen direkt oder indirekt übernommenen Daten und Konzepte sind unter Angabe der Quelle gekennzeichnet. Die Co-Autoren der Veröffentlichungen sind zu Beginn des jeweiligen Papers namentlich genannt.

Weitere Personen oder Organisationen waren an der Erstellung der vorliegenden Arbeit nicht beteiligt. Insbesondere habe ich hierfür nicht die entgeltliche Hilfe von Vermittlungs- bzw. Beratungsdiensten (Promotionsberater oder andere Personen) in Anspruch genommen. Niemand hat von mir unmittelbar oder mittelbar geldwerte Leistungen für Arbeiten erhalten, die im Zusammenhang mit dem Inhalt der vorgelegten Dissertation stehen. Die Arbeit wurde bisher weder im In- noch im Ausland in gleicher oder ähnlicher Form einer anderen Prüfungsbehörde vorgelegt.

Ort, Datum Jan Maik Wissing